Simulating the interaction of galaxies and the intergalactic medium

Robert Andrew Crain

Ph.D. Thesis, September 2008

Abstract

The co-evolution of galaxies and the intergalactic medium as a function of environment is studied using hydrodynamic simulations of the ΛCDM cosmogony. It is demonstrated with non-radiative calculations that, in the absence of non-gravitational mechanisms, dark matter haloes accrete a near-universal fraction ($\sim 0.9\Omega_b/\Omega_m$) of baryons. The absence of a mass or redshift dependence of this fraction augurs well for parameter tests that use X-ray clusters as cosmological probes. Moreover, this result indicates that non-gravitational processes must efficiently regulate the formation of stars in dark matter haloes if the halo mass function is to be reconciled with the observed galaxy luminosity function.

Simulations featuring stellar evolution and non-gravitational feedback mechanisms (photo-heating by the ultraviolet background, and thermal and kinetic supernovae feedback) are used to follow the evolution of star formation, and the thermo- and chemodynamical evolution of baryons. The observed star formation history of the Universe is reproduced, except at low redshift where it is overestimated by a factor of a few, possibly indicating the need for feedback from active galactic nuclei to quench cooling flows around massive galaxies. The simulations more accurately reproduce the observed abundance of galaxies with late-type morphologies than has been reported elsewhere.

The unique initial conditions of these simulations, based on the Millennium Simulation, allow an unprecedented study of the role of large-scale environment to be conducted. The cosmic star formation rate density is found to vary by an order of magnitude across the extremes of environment expected in the local Universe. The mass fraction of baryons in the observationally elusive warm-hot intergalactic medium (WHIM), and the volume filling factor that this gas occupies, is also shown to vary by a factor of a few

across such environments. This variation is attributed to differences in the halo mass functions of the environments.

Finally, we compare the X-ray properties of haloes from the simulations with the predictions of the White and Frenk (1991) analytic galaxy formation model, and demonstrate that deviations from the analytic prediction arise from the assumptions i) that haloes retain their cosmic share of baryons, and ii) their gas follows an isothermal density profile. The simulations indicate that a significant fraction of gas is ejected from low mass haloes by galactic superwinds, leading to a significant increase in their cooling time profiles and an associated drop in their soft X-ray luminosities, relative to the analytic model. Simulated X-ray luminosities remain greater than present observational upper limits, but it is argued that the observations provide only weak constraints and may suffer from a systematic bias, such that the mass of the halo hosting a given galaxy is overestimated. This bias also follows from the assumption that haloes exhibit isothermal density profiles.

Simulating the interaction of galaxies and the intergalactic medium

Robert Andrew Crain

A thesis submitted to the University of Durham
in accordance with the regulations for
admittance to the Degree of Doctor of Philosophy.

Institute for Computational Cosmology
Department of Physics
University of Durham
September 2008

Contents

List of Figures

List of Tables

Declaration

The work described in this thesis was undertaken between 2004 and 2008 while the author was a research student under the supervision of Prof. Carlos S. Frenk and Dr. Adrian R. Jenkins at the Institute for Computational Cosmology in the Department of Physics at the University of Durham. This work has not been submitted for any other degree at the University of Durham or any other university.

Parts of this work have appeared in the following paper:

- Crain, Robert A.; Eke, Vincent R.; Frenk, Carlos S.; Jenkins, Adrian; McCarthy, Ian G.; Navarro, Julio F.; Pearce, Frazer R., 2007, MNRAS, 337, 41C (Chapter 3)

All figures were produced by the author, except the following:

- Figure 1.1: NASA, ESA, S. Beckwith and the HUDF team
- Figure 1.2: The author and J.E Geach
- Figure 1.4: V. Quilis, B. Moore and R.G. Bower
- Figure 1.5: D. Clowe and collaborators
- Figure 1.6: C.S. Frenk
- Figure 2.1: Public domain image

The GADGET simulation code used throughout this thesis was written by Volker Springel (MPA, Germany). Modules of the GADGET3-BG variant were also written by Joop Schaye, Claudio Dalla Veccia & Rob Wiersma (Leiden Observatory, Netherlands), Tom Theuns (ICC, UK) and Luca Tornatore (SISSA, Italy). The SUBFIND code used here was written by Volker Springel and Klaus Dolag (MPA, Germany). All other software used here was written by the author.

Details of where simulations were run, and by whom, is provided below:

- RADIATIVE DWARF, Chapter 2: run by the author on the COSMA supercomputer, ICC, Durham University, UK.
- HIGH-MASS: run by F.R. Pearce (Nottingham University) on the JUPITER supercomputer, Nottingham University, UK. Baryon fraction analysis of this simulation also provided by F.R. Pearce.
- LOW-MASS: run by the author on the University) on the JUPITER supercomputer, Nottingham University, UK.
- DWARF: run by the author on the COSMA supercomputer, ICC, Durham University, UK.
- PANCAKE: run by the author on the COSMA supercomputer, ICC, Durham University, UK.
- GIMIC: run by A.R. Jenkins, T. Theuns and the author (ICC, Durham, UK) on the HPCX supercomputer, EPCC, Edinburgh University, UK and the COSMA supercomputer, ICC, Durham University, UK.

Acknowledgements

My sincere thanks to my supervisors, Carlos Frenk and Adrian Jenkins; research under their tutelage has presented me with fantastic opportunities. If a fraction of Carlos' scientific creativity and oratory brilliance, or of Adrian's attention to detail and mathematical wizardry, have rubbed off, I'll probably be ok. From day one, Vince Eke has always offered an open door and free advice on Numerical Recipes, the misuse of split infinitives and much more besides. Tom Theuns has had a huge impact on my work, steering me in the direction of GIMIC. Tom's willingness to try new methods of problem solving has changed the way I go about my work (mostly for the better), and his help with the analysis of the project has been invaluable. I've also been lucky to share Julio Navarro's expertise when in Durham; his contribution to my preheating paper was considerable. Amongst the less well paid people I've learned from: my thanks to Ian McCarthy, Takashi Okamoto, John Helly and Claudio Dalla Vecchia, without whom I'd never have learnt the importance of entropy or how to write code. My immeasurable gratitude also to the superhuman Lydia Heck, without whom the Universe would probably cease to function; I hope my departure grants her a little respite.

Durham has provided me with a great bunch of friends, too many to mention, but it'd be remiss of me to not mention Noam Libeskind and Richard Whitaker who first welcomed me into OC320, my former housemates Hugh Dickinson, Gareth Jones and (the irrepressible) Mark Norris, and great friends like Craig Booth, Kristen Coppin, Greg Davies, Andreea Font, David Murphy, Nic Ross and John Stott. Recently I've been indebted to David Wake, Tim Rawle and Ian McCarthy for keeping me within sight of the straight-and-narrow, and a special thanks to Jim Geach who, in addition to being a bloody good mate, is a master jokesmith (in training) and the only person willing to embark upon crazy schemes like volume rendering and Gout Night with me.

None of this would have been possible without my family. Kate, Nic and Greg have each ferried me and my belongings up the A1 over the last eight years and offered support for my perpetual studenthood and need to understand things seemingly irrelevant to most people. But most importantly, my greatest thanks is, of course, reserved for my parents. Without their love and support I could never have come this far. This thesis is for them.

Chapter 1 | *Introduction*

1.1 Background

The origin of cosmic structure is a broad and fundamental problem in modern Physics. It is underpinned by the events that took place in the earliest instants of cosmic history, and by the nature of the components that comprise the Universe. That our leading theories of cosmic evolution require the greater part of these components to be in forms that remain uncertain and potentially unknown to modern Physics - that is, *dark matter* and *dark energy*, collectively the *dark sector* - highlights the exciting challenges that lay ahead for cosmologists, astronomers and fundamental physicists alike.

This thesis, however, focusses primarily on evolution of the more familiar *baryons*, the matter with which we are all familiar from daily experience, under the influence of dark matter and dark energy. Modern cosmology posits that baryons represent only ~ 5 per cent of the content of the Universe, but they are of course the critical minority, since it is from the baryons that life itself is derived. From the practical point of view of the astronomer, baryons are also critical since they illuminate the Universe via the formation of stars, galaxies and quasars.

Moreover, it may be argued that the evolution of the cosmic baryons poses greater and more immediate questions to contemporary cosmology[1] than the dark sector, for two key reasons. Firstly, whilst our understanding of the dark sector is limited, in the context of cosmological structure formation it appears that the evolutionary effects of both dark matter and dark energy are relatively simple and well understood. In contrast, baryons are influenced by a richer array of physical processes, and it is the complexity of these processes that leaves the evolution of baryons, and in particular the formation of galaxies, as the most uncertain element in contemporary theories of structure formation.

[1]Throughout this thesis, we shall treat the astrophysics of baryons as a problem within the remit of cosmology.

Secondly, attempts to validate these theories by performing observational censuses of the baryons throughout the cosmos have so far found (approximately) only one half of the mass expected. Supposing the theories are accurate, it appears that Nature has hidden most of the cosmos from us, and then made most of that we should be able to see very difficult to find.

This latter point is succinctly illustrated by Figure 1.1. It shows the Hubble Ultra Deep Field (HUDF, Beckwith et al., 2006), the deepest image of the Universe ever taken in the visible spectrum. Of the ten thousand galaxies it captures, the most distant are seen as they were over thirteen billion years ago, when the Universe was only several hundred thousand years old. The fraction of the entire sky that is covered by the HUDF is tiny, approximately one part in thirteen million, and so it follows that the observable Universe is extraordinarily rich in galaxies. Yet in spite of the huge number of galaxies we can observe, each of which may have a stellar mass that is many billions of times the mass of the Sun, current theories estimate that at the present epoch galaxies represent only ~ 2.5 per cent (by mass) of all baryons (Bell et al., 2003; Eke et al., 2005), and so contribute ~ 0.1 per cent of the energy density of the Universe (Bennett et al., 2003; Spergel et al., 2003; Fukugita and Peebles, 2004; Spergel et al., 2007). By observing galaxies alone, we would fail to notice most of the cosmos, and so one must look to the vast regions between the galaxies in order to find the majority of the baryonic mass. This extra-galactic reservoir is, to use the term in its most general sense, the *intergalactic medium* (e.g. Field, 1972).

This diffuse gas was first probed by in detail by Gunn and Peterson (1965), who noticed the absorption of quasar light by intervening neutral hydrogen at the wavelength of the Lyman-α (hereafter Lyα) resonance transition. Quasar absorption spectra have since demonstrated that the IGM is mostly a plasma (ionised gas) whose temperature varies from a few thousand degrees Kelvin in the most under-dense regions, to hundreds of millions of degrees Kelvin in the centres of rich galaxy clusters. Figure 1.2 illustrates the spatial relationship between galaxies and the large-scale structure of dark matter that is traced by the IGM; in addition it provides a sense of the relative spatial scales that shall be contemplated throughout this thesis. The left hand box shows the present day large-scale distribution of dark matter within a simulated volume of side 500 h^{-1} Mpc, a volume comparable to that probed by the current generation of 'local' galaxy redshift

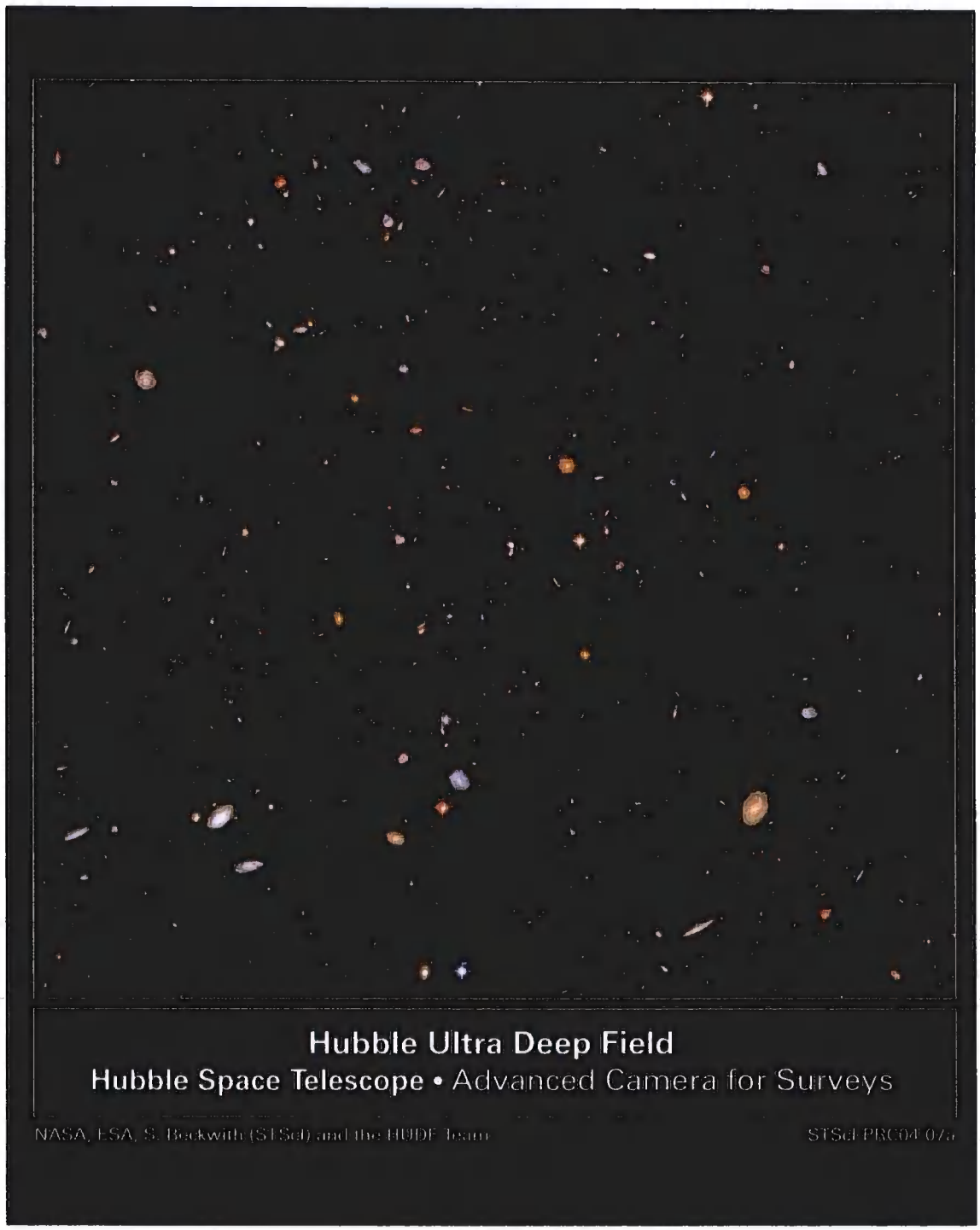

Figure 1.1: The Hubble Ultra Deep Field, the deepest optical-waveband image of the cosmos to be captured to date. The image peers back over 13 billion years, and contains approximately 10,000 galaxies whilst covering a tiny fraction (1 part in 13 million) of the entire sky. Actively star-forming galaxies are dominated by the blue light from short-lived, massive stars, whilst the light from dormant galaxies is primarily the redder light produced by older, less massive stars.

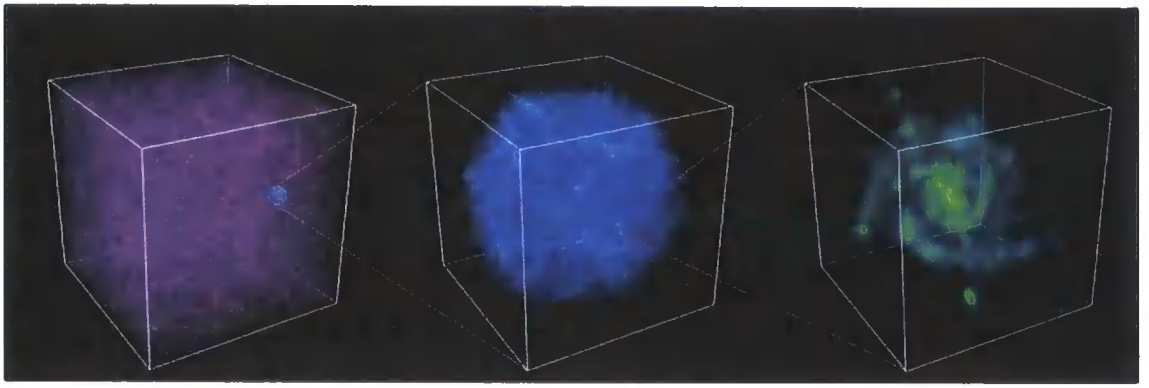

Figure 1.2: A demonstration of the dynamic range one must consider in cosmology. The left-hand panel shows the distribution of dark matter in a volume similar to that probed by the largest modern galaxy redshift surveys. The centre panel zooms in by a factor of ten to highlight the filamentary structure of the dark matter and its associated IGM. The right-hand panel zooms further by another factor of one thousand to show the intricate detail of a simulated spiral galaxy that is similar in size to our own Milky Way.

surveys, such as the Two-degree Field Galaxy Redshift Survey (2dFGRS, Colless et al., 2001) and the Sloan Digital Sky Survey (SDSS, York et al., 2000). The centre box zooms in by a factor of ten ($L = 50\,h^{-1}$ Mpc) to show in greater detail the characteristic filamentary structure of dark matter that is commonly referred to as the 'cosmic web'. Since the IGM closely traces the dark matter distribution when they are both at densities that are not greater than a few times the cosmic average, the left-hand and centre panels are also illustrative of the distribution of diffuse gas on large-scales. It is within the dense nodes that are strung along filaments where roughly spherical regions of dark matter collapse to form 'haloes'. The accretion of associated gas onto haloes triggers rapid radiative cooling that eventually leads to the formation of stars; the right-hand panel zooms in (by a further factor of one thousand) to show such a galaxy.

The relationship between galaxies and the IGM is dynamic and often dramatic. When the Universe was only a few hundred million years old the IGM was 'pristine', composed primarily of hydrogen that had cooled into the neutral, atomic state. In the absence of heavy elements that are later synthesised by nuclear processes in stellar cores, the first generation of stars, known as Population III objects, were necessarily very massive ($\sim 30 - 100$ M$_\odot$) and highly luminous (e.g. Abel et al., 2002; Bromm et al., 2002).

Figure 1.3: Violent gas and dust outflows in the disc galaxy M82, driven by winds that are triggered by ongoing star formation. These outflows have a dramatic effect upon the surrounding gas, potentially playing a key role the enrichment of the IGM and the regulation of galaxy growth.

Their copious ultraviolet emission is believed to have rapidly ionised all of the neutral hydrogen in the cosmos, a process termed cosmic reionisation[2]. That stars and galaxies enacted such a rapid and wholesale phase transition upon the very material from which they were derived highlights the strength of their mutual interaction with the IGM.

Dramatic interactions are not limited to the early Universe; Figure 1.3 shows the local starburst galaxy Messier 82 (M82), in a composite image formed from the compilation of infrared, visible and X-ray observations from the *Spitzer*, *Hubble* and *Chandra*

[2]The gas is said to be *re*ionised since in its first $\sim 10^5$ years the Universe had been too hot and dense for hydrogen to exist in the atomic state.

space telescopes respectively. The image is shown in false colour to illustrate the emission from outside of the visible spectrum: infrared emission is shown in red, the visible light is compressed into the orange-yellow-green part of the spectrum, whilst the X-ray emission appears blue. In order to emit X-rays, gas must reach very high-temperatures, at least several million degrees Kelvin, and consequently the prominent blue plumes emerging from the galaxy indicate the outflow of hot, energetic gas into the IGM. Such outflows are believed to be driven by many supernovae (SNe) detonations - the violent explosions that result when massive stars exhaust their nuclear fuel supply - that coalesce into galactic-scale outflows, or *winds*. Since the rate of SNe is directly linked to the rate at which a galaxy produces stars (e.g. Martin, 1999), it is not surprising that, in addition to an exceptional mass outflow rate, M82's exhibits a star formation rate that is ten times greater than the Milky Way (Barker et al., 2008).

The generation of outflows appears to be very common at early times, when star-forming galaxies are efficiently identified via their colours (as opposed, say, to their flux). The atmospheres of massive stars produce a very pronounced break in the Lyman continuum emission at 912Å, the 'Lyman-break'. The Doppler shift of light due to the expansion of the Universe, known as redshift, z, brings this far-ultraviolet feature into the optical spectrum for distant objects, and so the use of three band-pass filters (say U, G and R for $z \simeq 3$ or G, R, I for $z \simeq 4$) allows two colours to be measured that bracket this feature. The candidate galaxies are then readily identified since they appear very faint in the bluest filter (that transmitting the shortest wavelength light), yet bright in the redder (longer wavelength) ones, leading to the name 'dropouts' (e.g. U-band dropouts at $z \simeq 3$, G-band dropouts at $z \simeq 4$), or 'Lyman-break galaxies' (LBGs). Ambitious dropout surveys have yielded many thousands of 'regular' (although actively star-forming) galaxies at high redshift, and spectroscopic follow-up of these has shown that outflowing features - indicative of winds, and visible due to their redshift offset from the central galaxy - are common (Steidel et al., 2000; Pettini et al., 2001, 2002b,a; Steidel et al., 2002; Adelberger et al., 2003; Wilman et al., 2005). The apparent ubiquity of winds at early epochs has provided a plausible mechanism by which two key problems of cosmological relevance might not only be resolved, but also directly linked. Pettini (1999) first noted (but see also Pagel, 2002) that the mass of heavy elements locked up in LBGs falls far short of the quantity expected to be produced by stellar nucleosynthesis, suggesting that these

metals[3] either 'escape' from galaxies, or reside in some unobservable form. This apparent conflict has become known as the 'missing metals' problem. On the other hand, X-ray emission lines from heavy elements residing in the hot plasma of the intracluster medium (ICM) indicate that this baryon phase contains as much metal mass as the member galaxies of the group/cluster (Mushotzky et al., 1996; Renzini, 1997; Davis et al., 1999; Buote, 2000), demonstrating that significant fractions of the metals synthesised in a galaxy can indeed escape into the surrounding gas. However, as we shall discuss shortly, ram-pressure due to the hot plasma within groups and clusters is very effective at stripping gas (and metals) from galaxies, and so it was the detection of copious quantities of metals in the low-density gas of the diffuse IGM (Songaila and Cowie, 1996; Cowie and Songaila, 1998; Ellison et al., 2000) that firmly implicated winds as a mechanism for metal transport. The efficacy of this mechanism is highlighted by the early epochs ($z \gtrsim 6$) at which significant enrichment is detected (Becker et al., 2006; Ryan-Weber et al., 2006; Simcoe, 2006), and has driven considerable efforts to model this enrichment in simulations (e.g. Aguirre et al., 2001a,c,b; Thacker et al., 2002; Theuns et al., 2002; Oppenheimer and Davé, 2006; Davé and Oppenheimer, 2007).

It is not simply the case that galaxies affect the IGM; the converse is also true. Ram-pressure stripping of cold gas from galaxies that pass through the hot, pressurised gas at the centres of galaxy clusters is a prime example of this. Figure 1.4, taken from the simulations of Quilis et al. (2000), shows the dissipation of cold gas in a galaxy disc as it passes through the hot plasma of the intracluster medium at two different angles of incidence; in both cases the disc is stripped of all neutral hydrogen within 100 Myr. This mechanism is widely believed to be responsible for suppressing star formation in galaxies that are accreted onto galaxy clusters (e.g. Gunn and Gott, 1972; Dressler, 1980; Larson et al., 1980; Balogh et al., 2000; Quilis et al., 2000; Crowl et al., 2005; Baldry et al., 2006; Weinmann et al., 2006; McCarthy et al., 2008). The dramatic effect of ram-pressure stripping is consequently cited as a prime example of where the environment within which a galaxy and its host halo are embedded directly affects their evolution.

Reionisation, supernova feedback and ram-pressure stripping are fascinating examples of violent astrophysics, but it is their relevance to two aspects of modern cosmology that is the focus of this thesis. Firstly, the regulation of galaxy formation via baryon

[3]Elements with atomic number great than that of Helium are commonly termed 'metals' in astronomy

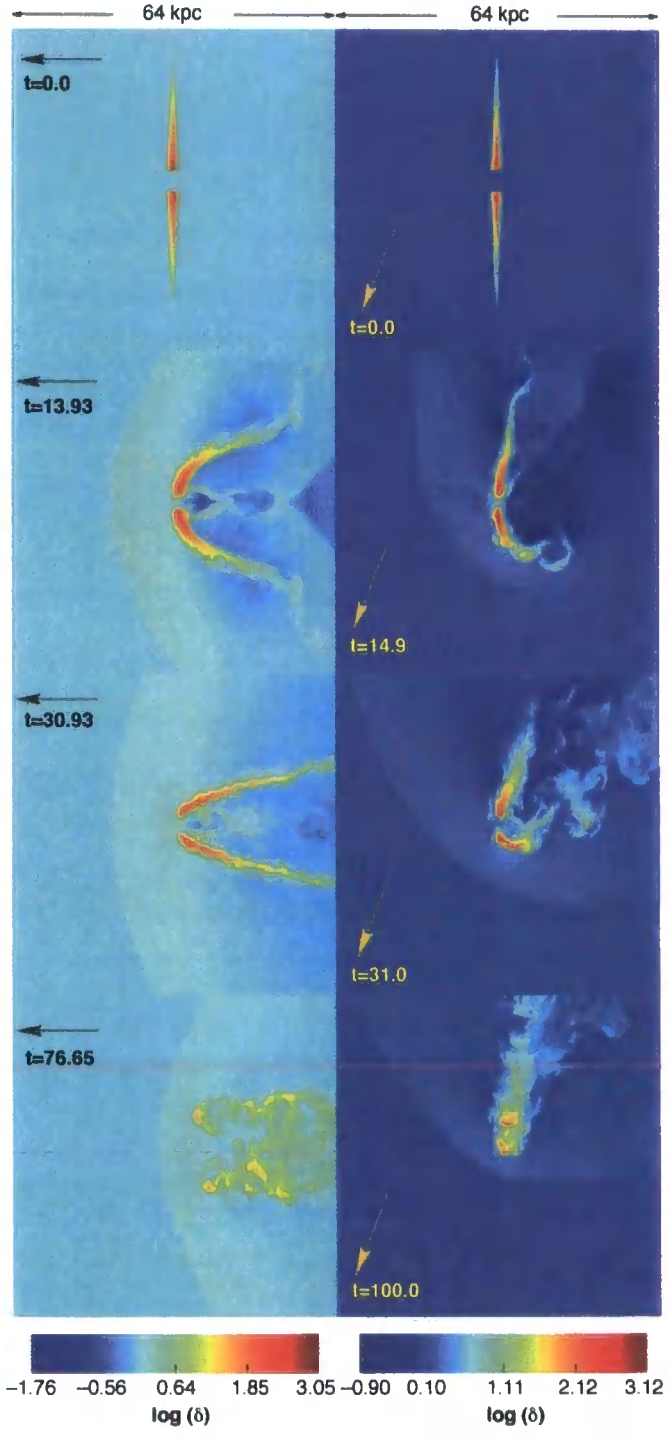

Figure 1.4: Snapshots from a simulation by Quilis et al. (2000) showing the effect of ram-pressure on the structure of a cold gas disc as it passes through the hot plasma of the intracluster medium. In the left-hand panel the disc is inclined face-on to the direction of motion, in the right-hand panel it is inclined at 20deg. In each case all disc gas is stripped within 100 Myr.

physics, in order that the star formation history of the Universe may be understood, and more specifically that the abundance of dark matter haloes expected within current cosmological models might be reconciled with the paucity and characteristics of observed galaxies. Secondly, elucidating the chemo- and thermodynamical evolution of the IGM. We therefore use supercomputer simulations of the formation of large-scale structures and galaxies to study the dynamic and evolving relationship between galaxies, the multiphase gas that is associated with their immediate environments, and the more diffuse gas at greater distances that comprises the IGM. Particular attention is paid to the processes that determine how gas becomes associated with dark matter haloes and is subsequently processed by radiative cooling, star formation and feedback due to SNe detonations. The role of large-scale environment in shaping these processes is also explored. By way of setting the scene for what follows in this thesis, this chapter begins by sketching a basic outline of the cosmological framework adopted herein.

1.2 Modern cosmology

Just as progress in the field is driven today, modern cosmology emerged from the synergy of key theoretical and observational advances. The former was the formulation of the General Theory of Relativity (Einstein, 1916), which describes gravity as a geometric property of space-time and remains today as the leading description of gravitation. The latter was the subsequent realisation (Hubble and Humason, 1931) that faint nebulae of stars external to the Milky Way - now known to be other galaxies - recede from the Milky Way with velocities, v, that increase in proportion to their distance from us, r, leading to the well known Hubble Law,

$$v = Hr, \tag{1.1}$$

where the proportionality constant, now known to vary over cosmic history but a constant over all space at any given epoch, is the *Hubble parameter*. This relation naturally leads to the notion, known as the *Cosmological Principle*, that the Universe, on large scales, is both isotropic (i.e. has no preferred direction) and homogeneous (i.e. has no preferred location). This principle, that until Hubble's discovery was merely a convenient *ansatz*, underpins all general relativistic theories of the dynamical evolution of the Universe.

The solution of the general relativistic field equations (Einstein, 1915) due to Fried-

man (1922) forms the basis of such dynamical models:

$$\frac{\ddot{a}}{a} = -\frac{4}{3}\pi G\left(\rho + 3\frac{P}{c^2}\right) + \frac{\Lambda}{3}c^2, \tag{1.2}$$

where $a(t)$ is the *expansion factor* of the Universe, normalised to unity at the present epoch. The matter-radiation fluid comprising the Universe is taken to have pressure, P, and density, ρ. The constants c and G are the speed of light and the gravitational constant respectively. The term Λ was added to the field equations (arbitrarily) by Einstein in order to facilitate solutions for a static Universe. The equation of state of the fluid can be posed as $P = w\rho c^2$; for a radiation-dominated fluid $w = 1/3$ whilst for pressureless fluids ('dust') $w = 0$. The Cosmological Principle requires that no heat flows into or out of the Universe - that it is *adiabatic* - and thus it is possible to recast Equation 1.2 as

$$H^2(a) \equiv \left(\frac{\dot{a}}{a}\right)^2 = \frac{8\pi G}{3}\rho + \frac{\Lambda}{3}c^2 - \frac{kc^2}{a^2}, \tag{1.3}$$

where $H(a)$ is the explicitly expansion-varying Hubble parameter, and k is the geometric curvature. Cast in this form, the Friedman equation reveals the intimate connection between the density and global geometry of the Universe. In the simplifying limit of no cosmological constant ($\Lambda = 0$), then for a specified expansion rate there exists a critical density, ρ_c, that yields a spatially flat Universe, $k = 0$, obeying Euclidean geometry:

$$\rho_c(a) = \frac{3H^2(a)}{8\pi G}. \tag{1.4}$$

In the case that the mean density of the Universe is super-critical, the curvature is positive, $k > 0$, and conversely a Universe that has sub-critical mean density exhibits negative curvature, $k < 0$. The simple Newtonian interpretation of the curvature indicates whether the density of the Universe is sufficient to gravitationally arrest its expansion. This is the case for positive curvature; the Universe is gravitationally bound and is destined to recollapse. Negatively curved models are unbound and destined to expand indefinitely, whilst critical Universes that exhibit no curvature represent the limiting case that the expansion continues for all times, but at an ever decreasing rate.

Since the ratio of the density of the Universe to the critical density so clearly defines its fate, it is conveniently expressed as a cosmological variable termed the *density parameter*:

$$\Omega_X = \frac{\rho_X}{\rho_c}, \tag{1.5}$$

The subscript X refers to a given component (or combination of components), for example radiation (γ), matter (m) or dark energy (Λ). Strictly, the total density parameter at the present epoch is denoted Ω_0, but we follow the convention of brevity and drop the subscript; the density parameter at other epochs shall therefore be denoted $\Omega(a)$. The density of these components evolves differently with the expansion; dust evolves $\propto a^{-3}$ simply by dilution, the density of radiation decreases more rapidly since an extra factor of a^{-1} is introduced by the redshift of its wavelength, whilst the dark energy density (if of the cosmological constant form) is independent of expansion factor since it is believed to be a property of space itself. This evolution is characterised observationally by the evolution of the Hubble parameter:

$$H(a) = H_0[\Omega_\Lambda + \Omega_m a^{-3} + \Omega_\gamma a^{-4} + (1 - \Omega_\Lambda - \Omega_m - \Omega_\gamma)a^{-2}]^{1/2}. \tag{1.6}$$

At this juncture, it is useful to introduce the concept of redshift, denoted z, which is simply related to the expansion factor a and is more directly observable, since:

$$z = \frac{\lambda_0 - \lambda_e}{\lambda_e} \tag{1.7}$$

where λ_0 is wavelength of radiation observed at time t_0, and λ_e is the wavelength of the same radiation when emitted at the earlier time, t_e, by a source that moves with the cosmological expansion. In this case it can be shown that $1 + z = a_0/a = 1/a$, and so all objects we observe have $z \geq 0$.

1.2.1 The inflationary Big Bang model

The Friedman equations show that models of the Universe composed of fluids described by $-1/3 < w < 1$ have a point in time where $a \to 0$ and the density diverges: the Big Bang (BB) singularity. For historical interest, it is noted that models circumventing what appears to be an instant of cosmic creation were constructed (e.g. 'steady-state' models Hoyle, 1948; Hoyle and Narlikar, 1964), but have been ruled out by observations of, chiefly, the cosmic microwave background (CMB) radiation and the cosmic abundance of deuterium. These observations are explained naturally by BB models. In spite of these successes, BB models were plagued by several problems:

- *The flatness problem*: the overall energy density of the Universe is of the order of the critical density, i.e. $\Omega \sim 1$. Energy densities of this order are unstable, since

slight perturbations away from $\Omega = 1$ at early times lead to rapid evolution away from this state. Therefore, within BB models, the current state of the Universe may only exist if its initial state was fine-tuned to one part in 10^{60} (e.g. Peacock, 1999) at the Planck time ($t \sim 10^{-43}$ s, the earliest epoch probed by current theories). Such a tuning process is not described by BB models.

- *Cosmological horizons*: whilst largely responsible for the preference of BB models over steady-state counterparts, the CMB radiation also poses a problem for the BB paradigm. The flux of the CMB is remarkably isotropic on the sky; angular deviations are of the order of one part in 10^5. This uniformity implies that the radiation was isotropic and homogeneous in regions on the *last scattering surface*, the spherical surface centered about an observer and at a distance corresponding to the look-back time of the epoch of recombination, $z_{\rm rec} \simeq 1000$. In order that anisotropies and inhomogeneities might be erased, one typically infers causal contact of photons within the entire volume enclosed by the last scattering surface, but the horizon for causal contact was approximately a factor of ten smaller than this at $z_{\rm rec}$ (e.g. Coles and Lucchin, 2002). BB models are unable to explain this apparent contradiction.

- *The monopole problem*: grand unified theories (GUTs), the leading descriptions of the early Universe, predict the existence of defects in the Higgs field that are manifest as massive magnetic monopole particles. Since no mechanism is known to remove such particles, their number density today is expected to be of the order of the baryon number density; this would yield an energy density of monopoles many, many orders of magnitude greater than unity.

These issues may be partially resolved by modifying the equation of state of the early Universe, such that it experienced a period throughout which it expanded faster than the photon horizon. Within such a model the causal horizon then encompasses the last scattering surface and the Universe is able to reach thermal equilibrium to within the levels required by observations of the CMB radiation. Inflationary models (e.g. Guth, 1981) posit such an expansion, (commonly exponential, $a(t) \propto e^{Ht}$), driven by a scalar field (or *inflaton*) whose potential later decays. Such expansion doubles (in fact, e-folds) the size of the Universe ~ 60 times (Peacock, 1999), with the effect of removing any

curvature from the geometry of the Universe ($k \rightarrow 0$), and diluting the number density of magnetic monopoles far beyond the level at which they would be observable.

Another attractive facet of inflationary theories is that they predict the existence of quantum fluctuations that are derived from the exponential expansion. In the absence of any mechanism to damp these fluctuations, they are subject to gravitational amplification throughout cosmic history and are consequently posited as the 'seeds' of all cosmological structure formation - responsible for all objects from galaxy clusters to human beings. Whilst bewildering, this possibility is of tremendous scientific appeal. Recent observations of both the CMB radiation by the *Wilkinson Microwave Anisotropy Probe* (WMAP) satellite (Spergel et al., 2003) and the clustering of galaxies by large-scale galaxy redshift surveys (Colless et al., 2001; York et al., 2000), indicate that the statistical distribution of structures is of the form expected to be produced by inflation: the scale-invariant Gaussian random field (e.g. Bardeen et al., 1986). Nonetheless, one should bear in mind that the development of inflationary models is driven primarily by phenomenology. Its predictions for the early Universe are consistent with observations but are not fully understood from first principles in a fashion that is consistent with the standard model of particle physics.

1.2.2 Dark matter

The existence of mass in a form that is detectable only via its gravitational effects, as opposed to, for example, emission or scattering of electromagnetic radiation, was inferred first by Zwicky (1933), whose modelling of the dynamics of massive galaxy clusters led him to infer that their mass was far in excess of that of the visible components. However, the significance of this discovery was overlooked for decades. The same situation was uncovered in spiral galaxies by Babcock (1939), who noted a steep rise in the mass-to-light ratio of our neighbouring galaxy M31 (Andromeda) as one moves to increasing galactocentric radii. Modern observations (a thorough review is given by Sofue and Rubin, 2001) show that galaxy rotation curves are near-universal in that they do not exhibit a Keplerian fall-off, $V \propto 1/r^{1/2}$, as would be expected if the mass enclosed within r converges to a constant value. On the contrary, that V remains constant to large radii (traced beyond the optical radius by neutral hydrogen and/or globular clusters) indicates that the enclosed mass is linearly divergent, $M(r) \propto r$. This simple observation is perhaps the

strongest evidence in support of a dark matter component in galaxies.

The modern view of galaxy groups and clusters remains similar to that found by Zwicky. In addition to the stellar component, the mass of hot gas bound to these massive overdensities is well constrained via its thermal bremsstrahlung emission in the X-ray range (e.g. Hughes, 1989; Vikhlinin et al., 2006; Croston et al., 2008), and is found to be larger than, but of the order of, their overall stellar mass; the luminous-to-dark mass ratio can therefore be ascertained. White et al. (1993) made this measurement for the Coma cluster, finding the baryon mass to be approximately 10 per cent of the overall mass. Galaxy clusters are also used in other, independent, tests of dark matter, for instance through the thermal Sunyaev-Zel'dovich effect (e.g. Sunyaev and Zel'dovich, 1980) which, as noted by Peacock (1999) compliments the former method since it has different dependencies on the electron density, n_e and the Hubble parameter.

Perhaps the most exciting test for the existence of dark matter is via direct imaging by gravitational lensing. Lensing tests have endured a chequered history, with discrepancies relative to X-ray methods of factors ~ 2 (Miralda-Escude and Babul, 1995). More recently, however, observations of the 'bullet cluster' (Figure 1.5), a very rare merger between two galaxy clusters, have been cited as direct empirical evidence of the existence of dark matter (Clowe et al., 2006). The concept of the test is simple: the kinetic energy of each cluster's gas component is violently thermalised by a hydrodynamic shock as the systems collide. The gas distribution is therefore readily imaged via X-ray emission. The galaxies are also easily traced with optical observations, whilst lensing of background objects by the gravitational potential of the merging systems indirectly images the overall mass distribution. Since this distribution clearly does not trace the dominant baryonic component, the hot gas that has collided, this system provides compelling evidence in support of a dark component. The evidence is particularly attractive since the mass distribution appears to trace two distinct clumps whose dynamics are consistent with a collisionless fluid of *cold dark matter* (Springel and Farrar, 2007), the form preferred by the current paradigm.

The precise nature of dark matter remains unclear. The simplest solution is, of course, that it is merely baryons in states that are difficult to detect owing to their compact size and/or weak electromagnetic emission. The catch-all term of massive compact halo objects (MACHOs) has been coined for these objects, such as black holes, neutron stars

Figure 1.5: The merging galaxy cluster 1E 0657-56, commonly known as the 'bullet cluster'. Most baryonic mass is in the form of hot gas (pink), imaged here via the X-ray emission it generates as it violently shocks. Analysis of the gravitationally lensed galaxies in the background demonstrates that most of the mass (blue) is located in two distinct structures that appear to have passed through each other, indicative of the presence of a collisionless dark matter fluid.

and brown dwarfs. However, limits set by detailed nucleosynthesis calculations indicate that Ω_b is much less than the value of Ω_m inferred from observations of clusters and the CMB power spectrum, so it appears that nuclear material is not the dominant mass component in the cosmos. Since nucleosynthesis considers reaction pathways involving baryons, photons and neutrinos, the latter, which we shall denote ν, is an obvious candidate for the dark matter particle. Whilst the standard model of particle physics posits that neutrinos are massless, a small mass can be accommodated by nucleosynthesis calculations, and in fact the phenomenon of *neutrino oscillation*, recently observed by the Super-Kamiokande experiment (Mohapatra et al., 2007), requires that the neutrino has mass. However, detailed analysis of a wealth of cosmological data, including the CMB radiation, distant SNe and the Lyα forest, allow a stringent upper limit to be placed on the contribution of neutrino mass to the overall matter density, and it is found to fall well short of the required level (Goobar et al., 2006).

Although recent analyses rule out the neutrino as a candidate for the dominant form of dark matter, this result has been suspected for some time. Non-baryonic dark matter candidates are commonly classified by their velocities at the epoch of matter-radiation decoupling; fast moving (relativistic) particles are termed *hot dark matter* (HDM), in analogy to their large quasi-thermal velocities. Conversely, particles that were non-relativistic at decoupling, with a negligible thermal velocity, are termed *cold dark matter*. Structure evolution proceeds in a dramatically different fashion for fluids dominated by CDM and HDM. Were the early Universe dominated by neutrinos, their large velocities at high-redshift would readily enable them to escape, or *free-stream*, away from the overdensities believed to result from the quantum fluctuations created during inflation. This damps small-scale power in the density field, delays the onset of galaxy formation, and requires that the earliest systems to form in the Universe were the most massive: galaxy clusters. The existence of smaller galaxies therefore requires a cluster fragmentation mechanism to operate in the HDM scenario. Conversely, the absence of small-scale damping in CDM models implies that structure formation proceeds *hierarchically*, with small systems forming at early times and coalescing into ever larger systems over time. The contrasting power spectra of the HDM and CDM scenarios are shown in Figure 1.6. The choice of a candidate non-baryonic dark matter particle is not obvious, but in order to avoid altering very successful nucleosynthesis calculations its effects must be

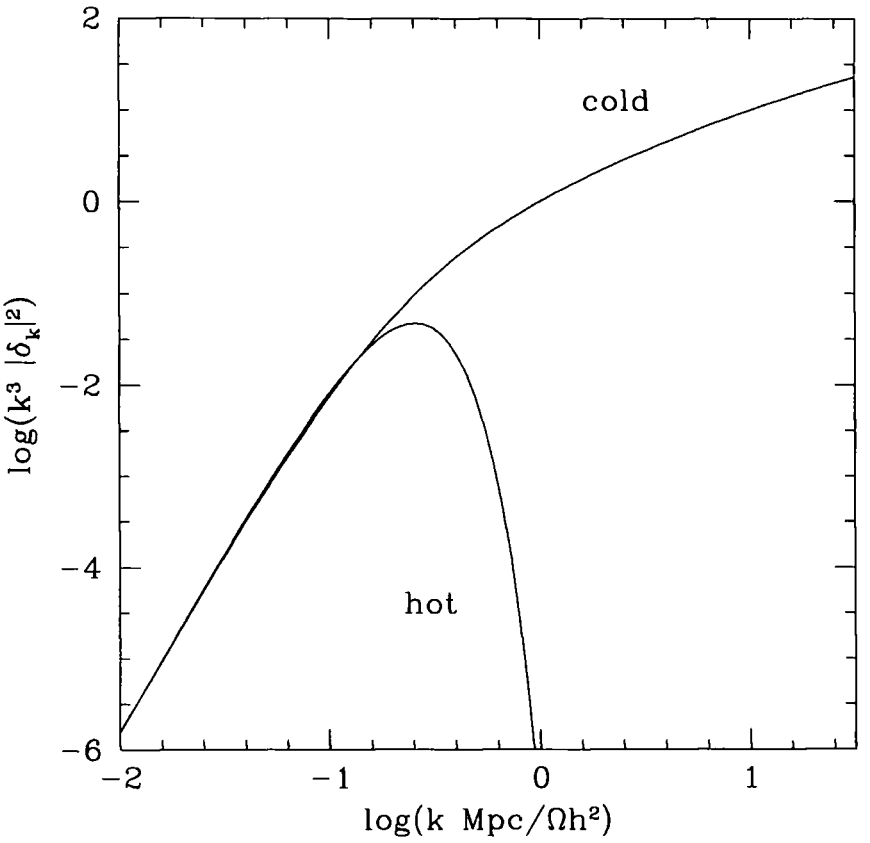

Figure 1.6: The linear power spectra of hot and cold dark matter. Large spatial scales correspond to the left-hand side of the x-axis. Whilst sharing similar power spectra on large scales, a cold dark matter Universe features much greater small-scale power since it is not affected by free-streaming due to large thermal motions in the fluid. Structure formation therefore proceeds hierarchically in cold dark matter models.

small, either by being very rare or even more weakly interacting than the neutrino. The consequence of either possibility is a fluid that, unlike one comprised of baryons, is *collisionless*.

So far we have outlined a framework that is based largely upon an analytical exploration of the early stages of the Universe. Constraints can also be made by studying the phenomenology of the Universe in its current state, and attempting to connect the two epochs. Since the gravitational evolution of fluids is strongly non-linear, this can only be achieved via direct numerical simulation of the fluid elements. This technique was introduced by Peebles (1970), who was largely responsible for the early development of CDM models (e.g. Peebles and Dicke, 1968; Peebles, 1970, 1971, 1973, 1974, 1980). This procedure was instrumental in establishing CDM, rather than HDM, as the leading description of matter evolution. In particular, an emphatic confirmation of the viability of the CDM paradigm was presented by Davis et al. (1985), whose models demonstrate the remarkable correspondence between the clustering of CDM structures and that of galaxies in the CfA redshift survey (Huchra et al., 1983).

1.2.3 Dark energy

In the previous section it was argued that X-ray observations provide compelling evidence that baryons contribute a relatively small fraction of the overall mass of galaxy clusters, thus highlighting the need for dark matter. In concert with nucleosynthesis arguments, the data are yet more instructive with regard to the composition of the Universe. White et al. (1993) demonstrated that, in spite of being a sub-dominant component, the mass density of baryons in the Coma cluster is at least three times greater than the global baryon mass density predicted by nucleosynthesis, if one assumes that $\Omega \equiv \Omega_{\rm m} = 1$. Since, as we shall demonstrate in unprecedented detail in Chapter 3, the overall baryon fraction of clusters is very similar to the global mean, this result indicates that at least one of two possibilities must be true: i) the very successful BB nucleosynthesis calculations are fundamentally flawed, or ii) the mean matter density is less than the critical density, $\Omega_{\rm m} < 1$. The latter possibility therefore requires a dark energy component, $\Omega_{\rm m} + \Omega_\Lambda = 1$, in order to render the Universe geometrically flat.

Since the White et al. study, clear evidence in favour of dark energy has emerged. Chief amongst these is the exquisite precision of cosmological parameter estimation

made possible by the WMAP satellite's detailed measurements of the CMB radiation. After three years of observations, the best estimate of the matter density parameter derived from these data is $\Omega_m h^2 = 0.1277^{+0.0080}_{-0.0079}$, where h represents a parametrisation of the Hubble parameter such that $H_0 = 100h$ km s^{-1} Mpc^{-1}. Assuming a canonical value of $h = 0.7$ (e.g. Freedman et al., 2001) yields $\Omega_m = 0.261$, an additional indication that some form of dark energy is required in order to flatten the Universe. Independent, and more direct evidence for dark energy has emerged in recent years via the use of type Ia SNe as standard candles. These allow a distance-redshift relation to be constructed over a significant fraction of cosmic history that illustrates the nature of the evolving cosmic expansion. Results from two independent teams (Riess et al., 1998; Perlmutter et al., 1999) demonstrated that the expansion history of the Universe is consistent with a flat Universe of matter density very similar to that inferred from the CMB power spectrum.

1.2.4 Towards a standard paradigm: ΛCDM

The remarkable agreement of cosmological models constrained by observations of the cosmic microwave background, the light element abundances, the large-scale structure of the Universe and the SNe Ia distance-redshift relation are compelling evidence in favour of a concordance cosmological framework. In the context of this thesis, this framework, which we term the Λ-cold dark matter (ΛCDM) paradigm, provides the stage upon which we shall conduct our tests of cosmological baryon physics. We shall summarise the paradigm before concluding this introductory chapter with a discussion of the motivation for our study:

- Dynamical models of the evolution of the Universe are constructed using the general theory of relativity under the assumption that the Universe is homogeneous and isotropic on large-scales.

- A period of rapid, exponential expansion shortly after the Big Bang, removed any traces of geometric curvature, allowed the Universe to attain thermal equilibrium to one part in 10^5, and imprinted quantum fluctuations that seeded the growth of all cosmic structure.

- Conservation of energy dictates that the expansion of the Universe is adiabatic, causing its mean temperature to drop with the expansion. When $T \simeq 3000$ K,

matter and radiation decoupled as the primordial plasma combined into neutral atoms. The relic radiation that last scattered at this epoch is observed now as a near-uniform cosmic microwave background radiation field with a near-perfect blackbody spectrum whose peak temperature has been redshifted to $T \sim 2.7$ K.

- The seed fluctuations imprinted by inflation began to collapse gravitationally at early times, and have been amplified over cosmic time. The baryonic component associated with the collapsing structures - called dark matter *haloes* - cools radiatively and begins to form molecular clouds and stars. Throughout the stellar lifecycle, heavy elements are produced by stellar nucleosynthesis.

- The first generations of stars produced copious ultraviolet radiation that reionised most of the neutral hydrogen in the Universe, potentially suppressing the formation of dwarf galaxies temporarily.

- The cooling of gas and formation of subsequent generations of stars is regulated by the complex interplay of gas cooling rates, heating from the ultraviolet background radiation, and feedback from SNe and black holes.

- Outflows of gas generated by the coalescence of rapidly moving SNe ejecta transport heavy elements from the local environment of galaxies into the diffuse intergalactic medium, where they are observable via their absorption of light from quasars.

Outstanding questions for the current paradigm

It should be noted that, in spite of the great breadth of observations that the current paradigm successfully predicts, often with great precision, open questions persist that threaten to undermine its validity. The key problems are:

- *Dark matter halo profiles*: the collapse of dark matter leads to the formation of virialised, roughly spherical overdensities called haloes. CDM models are universal in the prediction that the spherically averaged radial density profile of haloes is divergent towards the centre, $\rho \propto r^{\alpha}$ where the value of α is typically $\lesssim -1$. This steep density feature is referred to as a *cusp*, and it appears to be inconsistent with halo density profiles inferred from galaxy rotation curves, most notably those from

low-surface brightness whose dynamics one might expect to be dominated by dark matter at all radii (e.g. Carignan and Freeman, 1988; Flores et al., 1993; de Blok and McGaugh, 1997; Kravtsov et al., 1998; McGaugh and de Blok, 1998; Blais-Ouellette et al., 1999).

- *The missing satellites:* the hierarchical nature of CDM models produces a wealth of substructures around collapsed haloes. A naïve interpretation of galaxy formation within CDM models posits that each substructure hosts a dwarf galaxy, in which case we should expect to observe many more satellite galaxies around our own Milky Way. This problem may be considered as a subset of the issue of shaping the faint-end of the galaxy luminosity function.

- *Cosmic downsizing:* two key observations appear to be at odds with the hierarchical assembly scenario: i) the existence at relatively high-redshifts ($z \gtrsim 1$) of massive galaxies that appear to have concluded their star formation (Drory et al., 2003; Pozzetti et al., 2003; Fontana et al., 2004; Kodama et al., 2004; Bundy et al., 2005; Drory et al., 2005), and ii) the observation that massive galaxies appear to have higher star-formation rates at high-redshift than in the local Universe (Cowie et al., 1996; Juneau et al., 2005). A naïve interpretation of galaxy formation within CDM suggests that the most massive galaxies should be in the process of assembling at the present epoch. This has led to the (inaccurate and confusing) phrases 'cosmic downsizing' and 'anti-hierarchical galaxy formation'.

- *The nature of the dark energy and dark matter.* These are perhaps incomplete elements of the theory rather than weaknesses of the paradigm, but it is worth noting that no candidate CDM particle has yet been detected in the laboratory, and the nature of dark energy remains a mystery to modern Physics.

It is argued here that these four issues do not represent a crisis for the paradigm. It has been suggested that the determination of precise halo profiles using galaxy rotation curves is highly sensitive to the finite spatial resolution of the observations (e.g. Swaters et al., 2000; van den Bosch and Swaters, 2001), and it is not unreasonable to consider that the dynamical evolution of baryons within the central regions of galaxy haloes might drastically alter their halo profiles. The missing satellites problem is perhaps even less of a concern; the efficiency of star formation in small overdensities such as dwarf haloes and

substructures is believed to be strongly suppressed by a range of effects, such as photo-ionisation heating by the ultraviolet background, strong feedback from SNe winds, and ram-pressure stripping by the hot plasma within the host halo. Furthermore, the quality of data yielded by SDSS has facilitated the discovery of many new satellites in the last few years (Belokurov et al., 2006; Zucker et al., 2006b,a; Belokurov et al., 2007b,a, 2008). The apparent contradiction of downsizing in CDM was lucidly exposed as a misinterpretation of galaxy formation theory by Bower et al. (2006), who demonstrated that feedback from supermassive black holes (or active galactic nuclei, AGN) effectively shuts down star formation in massive galaxies by quenching cooling flows in galaxy clusters. Whilst it is difficult to comment upon whether the nature of the dark matter and dark energy are likely to be deduced in the near-future, making progress towards this end is a key motivation for the experiments enabled by the forthcoming commissioning of the *Large Hadron Collider* (LHC).

1.3 Motivation and context for this thesis

Having briefly sketched the framework within which our investigations are conducted, we may address in a more formal fashion why the interaction of galaxies and intergalactic gas is pertinent to open questions in baryonic astrophysics. Since this is a broad field, we focus in particular on how gravitational preheating, SNe feedback, and large-scale environment affects the growth of galaxies, the baryonic content of their host haloes, and the heating and chemical enrichment of the intergalactic gas that resides between them.

1.3.1 The non-radiative regime

After the following chapter, which describes the technical details of the modelling techniques used throughout this work, we present an investigation into the evolution of baryons under the influence of dark matter and dark energy in the *non-radiative* regime. Under this simplification we employ adiabatic hydrodynamics and non-adiabatic shocks, but neglect radiative heating/cooling and so prevent star formation, and the associated stellar evolution and feedback. This regime demonstrates the scaling of gas accretion with dark matter halo mass, from which we may infer how feedback should scale in or-

der to reconcile the flat faint end of the observed galaxy luminosity function (e.g. Cole et al., 2001; Kochanek et al., 2001; Bell et al., 2003; Eke et al., 2005) with the steep low-mass end of CDM mass functions (e.g. Jenkins et al., 2001; Reed et al., 2007). Indeed, it may demonstrate whether gravitational effects alone are sufficient to regulate galaxy formation, in the event that previous inferences of the need for SNe feedback have resulted from a lack of resolution in the simulations (e.g. Mo et al., 2005). Moreover, the non-radiative regime is a reasonable approximation for the gross hydrodynamics of systems that are close to hydrostatic equilibrium and therefore offers a simple and computationally inexpensive route to understanding aspects of their baryon physics (e.g Eke et al., 1998a). Since most of the gas associated with galaxy clusters has a cooling time that exceeds the Hubble time, they are particularly close to hydrostatic equilibrium, and as we have already discussed they are a prime diagnostic of the mean matter density, $\Omega_{\rm m}$, and also the rms linear theory amplitude of density fluctuations, smoothed on the fiducial scale of 8 h^{-1} Mpc, σ_8.

We have therefore run a suite of three non-radiative cosmological gas-dynamical simulations that span an unprecedented five decades in halo mass, from the hosts of dwarf galaxies to rich galaxy clusters. The suite includes the largest simulation of a non-radiative Universe reported to date *Millennium Gas Run*, which is a gas-dynamical counterpart to the *Millennium Simulation* (Springel et al., 2005) that follows the evolution of a ΛCDM Universe in a cubic volume of comoving length $L = 500\ h^{-1}$ Mpc. The large volume of the simulation encompasses a considerable sample of galaxy cluster haloes, in addition to many more smaller haloes. This large volume run is complemented by a smaller, higher resolution volume that resolves Milky Way-like haloes with $\gtrsim 10^5$ particles each of gas and dark matter. We also simulate at extremely high-resolution ($m_{\rm gas} = 10^4\ h^{-1}\ {\rm M}_\odot$) a dwarf galaxy halo to ensure numerical convergence. The smaller two simulations were also re-run with a basic model for photo-ionisation heating by the metagalactic ultraviolet background radiation to ascertain the effect on dwarf galaxy baryon fractions and assess the plausibility of the gravitational preheating model presented by Mo et al. (2005).

1.3.2 The radiative regime

The faithful modelling of galaxy formation and evolution requires an understanding of radiative processes. The role of radiative gas cooling in fixing the characteristic stellar masses of galaxies (Binney, 1977; Rees and Ostriker, 1977; Silk, 1977) was a critical step for the emerging picture of hierarchical galaxy formation. This idea was consolidated into the 'two-stage theory' of galaxy formation by White and Rees (1978), whereby the hierarchical clustering of dissipationless dark matter drives associated baryons to high densities in haloes, triggering radiative cooling and condensation into stars. All modern galaxy formation models can trace their ancestry to this classic study.

The dissipative physics of baryons is complex, however, and attempts to model them face considerable difficulties. Such difficulties catalysed the development of phenomenological, or semi-analytic, models for baryon evolution (e.g. Lacey and Silk, 1991; White and Frenk, 1991; Kauffmann et al., 1993; Cole et al., 1994, 2000). Semi-analytic models have proven a vital tool for extending and modifying the fundamental basics of galaxy formation theory, for example by demonstrating how various astrophysical mechanism can be invoked to reconcile the differing low-mass/faint-end slopes of the dark matter halo mass function and the observed galaxy luminosity function. More recently, semi-analytic models have also highlighted the possible importance of feedback from active galactic nuclei as a means to suppress the growth of galaxies at the centre of the most *massive* haloes (Bower et al., 2006; Croton et al., 2006). However, testing the specific details of phenomenological models requires more detailed *ab initio* modelling. Whilst the sheer dynamic range and physical complexity of the key mechanisms underpinning galaxy formation forces recourse to some form of phenomenological (or 'subgrid') modelling, key approximations inherent to semi-analytic prescriptions can be explored self-consistently within hydrodynamic simulations. Hydrodynamics were introduced into cosmological simulations nearly two decades ago, and many key algorithmic and physical advances have emerged since that time (e.g. Evrard, 1988, 1990; Hernquist and Katz, 1989; Barnes and Hernquist, 1991; Katz and Gunn, 1991; Navarro and Benz, 1991; Katz et al., 1992; Thomas and Couchman, 1992; Cen and Ostriker, 1993; Evrard et al., 1994; Frenk et al., 1996), but it remains the case that the greatest successes yielded by these techniques relate to galaxy clusters, where the gas can be modelled accurately as a non-radiative fluid, or the low-density, large-scale structure of the Universe, where

cooling is also relatively inefficient and star formation does not occur. Chief amongst the successes of the latter case was the demonstration that the Lyα forest, the densely packed features seen in the spectra of high-redshift quasars, is naturally explained by absorption due to the characteristic filamentary structures that arise in the CDM Universe (e.g. Cen et al., 1994; Zhang et al., 1995; Hernquist et al., 1996; Davé et al., 1999). Such simulations were also instrumental in elucidating the thermodynamic structure of the low-density regions of the diffuse IGM (e.g. Cen and Ostriker, 1993, 1999b; Davé et al., 1999; Cen and Ostriker, 2006). It is worth noting at this juncture that neither of these successes could be achieved with semi-analytic models, since they explicitly neglect the material that does not reside within dark matter haloes.

In common with semi-analytic models, the over-cooling problem is ubiquitous in numerical simulations of galaxy formation, resulting in the vast overproduction of stars in haloes with short cooling times (e.g. Navarro and White, 1994). However, implementing the feedback schemes that semi-analytic models indicate are necessary is particularly challenging. Since, as we shall show in Chapter 3, photo-ionisation heating effectively mitigates star formation only in haloes that are considerably smaller than the Milky Way, much effort has focussed on the implementation of energy injection from supernova detonations; conceptually this is simple since the assumption of an initial mass function (IMF) for the population modelled by stellar particles in the simulation yields an expected rate of energy input from supernovae. The difficulty lies in how this energy input is coupled to the surrounding gas.

The simplest solution is to inject the energy thermally into the gas surrounding newly-formed stars, however this proves to be ineffectual because the gas is modelled as a single phase medium. Since the gas is star-forming it is necessarily very dense and therefore has a very short cooling time, leading to the rapid radiative loss of the injected energy (Katz, 1992). This problem spawned a host of models that imposed somewhat arbitrary but nonetheless instructive schemes to circumvent this issue, such as artificially reducing the densities of star forming particles (Thacker and Couchman, 2000), temporarily disabling cooling in star-forming regions (Gerritsen and Icke, 1997), disabling cooling at high-redshift (Weil et al., 1998) or smoothing the temporal injection of the energy over several tens of megayears (Thacker and Couchman, 2001).

Yepes et al. (1997) made the considerable step of treating dense star-forming regions

as a multiphase gas within a Eulerian hydrodynamics code (whereby the gas properties are computed on a spatially fixed grid). This is of course a well motivated model, since the interstellar medium (ISM) is commonly considered as a two-phase medium (e.g. McKee and Ostriker, 1977), featuring cold, dense molecular clouds ($T < 100$ K) within which star-formation takes place, existing in pressure-equilibrium with warmer atomic gas that remains close to the minimum effective temperature of the atomic line emission cooling curve ($T \simeq 10^4$ K). This model invokes a phenomenological model of pressure support from turbulence on sub-resolution scales to provide feedback, and is operationally similar to the 'slow-thermalisation' mechanism used in earlier single-phase models. Similar treatments were first implemented in Lagrangian hydrodynamics codes (for which the gas-dynamics are traced by mobile particles) by Hultman and Pharasyn (1999) and Ritchie and Thomas (2001), and subsequently implemented into the cosmological simulation code GADGET (Springel et al., 2001b; Springel, 2005) with great success by Springel and Hernquist (2003a, hereafter SH03a), whose model demonstrated that feedback enables the self-regulation of star formation. With an ensemble of cosmological simulations of varying volume and resolution, they subsequently showed (Springel and Hernquist, 2003b, hereafter SH03b) that the shape of the star formation rate density curve, $\dot{\rho}_\star(z)$, can be reproduced, but its amplitude remains too high. They were able to reduce the star formation rate further by appealing to a kinetic feedback mechanism; this type of feedback had already been explored by Navarro and White (1993) and Mihos and Hernquist (1994), and is well motivated by observations of galactic winds at both high-redshift (Steidel et al., 2000; Pettini et al., 2001, 2002b,a; Steidel et al., 2002; Adelberger et al., 2003; Wilman et al., 2005) and in the local Universe (Heckman et al., 1990). The excellent foundation this model has proven to be is illustrated by the number of modifications that have been applied to it by various groups, including, but not limited to: advanced chemodynamical evolution, modified feedback prescriptions for supernovae, implementations of AGN feedback, explicit modelling of the formation of molecular clouds in the ISM, and heating by cosmic rays (e.g. Di Matteo et al., 2004; Okamoto et al., 2005; Scannapieco et al., 2005; Oppenheimer and Davé, 2006; Booth et al., 2007; Pfrommer et al., 2007; Sijacki et al., 2007; Okamoto et al., 2008b; Wiersma et al., 2008).

It is clear that numerical gas-dynamical simulations have enabled critical progress to be made on both the large scales defined by filaments and galaxy clusters, and the small-

scales defined by galaxies. Such simulations are well suited to addressing baryonic astrophysics on these scales, since questions concerning large-scale structure typically do not require high-resolution; the structure of the Lyα forest can be modelled without resolving overdensities greater than a few tens. Resolution may then be sacrificed at the expense of a greater simulation volume. Conversely, simulations of isolated galaxies are able to concentrate fluid elements into the comoving Lagrangian regions of a collapsing halo, which are typically less than a few tens of megaparsecs across for a system with comparable mass to the Milky Way. However, as discussed earlier in this chapter, the observational evidence linking the evolution of galaxies and the IGM is overwhelming. Elucidating the apparently violent and dynamic relationship between these components in detail requires a numerical approach that allows both of them to be followed. Clearly then, one must simulate a fairly large sample of galaxies and the large region of associated IGM that can influence, and be influenced by, these galaxies. Very high-resolution is also required in order to reproduce the detailed structure of galaxies and the streams of gas that flow in and out of their host haloes as gravity, cooling and feedback compete. The key, therefore, is to conduct simulations that sacrifice neither volume nor resolution too heavily.

This is clearly a demanding requirement, that is difficult to achieve without spatially adaptive techniques. This point is highlighted by the study of Cen and Ostriker (2006), that focussed on the impact of winds upon the thermo- and chemodynamical evolution of the IGM by Cen and Ostriker (2006). They used a uniform resolution mesh-code to simulate a periodic volume of side length $L = 85\ h^{-1}\,\mathrm{Mpc}$, and so even when employing a large, memory intensive mesh of 1024^3 cells, they obtained a spatial resolution of $83\ h^{-1}\,\mathrm{kpc}$, many times larger than the typical optical diameter of a galaxy disc. One might, therefore, reasonably suspect that the implementation of baryonic processes in this case is unconverged. The application of spatially adaptive Eulerian techniques, such as adaptive mesh refinement (AMR) in this area, remains limited (e.g. Kravtsov et al., 2002); AMR simulations remain computationally expensive and consequently they tend to focus upon the regime within which they are most competitive against Lagrangian techniques, such as the evolution of galaxy clusters (e.g. Bryan and Norman, 1998; Loken et al., 2002; Motl et al., 2004) and the formation of the first stars (e.g. Tassis et al., 2003; O'Shea et al., 2005; Abel et al., 2007; Wise and Abel, 2007). Using new simulations

of much greater spatial resolution that achieved by Cen and Ostriker (2006), we show in Chapter 5 that many aspects of the IGM's properties in simulations remain susceptible to numerical limitation, and so highlight the need for spatially adaptive techniques to be applied to this area of cosmological baryon physics.

The intrinsically adaptive nature of Lagrangian hydrodynamics lends itself ideally to simulations requiring large dynamic range, as is the case when studying both galaxies and the IGM at high resolution. Recently, a number of studies based upon SPH have focussed on the formation of many galaxies within periodic volumes. Croft et al. (2008) presented a simulation of a periodic cube of size $L = 33.75\ h^{-1}$ Mpc with the modified version of GADGET-2 described by Di Matteo et al. (2005). Featuring 486^3 particles each of gas and dark matter, their gas particle mass of $4 \times 10^6\ h^{-1}\ M_\odot$ resolves Milky Way-like haloes with $\simeq 10^5$ particles. Critically, the relatively small volume of the simulation only facilitated evolution to $z = 1$, since after this time fluctuations of size similar to the box size would become non-linear (e.g. Sirko, 2005). An additional limitation is that the relatively small box size yields a small range of cosmological environments and very few massive haloes. However, the simulation did yield a considerable sample of ~ 1000 galaxies resolved with > 5000 dark matter particles at $z = 1$, facilitating a comparison of their morphologies with intermediate redshift surveys such as DEEP2 (e.g. Coil et al., 2008); it was found that galaxies could be broadly classified as 'late' and 'early' types, with the former having smaller masses, lower circular velocities, younger stars, higher star formation rates and more disc-like morphologies.

The connection between galaxies and the IGM was more explicitly explored in the simulations of Oppenheimer and Davé (2006), Davé and Oppenheimer (2007) and Oppenheimer and Davé (2008a). They investigated a number of key issues, such as the impact of different winds implementations on the mass-metallicity relation and the temperature of the IGM, the enrichment history of the IGM and galaxies, and the dynamical evolution of gas and metals that are ejected from galaxies. These simulations use similarly sized boxes to the Croft et al. study ($L \leq 64\ h^{-1}$ Mpc), but typically lower resolution ($\leq 256^3$), and this relatively poor resolution does not necessarily allow for a detailed investigation of the degree to which their results are sensitive to numerical limitation. Moreover, in common with the Croft et al. study, the relatively small box size limits the range of environments and cosmic structures that can be followed.

In order to address the limitations of current simulations, we present in Chapters 4 & 5 a new set of cosmological gas-dynamical simulations: the *Galaxies-Intergalactic Medium Interaction Calculation* (GIMIC). The novel initial conditions of these simulations are described in detail in the first of these chapters, but it is noted here that they are unique in facilitating a wide-range of cosmological environments, including rare objects such as rich groups and clusters and deep, empty voids, to be traced with exceptionally high-resolution right up to the present epoch, without the need for exceptional super-computational resources. These simulations are therefore a timely addition to existing simulation sets, since the need for detailed predictions of the evolution of galaxies and the IGM over the redshift range $9 \gtrsim z \gtrsim 0$ is rapidly becoming acute. This is primarily due to the scale and detail of observations yielded by galaxy redshift surveys at the extremities of this range, and the imminent installation of the *Cosmic Origins Spectrograph* (COS) aboard the *Hubble Space Telescope* (HST), that is set to provide an unprecedented view of the thermal and chemical state of the local IGM. By running a subset of the simulations at two different resolutions, we are also able to explore the role of numerical limitations of our model implementations. The initial analysis of these simulations focusses on two key aspects in light of these observational drivers: i) the evolution of the star formation rate, and its variation between environments which we present in Chapter 4, and ii) the evolution of the various thermodynamic phases of the IGM, with a particular emphasis on its observationally elusive warm phase. This is presented in Chapter 5.

We turn first, however, to a brief discussion of key technical aspects of the software used to run cosmological simulations, and also that used to establish their initial conditions.

Chapter 2 | *Simulating the Cosmos*

2.1 Introduction

In this chapter the key technical elements of our simulation codes are described, with a particular emphasis upon the novel baryon physics routines that have been implemented in the simulation code used to conduct the radiative simulations we present in Chapters 4, 5 & 6. To illustrate the effects of several key elements of these new routines we present, as a case study, a dwarf galaxy halo simulation in the latter half of this chapter. We begin by reviewing why simulations are a necessary tool for studying structure formation.

The initial state of the Universe that is prescribed by inflation, and reflected in the observed properties of the CMB radiation, provides a well specified starting point for theories of structure formation. The first step in such theories is to understand how the spectrum of initial fluctuations within the cosmic fluid evolves under the influence of gravity. This evolution - specifically, how fluctuations on a given scale become either amplified or damped - is sensitive to the nature of the fluid and the cosmological parameters, and was studied in detail by Bardeen et al. (1986). They present *transfer functions*, whose convolution with the primordial spectrum of fluctuations specifies the initial conditions of structure formation.

Initially, gravitational instability leads to the linear growth of fluctuations. As described in detail by Peebles (1980), gravity leads to the expansion of over-dense regions being retarded relative to the expansion of the Universe as a whole, leading to an eventual collapse and the formation of strongly non-linear structures that reach dynamical equilibrium via *virialisation*. Whilst the early, linear phase of this evolution can be predicted analytically, the non-linearity and complex, three-dimensional dynamics of the later stages can only be followed explicitly with numerical schemes. Supercomputer simulations have therefore become an indispensable tool for studying structure forma-

tion, leading to fundamental theoretical advances such as the structural profiling of collapsed haloes (Dubinski and Carlberg, 1991; Navarro et al., 1995, 1996, 1997; Fukushige and Makino, 1997; Ghigna et al., 1998; Moore et al., 1998, 1999; Klypin et al., 2001), measurements of the dynamics of halo substructure (Tormen, 1997; Springel et al., 2001a; Diemand et al., 2008), the clustering properties of haloes and their mass function (Jenkins et al., 1998, 2001; Reed et al., 2007), the hydrodynamical properties of galaxy clusters (e.g. Evrard, 1990; Eke et al., 1998a; Kravtsov et al., 2005; Ettori et al., 2006), and demonstration of the origin of the Lyα forest (e.g. Cen et al., 1994; Zhang et al., 1995; Hernquist et al., 1996; Davé et al., 1999), and the warm-hot intergalactic medium (Cen and Ostriker, 1999b, 2006).

2.2 The gravity calculation

Since the dominant matter component in the ΛCDM paradigm is the collisionless CDM fluid that interacts solely via gravitational forces, the chief calculation in cosmological simulations is the determination of the gravitational acceleration acting upon each of the mass elements (e.g. particles) that are used to represent the spatially continuous density field of the cosmological fluid. Formally, this procedure requires the computation of the Laplacian of the peculiar gravitational potential, $\Phi(\mathbf{r})$, via Poisson's equation:

$$\nabla^2\Phi(\mathbf{r}) = 4\pi G\bar{\rho}(\mathbf{x})a^2\delta, \tag{2.1}$$

which is cast here in the comoving coordinate frame, and $\delta = \rho/\bar{\rho} - 1$ is the *overdensity*. Although we have described the dynamics of the Universe so far with general relativity, for the sake of structure formation this calculation may be accurately reproduced in the Newtonian limit because the length scales of concern occupy the broad dynamical range over which relativistic effects are negligible[1].

Since gravity is a long-range force, computing the accelerations it generates is a fundamentally intensive operation, because all mass elements influence, and are influenced by, all other mass elements:

$$\mathbf{F}(\mathbf{r}_i) = \Sigma_{j=1,j\neq i}^{N-1} \frac{Gm_i m_j}{(|\mathbf{r}_i - \mathbf{r}_j|)^2} \tag{2.2}$$

[1]These are the Schwartzchild radii of haloes on small scales, and the Hubble length, c/H, on large scales.

where m_i is the mass of a given element and $\mathbf{r}_i$ is its coordinate vector. It then follows that the number of calculations required to solve Poisson's equation for N mass elements scales as $\propto N(N-1) \simeq N^2$, and rapidly becomes unfeasibly expensive for even modest simulations. However, by sacrificing the precision of the force calculation in a controlled fashion, vast algorithmic speed-ups can be achieved. The focus here shall be on the gravity algorithms that are used in the simulations presented in the following chapters. These simulations were run with the GADGET2 code (or modified versions of it, Springel et al., 2001b; Springel, 2005), which employs two separate algorithms in order to maximise the efficiency of the gravity calculation. These algorithms are the *particle-mesh* and *hierarchical multipole expansion* methods.

2.2.1 Particle-mesh algorithm

Particle-mesh (PM) methods (Klypin and Shandarin, 1983; White et al., 1983) are the fastest schemes for computing gravitational forces. In a PM calculation, the discretised density field is mapped onto a regular mesh, via some kernel-based mass assignment scheme (Hockney and Eastwood, 1981) such as nearest grid point (NGP), cloud-in-cell (CIC) or triangular shaped clouds (TSC). These schemes differ in the way they balance the unavoidable trade-off between introducing noise and artificially smoothing the density field; GADGET2 uses the CIC scheme. The development of fast Fourier transform (FFT) algorithms (Cooley and Tukey, 1965) has made the PM gravity calculation very rapid if performed in k-space, whereby the Fourier transform of the mesh is multiplied by the Green function for the potential, and then inverse transformed. The gravitational force at each mesh cell is then computed by finite-differencing the potential, and interpolated back to particle coordinates, again using (for example) CIC.

Whilst very fast, a trade-off must be made when using a PM scheme between force accuracy and memory requirement. On scales comparable to the size of the mesh cells, the algorithm artificially suppresses the gravitational force; attaining high-spatial resolution therefore requires the use of very large FFT meshes that incur a severe memory cost. This problem can be offset to a degree by augmenting the gravity calculation with one or more additional schemes, such as additional PM meshes (Couchman, 1991), direct summation - a scheme termed particle-particle particle-mesh (P^3M, Hockney and Eastwood, 1981; Efstathiou et al., 1985), or a hierarchical tree to form a TreePM code (Xu,

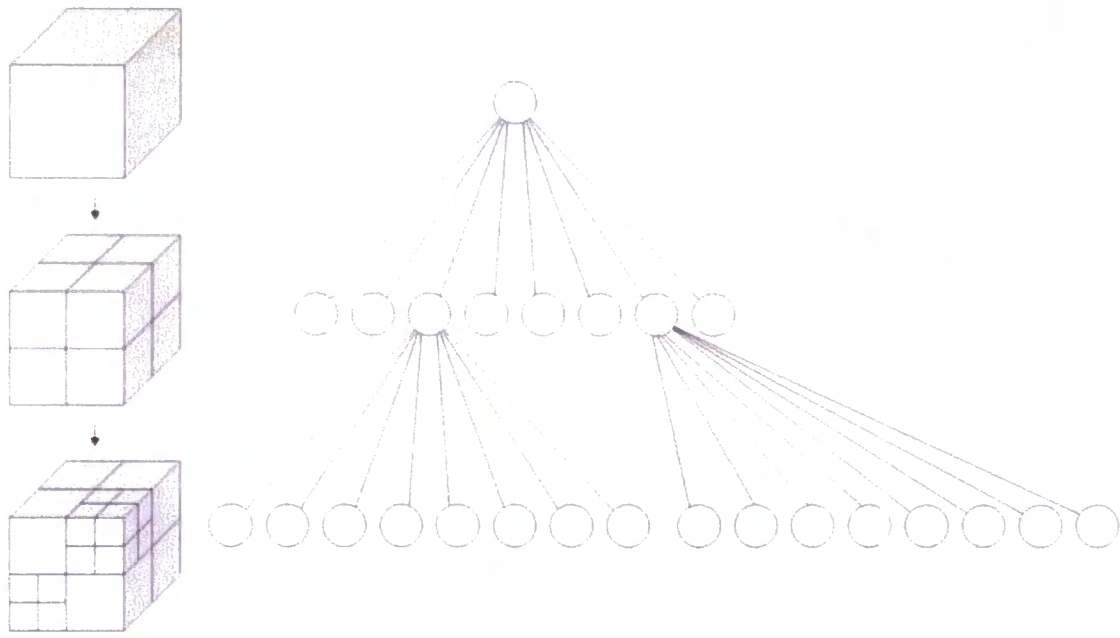

Figure 2.1: Schematic representation of the recursive spatial subdivision of a volume via a hierarchical oct-tree. At each recursion a cell is split in two along each Cartesian axis, splitting it into eight subcells. The structuring of the particles then resembles a tree.

1995). Whilst in theory a simple augmentation to the overall PM force is possible, the required correction is anisotropic. For this reason, the PM calculation is typically truncated on a scale that is slightly larger than that at which it begins to suppress the force, allowing for a more isotropic correction.

2.2.2 Hierarchical multipole expansion

In contrast to PM schemes, the computation of gravitational forces via hierarchical multipole expansion (Barnes and Hut, 1986; Dehnen, 2000) has no intrinsic resolution limit. As illustrated in Figure 2.1, this algorithm recursively subdivides the simulation volume into a hierarchy of cells, grouping the particles at each level of recursion until each contains no more than a prescribed maximum number of particles (perhaps a single particle). Schematically, the structuring of cells resembles a tree; the *root* node represents the entire volume, whilst *branches* split off at each level of recursion until the *leaf* nodes are reached, representing the finest level of splitting; this scheme is therefore commonly referred to as a tree algorithm. The subdivision can be achieved in a variety of ways;

the method shown in the figure is the oct-tree, which subdivides each dimension by a factor of two at each recursion, thus creating eight new subcells each time. We highlight this method since it is applied in GADGET2, owing to its 'shallow' nature; fewer internal nodes are required for a given number of leaf nodes when compared to, for example, a binary-tree, thus reducing the memory overhead.

The use of a tree allows distant particles to be grouped together, and their gravitational forces to be approximated; in this way the gravity calculation per particle scales as $\propto \ln N$ rather than the $\propto N$ scaling of direct summation. For each particle, partial forces are computed by 'walking' the tree, starting at the root node and checking whether an *opening criterion* is met that determines whether the approximation obtained at the current level of the hierarchy is sufficiently accurate. If not, the walk proceeds to the next level - a process termed 'opening the cell' - and the check is made once more, and so on, until the approximation is sufficient or the leaf node is reached. The opening criterion therefore allows control over the accuracy of the calculation. In GADGET2, a cell enclosing mass, M, and side length, l, at distance, r, is not opened if

$$\frac{GM}{r^2}\left(\frac{l}{r}\right)^2 \leq \alpha|\mathbf{a}|, \tag{2.3}$$

where α is a tolerance parameter and $|\mathbf{a}|$ is the magnitude of the acceleration at the previous timestep. For the first timestep, $|\mathbf{a}| = 0$ and so a purely geometric opening criterion is applied.

Forces in a tree algorithm are computed by multipole expansion; the number of multipole moments used in the force calculation also affects how far down a branch a tree walk must progress. With higher-order multipoles the tree walk can, in general, be shorter. As noted by Springel (2005), however, the advantage of higher order accuracy can be offset by additional processing and memory overhead, such that the performance of the scheme as a function of multipole order forms a broad maximum. GADGET2 adopts the simplicity of monopole moments, largely to optimise memory usage. By computing the monopole about the centre-of-mass of each cell, however, the dipole term vanishes and so the error scales as the quadrupole moment, and not the dipole as might be naïvely expected.

2.3 Hydrodynamics

The treatment of baryons in simulations requires additional algorithms, since they are subject to hydrodynamical forces in addition to gravity. Whilst gravity solvers essentially differ only in the accuracy with which they approximate the fluid potential, hydrodynamical algorithms differ in a more fundamental fashion that can produce significantly different results. The two primary approaches to hydrodynamics are i) to discretrise mass into fluid particles in a Lagrangian sense, or ii) to discretise space and represent gas properties on a mesh in a Eulerian sense. Both approaches are commonly used in cosmological simulations. Smoothed particle hydrodynamics (SPH, Gingold and Monaghan, 1977; Lucy, 1977) has emerged as the most popular Lagrangian approach (e.g. Evrard, 1988; Katz et al., 1996; Wadsley et al., 2004; Springel, 2005), whilst Eulerian codes have featured both fixed meshes (e.g. Cen and Ostriker, 1992; Yepes et al., 1995; Pen, 1998) and adaptively refined meshes (Bryan and Norman, 1997; Kravtsov, 1999; Norman and Bryan, 1999; Fryxell et al., 2000; Quilis, 2004).

The relative merits and drawbacks of these schemes remain only partially understood and continue to be the source of considerable research activity (e.g. Frenk et al., 1999; O'Shea et al., 2005; Agertz et al., 2007; Tasker et al., 2008). However, it is sufficient to say for the purposes of this work that, in general, Eulerian schemes offer superior shock-capturing capability and treatments of fluid instabilities, such as Kelvin-Helmholtz (due to velocity gradients) and Rayleigh-Taylor (due to density gradients) instabilities. However, fixed meshes lack the dynamic range required for cosmological applications and, whilst this is partially mitigated by the use of adaptive meshes, any scheme where the mesh does not move with the fluid suffers from non-Galilean invariant dynamics and spurious entropy generation by fluid mixing.

A key advantage of Lagrangian techniques is their inherent ability to cope with extremes of dynamic range and automatically increase resolution in over-dense regions. Operationally, particle based hydrodynamics are also appealing in cosmological applications since the gravitational forces on, and due to, the baryons are self-consistent with the dark matter component, which is also treated in a Lagrangian fashion. Since SPH is the method adopted in GADGET2, we shall focus on its basics here.

2.3.1 Smoothed particle hydrodynamics

SPH describes a fluid using tracer particles, with quantities being determined over all space, $\mathbf{r}$, by interpolation with a kernel function $W(\mathbf{r}, h)$ of extent (or *smoothing length*), h. The smoothing kernel is normalised to unity:

$$\int W(\mathbf{r} - \mathbf{r}', h) d\mathbf{r} = 1, \tag{2.4}$$

whilst the smoothing length is fixed by the resolution of the discretisation of the fluid, such that in the limit of infinite particles, $h \to 0$ and the kernel mimics Dirac's delta function:

$$\lim_{h \to 0} W(\mathbf{r} - \mathbf{r}', h) = \delta(\mathbf{r} - \mathbf{r}'). \tag{2.5}$$

Whilst the Gaussian form of the kernel is well motivated, it does not approach zero at a finite distance, and so the form of the kernel most commonly adopted is the spline kernel (Monaghan and Lattanzio, 1985),

$$W(r, h) = \frac{8}{\pi h^3} \begin{cases} 1 - 6\left(\frac{r}{h}\right)^2 + 6\left(\frac{r}{h}\right)^3, & 0 \leq \frac{r}{h} \leq \frac{1}{2}, \\ 2\left(1 - \frac{r}{h}\right)^3, & \frac{1}{2} < \frac{r}{h} \leq 1, \\ 0, & \frac{r}{h} > 1. \end{cases} \tag{2.6}$$

The fundamental basis of SPH is the density estimate for each particle,

$$\rho_i = \sum_{j=1}^{N} m_j W(|\mathbf{r}_{ij}|, h_i), \tag{2.7}$$

where $\mathbf{r}_{ij} = \mathbf{r}_i - \mathbf{r}_j$. The smoothing length, h, is adaptive over time, such that a sphere of this radius encloses either a fixed number of neighbours, N_{ngb}, or a fixed mass:

$$\frac{4\pi}{3} h_i^3 \rho_i = N_{\mathrm{ngb}} \bar{m}, \tag{2.8}$$

where $\bar{m}$ is the mean enclosed particle mass. Note that for consistency with Springel et al. (2001b) and Springel (2005), we assume the smoothing length tends to zero at h, rather than $2h$ as is commonly used in the literature.

The thermodynamic state of a particle is defined by one of i) its specific energy, u, ii) its specific entropy, s, or iii) the entropic function $A(s) = P/\rho^{\gamma}$, where γ is the ratio of specific heats. The value of a thermodynamic quantity Q at a given coordinate can be interpolated via

$$Q(\mathbf{r}) = \int Q(\mathbf{r}') W(\mathbf{r} - \mathbf{r}', h) d\mathbf{r}', \tag{2.9}$$

which is approximated in SPH by the summation over the particles:

$$Q(\mathbf{r}) = \sum_{i=1}^{N} Q_i \frac{m_i}{\rho_i} W(|\mathbf{r}_{ij}|, h_i). \tag{2.10}$$

For example, the substitution $Q(\mathbf{r}) = \rho_i(\mathbf{r}_i)$ demonstrates that Equation 2.7 is recovered. In the absence of shocks or additional heat sources or sinks, a fully reversible description of fluid dynamics is given by the fluid Lagrangian (Springel and Hernquist, 2002a; Springel, 2005):

$$L(\mathbf{q}, \dot{\mathbf{q}}) = \frac{1}{2} \sum_{i=1}^{N} m_i \dot{\mathbf{r}}_i^2 - \frac{1}{\gamma - 1} \sum_{i=1}^{N} m_i A_i \rho_i^{\gamma - 1}, \tag{2.11}$$

where $\mathbf{q} = (\mathbf{r}_1, \ldots, \mathbf{r}_N, h_1, \ldots, h_N)$, where the 'potential energy' of the Lagrangian is in fact a thermal energy that generates the motion of SPH particles, whose densities are a function of $\mathbf{q}$ (i.e. Equation 2.7). This leads to the equation of motion:

$$\frac{\mathrm{d}v_i}{\mathrm{d}t} = -\sum_{j=1}^{N} m_j \left[f_i \frac{P_i}{\rho_i^2} \nabla_i W_{ij}(h_i) + f_j \frac{P_j}{\rho_j^2} \nabla_i W_{ij}(h_j) \right], \tag{2.12}$$

where we have defined $W_{ij}(h) = W(|\mathbf{r}_i - \mathbf{r}_j|, h)$ and

$$f_i = \left(1 + \frac{h_i}{3\rho_i} \frac{\partial \rho_i}{\partial h_i} \right)^{-1}. \tag{2.13}$$

It should be noted that the assumption of a polytropic equation of state, $P = A\rho^{\gamma}$, is only accurate in adiabatic flows. In general, the entropic function grows owing to the action of discontinuities that are generated by micro-physics. SPH therefore appeals to an *artificial viscosity* that partially, and irreversibly, thermalises kinetic energy in convergent flows. GADGET2 implements a viscous force

$$\frac{\mathrm{d}v_i}{\mathrm{d}t} = -\sum_{j=1}^{N} m_j \Pi_{ij} \nabla_i \overline{W}_{ij}, \tag{2.14}$$

where the term $\Pi_{ij} \geq 0$ is non-zero only when particles approach each other in physical space, and $\overline{W}_{ij}$ is the arithmetic mean of the two kernels $W_{ij}(h_i)$ and $W_{ij}(h_j)$. Further details pertaining to the choice of artificial viscosity may be found in Monaghan and Gingold (1984) and Balsara (1995). We focus here, however, on the other mechanisms included in our simulations that directly affect the evolution of gas and are new to our code, namely radiative processes, star formation, chemical evolution, and feedback.

2.4 Additional physics

Although we restrict ourselves to the non-radiative regime in Chapter 3, in Chapters 4, 5 & 6 we conduct radiative simulations using GADGET3-BG[2]. This simulation code is based upon the non-public version of GADGET2 that features, in addition to the entropy-conserving SPH formalism of Springel and Hernquist (2002b), the radiative physics modules described by SH03a. In addition to significant alterations to the domain-decomposition scheme that drastically improve load-balancing for simulations run on massively-parallel supercomputers with many cores, this new version of the code features many changes and updates to the radiative physics modules, which we outline briefly here.

2.4.1 Radiative processes

As discussed in Section 1.3.2, radiative gas cooling is fundamental to the formation of the molecular cloud complexes within which stars are formed, and from which galaxies are built. A detailed treatment of cooling is therefore a key element of any calculations following the evolution of galaxies and the IGM. Most popular implementations are similar to that first proposed by Katz et al. (1996), in which the ionisation balance of hydrogen and helium is computed in the presence of a time-dependent metagalactic ultraviolet background radiation field, under the assumption of collisional ionisation equilibrium (CIE). Most models have since adopted the metallicity-dependent cooling rates calculated by Sutherland and Dopita (1993), since heavy elements are extremely efficient coolants and their presence significantly affects the evolution of enriched systems (e.g. Aguirre et al., 2005).

Besides altering the ionisation balance of elements within the gas, the ultraviolet background also heats the gas. We must therefore consider the *net heating* rate, $\Lambda(\rho, T, Z, z)$ which is a function of density, temperature, metallicity and - owing to the time-dependence of the ionisation radiation field - redshift. In most regimes we shall consider, the net heating rate is negative (i.e. cooling dominates) so for brevity, hereafter we shall refer to the cooling rate rather than heating rate, unless specifically discussing the regime where heating dominates. Since heating does indeed dominate in certain regimes, such as in the

[2]The suffix BG is a reference to the *Stella* IBM-BlueGene supercomputer in the Netherlands, where many of the initial simulations for the OWLS project (a sister project to GIMIC) were run.

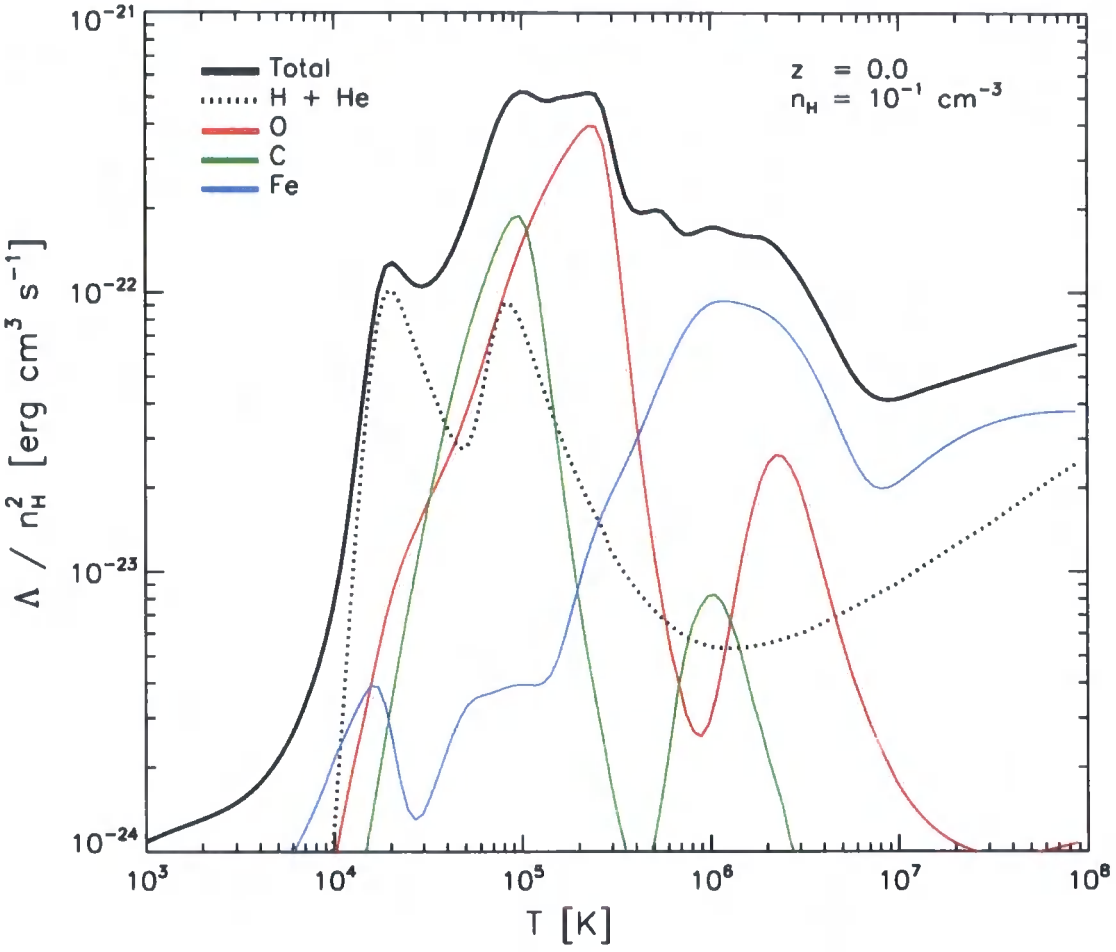

Figure 2.2: The radiative cooling rate (no heating is included here) of an optically thin gas with solar metallicity and abundance ratios, under the assumption of photo-ionisation equilibrium (PIE). PIE introduces an explicit density dependence into the rates, so we show the rates for $n_{\rm H} = 10^{-1}$ cm^{-3}, with the background at its $z = 0$ state as specified by Haardt and Madau (2001). The dotted line shows the contribution from hydrogen and helium; at solar metallicity the cooling rate contribution from metals clearly dominates the primordial rate in certain regimes, and is critical for accurate modelling of the cooling function.

low temperature, low density gas that is present in early-forming dwarf galaxies and the diffuse IGM, the inclusion of heating from the ultraviolet/X-ray radiation background, as specified by Haardt and Madau (2001), is a significant advance in GADGET3-BG. The heating and cooling rates, from line emission/absorption and thermal Bremsstrahlung, for primordial gas and nine separate metals (C, N, O, Ne, Mg, Si, S, Ca, Fe) were computed from grids of photo-ionisation models run with the CLOUDY software (version 07.02 Ferland et al., 1998). Prior to the epoch of reionisation, no ionising background is present and gas is therefore assumed to be in collisional ionisation equilibrium (CIE). The redshift dependence of cooling rates introduced by the evolution of the ionising background is therefore absent, allowing a single table to be used for $z > z_{\rm reion}$. For operational reasons, this table includes a very soft ionising background to prevent CLOUDY from computing additional cooling rates from molecular hydrogen, which we do not model here.

The calculation of individual cooling rates for each element allows the calculation of cooling rates for gas that is not at solar abundance, in contrast to the widely adopted cooling tables of Sutherland and Dopita (1993). This is particularly advantageous; as shown in Section 2.4, the vastly differing timescales of type II/Ia SNe and core dredging in Asymptotic Giant Branch (AGB) stars releases alpha elements, iron and carbon into the ISM at different stages of the temporal evolution of a stellar population. Abundance ratios should therefore be expected to vary with time. The cooling function for gas of solar composition and density $n_{\rm H} = 10^{-1}{\rm cm}^{-3}$ within the $z = 0$ metagalactic ultraviolet background is shown in Figure 2.2, and highlights the dramatic effect upon cooling caused by metal enrichment. Details relating to the creation of the cooling tables are given in Wiersma et al. (2008).

The tables also include the contribution to cooling from the inverse Compton scattering of CMB photons by energetic electrons in the IGM. This mechanism is particularly effective at high redshift, due to its strong dependence on the density of both CMB photons and free electrons. Prior to reionisation, this contribution is added analytically to the cooling rate of each particle, i:

$$\Lambda_{{\rm IC},i} = 4\sigma_{\rm SB}\sigma_{\rm T}k_{\rm B}\frac{T_{\rm CMB,0}}{m_{\rm e}c}\left[(T_i - T_{\rm CMB})(1+z)^4\frac{n_{\rm e}}{n_{\rm H}}\right], \tag{2.15}$$

where $\sigma_{\rm SB}$ is the Stefan-Boltzmann constant, $\sigma_{\rm T}$ is the Thomson scattering cross-section of the electron, $k_{\rm B}$ is the Boltzmann constant, T_i is the particle temperature, $T_{\rm CMB,0} =$

2.728 K is the present day temperature of the CMB, and $T_{CMB} = T_{CMB,0}(1+z)$ is the temperature of the CMB at redshift z. Note that we neglect molecular cooling, for instance the H_2 cooling that is important for the formation of the first stars, cooling from dust grains, or heating by cosmic rays.

Finally, we also include an empirically motivated treatment of photo-ionisation heating at the epochs of reionisation for hydrogen ($z = 9$) and helium ($z = 3.5$). A self-consistent treatment would require a radiative transfer scheme (e.g Abel and Haehnelt, 1999), which we do not implement here. Instead, heat is smoothly added to particles in the form of a Gaussian function that is centred on each reionisation redshift. Note that the two reionisation epochs can be treated independently since the timescale for mean density gas to cool back to thermal equilibrium after hydrogen reionisation is shorter than the ~ 1.3 Gyr timescale between $z = 9$ and $z = 3.5$. The overall energy input in each case is chosen such that gas of primordial composition at the mean density of the Universe is heated to $T = 10^4$ K in the case of HI reionisation, and is heated to match the temperature distribution measured by Schaye et al. (2000) in the case of HeII reionisation.

2.4.2 Star formation

Star formation remains a poorly understood ingredient within galaxy formation recipes, and its key physical processes occur on spatial and temporal scales that are too short to be modelled in cosmological applications. In general, this forces recourse to the assumption that the internal dynamics of the ISM (rather than those of individual molecular clouds, for instance) can be characterised by a sub-resolution model that acts in response to the spatially averaged properties of the surrounding gas medium. In this respect, direct numerical simulations treat star formation in a similar phenomenological fashion to semi-analytic models, although it can be argued that the 'input' to the phenomenological treatment (i.e. the thermo- and chemodynamics of the gas surrounding the ISM) is more realistically treated in numerical simulations.

The hybrid multiphase model of SH03a has been widely adopted. This scheme assumes that each SPH particle is comprised of cold, condensed clouds in pressure equilibrium with a hot ambient gas; the former acts as fuel for star formation and contributes to the particle's gravitational interactions, whilst the latter contributes to gravitational in-

teractions and also determines the hydrodynamic forces acting upon the particle. Mass and energy exchange between the two phases are controlled by differential equations guided by the ISM model of McKee and Ostriker (1977).

A number of groups have attempted to improve upon the hybrid model by treating the cold molecular clouds explicitly (e.g. Harfst et al., 2006; Booth et al., 2007), decoupling them from the dynamics of the hot, ambient phase. In such models, the condensed Giant Molecular Clouds (GMCs) are treated with, for example, 'sticky particles' that are ballistic (i.e. not subject to pressure forces) but can coagulate when they collide. However, the simulations we present in Chapters 4 & 5 are chiefly concerned with the interaction of the ISM with halo gas and the diffuse IGM, and not the detailed internal structure of the ISM. We therefore appeal to a *simplification* of the hybrid model, rather than an extension of it. In the scheme used for our simulations, the effective pressure of the ISM is specified *a priori*; this limits the degree to which the simulations rely upon the details of the sub-grid prescriptions and reduces the computational overhead of modelling the ISM. This scheme is discussed in detail by Schaye and Dalla Vecchia (2008, hereafter SDV08), and so we present only a brief overview here.

Our ignorance of star formation physics can be circumvented with the use of an empirical law that indicates the efficiency of star formation on scales that we are able to resolve with simulations. The laws of Schmidt (1959) and Kennicutt (1983, 1998) are frequently used for this purpose: the former specifies a star formation rate density as a function of the volume averaged gas density:

$$\dot{\rho}_\star \propto \rho_g^{n_S}, \tag{2.16}$$

as is required in theoretical models, whilst the latter uses surface densities rather than volumes:

$$\dot{\Sigma}_\star \propto \Sigma_g^{n_K}. \tag{2.17}$$

and is the natural expression of *observed* scalings. These relations are typically combined with a lower threshold below which star formation does not occur; the observed value of surface density threshold $\Sigma_c \sim 10\ M_\odot\ pc^{-2}$ was shown by Schaye (2004) to result from the triggering of gravitational instability by the transition from cold ($T \sim 100$ K) to warm ($T \sim 10^4$ K) phase gas; at lower densities the warm phase is stabilised by the ionising background. Kennicutt law exponents in the range $n_K \simeq 1 - 2$ are typically

found to match the data over many decades in gas surface density, in both quiescent and starbursting galaxies (e.g. Kennicutt, 1998). As discussed by SDV08, the exponents of the two laws, n_S and n_K are not generally the same, and so the construction of a Schmidt law for a simulation requires

$$n_S = \frac{(n_K - 1)\gamma_{\rm eff}}{2} + 1 \tag{2.18}$$

where $\gamma_{\rm eff}$ is the polytropic equation of state for an ideal gas, such that

$$P_{\rm tot} = P_{\rm tot,c}\left(\frac{\rho_g}{\rho_{g,c}}\right)^{\gamma_{\rm eff}}. \tag{2.19}$$

Clearly then, equality of the two exponents requires $\gamma_{\rm eff} = 2$ or $n_S = n_K = 1$, which is, in general, not the case. Our model assumes that in a self-gravitating system, the scale height of a star forming disc is similar to the local Jeans length, $\Sigma_g \sim \Sigma_{g,J} \equiv \rho_g L_J$, where the Jeans length is the radius of a pressurised, self-gravitating cloud for which the pressure and gravitational forces are balanced:

$$L_J = \left(\frac{15 k_B T}{4\pi G \mu \rho}\right)^{1/2}. \tag{2.20}$$

It follows then that the star formation rate, $\dot{m}_\star$ is:

$$\dot{m}_\star \equiv m_g \frac{\dot{\rho}_\star}{\rho_g} = A(1\,{\rm M}_\odot\,{\rm pc}^{-2})^{-n_K} m_g \left(\frac{\gamma}{G} f_g P_{\rm tot}\right)^{(n-1)/2}, \tag{2.21}$$

where γ is the ratio of specific heats (not to be confused with $\gamma_{\rm eff}$) and A follows from the Kennicutt law:

$$\dot{\Sigma}_\star = \begin{cases} 0 & \text{if } \Sigma_g < \Sigma_c \\ A\left(\Sigma_g / 1\,{\rm M}_\odot\,{\rm pc}^{-2}\right)^n & \text{if } \Sigma_g \geq \Sigma_c \end{cases} \tag{2.22}$$

Since the continuous gas density field is represented by a finite particle distribution, the star formation law must be implemented stochastically; each gas particle has a star formation rate $\dot{\rho}_\star$ and is converted to a star particle in a time-step of during Δt with a probability:

$$\text{Prob} = \max\left(\frac{\dot{m}_\star \Delta t}{m_g}, 1\right). \tag{2.23}$$

We adopt the simplification that one gas particle converts into one star particle; this conserves particle number throughout the simulation. It is worth noting two key points at this juncture: i) stellar particles in cosmological simulations are many orders of magnitude more massive than individual stars: we interpret them therefore as simple stellar populations that are described by the IMF of Chabrier (2003), and ii) the Schmidt and

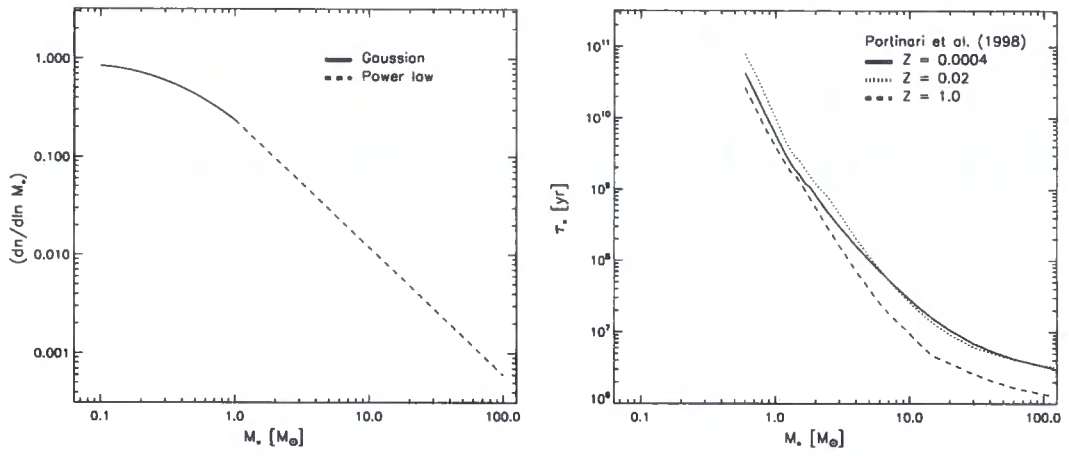

Figure 2.3: *Left*: The IMF presented by Chabrier (2003), which takes the form of a Gaussian at low masses and converts to the commonly adopted power law form at high masses. *Right*: the metallicity-dependent stellar lifetimes predicted by Portinari et al. (1998).

Kennicutt laws to which we appeal at all stages of our simulations are of course only precisely measured at low redshift, and may not hold at early times.

2.4.3 Stellar evolution

Stellar population models adopt an empirical function describing the mass function of stars formed from a single star formation event. This function, the initial mass function (IMF, ξ), is most commonly assumed to be a power law,

$$\xi(\log_{10} m) = Am^{-x} \tag{2.24}$$

such as the $x = 1.35$ form proposed by Salpeter (1955), where A is a constant such that:

$$\int_0^\infty m\xi(\log_{10} m)\mathrm{d}\log_{10} m = 1. \tag{2.25}$$

The Chabrier (2003) IMF (Figure 2.3; left) splices a Gaussian function onto the power law in order account for the abundance of low-mass stars:

$$\xi(\log m) = \begin{cases} A\exp\left\{-\frac{1}{2\sigma^2}[\log_{10}(m/m_c)]^2\right\} & \text{if } m \leq \mathrm{M}_\odot \\ Bm^{-x} & \text{if } m > \mathrm{M}_\odot \end{cases} \tag{2.26}$$

and it is this form we adopt in our simulations. The evolution of these stellar populations represented by star particles leads to two key effects: i) the synthesis of heavy elements

and ii) the injection of feedback energy. Although synthesis occurs at all stages of stellar evolution, the release of the metals takes place predominantly when the star enters the SNe/AGB phase, at the end of its lifetime. Our modelling therefore requires mass-dependent lifetime functions, where the lifetime is defined as the time taken to proceed from the zero-age main sequence (the epoch at which fusion of hydrogen begins within a collapsing molecular cloud; ZAMS), to the AGB or SNe phase. We adopt those presented by Portinari et al. (1998, Figure 2.3, right). It should be noted that stellar lifetimes may represent a key weakness within our models, since they cannot be observationally constrained; published lifetimes are commonly derived from stellar population modelling, as is the case for those adopted here. It is non-trivial, therefore, to assess the degree of systematic error inherent to this aspect of our scheme.

Chemical evolution

Metal synthesis proceeds primarily via three channels, all of which are treated in our simulations. These are core-collapse and progenitor accretion supernovae (type II and Ia SNe), and core-dredging within AGB stars. The differing lifetimes of the progenitors of these channels results in time-dependent metal release:

- **Type II SNe**: the end point of stellar evolution for highly luminous, massive stars ($M \gtrsim 8$ M$\odot$) with commensurately short lifetimes, these violent detonations occur within $\sim 10^7$ years of the formation of a stellar population, and primarily produce alpha-elements - oxygen, magnesium, neon, silicon - in addition to iron.

- **Type Ia SNe**: the origin of these explosions is uncertain, but is most likely due to the accretion of matter from a binary companion star onto a white dwarf ($M \lesssim 1.4$ M$_\odot$); eventually this accretion breeches the Chandrasekhar limit such that the dwarf's electron degeneracy pressure ceases to be sufficient to resist gravitational collapse. The release timescale is much longer in this case, $\sim 10^9$ years, and the chief product of the release is iron.

- **AGB stars**: The asymptotic giant branch phase is experienced by all low and intermediate mass stars ($M \lesssim 8$ M$_\odot$), when the core exhausts its hydrogen, ceases to burn, and contracts. In terms of chemical evolution, the key mechanism within this complex phase of evolution is that carbon is dredged from the core and re-

leased into the outer envelope of the star, which is later shed into its surroundings. The wide range of stellar masses found in this phase lead to a widely dispersed time-scale over which this carbon is deposited.

Each mechanism is associated with a yield specifying the mass of metals released per unit stellar mass. As per the lifetimes, we adopt the yields of Portinari et al. (1998) for type II SNe, those of Thielemann et al. (2003) for type Ia SNe, and those of Marigo (2001) for AGB stars. As is the case for lifetimes, yields are derived from stellar population models, which are relatively uncertain owing to the complexity of the physics associated with stellar nucleosynthesis and detonations.

Feedback

The various stages of stellar evolution described above return mass, metals and energy to the ISM. The generation of turbulence by stellar winds and SNe is key to the regulation of star formation since it disrupts molecular clouds on timescales much shorter than the Hubble time. This process is modelled in two ways in our model. As previously mentioned, we adopt a simple model for the ISM, reverting to a single-phase treatment and adopting an *imposed* equation of state, $P = A\rho^{\gamma_{\rm EoS}}$, for the ISM. The choice of $\gamma_{\rm EoS} = 4/3$ yields an ISM whose Jeans mass is independent of density, whilst the entropic coefficient A is tuned such that the imposed relation matches the pressure of non-ISM gas that is just below the density threshold at which the relation is imposed. The effect of this relation is to mimic the resistance to compression of the ISM that arises naturally from the increase in internal pressure that follows any localised compression of the ISM, owing to the triggering of star formation and therefore additional SNe energy output.

In the case where sufficient numbers of SNe occur, the overlap of their ejecta leads to the generation of galactic-scale outflows, which in small galaxies remove gas from the disc and even the parent halo, whilst in more massive galaxies the gaseous outflows are expected to rain back down onto the disc in a 'galactic fountain'. The canonical picture of core-collapse detonations involves an initial adiabatic expansion phase of the ejecta, since its radiative cooling time is much longer than the sound crossing time; during this phase, energy is conserved. Once radiative losses are significant, it is momentum that is conserved; as the ejecta sweeps-up the surrounding gas, it decelerates simply due to the hydrodynamical drag. As noted by Dalla Vecchia and Schaye (2008, hereafter DVS08),

the evolution of a 'super-bubble' driven by multiple SNe is very similar to that of an individual ejecta bubble, but once the bubble breaks out of the cold gas disc, the outflow is subjected to the ram-pressure of infalling cold gas.

The modelling of feedback is greatly hampered by the inability of cosmological simulations to resolve the spatial structure of outflows. Since they are smoothed over many resolution elements, their expansion velocities and cooling rates are significantly underestimated; the initial cooling time is hence (artificially) shorter than the sound crossing time, the adiabatic phase never occurs and a significant fraction of the input energy is radiated away (e.g. DVS08), as was discussed in Section 1.3.2. The injection of the SNe directly as kinetic energy alleviates this problem to a degree, since the energy is injected into a relatively small number of particles surrounding the disc, suppressing the degree to which the outflow velocity is underestimated. We therefore adopt a kinetic feedback scheme for our simulations. Our particular scheme is described by DVS08, and is adaptated from the SH03a scheme but features two key differences:

- **Hydrodynamic decoupling**: the original scheme of SH03a temporarily decouples wind particles from hydrodynamic forces in order to assist their escape from the dense disc of the ISM. This effect increases, for instance, the mass of gas and metals that reach the IGM and also reduces the effect of numerical resolution. However, it prevents winds from driving turbulence in the disc or from naturally creating 'chimneys' in the disc that result in anisotropic, collimated outflows. In the DVS08 implementation, the wind particles remain coupled at all times; a key result is that the effective mass loading of winds in dwarf galaxies is increased, and the snow plough removes a greater mass of gas. In more massive galaxies, the efficacy of winds is reduced, as the coupling renders it harder for the winds to penetrate the dense gas surrounding the disc.

- **Localised outflows**: in SH03a, the stochastic scheme that selects wind particles uses the global star formation rate to determine how many particles are launched in winds, and considers all gas particles as potential candidates. In the DVS08 implementation, the procedure is localised, such that particles launched in winds are constrained to be close neighbours of newly formed star particles. This is crucial, for example, for the self-consistent treatment of heavy element enrichment by outflows.

Following (Aguirre et al., 2001c), our implementation is described by two parameters, the initial mass loading:

$$\eta = \frac{\dot{M}_{\rm w}}{\dot{M}_{\star}} \tag{2.27}$$

where $\dot{M}_{\star}$ is the mean star formation rate of SPH neighbours and $\dot{M}_{\rm w}$ is the mass launched in winds, and secondly the wind speed, $v_{\rm w}$. Assuming that all stars $M_{\star} > 6\,{\rm M}_{\odot}$ end as a type II SNe, the Chabrier IMF yields an injection energy of $\epsilon_{\rm SNe} = 1.8 \times 10^{49}\,{\rm erg\,M}_{\odot}^{-1}$. The fraction carried by the wind is then:

$$f_{\rm w} = \frac{1}{2}\eta v_{\rm w}^2/\epsilon_{\rm SNe} \tag{2.28}$$

$$\approx 0.4\left(\frac{\eta}{2}\right)\left(\frac{v_{\rm w}}{600\,{\rm km\,s^{-1}}}\right)^2\left(\frac{\epsilon_{\rm SNe}}{1.8\times10^{49}\,{\rm erg\,M_{\odot}^{-1}}}\right)^{-1}, \tag{2.29}$$

Following observations of outflows (e.g. Shapley et al., 2003), we choose $v_{\rm w} = 600\,{\rm km\,s^{-1}}$ and have fixed the mass loading by running a grid of simulations with varying values and selecting that which most accurately reproduces the evolution of the global star formation rate density, $\dot{\rho}_{\star}$, as determined by a range of observational indicators (e.g. see Hopkins, 2004, for a compilation). The choice of η therefore depends sensitively upon the assumed cosmological parameters; for the parameters assumed in all radiative simulations in Chapters 4, 5 & 6, the choice of $\eta = 4$ is optimal, and so winds carry eighty per cent of the available energy produced by type II SNe: the remaining twenty per cent is assumed to be radiated away.

Star particles become eligible for launching winds once they reach an age of 3×10^7 years, roughly corresponding to the maximum lifetime of a type II SNe progenitor star; this delay ensures that gas particles are enriched by type II SNe before being launched. A randomly-oriented velocity kick, $v_{\rm w}$, is added to the velocity vector of one or more neighbours of the star particle; the particles are selected stochastically from those gas particles that lie within the SPH smoothing kernel of the star, such that:

$${\rm Prob} = \eta\frac{m_{\star}}{\sum_{i=1}^{N_{\rm ngb}} m_{{\rm g},i}} \tag{2.30}$$

where $N_{\rm ngb} = 48$ is the number of neighbours within the SPH smoothing kernel. Note that the sum explicitly omits any particles already in a wind. A particle is considered 'in a wind' for a period of $t_{\rm w} = 1.5 \times 10^7$ years, so that it cannot be kicked more than once over this duration, nor can it be converted into a star particle. This ensures that unrealistically high-velocity baryonic particles are not created.

In common with other elements of our additional physics, the implementation of feedback is a rather uncertain element of the modelling. Indeed, the combined uncertainties in both the implementation of these schemes, and the observational constraints that guide them, are the primary reasons why modelling structure formation in the regime where baryon physics is important is so much less precise than modelling, for instance, large-scale structure formation. Constraints on the mass loading of winds are at present rather poor, leaving approximately three orders of magnitude of flexibility, $\eta \sim 0.01 - 10$ (Veilleux et al., 2005), and it is not clear *a priori* how strongly the initial (input) mass loading and velocity evolve once a wind is launched and becomes influenced by the ram-pressure and gravity of the disc and its environment. This uncertainty was probed by DVS08 who found that, as one might expect, the outflow velocity decreases with time as it ploughs through surrounding gas, leading to mean values far below the input value of v_w. A more complex situation was found for the mass-loading; in low-mass discs, the net outflow rate exceeds the input mass-loading (by up to an order of magnitude), whilst in more massive discs the converse is true. DVS08 attribute this to the greater ram-pressure of more massive discs, which confines outflows to the immediate vicinity of the disc.

With a fixed energy budget derived from the IMF, one may alter the wind parameters whilst still satisfying energy constraints, by trading off mass-loading and the wind speed. DVS08 report that their fiducial model results are reproduced for any scalings of the two, so long as a minimum wind velocity is imposed that is a function of disc mass (more specifically, the ISM pressure). One may also go further, and scale both η and v_w with halo mass in order that, for example, dwarf galaxies produce outflows of a lower velocity than more massive discs. Some evidence does indeed exist to support this idea, although the situation is rather confusing. Initial studies (e.g. Martin, 1999; Heckman et al., 2000) found little evidence of any trends in outflow velocity with galactic mass, but more recent observations now support then idea that higher velocity winds are driven by more massive galaxies (e.g. Martin, 2005; Rupke et al., 2005), such that the terminal velocity of the wind scales linearly with circular velocity. This motivated Oppenheimer and Davé (2006) to investigate the evolution of galaxies using a modified version of the SH03a prescription, whereby the mass loading scales as $\eta = \sigma_0/\sigma$ and wind velocity scales as $v_w = 3\sigma(f_L - 1)^{1/2}$. In these equations, σ is the velocity dispersion of the galaxy

(σ_0 then sets some normalisation for the mass loading; they opt for 300 kms^{-1}) and f_L is the 'luminosity factor' of the galaxy, in terms of the Eddington value; the value of this parameter is ~ 2, but depends weakly upon metallicity in their scheme.

Algorithmically, Oppenheimer and Davé (2006) derive the velocity dispersion of particles via the virial theorem such that $\sigma = \sqrt{-\frac{1}{2}\Phi}$, where Φ is the global gravitational potential of the particle. Clearly, this implementation is inappropriate since the global potential should have no bearing on the evolution of a galaxy; for example this scheme gives vastly different wind velocities for dwarf galaxies depending upon whether they are in the field or in close proximity to a galaxy cluster. This scheme was updated in a subsequent study, Oppenheimer and Davé (2008a), such that the velocity dispersion followed from an estimate of the galaxy mass derived from a FoF algorithm that was run on-the-fly during the simulation:

$$\sigma = 200 \left[\frac{M_\mathrm{gal}}{(5 \times 10^{12}\, h^{-1}\, \mathrm{M}_\odot)} \frac{\Omega_\mathrm{m}}{\Omega_\mathrm{b}} h \frac{H(z)}{H_0} \right]^{1/3} \mathrm{km\,s}^{-1}, \tag{2.31}$$

where the $\Omega_\mathrm{m}/\Omega_\mathrm{b}$ term converts the baryonic M_gal returned by the FoF algorithm (that considers only the gas and star particles) into a dynamical mass. This scheme is much better motivated that the Oppenheimer and Davé (2006) and, as expected, produces significantly different results. However, in light of the uncertainties (and apparent contradictions) reported in the literature regarding scalings, and the significantly differing results one is able to obtain with different algorithmic implementations of the same physical process, we opt for the simplest possible model: fixed values of η and v_w. We shall also argue in Chapter 5 that the poor resolution of the OD06 simulations is likely to have imposed severe numerical limitations upon their findings, and so the interpretation of their results is uncertain. Clearly, the numerical modelling of galactic outflows remains a subject in its infancy, and we argue here that it is preferable to start with a basic model in order to more readily understand its predictions, and the weaknesses of its implementation, before constructing more elaborate models.

2.5 Initial conditions: dwarf halo

The starting point of any simulation is its initial conditions (ICs), and their accurate creation is a crucial and non-trivial task. With one exception (the *Millennium Gas Run*

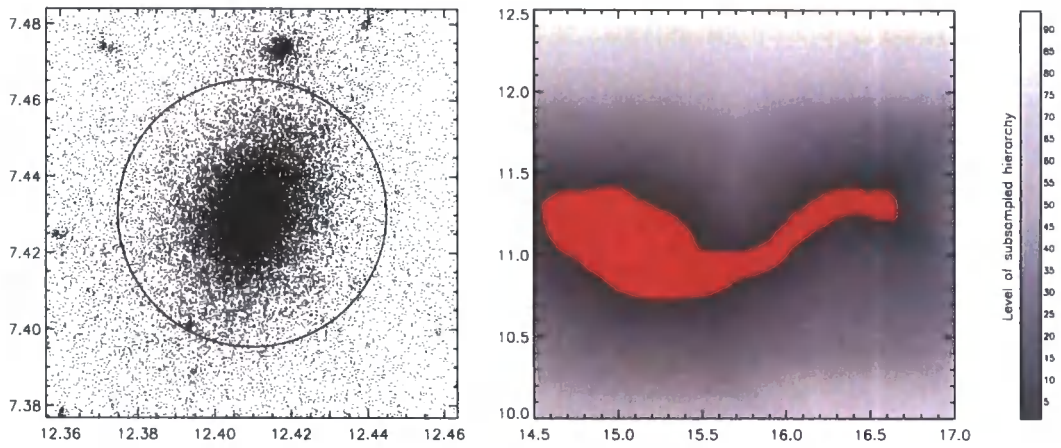

Figure 2.4: *Left*: A projection along the x-axis (i.e. the y-z plane) of a cube centered on the dwarf galaxy halo identified within the parent simulation. Coordinates are displayed in units of h^{-1}Mpc. The over-plotted circle denotes the virial radius, $r_{200} \simeq 35\ h^{-1}$ kpc. *Right*: the central y-z slice of a cubic grid featuring 400^3 cells that is placed over the selected particles at their $a \rightarrow 0$ coordinates. Within this mask, cells containing the traced particles are coloured red, whilst the grey-scale shading denotes the hierarchy of cell indexing that is used to degrade the resolution away from the particles destined to comprise the object at late times.

presented in Chapter 3), all of the simulations featured in this thesis rely on *zoomed* cosmological ICs in order to focus resolution, and therefore computational effort, onto specific objects or environments. It is appropriate to describe the general procedure used to generate zoomed ICs here; the specific aspects of the IC generation procedure in the case of GIMIC are deferred until Chapter 4. In order to illustrate the procedure, we shall present the creation of ICs for a dwarf galaxy halo that is simulated in the non-radiative regime in Chapter 3.

Candidate selection and mask generation

The first stage is to identify a candidate object or region (for example a dark matter halo and its immediate environs) from a pre-existing parent simulation. For this example, the parent simulation is a purely collisionless cubic ΛCDM volume of comoving side length $L = 35.325\ h^{-1}$ Mpc. Some criterion is then applied to find an object or region of

interest within this volume; in this case we have identified virialised structures with a friends-of-friends (FoF, Davis et al., 1985) algorithm, and selected a halo with a mass of approximately $10^{10}\,h^{-1}\,\mathrm{M}_{\odot}$.

The region we wish to reproduce at the highest level of refinement in our zoomed initial conditions is defined by a selection of particles. This selection should include: i) all of the particles comprising the object (say within the virialised radius), and also ii) particles that are likely to interact directly with the particles comprising the object at some stage of the simulation. The second criterion ensures that the particles of the object only experience interactions with other high-resolution particles, thus suppressing numerical heating effects. The definition of this criterion is vague - it is common to include all particles within 2-3 virial radii, although in the case of our example, a new code has been developed to search through all snapshots of the parent simulation and identify all particles that come within some distance of particles identified by the first criterion.

The selected particles are traced back to their coordinates in the initial conditions of the parent simulation. As we shall discuss later in this section, particle coordinates in initial conditions are determined by perturbing them from their force-free coordinates (i.e. the coordinates they tend to in the limit $a \rightarrow 0$) using the Zel'dovich approximation (Zel'dovich, 1970). Therefore the reverse process can be used to map the coordinates and velocities of the particles from the initial conditions to the force-free ($a \rightarrow 0$) state. A cubic 'mask' is made at this epoch that ensures the masked region is 'simply connected'; owing to the strongly non-linear dynamics of gravitational clustering, it is possible that the final object is comprised of particles that started their evolution at a considerable distance from other particles that they are destined to neighbour at later times. The mask is defined by a mesh surrounding the particles, and all cells containing a particle from the traced object are flagged as 'level 0'. Those neighboring level 0 cells are flagged as level 1, and so on until all cells are assigned a hierarchical index, that defines the level of refinement desired at the spatial location of the cell. The particle distribution of the dwarf halo at $z = 0$, and the resulting mask in the limit $a \rightarrow 0$, are shown in Figure 2.4; the latter contains 95 shells surrounding the level 0 cells.

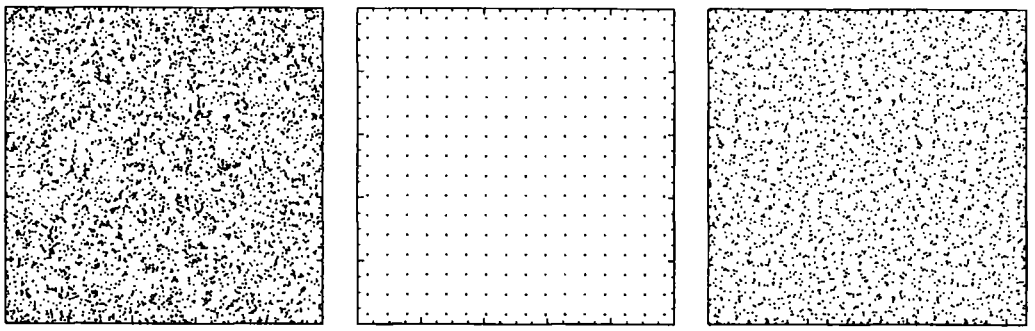

Figure 2.5: Three types of unperturbed particle distributions, from left to right: random, grid and glass. Each distribution contains $16^3 = 4096$ particles, although in the case of the grid distribution their alignment along the projection axis allows only $16^2 = 256$ to be seen. The white noise spectrum of random distributions introduces unwanted power into the fluctuation spectrum. Grid and glass distributions do not, and the latter is often used since it introduces no preferred directions on large scales.

Generation of the particle distribution

The mask defines a region within which we create a new uniform particle distribution, with greater resolution than in the original parent simulation, that is ideally free of any *net* gravitational forces. One might imagine that the simplest method is to place particles randomly throughout the masked region, however random distributions introduce Poisson noise into the power spectrum. More commonly a grid distribution is used, with particles evenly spaced along the three Cartesian axes of the volume. However, as discussed by White (1994), this introduces preferred directions into the ICs. The optimal choice of initial state is the *glass* distribution, whereby an initially random distribution is evolved as an Einstein-de Sitter Universe (i.e. $\Omega = \Omega_{\rm m} = 1$) under *reversed* gravity for many expansions (typically tens of thousands) within periodic boundaries such that all particles repel one another until eventually the distribution is smoothed and no residual power or preferred directions remain. The random, grid and glass distributions are shown in Figure 2.5.

The cubic mask is filled with a grid or glass distribution at the maximum desired resolution. Particles within cells marked as level 1 or greater are then are binned via a binary scheme that uses the hierarchical index of the cell to determine the degree of

binning. The remainder of the simulation volume (that external to the cubic mask) is then filled with a series of concentric 'cubic shells'. Within each shell, $N_{\rm sh}$ cells are aligned with the side of the enclosed cube, and so each shell features $N_{\rm sh}+2$ cells along a side. Since this outermost cubic shell must enclose the entire simulation volume, there is a quantisation condition placed upon the size of the high-resolution mask about which the shells are overlaid:

$$L_{\rm mask} = \left(\frac{N_{\rm sh}}{N_{\rm sh}+2}\right)^n L_{\rm box}, \tag{2.32}$$

where n is the number of shells, $L_{\rm mask}$ is the side length of the inner high-resolution mask, and $L_{\rm box}$ is the side length of the entire simulation volume. The increasing size of cells within each successive shell naturally degrades the resolution of the particle load as one progresses further from the high-resolution cube, and since the mass of the cells scales as $M_{\rm cell} \propto r^3$, where r is its distance from the origin of the shells, gravitational tides acting upon the high-resolution object are modelled with an accuracy that is approximately independent of range. Note that the choice of $N_{\rm sh}$ is rather arbitrary, but should not be so small that the shells are too large, nor so large that the resolution outside of the high-resolution cube is unnecessarily high. Following empirical tests, we adopt $N_{\rm sh} = 39$.

For the dwarf example, the high-resolution region was filled with 300^3 particles, derived from a 30^3 periodic tiling of a glass distribution comprising 10^3 particles. The size of the high-resolution region is $L_{\rm hi} = 1.83\,h^{-1}\,{\rm Mpc}$, and so with $\Omega_{\rm m} = 0.3$ for this simulation, this yields a high-resolution particle mass of $1.88 \times 10^4\,h^{-1}\,{\rm M}_\odot$. Binning those hi-resolution particles not within the level 0 cells reduces the overall number of high-resolution particles from $300^3 = 2.7 \times 10^6$ to $\sim 1.21 \times 10^6$. The volume exterior to the mask was filled with 170 cubic shells, yielding $170 \times (41^3 - 39^3) \simeq 1.63 \times 10^6$ multimass particles used to reproduce the gravitational tidal field.

Generating fluctuations

The aim is now to impose the original power spectrum from the parent simulation upon the new force-free particle distribution, as a Gaussian random field. However, the existence of a high-resolution region within the particle distribution requires that the power spectrum extends to larger wavenumbers. Since fluctuations on a scale below the Nyquist frequency cannot be imposed upon a particle distribution - but are rather aliased to lower frequencies, resulting in an erroneous power spectrum - fluctuations are im-

posed upon particles in two stages. Initially all particles receive power from a spectrum that is truncated on small scales, and then the small-scale fluctuations are added to the high-resolution particles separately. The truncation wavelength is therefore the longest wavelength specifically added to the high-resolution region. Since the periodicity of the simulation volume dictates that it can only accommodate a finite number of discrete wavelengths across it, the truncation wavelength should be considerably smaller (by a factor of ~ 10) than the largest wavelength imposed upon the entire simulation box, in order that fluctuations on the truncation scale be adequately represented. The side length of the high-resolution region should therefore be at least a factor of ~ 10 smaller than that of the simulation box.

The overdensity field is most naturally expressed as a superposition of modes in Fourier space:

$$\delta(\mathbf{x},t) = \left(\frac{L}{2\pi}\right)^3 \int \tilde{\delta}(\mathbf{k},t)\exp\left(-i\mathbf{k}\cdot\mathbf{x}\right)\mathrm{d}^3k, \tag{2.33}$$

where

$$\tilde{\delta}(\mathbf{k},t) = \frac{1}{L^3}\int \delta(\mathbf{x},t)\exp\left(i\mathbf{k}\cdot\mathbf{x}\right)\mathrm{d}^3x. \tag{2.34}$$

By definition the overdensity field averages to zero, $<\delta(\mathbf{x},t)>=0$, so we infer that $\tilde{\delta}(0)=0$. The function $\tilde{\delta}$ is the Gaussian random field that we wish to reproduce with a set of particles. The field is specified by its power spectrum,

$$P(\mathbf{k}) \equiv |\tilde{\delta}(\mathbf{k})|^2, \tag{2.35}$$

which by the isotropy assumption must be independent of direction, $<P(\mathbf{k})>=P(k)$, and since most inflation models predict a scale-invariant power spectrum, a good approximation is that the primordial power spectrum is:

$$P_{\mathrm{pri}}(k) = Ak^n \tag{2.36}$$

where A and n are the amplitude and normalisation of the power spectrum. We wish to commence our simulations at redshifts significantly smaller than that of the inflationary epoch, and so we must also consider the CDM transfer function that accounts for the early linear evolution of the fluid:

$$P(k) = Ak^nT^2(k) \tag{2.37}$$

We compute the transfer function numerically using the publicly available code CMBFAST (Seljak and Zaldarriaga, 1996).

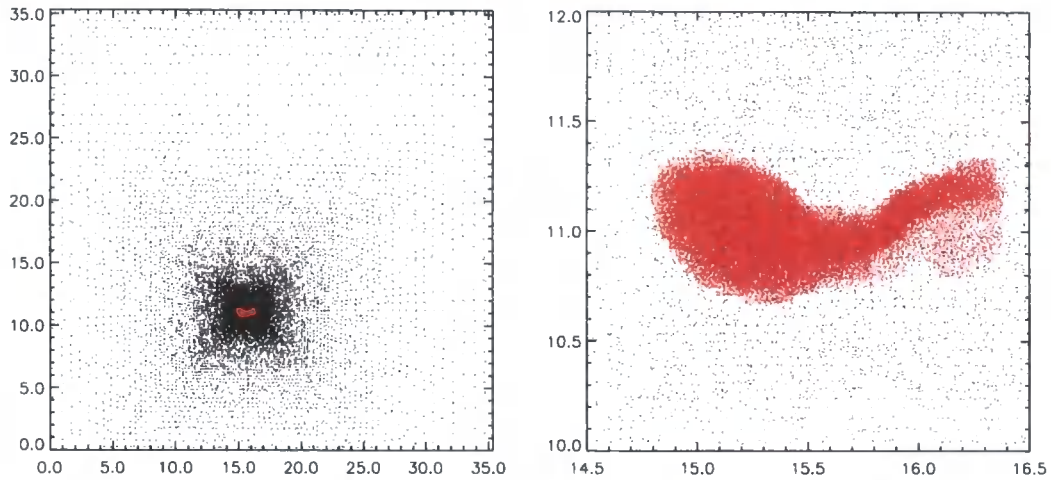

Figure 2.6: Projection in the y-z plane of the initial conditions used for the dwarf simulation. Coordinates are shown in units of h^{-1}Mpc. The left-hand panel shows the distribution throughout the entire volume ($L = 35.325\ h^{-1}$ Mpc), whilst the right-hand panel zooms into the region containing the high-resolution particles, which are shown in red in both panels. The panels highlight the large dynamic range that the ICs achieve, and the ability of our technique to adapt to complex initial morphologies. Note that the particles in the plot have been random-sampled to avoid saturation, hence the apparent 'missing particles'.

At each discrete wavevector in Fourier space, we sample the fluctuations over a finite range of wavenumbers by drawing amplitudes and phases. Amplitudes are drawn from a Rayleigh distribution, which for all $x \geq 0$ is described by

$$f(x|\sigma) = \frac{xe^{\left(-\frac{x^2}{2\sigma^2}\right)}}{\sigma^2}, \tag{2.38}$$

and is the probability distribution that arises when the orthogonal components of a wavevector are uncorrelated and normally distributed, as is the case for our fluctuation amplitudes. Phase angles are drawn at random from a uniform distribution. The inverse transform of this Fourier field yields the initial density field in real space, which is then interpolated to the particle coordinates with a CIC scheme.

Imposing the perturbations

The next step is to impose perturbations upon the particles - that is, to displace them from their force-free coordinates and assign their velocities - in order that they exhibit the desired power spectrum. At early times it is safe to assume that the dynamics are linear, and so the evolution of a particle at a given Lagrangian coordinate, $\mathbf{x}$, evolves as:

$$\delta(\mathbf{x}, \tau) = D(\tau)\delta_0(\mathbf{x}), \tag{2.39}$$

where $\mathrm{d}\tau = \mathrm{d}t/a$ is the *conformal time* and $D(\tau)$ is the linear growth factor, whose solution is sensitive to the assumed cosmology; detailed solutions are given by Peebles (1980). As outlined by White (1994), this leads to the notion of a *self-similar* temporal evolution of the density field and also the peculiar potential, such that it can be predicted from its present value, $\Phi_0(\mathbf{x})$, via

$$\Phi(\mathbf{x}, \tau) = \frac{D}{a}\Phi_0(\mathbf{x}) \tag{2.40}$$

where

$$\nabla^2\Phi_0(\mathbf{x}) = 4\pi G\bar{\rho}a^3\delta_0(\mathbf{x}). \tag{2.41}$$

Zel'dovich (1970) used this assumption to derive an approximation for the initial dynamics of structures, such that

$$\mathbf{x} = \mathbf{x}_0 - \frac{D(\tau)}{4\pi G\bar{\rho}a^3}\nabla\Phi_0, \tag{2.42}$$

and

$$\mathbf{v} = -\frac{\dot{D}(\tau)}{4\pi G\bar{\rho}a^2}\nabla\Phi_0 = -\frac{1}{4\pi G\bar{\rho}a^2}\frac{a\dot{D}}{D}\nabla\Phi. \tag{2.43}$$

We hence use these equations to advance the unperturbed coordinates and velocities of the particles to those applied in the initial conditions for a desired initial redshift. The final, perturbed, particle distribution of the dwarf is shown in Figure 2.6.

Adding gas

The particle distribution we have created represents the entire matter fluid; that is, the particles are essentially a composite of baryons and dark matter. If studying large-scale structure, then it is sufficient to evolve these particles collisionlessly, since the fluid dynamics are dominated by gravity. For hydrodynamic simulations, the composite particles are split into two: one particle represents the dark matter (and so remains as a

collisionless particle) and the other is treated as a gas particle upon which the SPH algorithms act. Each composite particle of mass m_p is therefore split into a CDM and a gas particle of mass $m_{cdm} = m_p(\Omega_m - \Omega_b)/\Omega_m$ and $m_{cdm} = m_p\Omega_b/\Omega_m$ respectively. The particles are offset, in each dimension, from the composite particle's coordinate by a mass weighted fraction of the mean inter-particle separation, so as to maintain the overall centre of mass of each gas-dark matter particle pair.

2.6 Evolution of the dwarf galaxy halo

The simulation was run on 64 processors in a wallclock time of ~ 30 hours. The initial conditions were created at $z = 75$ and the simulation was evolved to $z = 0$, producing 950 outputs[3] that were spaced logarithmically in expansion factor between $z = 30$ and $z = 0$.

Gas evolution and star formation rate

The evolution of the system is delineated by a number of key periods, which are illustrated by panels in Figure 2.7:

- **Pre-reionisation era**, *upper left panel*: the high-resolution of the simulation enables very small proto-galactic progenitors to be followed. In the absence of the ultraviolet background, gas associated with these overdensities cools efficiently and the star formation rate rises rapidly. Small fluctuations in the star formation rate are seen when mini-starbursts trigger winds that temporarily eject cooling gas from the star-formation sites, but cooling is so efficient that star formation rapidly recommences.

- **Epoch of reionisation** *upper right panel*: at $z = 9$ the photo-ionising background appears. This very rapidly heats the cold gas to $T \sim 10^4$ K; this temperature is greater than the 'virial temperature' of many of the proto-galactic progenitors and proto-filaments surrounding the main progenitor, so this gas ceases to collapse and returns to a diffuse state. This quenches the supply of cold gas for star formation, and the star formation rate plummets.

[3]This large number of outputs was produced in order to allow very high time-resolution studies.

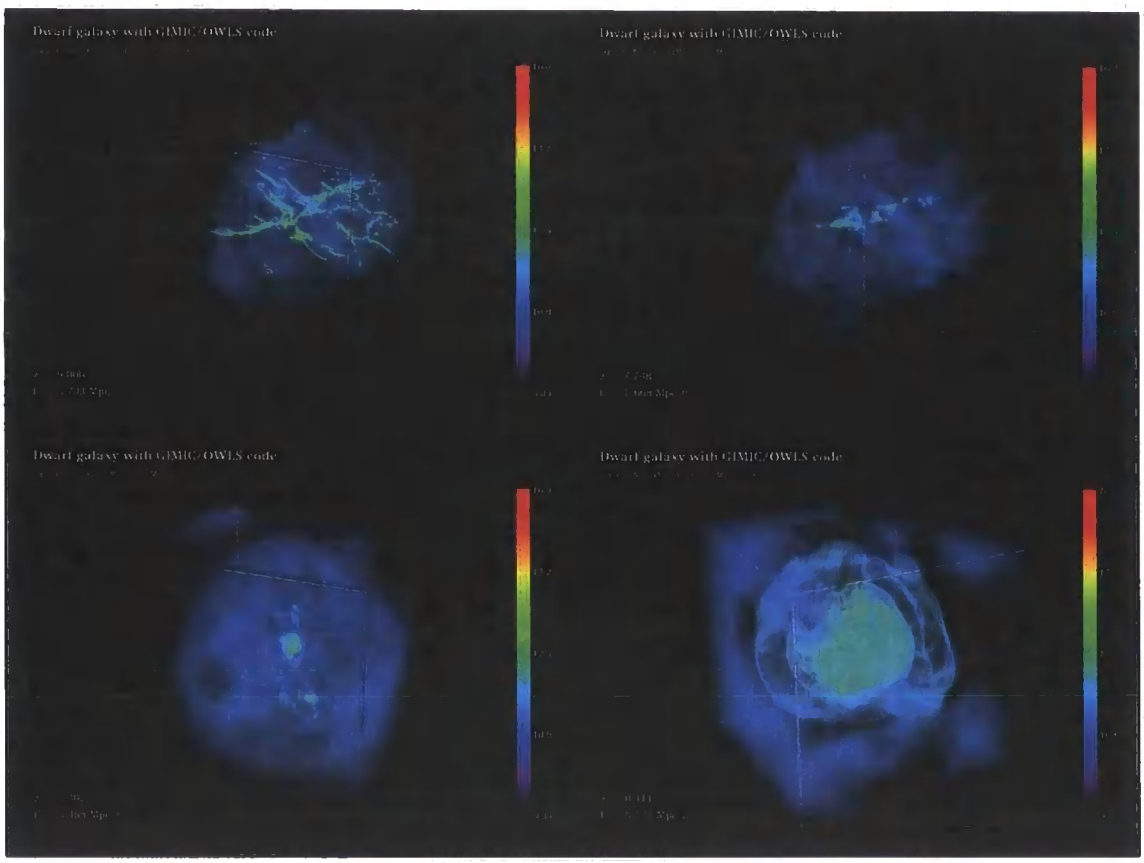

Figure 2.7: The four key epochs in the evolution of the dwarf galaxy. See text for description.

- **Post-reionisation** *lower left panel*: the imposed, evolving photo-ionising background significantly shifts the ionisation balance in cold gas, reducing the cooling rate. As such the star formation rate never returns to its pre-reionisation epoch level. The star formation rate is determined by a balance between cooling and the mitigating action of winds, with peaks in the star formation rate (triggered by mergers between progenitor haloes) being followed by temporary drops as winds are driven by type II SNe.

- **Merger at low-redshift** *lower right panel*: the final halo is formed at fairly low-redshift by the merger of two progenitors of similar mass. This merger triggers a jump in star formation that is localised within a single object, triggering strong winds that drive nearly all of the gas (and metals) associated with the final object into the IGM, and quenching any further star formation.

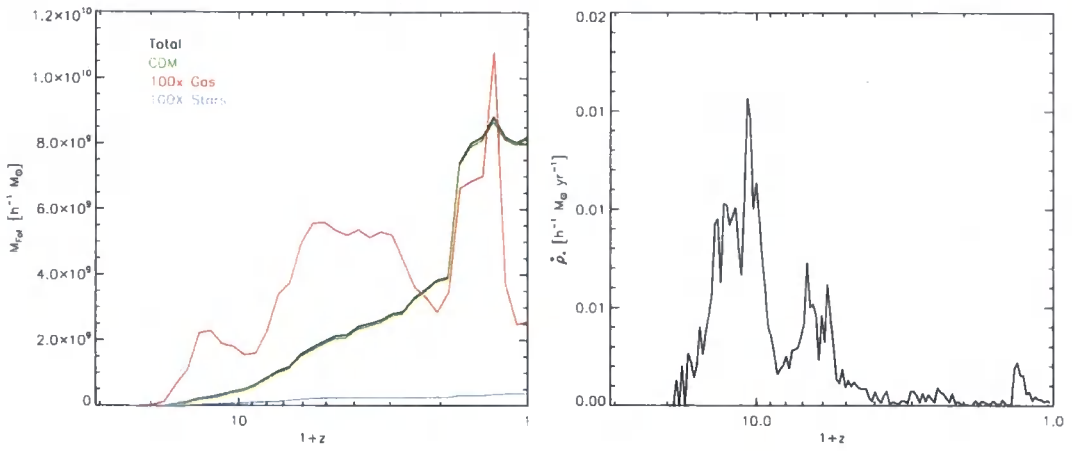

Figure 2.8: *Left*: The mass evolution of the dwarf galaxy, in terms of its resolved FoF halo mass; our FoF algorithm attaches baryons within a linking length of the dark matter halo, allowing them to be traced also. The total mass (black) is dominated by the CDM mass (green), as strong feedback from winds suppresses the accretion of gas (red) and the formation of stars (blue), the masses of both are boosted in this plot by a factor of 100 to allow comparison with the CDM component. A major merger in the galaxy is evident at $z \simeq 0.3$. *Right*: The evolution of the star formation rate of the dwarf galaxy. Star formation is relatively efficient at early times, but is suppressed at $z = 9$ by the onset of hydrogen reionisation, and declines strongly at low redshift as winds efficiently eject cooling gas. A late spike in star formation rate is seen at the epoch of the merger, but the strong winds generated by this starburst effectively shut down all further star formation.

The evolution described above is succinctly captured by following the mass of the main progenitor halo, and its star formation rate. These are shown in Figure 2.8. The main progenitor is defined here as the most massive halo in the simulation identified by the FoF ($b = 0.2$) algorithm; since the halo features a quiescent merger history and few major substructures, this is a sound definition. We have generalised the FoF algorithm to associate baryons with dark matter haloes; any baryonic particles within a linking length of a grouped dark matter particle are attached to the host halo of the dark matter particle; any baryonic particles linked to two or more haloes are attached to the most massive halo. We therefore trace the build-up of gaseous and stellar mass in addition to the CDM mass. At early times the mass of the main progenitor is underestimated by the inability of the simulation to resolve the very first proto-galactic haloes. However, as shown in

the left-hand plot of Figure 2.8, the build-up of dark matter mass in the main progenitor is smooth until it merges with a second halo of only slightly lower mass. The effect of winds upon the evolution of the halo gas mass is imprinted clearly in Figure 2.8; the steady build-up of the dark matter is contrasted by the gas, which features several dips that are the signature of outflow. The build-up of stellar mass, which is reliant upon the supply of cold gas to the centre of the halo, therefore grows much less rapidly than the halo dark matter mass. The signatures of the four evolutionary periods described above are clearly reflected in the star formation rate: i) a rapid rise as proto-haloes collapse and trigger efficient gas cooling, ii) a sharp decline at the epoch of reionisation, iii) a fairly quiescent period interspersed with bursts of star formation that are quickly quenched by winds, and iv) a peak in star formation at the epoch of the merger that induces strong winds and blows most of the gas out of the halo.

The effect of reionisation

Reionisation is widely believed to affect the formation of galaxies in haloes that are significantly less massive than, say, the Milky Way's halo (e.g. Doroshkevich et al., 1967; Couchman and Rees, 1986; Rees, 1986; Efstathiou, 1992; Thoul and Weinberg, 1996; Gnedin, 2000). Indirectly, this also affects the evolution of more massive galaxies, since they are assembled hierarchically from smaller haloes. A simple understanding of the effect may be gained from inspection of the upper panels of Figure 2.9, which depict the gas distribution shortly prior to, and after, the onset of reionisation at $z = 9$. Beforehand, most gas is cold, having evolved adiabatically from $z \sim 100$ when the gas decoupled from the CMB temperature, and so:

$$T_{\rm min}(\rho) = T_0 \left(\frac{\rho}{\bar{\rho}}\right)^{\gamma-1}, \tag{2.44}$$

where $\gamma = 5/3$ and

$$T_0 \sim T_{\rm CMB,z=100} \left(\frac{1+100}{1+z}\right)^2. \tag{2.45}$$

Consequently, it traces the intricate filamentary structure of dark matter filaments and flows readily into proto-haloes. The distribution in the ρ-T plane is shown in the upper left-hand panel of Figure 2.9; most gas lies in a pillar around the mean density. As the upper right-hand panel shows, the only radiative process operating is cooling, and as the gas is heated by compression and shocks towards $T = 10^4$ K, its cooling rate is boosted

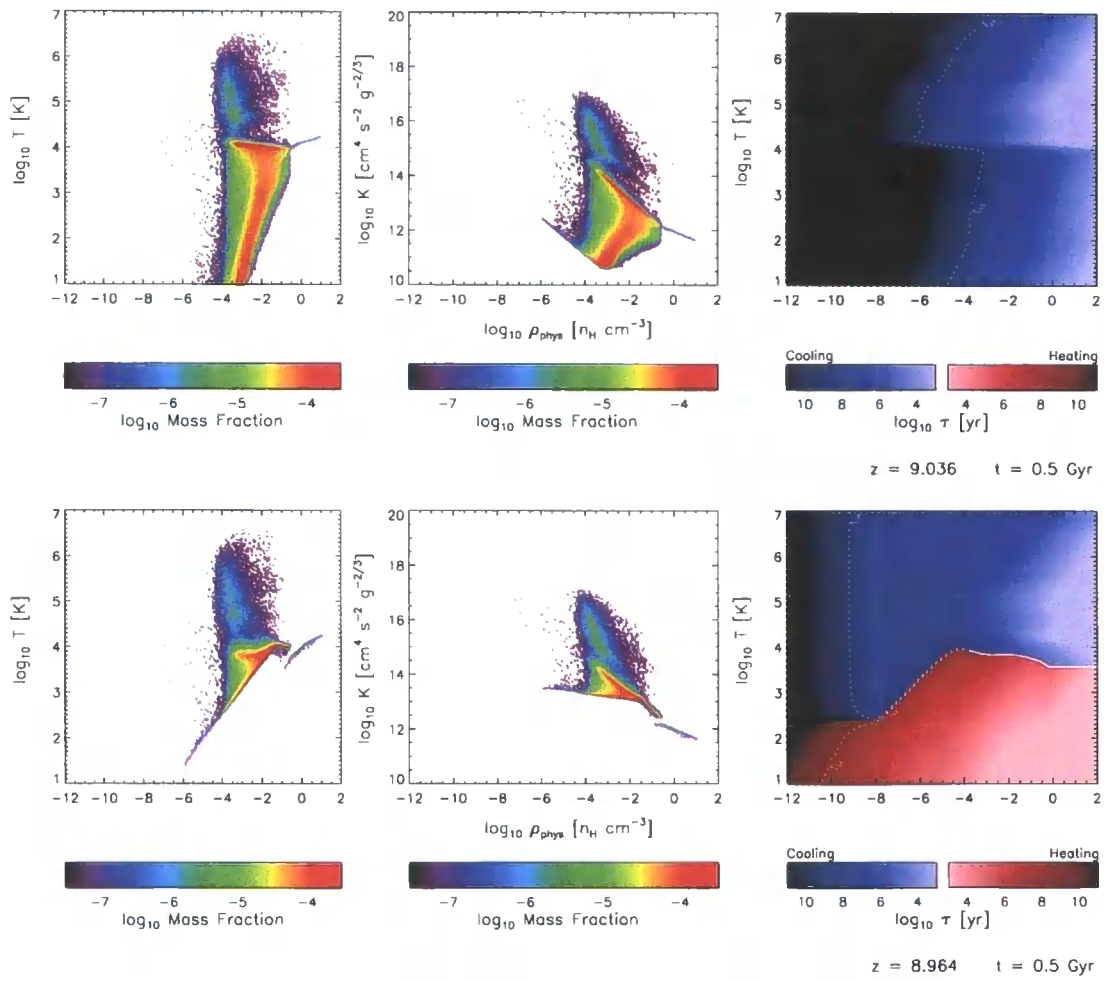

Figure 2.9: Gas thermodynamics immediately prior to (top), and after (bottom), the epoch of reionisation ($z = 9$ in our simulations). The left-hand column shows the density-temperature plane, the centre row shows the density-entropy plane, and the right-hand column shows the cooling time t_c in the density-temperature plane. At $z > 9$ most gas lies in a pillar in the ρT plane, and remains cool as its density increases owing to the peak in the cooling function at $T \sim 10^4$ K, which is visible in the cooling time plot. The onset of reionisation rapidly heats this pillar of gas, and an equilibrium track where heating and cooling balance is established ($\mathcal{H} = \mathcal{C}$), requiring that gas must heat as it becomes more dense, before the cooling function at higher densities enables it to cool once more. This has significant consequences for the evolution of small galaxies.

dramatically by the peak in the cooling curve due to hydrogen line emission. Gas only progresses to higher temperatures therefore via strong shock heating (most likely due to the ram-pressure of winds), or by entering the ISM whereupon it is subjected to our polytropic equation of state. As discussed earlier, the temperature of SPH particles in the ISM is somewhat artificial - these particles are visible in the ρT plane as the small spike at high-densities.

The lower right-hand panel of Figure 2.9 shows how, after the epoch of reionisation, low temperature gas is dominated by radiative (photo-)heating. Defining the net radiative cooling time as:

$$\tau_c(\rho, u) = \frac{u}{\dot{u}} = \frac{3k_B T}{2\mu} \frac{m_H}{\rho(1-Y)^2(\mathcal{C}-\mathcal{H})}, \tag{2.46}$$

where μ is the molecular weight of the gas, Y is the mass fraction of helium, and $\mathcal{C}, \mathcal{H}$ are the normalised cooling and heating rates respectively, then when $\tau_c < \tau_H = 1/H(z)$, where $H(z)$ is as defined in Equation 1.6, a new power-law is established. This time, the temperature is fixed by adiabatic expansion cooling and photo-heating, thus altering the effective equation of state (Hui and Gnedin, 1997):

$$T(\rho, z) = T_0(z) \left(\frac{\rho}{\bar{\rho}}\right)^{\gamma_{IGM}-1}, \tag{2.47}$$

where $\gamma_{IGM}(z) \sim 1 - 1.62$. The equilibrium is maintained as below this temperature the heating time is short, and conversely at higher temperatures the cooling time is short. In terms of the evolution of our dwarf, most of the gas in filaments that would otherwise have flowed into proto-galaxies and rapidly formed stars, is rapidly heated. It becomes unbound from the weak gravitational potentials of the filaments and is not reaccreted until the dark matter structures have grown sufficiently massive that their virial temperatures,

$$T_{200} = \frac{\mu m_H v_c^2}{2k_B}, \tag{2.48}$$

where $v_c = (GM/r_{200})^{1/2}$ is the circular velocity of the gas at the virial radius, exceed the temperature of this gas. This unbinding can be seen by comparing the gas distribution in the upper panels of Figure 2.7.

Halo structure at the present epoch

At $z = 0$ the halo has acquired a total FoF mass of $8.2 \times 10^9\ h^{-1}\,M_\odot$, of which over 99 per cent is dark matter; the associated gas and stellar masses are $2.6 \times 10^7\ h^{-1}\,M_\odot$ and $3.8 \times$

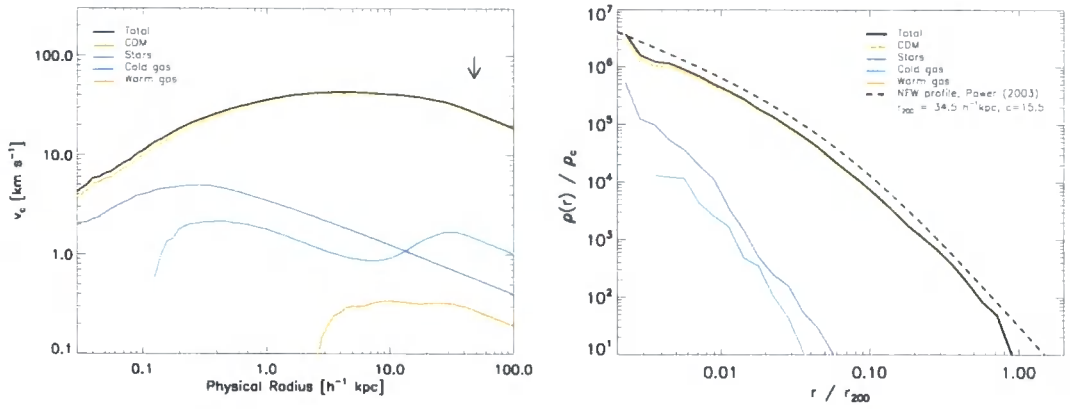

Figure 2.10: *Left*: The spherically averaged radial profile of the circular velocity of the dwarf halo at $z = 0$, showing the total (black) and contributions from dark matter (yellow), stars (blue), cold gas ($T < 10^5$ K, cyan) and warm gas ($T > 10^5$ K, orange). The dwarf is dark matter-dominated at all radii, and has very little baryonic mass. *Right*: The analogous density profile, which clearly deviates from the NFW profile (dashed line) at the centre.

$10^6\, h^{-1}\, M_\odot$. This tiny baryon fraction is indicative of the efficacy of gas ejection in dwarfs in our model. The spherically averaged radial distribution of matter is shown in Figure 2.10, as both circular velocity and density profiles. The dominance of the dark matter produces a flat circular velocity profile of the form commonly inferred from observed rotation curves, over the range $r \simeq 1 - 10h^{-1}$ kpc. In the right-hand panel, we overplot the Navarro-Frenk-White density profile (Navarro et al., 1996, 1997, hereafter NFW) that was derived by Power (2003) for the dwarf when simulated with collisionless dynamics. This profile takes the form:

$$\rho(r) = \frac{\rho_c \delta_c}{(r/r_s)[1 + (r/r_s)]^2}, \tag{2.49}$$

where $r_s = r_{200}/c$, c is the *concentration parameter*, and

$$\delta_c = \frac{200}{3} \frac{c^3}{\ln(1+c) - [c/(1+c)]}. \tag{2.50}$$

It is interesting to compare this fit with the profile from the radiative simulation; the density of the dwarf has been significantly reduced by the baryon physics, although this is perhaps unsurprising when one considers that winds have reduced the baryon fraction of the halo to less than 1 per cent. The baryonic mass component of the col-

lisionless simulation is of course represented by composite particles, and so the mass of the dwarf in this case is approximately 15 per cent greater, since these simulations assume $\Omega_b/\Omega_m = 0.045/0.3 = 0.15$. Note that the shape of the density profile remains remarkably similar, except at the very centre ($r \lesssim 100$ pc) where the presence of a stellar core steepens the profile in the radiative simulation.

Metallicity evolution

It is appropriate here to demonstrate the combined role of our new implementations of chemical enrichment and feedback in GADGET3-BG, since these schemes underpin one of the key motivations for the simulations in this thesis, namely the role of galactic winds in enriching the IGM. Although dwarfs produce a relatively small mass of stars, and therefore metals, they might be of paramount importance owing to their abundance, and the fact that their shallow potentials may render it easier for their outflows to escape into the IGM.

Indeed, the escape of metals from our dwarf is seen clearly in Figure 2.11. The relatively high star formation rate of the dwarf in the pre-reionisation era means that by $z = 9$, ~ 25 per cent of the total metal mass that the dwarf will eject into the IGM by $z = 0$ is already there (Figure 2.12). These metals remain in the vicinity of the progenitor proto-galaxies, until winds begin to drive outflows that are able to transport the metals farther afield. This is illustrated in the lower-left panel of Figure 2.11, which shows the dramatic effect of ram-pressure on the outflows: the winds naturally find the easiest path out of the galaxy and so become roughly collimated. Eventually their kinetic energy is entirely thermalised by the ram-pressure of the ambient gas, diffusing metals roughly orthogonal to the outflow direction. These shells, however, continue to be driven farther into the IGM by winds from subsequent episodes of star formation. Indeed, the burst of star formation that is triggered by the merger at $z \simeq 0.3$ (bottom-right panel) expels nearly all of the gas, and gas-phase metals, from the halo.

The time evolution of metal synthesis in the dwarf is shown in Figure 2.12. The metals act as a fossil record of the star formation history of the galaxy, and so trace the stellar mass assembly that is plotted in Figure 2.8. As fixed by the yields in our stellar evolution model, the metal budget is dominated by oxygen, which is predominantly synthesised by the massive progenitor stars of type II SNe. The temporal evolution of

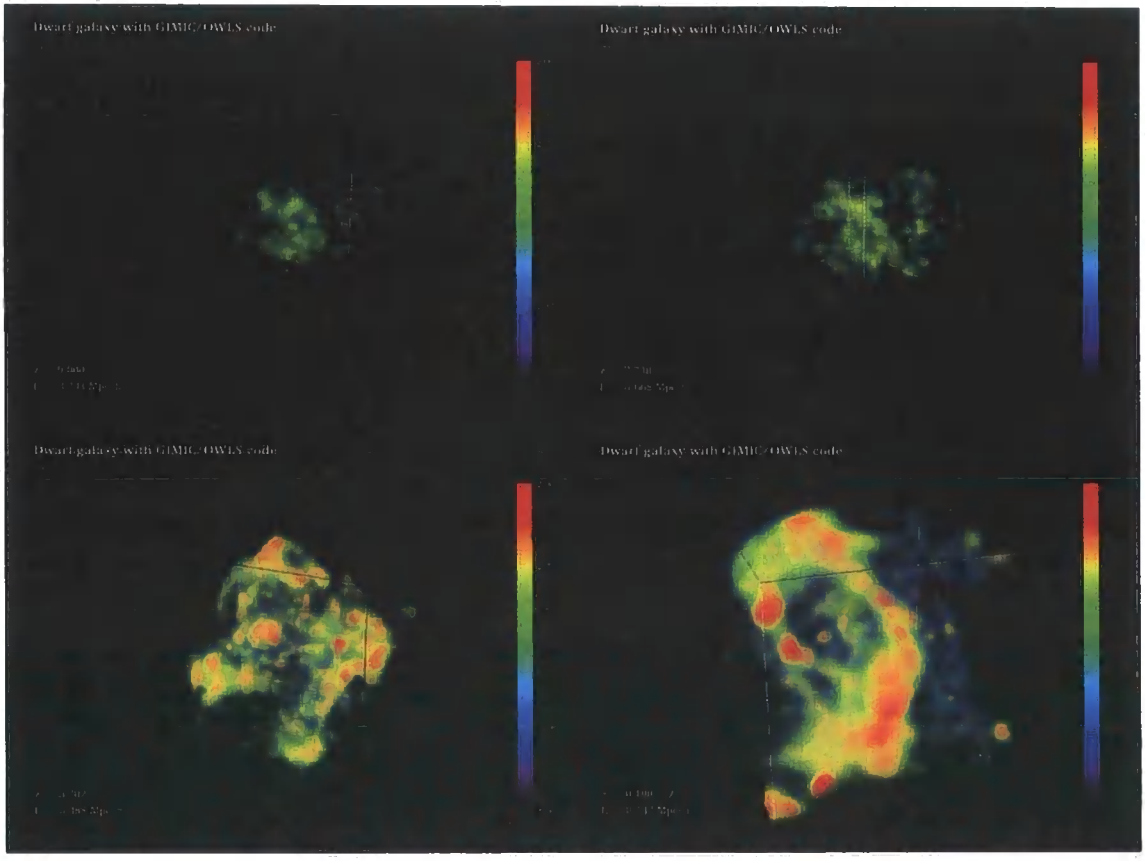

Figure 2.11: The formation and transport of metals synthesised in the dwarf galaxy halo. The epochs of the first three panels correspond to those in the same location in Figure 2.7, the final panel in figure is at a slightly later epoch than its analogue in Figure 2.7. As early as $z = 9$, winds have acted to push metals into the IGM, and at $z = 3.4$ (lower-left panel), collimated outflows can be seen punching through the inflowing gas and then spreading out at larger radii once their kinetic energy is thermalised by ram-pressure. The final panel shows a strongly enriched outflow that was triggered by the merger at $z \sim 0.5$, illustrating the potential role of winds in the enrichment of the IGM.

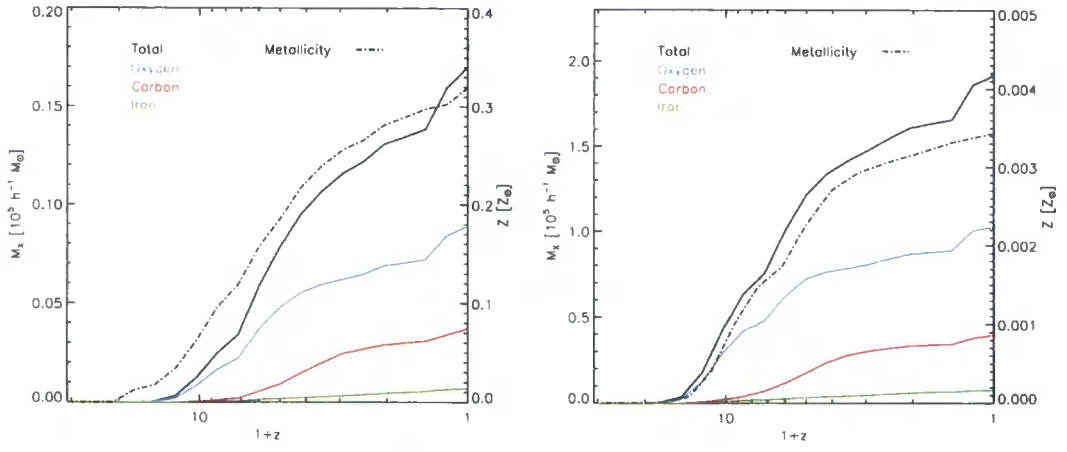

Figure 2.12: The evolution of the total metal mass (solid black), and the contribution to this from oxygen (blue), carbon (red) and iron (green) in the stars (left-hand plot) and gas surrounding the galaxy (right-hand plot). The mean metallicity (dot-dashed black) of the galaxy's stars and gas is shown on the right-hand y-axis of each plot. The build up of metal mass is steady, tracing the star formation rate, and can be seen to jump at the epoch of the merger ($z \sim 0.3$).

this model is also evident, as both the gas (left) and stars (right) exhibit significant oxygen enrichment prior to the carbon that primarily comes from AGB-phase stars, and iron that is primarily from type Ia SNe. These plots illustrate the efficacy of dwarfs as sources of heavy elements for enriching the IGM; at all epochs the mass of metals that has been ejected in the gas phase is ~ 100 times greater than the mass retained in stars. This quantitative measurement confirms the qualitative indication suggested by Figure 2.11: collimated, enriched outflows punch through the infalling, cold gas and carry metals far away from the galaxy, such that subsequent generations of stars do not become as enriched as might be naïvely imagined.

It should be noted that the structure and dynamics of the outflow are very likely to be sensitive to the details of their algorithmic implementation and the resolution of the simulation. The persistent hydrodynamic coupling of winds in our model is therefore clearly advantageous, since it is clear that the collimation and subsequent thermalisation of outflows in the dwarf is a direct result of the hydrodynamic forces. Moreover, the generation of winds in this case is triggered by purely local effects, as is of course the case in nature. It is unclear whether models based on the SH03a model, in which winds

are temporarily decoupled from hydrodynamic forces and triggered in response to the globally averaged star formation rate, would reproduce the structure and dynamics of the outflows seen in this example.

2.7 Summary

We have described the key algorithms that are implemented in simulation codes, focussing in particular on those baryonic physics modules that feature in the GADGET3-BG code that we use to evolve the simulations featured later in Chapters 4, 5 & 6. We have also outlined the procedure used to generate the zoomed initial conditions featured in all but one of the simulations presented in this thesis. In the following chapter we turn to the more simple non-radiative regime in order to elucidate, with unprecedented statistical power and spatial resolution, the properties of halo gas that arise in the absence of feedback. We shall show that these properties motivate the computationally expensive radiative simulations we later conduct.

Chapter 3

Baryon evolution in the non-radiative regime

3.1 Introduction

The role of radiative processes in the formation of galaxies and their co-evolution with the IGM was discussed in Chapter 1, and in Chapter 2 the key effects of several of these processes were demonstrated with a case study simulation featuring a dwarf galaxy. However, we shall demonstrate in this chapter that non-radiative simulations, which are less resource-intensive than their radiative counterparts, remain a useful tool for studying various aspects of the evolution of cosmic baryons.

To recap, in the current paradigm of cosmic evolution (ΛCDM), structures grow from an initially smooth density field into a rich network of filaments and haloes. Initially, baryons approximately follow the collisionless dark matter, but the two components evolve differently in non-linear regions after recombination. In protogalactic haloes, for example, the kinetic energy of the collapse is thermalised in shocks by the baryons, but rapid radiative cooling losses allow for further collapse, leading to the formation of dense gaseous discs susceptible to swift transformation into stars (White and Rees, 1978).

The efficient gas cooling that accompanies the collapse of protogalactic haloes at high redshift underlies one of the central apparent conflicts between hierarchical models of structure formation and observation. Indeed, Cole (1991) and White and Frenk (1991) highlighted that, in the absence of additional physics, hierarchical models predict that essentially the entire baryonic content of the Universe should have cooled at high redshift and, presumably, turned into stars by the present epoch. This is in strong contradiction with observations, which suggest that stars make up less than 5% of the baryons

in the Universe (for a review, see Balogh et al., 2001). To avoid this 'cooling catastrophe', models of galaxy formation frequently invoke various astrophysical mechanisms that counteract cooling and, in some cases, reheat cold gas.

One consequence of the cooling catastrophe is the difficulty in reconciling the galaxy luminosity function with the ΛCDM halo mass function. This was recognised in the pioneering work of White and Rees (1978), and it is now widely accepted that a heating mechanism (usually referred to as 'feedback') is required to explain the reduced star formation efficiency required to match the shallow faint end, as well as the sharp cut-off at the bright end, of the galaxy luminosity function (e.g. Kauffmann et al., 1999; Somerville and Primack, 1999; Cole et al., 2000; Benson et al., 2003; Bower et al., 2006; Croton et al., 2006).

The main heating mechanisms are commonly believed to be: (i) photo-heating by the energetic photons that reionised the Universe at high redshift, (ii) the thermal and kinetic output of evolving stars and supernovae (SNe), and (iii) the energy released by accretion of matter into the supermassive black holes responsible for active galactic nuclei (AGN). The importance of each of these processes varies as a function of halo mass. Whereas (i) is thought to curtail star formation in extremely low-mass haloes and substructures, (ii) is assumed to regulate the star formation history of dwarf and normal galaxies. The role of (iii) is expected to be most relevant for the formation of giant galaxies, typically ellipticals found predominantly in the dense cores of galaxy clusters (e.g Richstone et al., 1998).

Of all these, mechanism (ii) is the best studied, but there is still no consensus concerning its role in regulating star formation. Although it is energetically possible for SNe to suppress star formation in galactic haloes (Dekel and Silk, 1986; White and Frenk, 1991), it has long been recognised that the efficiency required for this process to be viable is uncomfortably high (Benson et al., 2003; Kang et al., 2005). Hydrodynamical simulations, for example, show that under normal circumstances SNe are far less efficient at expelling mass and reheating the IGM than required by galaxy formation models in order to match the faint-end of the luminosity function (Mac Low and Ferrara, 1999; Strickland and Stevens, 2000). Identifying an additional or alternative source of feedback is therefore highly desirable.

In a recent paper, Mo et al. (2005, hereafter M05) proposed an elegant alternative,

namely, that the collapse of large-scale pancakes and filaments might heat the gas prior to the assembly of low-mass haloes. M05 sketch analytic arguments in support of the idea that this 'pre-virialisation' gravitational heating might generate enough entropy, at low redshift ($z \lesssim 2$), to inhibit the accretion of gas into low-mass haloes. If efficient enough, this mechanism may offer a simple and attractive resolution to the cooling crisis, and a possible explanation of the form of the faint end of the galaxy luminosity function without the need to invoke feedback from non-gravitational sources, such as photo-ionisation or SNe.

This is clearly an intriguing proposition, and we present here a suite of cosmological gas-dynamical simulations aimed at assessing the viability of the pre-virialisation heating hypothesis in the ΛCDM cosmogony. Our simulations allow us to probe a vast range of halo masses, from $10^{10}\ h^{-1}\ \mathrm{M}_{\odot}$ to roughly $10^{15}\ h^{-1}\ \mathrm{M}_{\odot}$. The simulations assume that baryons evolve as a non-radiative fluid. This is a conservative assumption when testing the pre-virialisation hypothesis, because radiative losses would only serve to facilitate the collapse of baryons into protogalactic haloes.

We also use the same suite of simulations to explore the baryon fraction at the opposite end of the halo mass function, i.e., in galaxy cluster haloes. Adopting a non-radiative gas approach is a reasonable simplification here, since the majority of the intracluster medium (ICM) has a cooling time that exceeds the age of the Universe. The most massive galaxy clusters are of particular cosmological interest since their baryon fractions are expected to trace accurately the cosmic mean. Indeed, the comparison of cluster baryon fractions (f_b) with the baryon density parameter (Ω_b) implied by Big-Bang nucleosynthesis calculations provides decisive evidence for a Universe with (dark) matter density well below the critical density for closure (White et al., 1993).

In addition, the apparent redshift dependence of cluster baryon fractions can be used to constrain the geometry of the Universe (Sasaki, 1996), its deceleration (Pen, 1997), and by extension, the dark energy equation of state (Allen et al., 2004). These tests exploit the redshift dependence of angular diameter distances and rely on cluster baryon fractions being roughly universal and non-evolving over the redshift range where they can be observed (typically $z < 1$).

Our simulation suite provides the largest sample of haloes with non-radiative gas dynamics reported to date. This allows us to investigate the mass dependence, evolu-

tion and dispersion of halo baryon fractions with unprecedented statistical reliability. These results can be used to test critically the viability of the pre-virialisation heating hypothesis and to examine the stability and evolution of cluster baryon fractions.

In the following section we describe our simulation suite, and in Section 3 we outline our analysis methods and main results. We discuss them in Section 4 and conclude with a brief summary in Section 5.

	$m_{\rm gas}$ $[h^{-1}\,{\rm M}_\odot]$	$m_{\rm dm}$ $[h^{-1}{\rm M}_\odot]$	$N_{\rm p}$	$\epsilon_{\rm com}$ $[h^{-1}\,{\rm kpc}]$	$\Omega_{\rm b}$	Ω_0	L $[h^{-1}\,{\rm Mpc}]$	$z_{\rm init}$
HIGH-MASS	3.12×10^9	1.42×10^{10}	5.0×10^8	100.0*	0.045	0.25	500	49
LOW-MASS	1.65×10^6	8.70×10^6	2.6×10^6	5.0	0.040	0.25	100	127
DWARF	1.20×10^4	7.80×10^4	3.4×10^5	0.4	0.040	0.30	35.325	74
PANCAKE	1.20×10^6	7.83×10^6	3.5×10^5	10.0	0.040	0.30	N/A	145

Table 3.1: Parameters for the various simulations. Note that each simulation contained an equal number, $N_{\rm p}$, of both gas and high-resolution dark matter particles. Softening lengths, ϵ, are quoted in comoving coordinates hence we mark the HIGH-MASS simulation with an asterisk to denote that its softening was switched to physical units at $z = 3$. The PANCAKE simulation has no boxsize, L, since it was run with vacuum boundary conditions.

3.2 Simulation Details

To maximise the dynamic range of our halo sample we analyse two simulations of different volumes. One (labelled LOW-MASS) is a high-resolution 'zoomed-in' simulation of a relatively small volume designed to study low-mass haloes. The other (HIGH-MASS) is a gas-dynamical realisation of the *Millennium Simulation* (Springel et al., 2005), a large volume containing many well resolved galaxy clusters. We address numerical convergence issues by simulating the collapse of a 'pancake' at varying numerical resolution. And, finally, we test explicitly the robustness of our results in the LOW-MASS simulation by re-simulating at much higher resolution a single (DWARF) halo with virial mass $10^{10}\ h^{-1}\ \mathrm{M}_{\odot}$. The numerical parameters and other details of the simulations are listed in Table 3.1.

We evolve our initial conditions in all cases using the publicly available parallel code GADGET-2 (Springel, 2005), with non-radiative[1] baryon physics implemented by an entropy-conserving formulation of smoothed particle hydrodynamics (SPH) (Springel and Hernquist, 2002a). We smooth SPH quantities over 40 neighbour particles in each simulation, with the exception of HIGH-MASS, in which 33 neighbours were used.

3.2.1 HIGH-MASS simulation

Our sample of high-mass haloes is drawn from a non-radiative gas-dynamical realisation of the *Millennium Simulation*. It adopts the same displacement field and cosmology as the original simulation, but has lower mass resolution: 5×10^8 gas and dark matter particles within a periodic simulation box of side $500\ h^{-1}$ Mpc. The baryon density parameter $\Omega_{\mathrm{b}} = 0.045$ results in particle masses of $m_{\mathrm{gas}} = 3.12 \times 10^9\ h^{-1}\ \mathrm{M}_{\odot}$; for the dark matter we adopt $\Omega_{\mathrm{dm}} = 0.25$, implying a particle mass of $m_{\mathrm{dm}} = 1.42 \times 10^{10}\ h^{-1}\ \mathrm{M}_{\odot}$. We choose a comoving gravitational softening of $100\ h^{-1}$ kpc until $z = 3$, at which point it is fixed in physical units to $25\ h^{-1}$ kpc. Gravitational forces are computed in this simulation with a TreePM algorithm, wherby short-range forces are computed by hierarchical multipole expansion and long range forces are computed with a particle-mesh (PM) scheme based on Fast Fourier Transforms (FFTs). A mesh of 1024^3 cells was adopted for the PM

[1] We avoid the common practice of terming non-radiative simulations 'adiabatic', since they include non-adiabatic shocks.

algorithm. Further discussion of the simulation details and analysis shall be presented in a forthcoming paper (Pearce et al., *in prep*).

3.2.2 LOW-MASS simulation

In order to analyse a representative region of the Universe whilst still resolving low mass haloes, we simulate the evolution of a spherical region of radius 7 h^{-1} Mpc, identified at $z = 0$ in a simulation of a box 100 h^{-1} Mpc on a side with the same cosmological parameters as the *Millennium Simulation*. The sphere was chosen at random from a sample of spherical regions with mean density within 10% of the cosmic mean, and devoid of haloes with mass $M_{200} > 10^{13}\ h^{-1}\ \mathrm{M}_{\odot}$, in order to prevent the region from being dominated by a single halo. Randomly placed spheres satisfy the density selection criterion slightly less than 10% of the time, since the volume is dominated by underdense regions. Approximately one-third of spheres satisfying the density criterion lack haloes more massive than $10^{13}\ h^{-1}\ \mathrm{M}_{\odot}$.

Our initial conditions are generated by resampling the region with a greater number of particles and adding additional short wavelength perturbations, whilst coarse sampling the external mass distribution with multi-mass collisionless particles to reproduce the large-scale gravitational field. Our resampling algorithm is based upon the procedure outlined by Frenk et al. (1996), and is described in detail by Power et al. (2003). Gas is added to the high-resolution region by splitting each particle into a dark matter particle and a gas particle, with mass ratio given by the adopted baryon and dark matter density parameters. This implies that each gas particle has a corresponding dark matter 'partner' associated with a unique volume element at high redshift, a useful feature when tracing the differences in the evolution of the two components in the non-linear regime.

The LOW-MASS simulation features 2.5×10^6 gas particles of masses $m_{\mathrm{gas}} = 1.65 \times 10^6\ h^{-1}\ \mathrm{M}_{\odot}$ and an equal number of high resolution dark matter particles, of mass $m_{\mathrm{dm}} = 8.70 \times 10^6\ h^{-1}\ \mathrm{M}_{\odot}$. At this resolution, the simulated volume yields a sample of ~ 1300 well resolved (i.e., $N_{\mathrm{dm}} > 150$) low mass haloes at $z = 0$ whilst remaining relatively computationally inexpensive. We adopt a TreePM algorithm to compute gravitational forces, this time also using a second PM grid, nested within the primary grid and enclosing the high-resolution particles, to compute intermediate range forces. We

use PM meshes of 256^3 cells in this case.

3.2.3 DWARF simulation

In order to assess the robustness of our results for low-mass haloes we re-simulate a single dwarf halo ($10^{10}\ h^{-1}M_\odot$) at much higher resolution than its counterparts in LOW-MASS. Because pre-virialisation heating is expected to be most effective in haloes assembling late, we select for resimulation a dwarf halo with relatively late formation time for its mass. The most massive progenitor first exceeds half the final mass of the halo at $z = 0.6$, whilst the extensions to the Press-Schechter theory (Press and Schechter, 1974) described by Lacey and Cole (1993) suggest that the most probable formation time for a halo of this mass is $z \sim 2$.

We selected the halo from a parent simulation of box length 35.325 h^{-1} Mpc and density parameters $(\Omega_m, \Omega_\Lambda = 0.3, 0.7)$. We apply the same resimulation technique as for LOW-MASS, using 3.4×10^5 gas and high-resolution dark matter particles. We adopt a baryon density parameter of $\Omega_b = 0.04$, which implies particle masses of $m_{gas} = 1.20 \times 10^4\ h^{-1}\ M_\odot$ and $m_{dm} = 7.8 \times 10^4\ h^{-1}\ M_\odot$. At $z = 0$, the halo has mass $M_{200} = 9.5 \times 10^9\ h^{-1}\ M_\odot$, virial radius $r_{200} = 34.5\ h^{-1}$ kpc, and circular velocity $V_{200} = 35$ km s^{-1}. As for the LOW-MASS simulation, we adopt the TreePM gravity algorithm with two PM meshes. In this case meshes of 128^3 cells were employed.

3.2.4 PANCAKE simulation

The pre-virialisation mechanism outlined by M05 assumes that gas is heated during the pancake-like collapse of the large-scale structure within which dwarf haloes are embedded. It is therefore important to explore whether our numerical techniques are suitable to describe this process accurately, as well as whether the results are not artificially marred by limited numerical resolution.

We investigate this by simulating the collapse of an idealised pancake with similar numerical resolution as that of the LOW-MASS simulation, and then vary the resolution in order to assess convergence. The simulation involves the collapse of a uniform spherical region of mass $3 \times 10^{12}\ h^{-1}\ M_\odot$, initially perturbed so that it collapses along one axis to form a flattened pancake at $z = 2$. We use a 'glass' rather than a grid in order to minimise the artifacts introduced by anisotropies in the grid. The desired dynamics are achieved

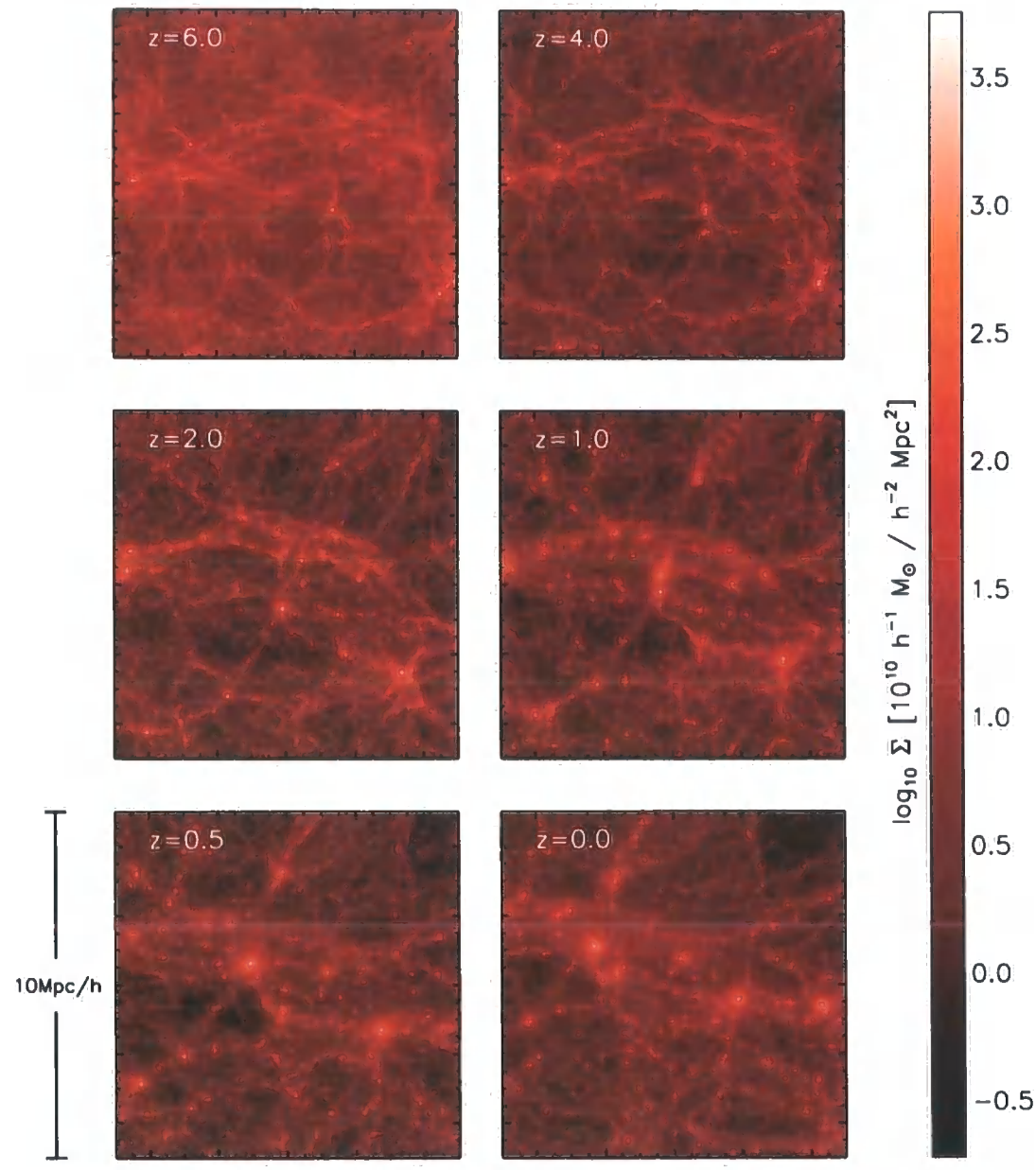

Figure 3.1: Redshift-progression of the projected gas density within a cube of side $10\,h^{-1}$ Mpc (comoving) in the LOW-MASS simulation. The progression clearly illustrates that by $z = 2$ many dark matter haloes have already collapsed, driving their associated gas to high overdensities. Such gas is afforded stability against the shocks that develop as the large-scale environment, within which it is embedded, collapses into pancakes and filaments.

by compressing the sphere along one axis and expanding it by half of the compression factor along the other two axes, with initial velocities computed using linear theory. We compute gravitational forces in this simulation using only a tree algorithm.

The choice of parameters for this simulation is motivated by the discussion of M05, who argue that such 'pancakes' might represent the typical environment where dwarf galaxy halos are formed, and that pre-virialisation heating might have been missed in early simulations because of inadequate resolution. As noted by M05, a collapsing pancake forms shocks on both sides, so a faithful treatment of its thermodynamic evolution requires $\gtrsim 8$ smoothing lengths across its collapsing axis. Following M05, and assuming that shocks operate as the collapsed structure approaches an overdensity of ~ 10, this implies a pancake thickness of 200 h^{-1} kpc (comoving) and a minimum resolution of 25 h^{-1} kpc, again comoving. We fulfil this criterion using a particle mass similar to that of the LOW-MASS simulation. At an overdensity of 10 $\Omega_b \rho_c(z)$ a mass of 40 m_p particles (comparable to what is used to define the SPH smoothing length scale) is contained within a sphere of comoving smoothing length $h_{sml} \sim 25\, h^{-1}$ kpc.

3.3 Analysis & Results

Figure 3.1 shows various snapshots of the LOW-MASS simulation. Each box is 10 h^{-1} Mpc on a side and shows the positions of gas particles, colour-coded according to density. This figure shows clearly the highly anisotropic nature of the large-scale structure, but also highlights the points that many dwarf dark matter halos had already collapsed by $z \sim 2$. As we discuss below, this has important implications for the efficiency of pre-virialisation heating and its effects on the baryon fraction of collapsed systems.

3.3.1 Halo finding algorithm

We use a friends-of-friends group finding algorithm (Davis et al., 1985) with a short linking length ($b = 0.05$) to locate the cores of haloes in the simulation volumes. The centres of these haloes are used as starting points for an iterative algorithm that finds spherically overdense regions of mean enclosed density $200\rho_{crit}(z)$, whose centres coincide with their centres of mass. We define the virial radius, r_{200}, as the radius of this sphere. Other 'virial' quantities quoted for haloes refer to measurements within this radius, un-

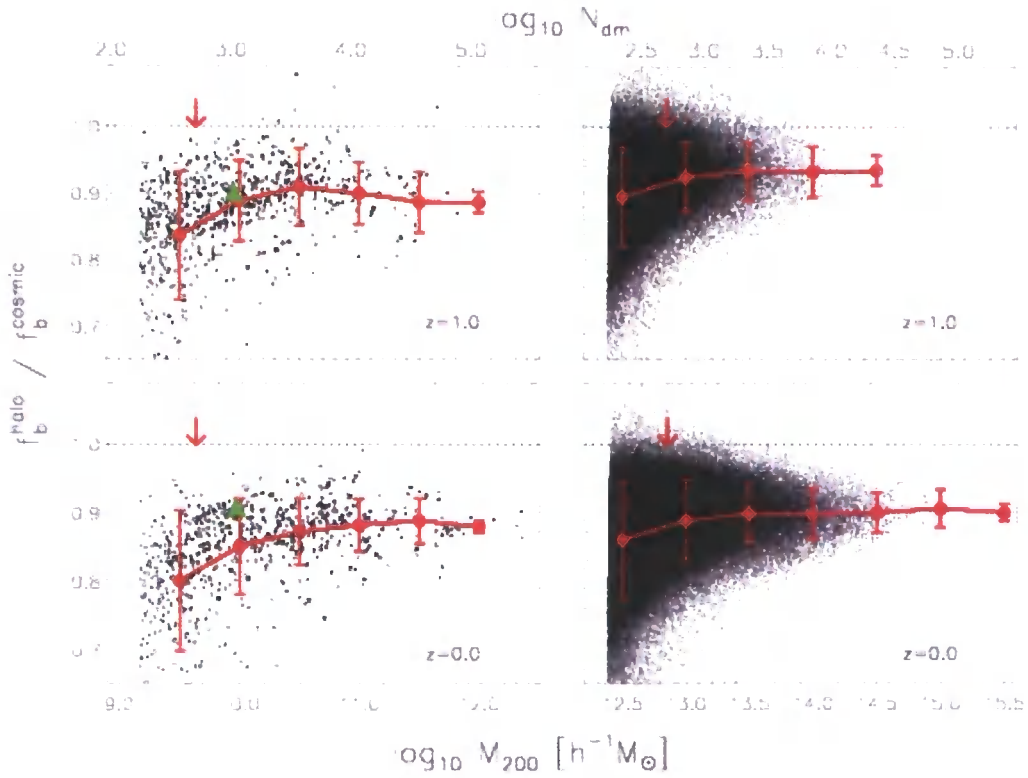

Figure 3.2: Baryon fractions, in units of the universal value, of well resolved haloes ($N_{\rm dm} > 150$) drawn from the LOW-MASS (*left-hand panels*) and HIGH-MASS (*right-hand panels*) simulations at $z = 1$ (*upper panels*) and $z = 0$ (*lower panels*). The large dots and error bars show the mean and rms of the distribution, respectively. The green triangle marks the baryon fraction of the halo in the DWARF simulation. The upper horizontal axis gives the equivalent number of dark matter particles at a given mass scale. The downward arrows in each plot illustrate the mass scale corresponding to 500 dark matter particles.

less otherwise specified.

We consider only haloes with at least 150 dark matter particles in order to minimise the effects of poor numerical resolution, and clean the sample by removing haloes partially contained within other haloes. In the case of LOW-MASS we also disregard haloes located closer than 200 h^{-1} kpc from the boundary of the resimulated region at $z = 0$, since they may have been subject to boundary effects. This criterion further guarantees that all haloes considered from this simulation are free from contamination by low-resolution boundary particles.

3.3.2 Baryon fractions

HIGH-MASS

The right-hand panels of Figure 3.2 show the baryon fraction in haloes identified in the HIGH-MASS simulation at $z = 1$ and at $z = 0$. These panels show the largest sample of haloes simulated with non-radiative gas physics reported to date, with approximately 49,500 and 115,000 haloes resolved at $z = 1$ and $z = 0$ respectively. The panels show that the baryon fraction is independent of mass, and has not evolved at least since $z = 1$, the highest redshift for which cluster baryon fractions can be estimated reliably from X-ray observations (e.g. the observations of Allen et al. (2004) span the redshift range $0.07 < z < 0.9$).

The mean cluster baryon fraction within the virial radius is approximately 90% of the cosmic mean, with relatively small scatter; the root-mean-square dispersion is less than 3% for haloes of mass $M_{200} \gtrsim 3 \times 10^{14}\ h^{-1}\ \mathrm{M}_{\odot}$, and the difference between the 10^{th} and 90^{th} percentiles is always less than 7.5% over the same mass range. The scatter remains small for all well resolved haloes; the rms scatter is less than 6% for haloes resolved by at least 500 dark matter particles. This result is in broad agreement with previous simulations of cluster baryon fractions in the non-radiative regime using SPH codes (e.g. Navarro et al., 1995; Eke et al., 1998b; Frenk et al., 1999; Ettori et al., 2006).

These results are only weakly dependent on radius; within a radius encompassing a mean inner density 500 times greater than critical, r_{500}, the results are very similar to those within r_{200}: for $M_{200} \gtrsim 3 \times 10^{14}\ h^{-1}\ \mathrm{M}_{\odot}$ the baryon fraction remains, on average, 90% with an rms dispersion of 3%. This radius, which is $\sim 0.7 r_{200}$ for an NFW profile

(Navarro et al., 1996, 1997) with concentration $c = 5$, is roughly the maximum radius for which total cluster masses can be estimated reliably from X-ray observations (e.g. Vikhlinin et al., 2006).

LOW-MASS

The left-hand panels of Figure 3.2 show that a similar result applies to the halo sample identified in the LOW-MASS simulation. The baryon fraction of galactic and dwarf haloes is also about 90% of the cosmic mean, and shows no discernible dependence on mass or redshift.

A noticeable downturn is observed below about $10^{10}\ h^{-1}M_{\odot}$, but this may be ascribed to the poorer resolution affecting such haloes, since an underestimate of the gas density at accretion shocks leads to artificially high post-shock entropies. Note that a similar downturn is also seen in the HIGH-MASS sample for haloes resolved with fewer than ~ 500 particles. Downward arrows show the mass scale corresponding to 500 dark matter particles in each simulation.

DWARF

Figure 3.2 suggests that for haloes resolved with more than $\sim 500 - 1000$ particles, numerical resolution does not affect the measured baryon fractions. Further supporting evidence comes from the results obtained for the high resolution individual DWARF halo. These are shown in Figure 3.2 with a filled triangle, and are consistent with LOW-MASS haloes of similar mass.

PANCAKE

One may still worry that, despite the apparent convergence of the results shown in Figure 3.2, the numerical resolution is insufficient to capture the shocks during the pancake collapse phase that accompanies the formation of haloes. We can test this by examining the PANCAKE simulation.

Figure 3.3 shows the evolution of the entropy (measured by $s = T/n_{\rm e}^{2/3}$), and of the temperature of the gas during the collapse of the sphere to a pancake configuration. Note that when computing the electron density, $n_{\rm e}$, we assume the gas is fully ionised and of primordial composition. At $z = 2$ the system reaches maximum asphericity, and

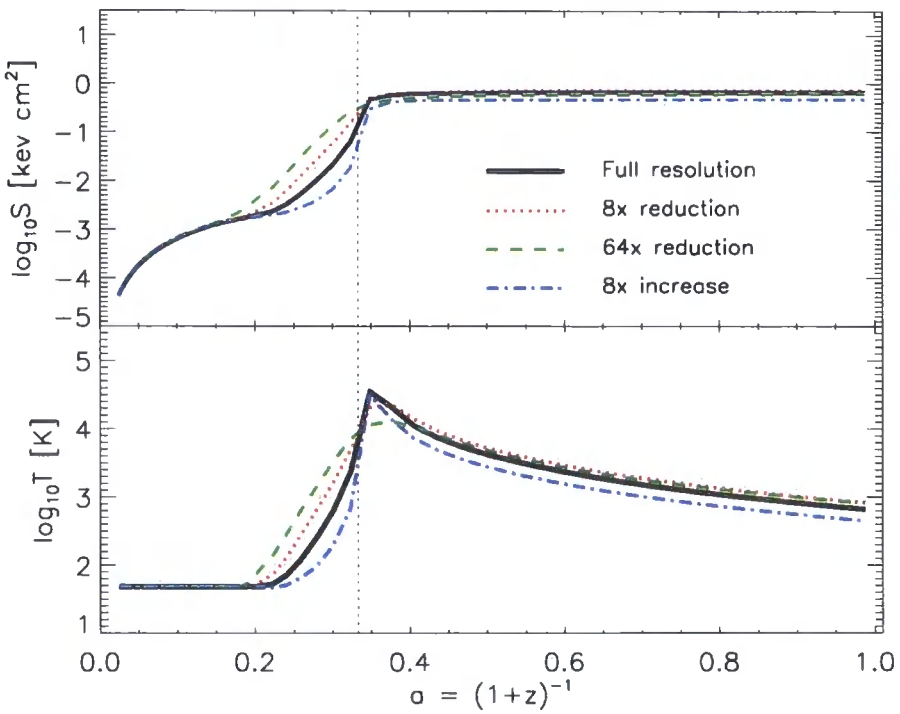

Figure 3.3: The evolution of the median entropy parameter (*top*) and median temperature (*bottom*) of gas particles within the PANCAKE collapse simulation. The solid line in each case represents the simulation featuring particle mass resolution identical to the LOW-MASS simulation. We supplement this run with degraded resolution runs with particle number reduced by a factor of 8 (*dotted line*) and 64 (*dashed line*). An improved resolution run is also presented, with particle number a factor of 8 greater (*dot-dashed line*). The vertical dotted line marks $z = 2$.

is well described by a plane of comoving thickness 25 h^{-1} kpc (c.f. comoving softening of 10 h^{-1} kpc) and comoving radial extension of 1.5 h^{-1} Mpc.

The collapse heats gas to a median temperature of 3×10^4 K, and the median specific entropy reaches $s \simeq 1$ keV cm^2. We test explicitly the effect of resolution by re-running the PANCAKE simulation with particle numbers reduced by factors of 8 and 64 relative to the standard resolution of LOW-MASS; we complete the resolution study by running a higher-resolution case where the number of particles was increased by a factor of 8. Gravitational softenings were scaled as $\epsilon \propto N_{\rm p}^{-1/3}$.

As shown in Figure 3.3 the post-shock median entropy and temperature jumps are quite insensitive to numerical resolution, although the transition becomes noticeably sharper as the resolution increases. This test shows that limited resolution does not lead to a substantial underestimate of the entropy jump in numerical simulations of pancake-like collapse. Actually, poor resolution leads typically to underestimation of the true densities: entropies are therefore typically *overestimated* in poor resolution simulations. This result, together with the consistency between the LOW-MASS and DWARF simulations, gives us confidence that baryon fractions in our simulations are not unduly affected by resolution effects.

3.3.3 Photo-heating

The one feedback mechanism that is certainly present at early times is associated with the energetic photons that reionised the Universe at high redshift. This has long been recognised as having the potential to inhibit the formation of galaxies in low-mass haloes, although there is still no consensus concerning the mass scale below which photo-heating becomes effective at halting galaxy formation (Blumenthal et al., 1984; Efstathiou, 1992; Quinn et al., 1996; Thoul and Weinberg, 1996; Bullock et al., 2000; Benson et al., 2002). Most semianalytic galaxy formation models have so far adopted the prescription of Gnedin (2000) to determine the gas accreted by haloes for given IGM pressure, but recent results presented by Hoeft et al. (2006) suggest that Gnedin's approach may substantially overestimate the mass scale of photo-heating.

This motivates us to include a simple photo-ionisation heating model in our simulations. The aim is twofold. On the one hand, we wish to shed light on the disagreement about the effects of photo-heating on gas fractions, but, on the other hand, we would also

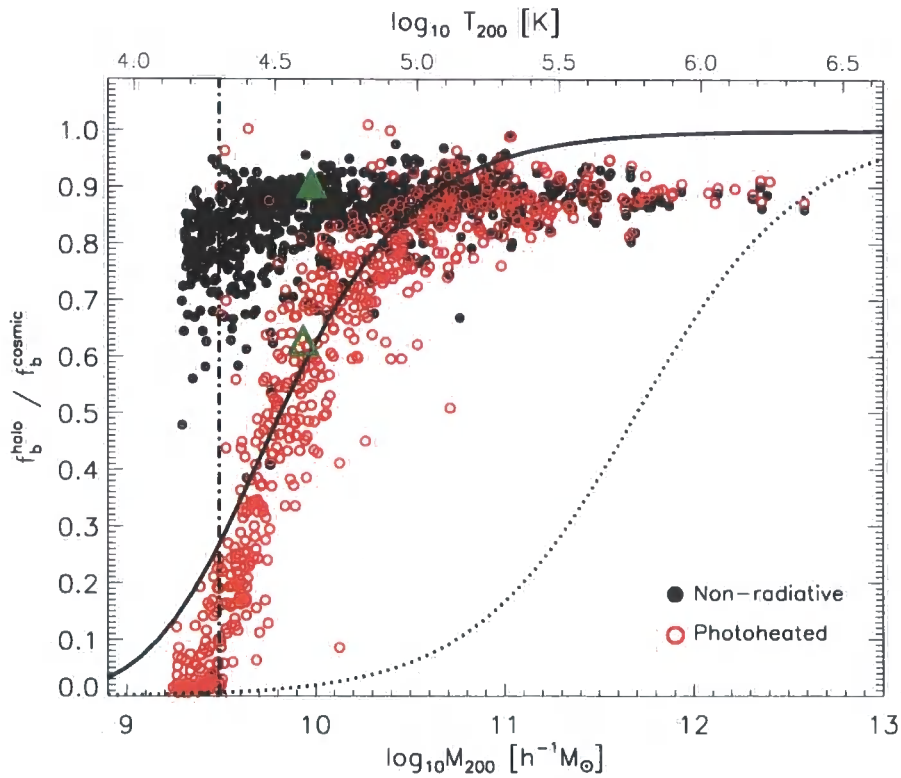

Figure 3.4: Baryon fractions, in units of the universal value, at $z = 0$ for the LOW-MASS simulation with and without our photo-ionising background model. The open and solid green triangles show the baryon fraction of the DWARF halo with and without the same model, whilst the vertical dot-dashed line marks the virial mass and virial temperature equating to the temperature floor. The solid line denotes the baryon fractions predicted by M05 for haloes in the presence of a UV background, whilst the dotted line shows the prediction of the M05 gravitational preheating model.

like to explore whether photo-heating may act to suppress the efficiency of gas accretion in the early phases of the hierarchy, facilitating and enhancing the thermodynamic effect of pancake-driven shocks.

We investigate the combined effect of gravitational and photo-heating by re-running the DWARF and LOW-MASS simulations, again with non-radiative gas physics, but, motivated by the third-year *WMAP* data (Spergel et al., 2007), imposing a spatially uniform temperature floor for all gas particles at $z = 11$. To aid as much as possible the pre-virialisation generation of entropy, we adopt for the temperature floor a rather high value, $T_{\rm floor} = 2 \times 10^4$ K, consistent with the maximum temperature of the IGM at mean density, as probed by QSO absorption spectra (Schaye et al., 2000).

This should clearly impact gas accretion on dwarf galaxy haloes and, in particular, our DWARF halo, where the virial temperature is only $\sim 4.4 \times 10^4$ K at $z = 0$, only a factor of 2.2 above $T_{\rm floor}$. We therefore expect that a considerable fraction of the gas bound to small halo progenitors at high redshift should be photo-evaporated from this structure.

Figure 3.4 illustrates the effect of the additional heating on the baryon fractions of the LOW-MASS halo sample (open circles) and compares them with the results of the non-radiative run (filled circles). Photo-heating introduces a well-defined mass scale below which gas accretion is strongly suppressed. Below $M_{200} \sim 10^{10}\ h^{-1}\ {\rm M}_\odot$, haloes are able to retain less than one half of their share of baryons within their virial radii; the effect is as large as 90% in haloes below $3 \times 10^9\ h^{-1}\ {\rm M}_\odot$, corresponding to an effective virial temperature very similar to the photo-heating temperature floor.

3.4 Discussion

The main result of the previous section is that, in the non-radiative approximation, the baryon fraction of ΛCDM haloes is independent of redshift as well as of mass, in the range resolved by our simulations (10^{10}-$10^{15}\ h^{-1}\ {\rm M}_\odot$). Photo-ionisation reduces the baryon fraction only in haloes with virial temperature comparable to, or less than, that imposed by the ionising photons, typically just above 10^4 K. We discuss below the implication of these results for models of galaxy formation and for the interpretation of observations of baryon fractions in clusters.

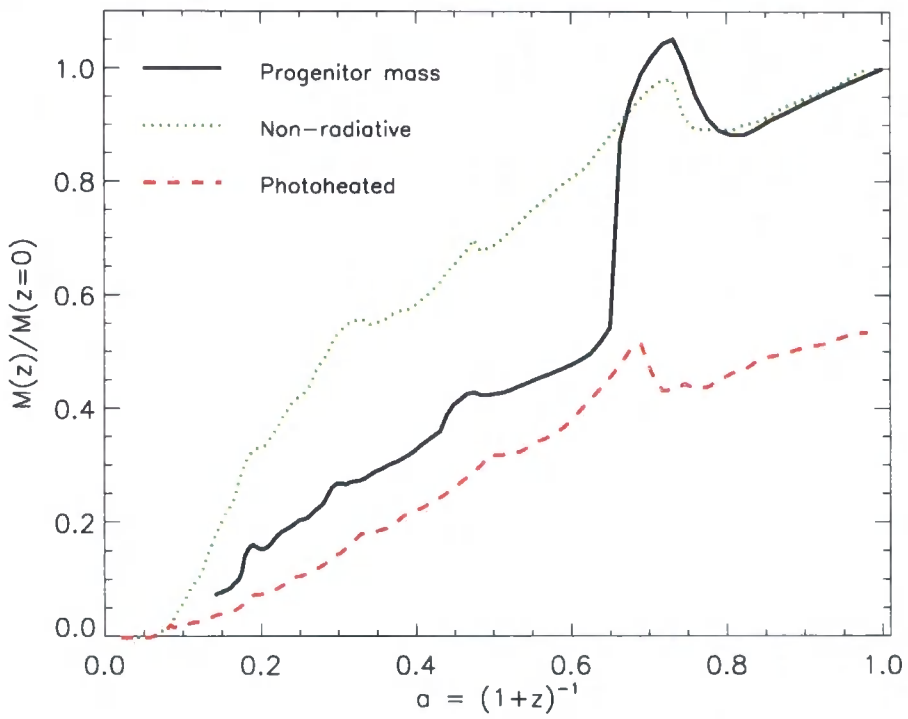

Figure 3.5: A comparison of the evolution of the mass of the main DWARF halo progenitor (*black solid line*), with the evolution of the final halo gas mass that is already collapsed at redshift z, as defined by the condition that its density exceeds $10\rho_c(z)$ (*green dotted line*). The data are normalised to their values at $z = 0$. The latter quantity is also shown for the case when our photo-heating treatment is applied (*red dashed line*), this time normalised to the $z = 0$ value of the purely non-radiative case.

3.4.1 Baryon fraction bias

The lack of dependence of baryon fractions on halo mass is intriguing, as is the fact that the mean value within the virial radius is only $\sim 90\%$ of the cosmic mean. The same result has been observed in other simulations (Navarro et al., 1995; Eke et al., 1998b; Frenk et al., 1999; Kravtsov et al., 2005; Ascasibar et al., 2006), and has been ascribed to the collisional *vs.* collisionless nature of the baryons and dark matter, coupled to the hierarchical assembly of haloes in the ΛCDM cosmogony. Indeed, during the many mergers that mark the formation of a halo, shocks act to stop the gas whilst the dark matter streams through freely. This leads to a temporary spatial offset between dark and gaseous components during which energy and angular momentum are transferred from the dark matter to the baryons, as discussed in detail by Navarro and White (1993). The energy gained during mergers results in a more extended gaseous component, and an overall (slight) reduction in the baryon fraction relative to the cosmic mean.

3.4.2 Pre-virialisation heating

The results of Figure 3.2 imply that pre-virialisation heating is ineffective at preventing the collapse of baryons into low-mass haloes, even for masses as low as $10^{10}\ h^{-1}\ \mathrm{M}_{\odot}$. Figure 3.4 compares the baryon fractions of LOW-MASS haloes at $z = 0$ (filled circles) with the predictions of the M05 model (dotted line). M05 argue that the IGM in low-mass haloes should have been heated by shocks to roughly ~ 10 keV cm^2 prior to halo assembly, and that this would lead to a reduction of $\gtrsim 50\%$ in the baryons filling haloes of mass $< 6 \times 10^{11}\ h^{-1}\ \mathrm{M}_{\odot}$. M05 propose a fitting formula to characterise this effect;

$$\frac{f_{\mathrm{b}}^{\mathrm{halo}}}{f_{\mathrm{b}}^{\mathrm{cosmic}}} = \frac{1}{(1 + M_{\mathrm{c}}/M)^{\alpha}}, \tag{3.1}$$

where $\alpha = 1$ and $M_{\mathrm{c}} = 5 \times 10^{11}\ h^{-1}\ \mathrm{M}_{\odot}$ is a characteristic mass scale. This function clearly fails to reproduce our results, and suggests that the hypotheses on which M05 base their model are not satisfied in our simulations.

The main premise of M05's model is that most low-mass haloes form in extremely aspherical regions where their assembly might be delayed, allowing for pancake-driven shocks to elevate the entropy of the IGM prior to halo assembly. Our simulations, however, indicate otherwise.

Firstly, low-mass haloes surviving to the present were, at the time of their formation, in regions where pre-virialisation shocks were weaker than envisaged by M05. For example, we find a typical post-collapse entropy of ~ 1 keV cm^2 in our pancake collapse simulations, about an order of magnitude lower than adopted by M05 to compute the model shown by the dotted curve in Figure 3.4. Qualitatively, our findings concur with those of Sandvik et al. (2007), whose excursion set analysis led them to conclude that the progenitor pancakes of dwarf galaxy haloes are typically one or two orders of magnitude less massive than required by the M05 model. Our baryon fractions drawn from the simulations suggest that the halo assembly process is approximately scale-free; if pre-virialisation heating does indeed occur, it affects *all* haloes in similar measure, leaving no particular signature in low-mass haloes.

Secondly, the material destined to make a low-mass halo collects into dense, early-collapsing clumps prior to the collapse of the surrounding 'pancake'. The pancake, in other words, is not a nearly uniform aspherical structure where shocks may propagate freely, but rather a large-scale feature where a substantial fraction of the mass is in collapsed clumps.

We illustrate this in Figure 3.5, where we plot (dotted line) the fraction of the final DWARF halo gas that resides in collapsed structures, as quantified by the condition $\rho > 10\,\rho_{\rm crit}(z)$. By this rather strict measure, half the DWARF gas is already in collapsed structures prior to $z \sim 2$, although by then the most massive halo progenitor (solid line) has only about $\sim 25\%$ of the final mass. This early aggregation of the halo gas into dense structures prevents it from being shock-heated by the pancake-driven shocks, reducing further the pre-virialisation heating efficiency.

3.4.3 Photo-heating

As shown in Figure 3.4, the baryon fraction may be reduced because of heating by a photo-ionising background, but the effect (at $z = 0$) is restricted to haloes with virial temperatures $\lesssim 2.2 T_{\rm floor}$. This implies that ionising photons, which are unlikely to heat the gas to temperatures much higher than $\sim 2 \times 10^4$ K are only able to influence the formation of galaxies in haloes less massive than $\sim 10^{10}\,h^{-1}\,{\rm M}_\odot$. Our results for the baryon fraction in this case are well described by Eqn. 3.1, but with the revised parameters suggested by M05 for their photo-heating model: $\alpha = 3$ and $M_{\rm c} = 1.7 \times 10^9\,h^{-1}\,{\rm M}_\odot$; we

show this fit in Figure 3.4 as a solid line.

The results shown in Figure 3.4 agree with those of Hoeft et al. (2006), who used a more detailed treatment of the UV background; the similarity of our findings is rather encouraging. We concur with their assessment that the characteristic mass scale of photo-evaporation is probably considerably lower than derived from the filtering mass formalism of Gnedin (2000). Thus, although photo-heating can reduce the baryon fraction in low-mass systems, it appears to be less efficient at shaping the extreme faint end of the galaxy luminosity function than previously inferred through semi-analytic modelling (e.g. Benson et al., 2002; Somerville, 2002).

Our results seem to be robust to numerical resolution, as shown by the good agreement between the baryon fraction of the LOW-MASS and the DWARF haloes plotted in Figure 3.4. In the latter case, photo-heating reduces the baryon fraction by 50% but there is no evidence that pre-virialisation has played a rôle; indeed, inspection of the evolution of the collapsed gas fraction (red dashed line in Figure 3.5) shows no discernible feature that may be associated with the collapse of the large-scale structure.

M05's pre-virialization model, shown as a dotted line in Figure 3.4, requires baryon fractions to be halved in haloes as massive as 5×10^{11} $M_{\odot}$; this is an order of magnitude larger than the mass of haloes significantly affected by photo-heating and pre-virialisation in our simulations. Our results suggest, then, that other feedback mechanisms are required to match the faint end of the galaxy luminosity function in the ΛCDM scenario.

3.4.4 Application to cluster surveys

Our HIGH-MASS simulation also features over 115,000 galaxy cluster-sized haloes, and demonstrates that, in the non-radiative regime, cluster baryon fractions are independent of virial mass, display little dispersion, and do not evolve significantly over the redshift range $0 < z < 1$. Observationally, mass profiles of clusters are typically only estimated reliably out to a maximum radius of r_{500}; the results within that radius are very similar to those plotted in Figure 3.2 at the virial radius. In haloes where the region interior to r_{500} is resolved by at least 500 dark matter particles, the mean cluster baryon fraction within r_{500} at $z = 0$ remains approximately 90% of the cosmic mean, again with an rms dispersion of $\sim 6\%$.

The key to the applicability of our results to cosmological tests is the validity of our non-radiative treatment of the ICM. Whilst the failure of purely non-radiative models to match some of the global scaling relations exhibited by clusters is well documented (e.g. Evrard and Henry, 1991; Kaiser, 1991; Navarro et al., 1995; Eke et al., 1998b), this does not necessarily imply that non-radiative models give the wrong fraction of hot baryons in observed clusters. Since the ρ^2 dependence of thermal bremsstrahlung implies that the X-ray emissivity of clusters is dominated by the central region, it is possible to obtain agreement with the observed X-ray scaling relations by modifying only the central gas density (for instance, with radiative cooling or AGN feedback), whilst leaving the density of the bulk of the gas unchanged (e.g. Balogh et al., 1999; Voit et al., 2002, 2003; McCarthy et al., 2002, 2004).

It should be noted, however, that the X-ray luminosity-temperature relation can also be explanied by models that do affect baryons at large radii (e.g. Kay et al., 2004; Kravtsov et al., 2005; Ettori et al., 2006). In such models the hot baryon fraction at r_{500} can be reduced by up to $\sim 30\%$, even for clusters with $M_{200} > 10^{15}\, h^{-1}\, \mathrm{M}_{\odot}$. However, such large-scale reductions by means of cooling and star formation conflict with optical constraints (e.g. Balogh et al., 2001), and the necessary level of feedback from SNe also appears unfeasibly high (Benson et al., 2003; Scannapieco and Oh, 2004).

The effect of non-gravitational processes on the large-scale properties of rich clusters remains a source of debate. We anticipate that analyses of the large samples of rich clusters provided by the *Chandra* and *XMM-Newton* observatories will foster the development of a definitive picture of the ICM. This picture may well show that baryons at large radii are only minimally affected by non-gravitational processes, thus validating our results that rich cluster baryon fractions do not evolve for $z < 1$ and exhibit little dispersion.

3.5 Conclusions

We have measured the baryon fractions of a large sample of haloes drawn from a suite of non-radiative gas-dynamical simulations of the ΛCDM cosmology. The haloes span five orders of magnitude in virial mass, from dwarf galaxy haloes to large clusters. Within the virial radius, the baryon fraction averages 90% of the cosmic mean, with a fairly small

dispersion ($\sim$ 6% rms) and shows no dependence on redshift for well-resolved systems. This is at odds with the 'pre-virialisation' gravitational heating proposed by Mo et al. (2005). Pre-virialisation, if at all present, plays only a minor role in setting the budget of baryons that accrete into low-mass haloes.

Photo-heating, modelled here as resulting from a uniform temperature 'floor' of 2×10^4 K imposed on the baryons from $z = 11$, is only able to reduce the baryon fraction in haloes with virial temperatures comparable to the photo-heating floor. The absence of a strong mass trend in the baryon fractions of low mass haloes highlights the need for non-gravitational feedback as a means to regulate gas cooling and star formation in low-mass haloes, in order to reconcile the ΛCDM halo mass function with the observed galaxy luminosity function.

In addition, our use of non-radiative simulations demonstrates that at r_{500}, the typical maximum radius at which current X-ray telescopes can probe cluster temperatures, the baryon fraction remains similar to that at r_{200}, again with similarly small dispersion. It seems unlikely that non-gravitational physics can substantially modify the baryon fraction of massive ($M_{200} \gtrsim 3 \times 10^{14}$ $M_\odot$) clusters within r_{500}, we therefore conclude that studies of the baryon fraction of clusters, as a function of redshift, offer a good prospect for a robust and reliable estimate of the matter density parameter and the dark energy equation of state.

Having firmly established the need for radiative physics as a means to regulate the accretion of baryons onto dark matter haloes, particularly those of a low mass, we are motivated to conduct a series of numerical simulations featuring a broad range of the relevant mechanisms. We therefore turn to these simulations in the following chapters.

Chapter 4

Environmental variation in the cosmic star formation rate density

4.1 Introduction

As we have discussed in previous chapters, numerical simulations have proven central to the exploration of hierarchical assembly models that aim to describe the formation and evolution of cosmic structures. In particular, they have yielded detailed predictions for the large-scale clustering of matter since in this regime the dynamics are simplified by the dominance of gravitational forces. Modelling the evolution of the cosmic baryons on small scales is a more challenging prospect, owing to the complexity of the physics needed and the greater uncertainties inherent to the techniques used to model them numerically. The ability of numerical simulations to yield detailed predictions in the regime where baryonic processes are non-negligible is commensurately reduced, and this problem is particularly acute when moving from the non-radiative regime to that in which cooling operates.

The inherent difficulties and computational expense of modelling baryons in this regime has fostered the development of semi-analytic techniques (White and Frenk, 1991; Kauffmann et al., 1993; Cole et al., 1994, 2000; Baugh, 2006), whereby simplified prescriptions for the evolution of baryons are grafted onto descriptions of the merger histories of dark matter haloes. These histories can be constructed analytically using Monte Carlo techniques, or extracted directly from N-body simulations. Key examples of the latter procedure are the studies of Bower et al. (2006), Croton et al. (2006) and De Lucia et al. (2006), which each used merger histories derived from the Millennium Sim-

ulation (Springel et al., 2005). The scale and resolution of this collisionless simulation permits semi-analytic calculations to trace the evolution of all galaxies more massive than the Small Magellanic Cloud within a comoving volume similar to that probed by the 2dFGRS and SDSS at their median redshifts.

Whilst this form of simplified modelling has yielded critical insights into the effects of baryonic processes on the observable Universe, the simplifications inherent to semi-analytic models necessarily limit their predictive power. Chief amongst these limitations is the inability of semi-analytic models to explore the evolution of the IGM and its potentially crucial and dynamic interactions with galaxies and the gas that is assocated with their host dark matter haloes. In contrast, this relationship can be examined in detail with *ab initio* calculations that trace the evolution of baryons explicitly with direct, numerical schemes. The introduction and early development of hydrodynamics within the framework of cosmological simulations (e.g. Evrard, 1988, 1990; Hernquist and Katz, 1989; Barnes and Hernquist, 1991; Katz and Gunn, 1991; Navarro and Benz, 1991; Katz et al., 1992; Thomas and Couchman, 1992; Cen and Ostriker, 1993; Evrard et al., 1994; Frenk et al., 1996), has fostered key advances in our understanding of the cosmos. For example, the connection of large-scale structure to the the Lyman-α forest was first emphatically demonstrated by hydrodynamical simulations (e.g. Cen et al., 1994; Zhang et al., 1995; Hernquist et al., 1996; Miralda-Escudé et al., 1996; Zhang et al., 1997; Theuns et al., 1998). At the opposite end of the density scale, hydrodynamic simulations of the formation of individual galaxies have advanced steadily, both in terms of their resolution and complexity. Such calculations have established the generic requirement for energy feedback mechanisms within cold dark matter models to prevent over-cooling. Otherwise the efficient radiative cooling of gas within dense halo centres leads to the formation of galaxies that are too massive and too centrally concentrated (e.g. Weil et al., 1998; Sommer-Larsen et al., 1999; Thacker and Couchman, 2001; Abadi et al., 2003a,b; Sommer-Larsen et al., 2003; Governato et al., 2004; Robertson et al., 2004; Okamoto et al., 2005).

As briefly discussed in Chapter 1, the focus of hydrodynamical simulations on the extreme ends of the overdensity scale is convenient, because it allows a trade-off between the necessary resolution and volume of the calculation. However, the production of unbiased statistical samples of galaxies simulated at moderate- to high-resolution remains

a considerable computational challenge, since the volume of the simulation cannot be heavily sacrificed. A recent attempt to produce such a sample was made by Croft et al. (2008), who evolved a periodic volume of length $L = 33.75\ h^{-1}$ Mpc with 486^3 particles each of gas and dark matter, allowing them to resolve the haloes of galaxies similar to the Milky Way with $\sim 10^5$ particles. Whilst resolving ~ 1000 galaxies, the relatively small volume of this simulation featured only a limited range of cosmological environments, and few massive galaxies. A further technical limitation of relatively small volumes is that fluctuations on scales comparable to the size of the box become non-negligible at a relatively high redshift (Bagla and Ray, 2005; Sirko, 2005), after which the simulation cannot be considered a faithful representation of the evolution of the underlying model. For this reason, the Croft et al. (2008) simulation was halted at $z = 1$, prohibiting an exploration of its low-redshift properties.

The requirement for detailed predictions of the properties of the low-redshift IGM, and the evolution of galaxies over the interval $0 < z \lesssim 1$ is now particularly acute. Observations of the Lyα forest are beginning to probe in detail the topology of the diffuse baryons that are expected to be associated with the filaments comprising the cosmic web (e.g. Pichon et al., 2001; Caucci et al., 2008), and the forthcoming installation of the *Cosmic Origins Spectrograph* (Green et al., 2003) aboard the *Hubble Space Telescope* (HST), is likely to yield significant advances in the understanding of the low-redshift IGM. Such observations may also prove central to the resolution of the 'missing baryons' problem (Nicastro et al., 2005); having indicated that filaments might host approximately half of all baryonic mass in the observationally elusive WHIM phase (e.g. Cen and Ostriker, 1999c; Davé et al., 1999), simulations will continue to play a key role in elucidating the nature of low-redshift absorbers (e.g. Oppenheimer and Davé, 2008b). Tracing the low-redshift evolution of galaxies with detailed models is also useful as a means to connect the detailed snapshots of cosmic evolution provided by large galaxy redshift surveys of the local Universe such as the 2dFGRS and SDSS, with those focussing on intermediate redshifts ($z \sim 1$), for example DEEP2, VVDS and COMBO-17.

In order to trace a sample of galaxies, simulated at high-resolution within a wide range of cosmological environments, from prior to the cosmological dark ages until the present epoch, we have conducted a novel series of numerical gasdynamical simulations: the *Galaxies-Intergalactic Medium Interaction Calculation*. GIMIC features 'zoomed'

initial conditions (Frenk et al., 1996; Power et al., 2003; Navarro et al., 2004), the generation of which was discussed in Chapter 2. We use the large volume ($L = 500\ h^{-1}$ Mpc), high-resolution (10^{10} particles, $M_p = 8.6 \times 10^8\ h^{-1}\ \mathrm{M}_\odot$) Millennium Simulation as the parent volume for these zoomed regions, confining our high-resolution sampling and gas dynamics to five roughly spherical regions of radius $\sim 20\ h^{-1}$ Mpc (0.13 per cent of the total volume). In contrast to small, periodic, simulations our use of the Millennium Simulation facilitates evolution to $z = 0$, since by this epoch fluctuations on the scale of the simulation box are still well described by linear theory. Moreover, such a large volume contains the full range of cosmological environments expected to be found within the volumes probed by modern low-redshift surveys. Judicious selection of the five GIMIC regions across environmentally diverse regions therefore yields a sample that spans the range of structures found within the Millennium Simulation and yet remains feasible to simulate with a detailed gasdynamical treatment that. In the high-resolution realisations, therefore, the Jeans scale in the IGM after the epoch of reionisation is fully resolved. A further advantage of the Millennium Simulation basis is that GIMIC complements the existing semi-analytic calculations that use merger histories derived from the Millennium Simulation (Bower et al., 2006; Croton et al., 2006; De Lucia et al., 2006). The extent of the dynamic range afforded by this procedure is highlighted by Figure 1.2, which starts with the full Millennium Simulation volume ($L = 500\ h^{-1}$ Mpc) and zooms-in, first by a factor of 10 to show a full GIMIC sphere in the centre-panel, and then by a further factor of 1000 to show a disc galaxy within this region.

As discussed in Chapter 2, the simulations are evolved with GADGET3, a significantly updated variant of the GADGET2 code described by Springel and Hernquist (2003a), featuring new treatments of the key baryonic processes, such as radiative cooling, heating by the metagalactic ultraviolet background radiation, star formation, and stellar feedback. The simulations are therefore ideally suited to the exploration of a wide range of issues in galaxy formation and extragalactic astrophysics, many of which are readily accessible to observations. In this chapter we present a broad overview of the simulations and discuss the aspects of the generation of the initial conditions that are specific to GIMIC (and were not, therefore, covered in Chapter 2). The first results from the simulations are also presented in this chapter, focussing initially on the role of cosmological environment (ranging from deep voids to rich clusters) in shaping a fundamental

cosmological quantity, the evolution of the star formation rate (SFR) density (or 'Lilly-Madau diagram', Lilly et al., 1996; Madau et al., 1996). Combining this quantity for each GIMIC region, we present an estimate of the star formation rate density for the entire Millennium Simulation, from the pre-reionisation era to the present epoch, that compares favourably with the latest observational measurements. We continue our discussion of GIMIC in Chapter 5, where the focus is an evolutionary census of the baryons. The following parameters are assumed for these simulations: $\Omega_0 = 0.25$, $\Omega_\Lambda = 0.75$, $\Omega_b = 0.045$, $\sigma_8 = 0.9$, $H_0 = 100\,h$ km s^{-1} Mpc^{-1}, $h = 0.73$.

4.2 The simulations

We do not describe the simulation code here, since an overview of the key changes to the SH03a implementation of GADGET2 is given in Section 2.4. The reader is also referred to Schaye and Dalla Vecchia (2008), Dalla Vecchia and Schaye (2008) and Wiersma et al. (2008) for further details. We focus here on the key defining aspect of GIMIC: its initial conditions.

4.2.1 Initial Conditions

In order to trace a representative sample of the *Millennium Simulation* volume, the five regions simulated were selected to enclose cosmological 'environments' spanning a wide range of densities. The resolution of the simulations was, in part, dictated by the requirement to resolve the Jeans scale in the IGM after the epoch of reionisation, whilst the sizes of the regions were limited by computational expense. An approximate comoving radius of 18 h^{-1} Mpc was adopted; we therefore aimed to select five regions whose overdensities, at $z = 1.5$, represented $(-2, -1, 0, +1, +2)\sigma$ deviations from the mean on this spatial scale. We desired that the $+2\sigma$ sphere to contain a rich cluster at $z = 0$. The mass of a mean density sphere of comoving radius 18 h^{-1} Mpc is $1.7 \times 10^{15}\ h^{-1}\ \mathrm{M}_\odot$, a mass comparable to that of the largest cluster in the Millennium Simulation volume. This, therefore, precludes the possibility of finding a sphere of radius 18 h^{-1} Mpc that simultaneously satifies the requirement of containing a rich cluster and has an overdensity corresponding to a $+2\sigma$ deviation from the mean at $z = 1.5$. We therefore elected to use a larger radius for this sphere, 25 h^{-1} Mpc, and selected regions featuring $+2\sigma$

overdensities on this scale. We create two realisations of the 18 h^{-1}1 Mpc spheres, at intermediate- and high-resolution, whilst we create the 25 h^{-1} Mpc, $+2\sigma$ region, only at intermediate-resolution owing to its far greater demands on computational resources.

The four spheres (-2,-1,0,+1)σ were selected from a target list of 10^5 randomly placed spheres of radius 18 h^{-1} Mpc in the Millennium Simulation volume at $z = 1.5$. Since by $z = 1.5$ the overdensity distribution becomes significantly skewed (i.e. non-Gaussian), we have defined the overdensities corresponding to $(-2, -1, 0, +1)\sigma$ regions to be those that correspond in terms of the rank ordering by overdensity, to those of a Gaussian distribution; the overdensities for $(-2, -1, 0, +1)\sigma$ regions are $(-0.407, -0.243, -0.032, 0.241)$ respectively. From the complete list of 10^5 spheres a candidate list of centres was generated for each of the $(-2, -1, 0, +1)\sigma$ regions by selecting all spheres with overdensities within 0.002 of the respective limits.

The procedure for the $+2\sigma$ sphere was necessarily different, because of the requirement that a rich cluster would form at its centre by $z = 0$. The starting point was to identify the particles that form the 126 most massive groups in the Millennium Simulation volume at $z = 0.0$, identified by the FoF algorithm with linking length $b = 0.2$. This number of groups was chosen to produce an approximate characteristic group separation of 100 h^{-1} Mpc. These particles were traced back to $z = 1.5$, and their centres of mass were used as centres for spheres of radius 25 h^{-1} Mpc. The $+2\sigma$ sphere was then selected from a randomly sorted list of twelve candidates that had close to the appropriate overdensity. Since the first cluster had a mass at $z = 0$ of $M_{200} = 4 \times 10^{14}\ h^{-1}\ \mathrm{M}_\odot$, which is rather low for a 'rich' cluster, we chose the second sphere on the list, with a mass of $M_{200} = 8 \times 10^{14}\ h^{-1}\ \mathrm{M}_\odot$ at $z = 0$. This cluster is relatively isolated, with no material in the 25 h^{-1} Mpc contributing to another rich cluster.

Having selected the centre for the $+2\sigma$ sphere, and made candidate lists of centres for the four other spheres, we selected our final five sphere centres from a list of all five centres generated as follows. We selected a sphere, at random, from each of the candidate lists of centres for the $(-2, -1, 0, +1)\sigma$ regions and added the unique $+2\sigma$ sphere centre to form a quintet of candidate centres. Each quintet was considered eligible for the final list if it satisfied two criteria: (i) none of the five centres had one or more of their x,y or z coordinates within 50 h^{-1} Mpc of the periodic boundary of the simulation volume and (ii) each centre was at least 200 h^{-1} Mpc away from the other four sphere centres in the

quintet. The first criterion was imposed to maintain the same coordinate system as the Millennium Simulation, and also enable the use of an intermediate-resolution particle-mesh (PM) force algorithm implemented within our simulation code, which requires that the isolated mesh used for this calculation does not cross the periodic boundaries of the simulation volume. The second choice was made to prevent two or more spheres being near neighbours, and to force the five spheres to extend over a significant range of the Millennium Simulation volume, so as to be relatively independent of each other. It is possible to find many quintets satisfying these conditions; we chose the first quintet generated by the code, which used a pseudo-random number generator to search for candidates. The centres and radii of all five spheres are presented in Table 4.1.

Region	x [h^{-1}Mpc]	y [h^{-1}Mpc]	z [h^{-1}Mpc]	Comoving radius [h^{-1}Mpc]	$M_{\rm gas}$ (int. res) [$h^{-1}M_\odot$]	$M_{\rm gas}$ (high res) [$h^{-1}M_\odot$]	N (int. res)	N (high res)	$z_{\rm final}$ [int. res, high res]
-2σ	153.17	347.90	424.81	18	1.16×10^7	1.45×10^6	2.23×10^7	1.78×10^8	[0,0]
-1σ	387.91	316.48	113.46	18	1.16×10^7	1.45×10^6	2.80×10^7	2.24×10^8	[0,2]
0σ	271.94	108.29	107.45	18	1.16×10^7	1.45×10^6	3.44×10^7	2.75×10^8	[0,2]
$+1\sigma$	179.51	379.22	196.64	18	1.16×10^7	1.45×10^6	4.30×10^7	3.44×10^8	[0,2]
$+2\sigma$	233.10	139.30	387.38	25	1.16×10^7	1.45×10^6	1.24×10^8	-	[0,-]

Table 4.1: Key parameters for the five GIMIC regions. The first four columns present the spatial location (in Millennium Simulation coordinates) and the nominal comoving radius of the regions at $z = 1.5$. The following two columns give the mass of the gas particles in both the intermediate- and high-resolution simulations. The dark matter particle mass is a factor of $(\Omega_{\rm m} - \Omega_{\rm b})/\Omega_{\rm b}$ greater. The next two columns show the number of particles of gas (or equivalently, CDM) particles within the zoomed region of the simulation, whilst the final column denotes the redshift at which each simulation was terminated. Note that the $+2\sigma$ region was not run at high-resolution.

In order to maximise the load and memory efficiency of the intermediate-resolution PM algorithm in our code, which automatically resizes to encompass all high-resolution particles, we chose to make five separate sets of initial conditions, one for each of the regions chosen[1]. The procedure for making the initial conditions is identical for all five regions and consists of two main stages: (i) the creation of a multi-mass particle distribution to represent the uniform, unperturbed particle distribution, and (ii) the recreation of the displacement field used by the Millennium Simulation, with the addition of extra short wavelength power, sampled from the same power spectrum, down to the appropriate Nyquist frequency.

The multi-mass uniform particle distribution is based upon a cubic mesh of 320^3 cells that encloses the entire simulation volume. Each cell of the mesh is treated independently. Particles, which at this point are composite and represent both dark matter and gas, are placed in each cell so that the mean density of all cells is equal to the matter density of the Universe. A total of n^3 equal mass particles is placed in each cell, arranged as a cubic grid with a spacing of $1/n$ of the cell size and with the centre of mass of all the particles coinciding with the cell centre. The value of n varied from 32, for the high-resolution region encompassing the sphere itself, to unity for cells that are distant from the sphere and are needed only to provide the correct tidal forces on the region of interest.

The value of n, as a function of cell position, was determined by the following algorithm: all of the particles from the Millennium Simulation inside or within 0.5 h^{-1} Mpc (1 h^{-1} Mpc for the $+2\sigma$ sphere) of a particular GIMIC sphere at $z = 1.5$ were traced back to the grid cells from which they originated at very high redshift. Any cell occupied by one or more of these particles is labelled as a high-resolution cell. A check is made to determine if the high-resolution cells form a single contiguous region, where contiguous cells are defined as those sharing a face. If there were non-contiguous cells present, then any cells contiguous to a high-resolution cell are additionally defined as high-resolution cells, and this process is continued until all high-resolution cells are contiguous. A set of boundary layers is then defined as follows: level 1 boundary cells

[1]Including all five spheres within a single set of initial conditions would create an isolated mesh that fills most of the simulation volume. This would incur a significant memory cost and offer little speed up relative to the main PM algorithm.

are defined as those cells adjacent (i.e. sharing a face, an edge or a vertex) to a high-resolution (of level 0) cell. Level 2 boundary cells are then adjacent to level 1 boundary cells, and so on until level 9, which in addition includes all cells that have not yet been assigned. We then realise the zoomed initial conditions at two resolutions; since the original Millennium Simulation represents our low-resolution basis, we refer to the two GIMIC realisations as high- and intermediate-resolution. For the high-resolution realisation, we apply $n = 32$ in the high-resolution cells, while the neighbouring boundary cells had $n = (20, 15, 10, 8, 6, 4, 3, 2, 1)$ for the boundary levels 1-9 respectively. This yields a mass for the composite (i.e. dark matter and gas) particles in the high-resolution region of $8.08 \times 10^6\ h^{-1}\ \mathrm{M}_\odot$. For the intermediate-resolution realisation, we effectively halve the value of n in each level, yielding initial conditions with composite particle masses a factor of eight greater than the high-resolution case, $6.46 \times 10^7\ h^{-1}\ \mathrm{M}_\odot$. We therefore resolve haloes of mass $10^{12}\ h^{-1}\ \mathrm{M}_\odot$ (comparable to the Milky Way's halo) with $\sim 18,880$ particles at intermediate resolution, and $\sim 151,000$ at high-resolution. The total number of particles used in each simulation is presented in Table 4.1.

Having created the particle distribution, a displacement field was calculated for each particle. The displacement consists of two parts; on large scales the same mode amplitudes and phases were used as in the Millennium Simulation, whilst short wavelength power, down to the Nyquist frequency, was added in a cubic region of dimension $50 - 76\ h^{-1}$ Mpc containing all of the high-resolution cells. The break between the long wavelength and short wavelength power was chosen such that only wavenumbers $\vec{k} = (k_x, k_y, k_z)$ satisfying $\max(|k_x|, |k_y|, |k_z|) < \pi h\ \mathrm{Mpc}^{-1}$ were retained from the Millennium Simulation. This scale is sufficient to ensure that haloes resolved with at least a few hundred particles in the Millennium Simulation are present in the GIMIC simulation. A large mesh of 2048^3 cells was used for all Fourier transforms to minimise interpolation errors. Finally, the high-resolution composite particles were split into gas and dark matter particles, with masses appropriate to yield a cosmic baryon fraction of $\Omega_\mathrm{b}/\Omega_0 = 0.045/0.25 = 18$ per cent. The gas and dark matter particles were offset in each dimension from their common centre of mass by a mass-weighted fraction of one interparticle separation.

4.2.2 Sampling the regions

The use of zoomed initial conditions introduces one key problem into the interpretation of simulations, owing to the presence of an artificial boundary between the high-resolution region, within which baryons are modelled explicitly with SPH particles, and the external boundary region that is populated by composite particles (representing both baryons and dark matter) whose dynamics are collisionless. Clearly, the collisionless region should be excluded from any analysis, but the existence of the boundary has other indirect effects. For example, the absence of gas beyond the boundary artificially reduces the mass of gas that might accrete onto nearby haloes. Moreover, it renders the external region pressureless and therefore allows the easy escape of galactic outflows into the vacuum of the boundary region.

In most of the analyses that follow therefore, we consider only particles that are within 18 h^{-1} Mpc (or 25 h^{-1} Mpc for the $+2\sigma$ region) of the centre of mass of all baryonic and high-resolution dark matter particles; in the case of analyses conducted using a mesh, we consider those cells whose geometric centres lie within this radius. The use of a simple and time-invariant sampling geometry (a sphere of constant radius) is attractive since it allows for a trivial volume normalisation of various quantities, such as the star formation rate density, $\dot{\rho}_\star$.

However, for $z \neq 1.5$, the morphology and comoving volume of each region deviates slightly from that of the sphere they were defined to be at $z = 1.5$. This is due to the varying overdensities of the regions, since the underdense regions expand, and the overdense regions contract, in comoving space as the matter fluid evolves over time. This effect is shown in Figure 4.1; at $z = 6$ (top row), the overdense $+2\sigma$ region occupies a greater comoving volume than its sampling sphere of 25 h^{-1} Mpc radius (shown in projection by the red circle), whilst the underdense -2σ barely fills its sampling sphere of radius 18 h^{-1} Mpc. At $z = 1.5$ (centre row), by design, each region occupies its sampling sphere with a small padding region being external to this. At $z = 0$ (bottom row), the converse of the $z = 6$ situation exists; the overdense region has collapsed, leaving some volume of its sampling sphere unoccupied. The underdense region has expanded in comoving space, and so extends beyond the sampling volume.

We note therefore that our use of a fixed comoving sampling volume means that, formally, each region only represents the desired σ at $z = 1.5$. It is also clear that some

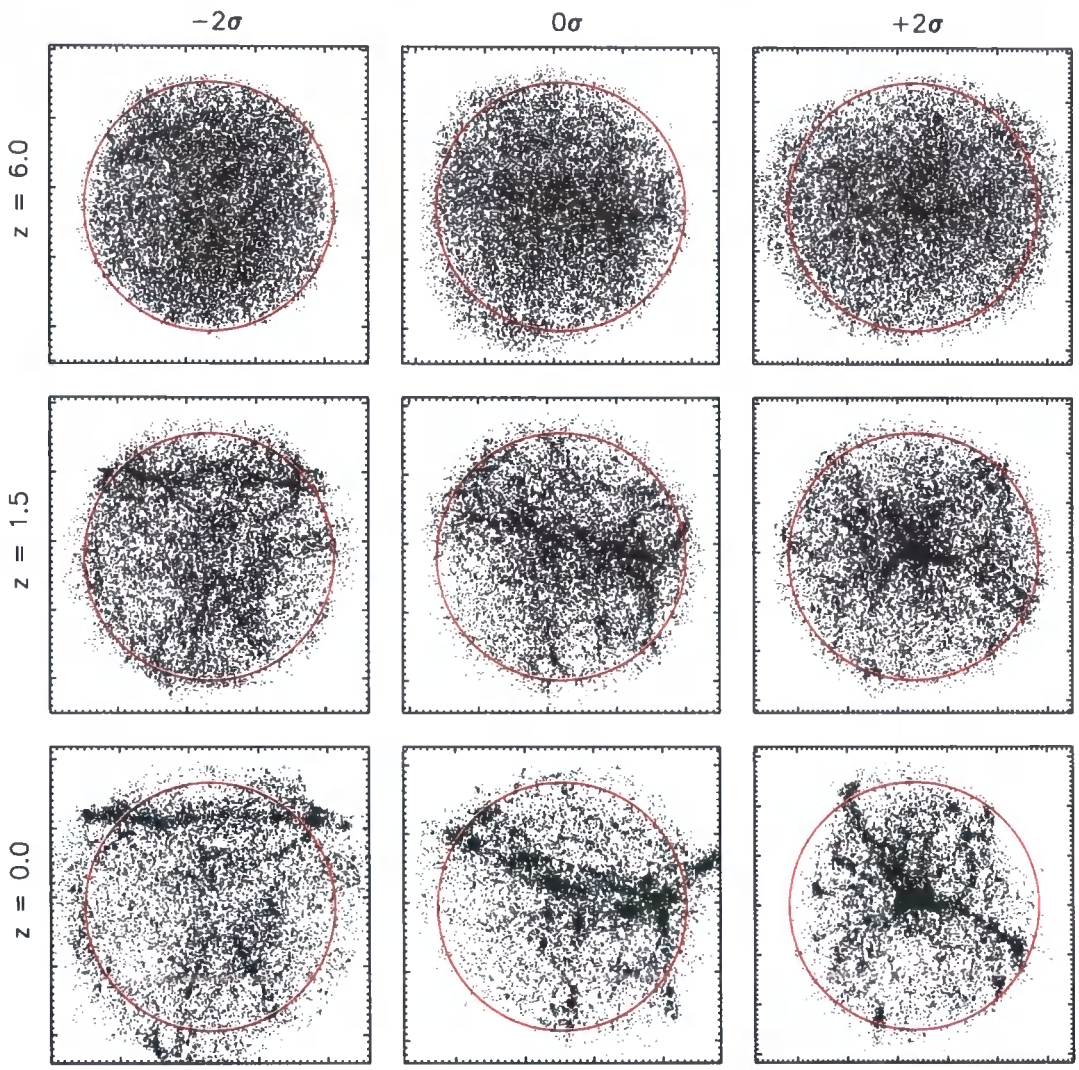

Figure 4.1: Distribution in comoving space of high-resolution dark matter particles in the -2σ (left column), 0σ (centre column) and $+2\sigma$ (right column), at $z = 6$ (top row), $z = 1.5$ (when each region was selected, centre row) and $z = 0$ (bottom row). In each case the distribution has been random sampled to show approximately 15,000 particles. The red circle is centered on the centre of mass of the particles and has radius equal to the fiducial comoving radius of each sphere (18 h^{-1} Mpc for -2σ and 0σ, 25 h^{-1} Mpc for $+2\sigma$).

fraction of the sampled volume for the overdense (underdense) regions at $z < 1.5$ ($z > 1.5$) might be occupied by boundary particles and be devoid of baryons. However, we have chosen to retain the simple fixed comoving sphere approach, since maintaining the desired σ at each epoch would require the same set of particles to be followed at each epoch, in a Lagrangian sense, thus producing a non-spherical sampling geometry for $z \neq 1.5$, for which it is difficult to normalise by volume. The deviation from the desired σ is not likely to be severe, and should not significantly bias estimates of properties of the Millennium Simulation volume as a whole, particularly since properties of the 0σ region are always assigned the greatest weight when performing this extrapolation, and this region suffers least from boundary effects since it is always close to the mean density of the Universe. Moreover, as can be seen from Figure 4.1, the volume of the sampling region that is unoccupied by high-resolution dark matter (and baryons), and is therefore occupied by boundary particles, is small. To ensure that boundary effects do not adversely bias our measurements, we have explicitly checked that haloes towards the edge of the volume do not differ significantly from those at the centre, for instance in terms of their baryon fractions, star formation rates or metallicities, and so we do not consider this a problem.

In Figure 4.2 we present the overdensity evolution of the sampled regions within each simulation. At early times the regions necessarily have the mean density of the Universe, but their enclosed overdensities clearly diverge as they evolve. This figure therefore highlights the advantage of zoomed initial conditions as a means to probe extreme environments, since a periodic volume maintains $\delta = 0$ at all epochs. The dip in the overdensity of the $+1\sigma$ region at $a \simeq 0.5$ ($z \simeq 1$) results from the departure of a high-mass halo with a large peculiar velocity from the spherical 'analysis' region. This eventuality was not foreseen in the original selection of the regions, since our original intention was to terminate the simulations at $z = 1.5$; however the performance enhancements derived from the improved load-balancing algorithm within this version of GADGET-3 made continuing the simulations to $z = 0$ computationally feasible.

In the following sections we present an overview of the formation of stellar mass in the simulations, and the influence of large scale cosmological environment and dark matter haloes upon this process. As shall become clear throughout both this chapter and Chapter 5, the origin of several environmental influences can be traced to differences

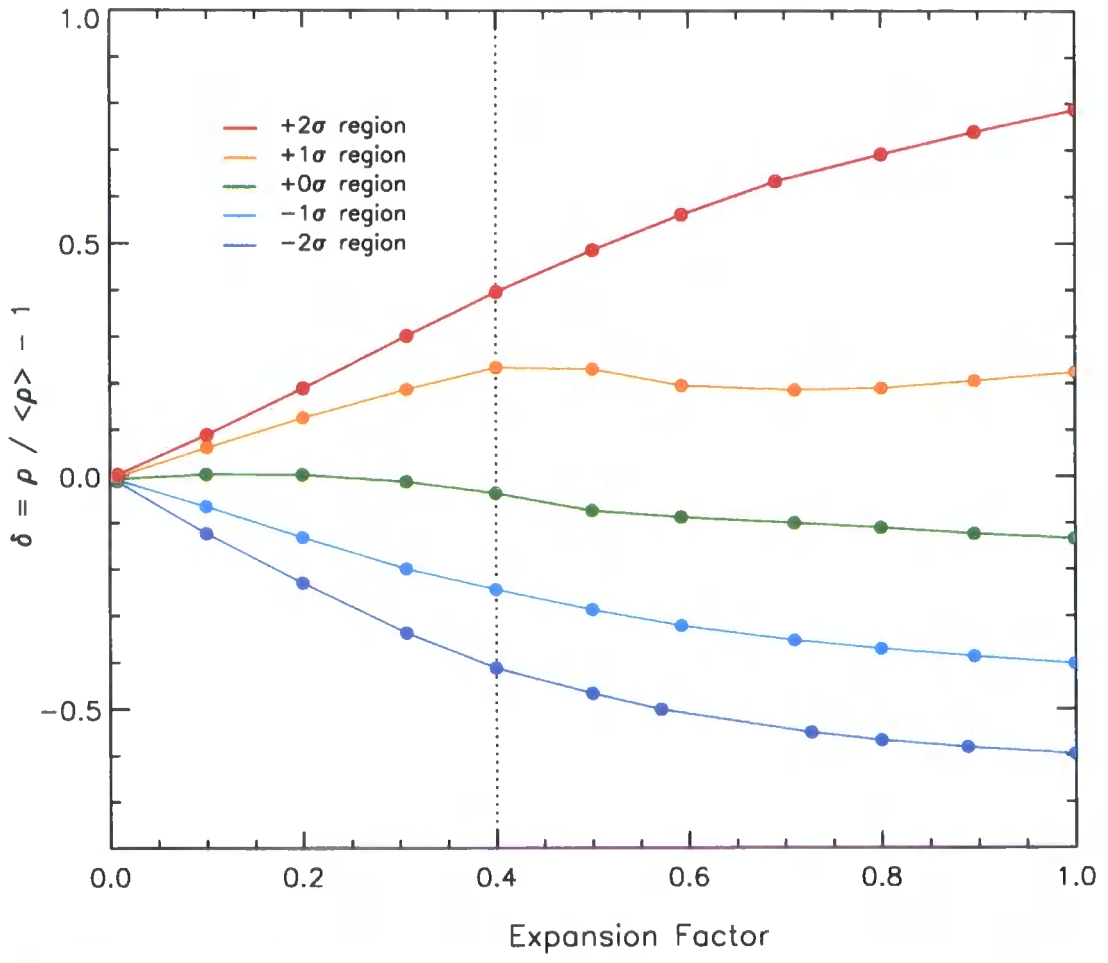

Figure 4.2: The overdensity evolution of the five spherical regions at intermediate resolution. The vertical dotted line denotes the epoch at which the regions were selected ($z = 1.5$). This colour scheme is retained for all subsequent plots in which the five regions are shown together. Notice the drop, after $z = 1.5$, in overdensity of the $+1\sigma$ region; this results from a massive halo with high peculiar velocity leaving the spherical region.

in the mass function of dark matter haloes between the regions that are used to define a particular environment. We therefore preface discussion of these effects with a brief overview of the evolution of the halo mass function in each region.

4.3 Evolution of haloes

4.3.1 Friends-of-friends haloes

We identify haloes by applying the FoF algorithm to dark matter particles, using the standard value of the linking length in terms of the mean interparticle separation ($b = 0.2$). Below we will only consider haloes with at least twenty dark matter particles. The break-up of dark matter overdensities in haloes using FoF sometimes leads to artificial clustering of small haloes around a more massive one. This is because the FoF algorithm identifies isodensity contours of $\delta \simeq 3/(2\pi b^3) \simeq 60$ (Lacey and Cole, 1994), but noise in the particle distribution introduces small islands outside of haloes where this criterion is also satisfied. Although the properties of these small haloes depend on resolution, the mechanism operates at any resolution. Since these artefacts tend to be transient, we perform a binding calculation and omit from our analyses any FoF haloes that do not have at least one self-bound substructure.

We associate any baryonic (i.e. gas or star) particle within a linking length of CDM particle belonging to a FoF group, to that group; in the event that such a particle belongs to more than one FoF group we assign it to the group with the greater dark matter mass. As discussed by Dolag et al. (2008), the identification of galaxies with a FoF algorithm is a non-trivial problem, and so we do not attempt to group the star particles within FoF groups into galaxies at this stage. Our method of associating baryonic particles with dark matter FoF haloes occasionally introduces artefacts, mostly for groups with few particles. For example we find that the baryon fraction for low-mass haloes varies very widely, from haloes with almost no baryons, to haloes with more than the cosmic mean baryon fraction, most probably owing to the fact that our scheme allows the baryon distribution around a halo to be more extended (by one linking length) than the dark matter. Since these problems are mostly restricted to small haloes close to the resolution limit we have not attempted to overcome them.

When quoting halo masses, we refer to the total mass of the FoF halo, in all compo-

nents (i.e. gas, stars and cold dark matter). In some cases, however, it is appropriate to modify this definition slightly; when comparing results with simulations featuring only dark matter (e.g. Section 4.3.2), we make a more direct comparison by considering only the cold dark matter component of FoF haloes but boost their mass by a factor of $(\Omega_0 - \Omega_b)/\Omega_0$ to account for the baryonic component. Additionally, when measuring baryon fractions it is common to specify fractions within the well-defined volume of a spherical overdensity (SO) group (e.g. Lacey and Cole, 1994); in this case we therefore quote the mass of a sphere, centred on the local minimum of the gravitational potential, whose radius encloses a mean density of $200\rho_c$. We also quote the circular velocity, v_c, of haloes at this radius, r_{200}.

4.3.2 Halo mass function

The mass function[2] of dark matter haloes varies significantly between different regions (Figure 4.3). At the earliest snapshot shown ($z = 6$), the mass function of the overdense regions is mostly a scaled-up version of the underdense regions, however at $z = 0$, the -2σ mass function has markedly different shape from that of the $+2\sigma$ region, with a very pronounced lack of massive haloes as expected (Sheth and Tormen, 2002). Giving the mass function of each region a weight corresponding to its Gaussian probability (with an additional factor of $(18/25)^3$ to account for the larger volume of the $+2\sigma$ region; Table 4.2), we can combine them to predict the mass function of the Millennium Simulation volume as a whole (thick histogram). This combined mass function is close to the mass function of the mean density (0σ) region, as well as the universal halo mass function presented by Reed et al. (2007, dotted line) at all epochs. We have verified that the deviations from the Reed et al. fit are consistent with the expected variance between spheres (the combined volume of the five GIMIC regions is only ~ 0.13 per cent of the entire Millennium Simulation volume.) The good agreement between the Reed et al. fit and the combined mass function is encouraging, and suggests it is possible to combine the five regions to make accurate quantitative predictions that apply to the Millennium Simulation volume as a whole, for example in terms of star formation, gas dynamics,

[2]Note that we show the *multiplicity function*, that is, the fraction of total mass bound into haloes of mass $(M, M + dM)$. We prefer this version of the mass function since it decreases the dynamic range of the plot and hence serves to highlight more clearly the differences between the regions.

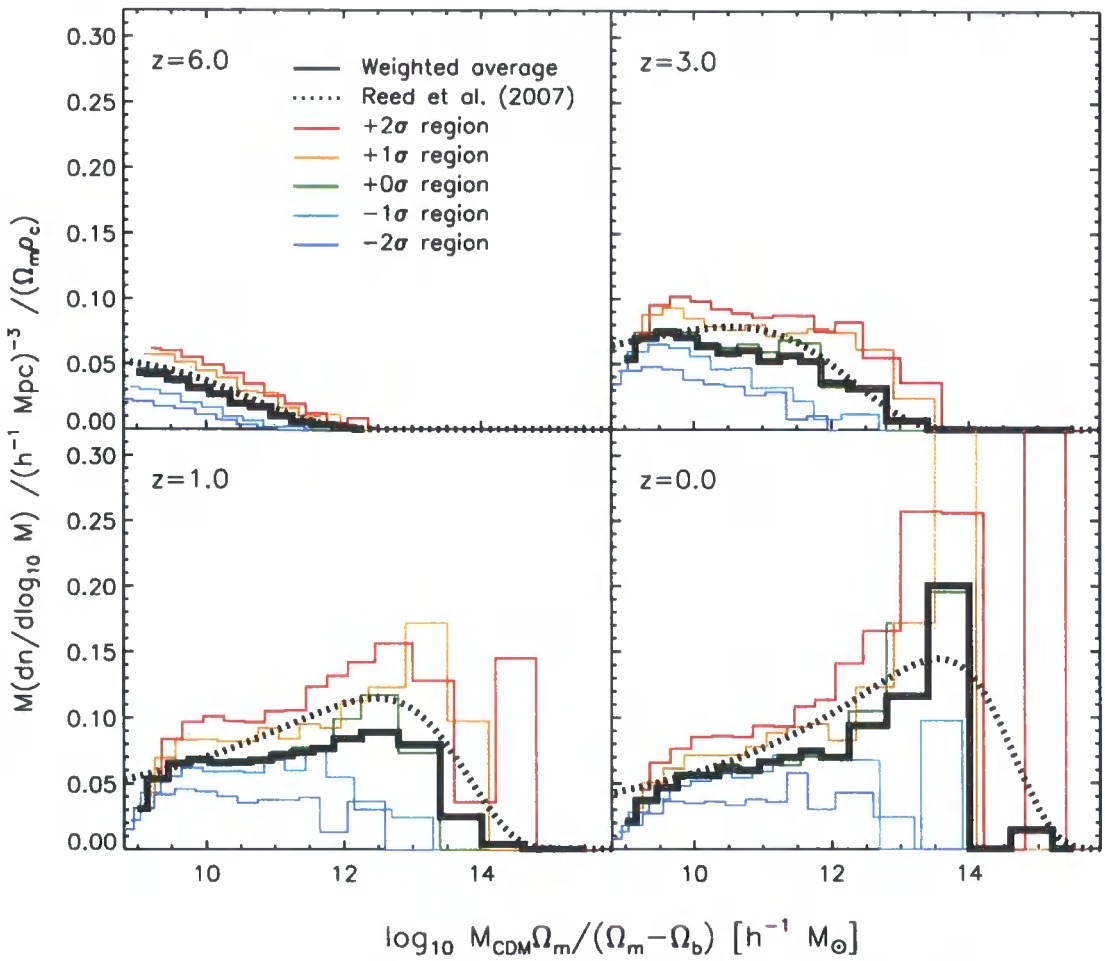

Figure 4.3: The halo mass function of the five regions from the intermediate resolution simulations. The functions have been multiplied by the bin mass and normalised by the mean matter density in order to highlight more clearly the strong environmental variation. The mass functions are similarly shaped at the low-mass end, with their offsets being a monotonic function of overdensity. The black histogram is the mass function yielded by our weighting procedure used to generate estimates for the Millennium Simulation volume from the GIMIC regions. For comparison, we show the universal mass function fit of Reed et al. (2007) as a dotted black line.

Sphere	Gaussian deviate range	Probability density	Volume weight	Overall weight
-2σ	$(-\infty, -1.5]$	0.0668	1	0.0668
-1σ	[-1.5:-0.5]	0.2417	1	0.2417
0σ	[-0.5:0.5]	0.3829	1	0.3829
$+1\sigma$	[0.5:1.5]	0.2417	1	0.2417
$+2\sigma$	$[1.5, \infty)$	0.0668	$(18/25)^3$	0.0249

Table 4.2: Numerical weights applied to each GIMIC region when extrapolating statistics to the whole 500^3 $(h^{-1}$ Mpc$)^3$ Millennium Simulation volume. The net weight (final column) is the product of the Gaussian probability for the region (second column) and the volume fraction (third column). The latter is applied to account for the larger volume of the $+2\sigma$ region.

and metal enrichment. We do so below.

4.4 Evolution of the stars

4.4.1 Large-scale environmental variation

For each region we consider all gas particles within the spherical region discussed in Section 4.2.2, and use the volume of that sphere to compute the star formation rate per unit volume, $\dot{\rho}_\star(z)$. This is shown in Figure 4.4, from which we conclude that:

- $\dot{\rho}_\star(z)$ increases by a factor ~ 10 from $z = 10$ to $z = 2$, then drops rapidly by a similar factor to $z = 0$;
- the shape of $\dot{\rho}_\star$ is similar for all regions;
- the amplitude of $\dot{\rho}_\star(z)$ varies by *an order of magnitude* between the regions, at all z.

Comparing to the higher resolution simulation (dotted lines) shows that

- the higher resolution simulations predict a considerably higher $\dot{\rho}_\star(z)$ above $z = 6$ so that $\dot{\rho}_\star(z)$ only increases by a factor ~ 3 between $z = 9$ and $z = 2$;
- the peak in $\dot{\rho}_\star(z)$ still occurs around $z \sim 2$;

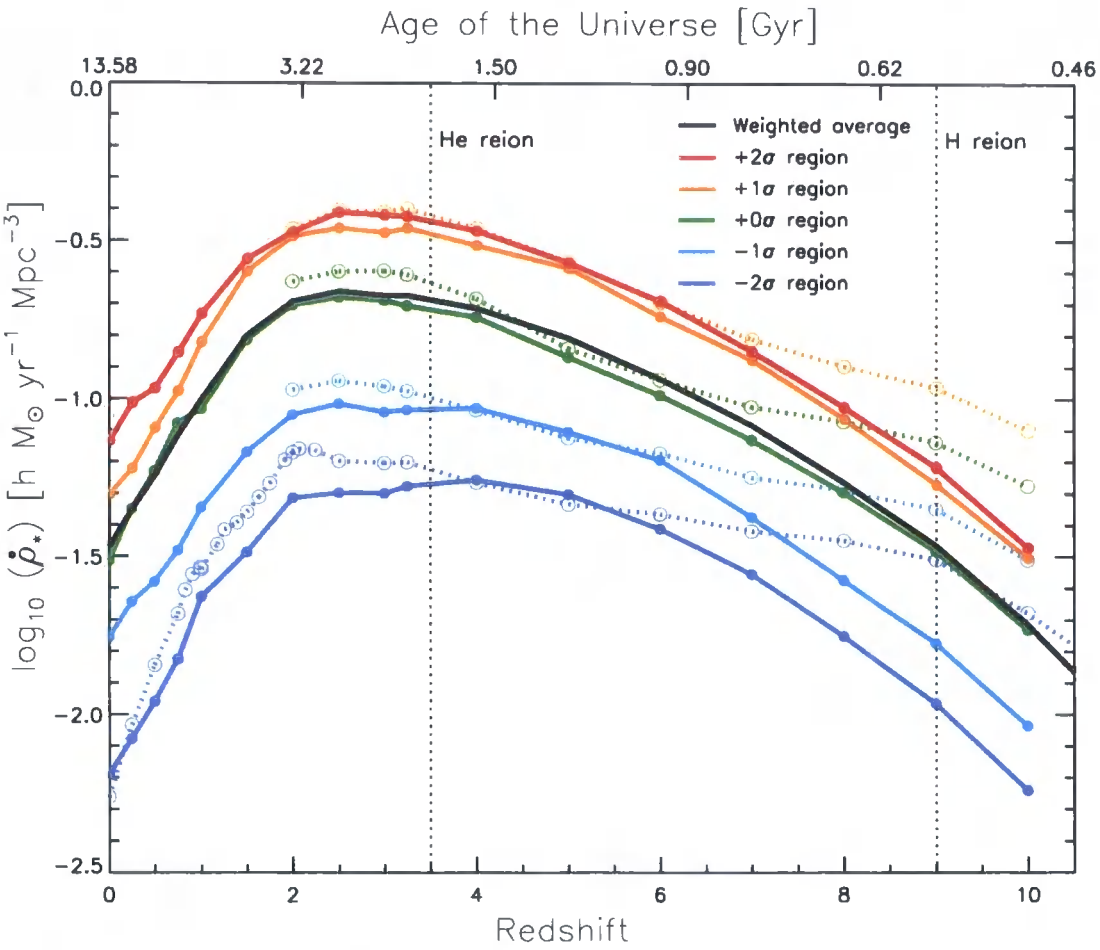

Figure 4.4: Star formation rate density, $\dot{\rho}_\star(z)$, as function of large-scale overdensity obtained from the GIMIC regions (different colours), at intermediate- (*solid lines*) and high-resolution (*dotted lines*). We have not run the $+2\sigma$ simulation at high-resolution. The vertical dotted lines at $z = 9$ and $z = 3.5$ denote the epochs of reionisation of hydrogen (HI) and helium (HeII) respectively. The variation in $\dot{\rho}_\star$ across the large-scale environments is striking, with the most extreme regions differing by approximately an order of magnitude at all epochs. The star formation rate of the simulations is particularly sensitive to resolution at high-redshift; the intermediate resolution simulations are not converged for $z > 6$ where they underestimate the star formation rate. The high resolution simulations resolve the Jeans mass in the IGM after reionisation, and resolve the quenching of star formation at $z = 9$ when small haloes stop forming stars following the entropy injection as the IGM gets ionised and heated: this is clearly visible in the figure as a kink in the high-resolution star formation rate density at $z = 9$.

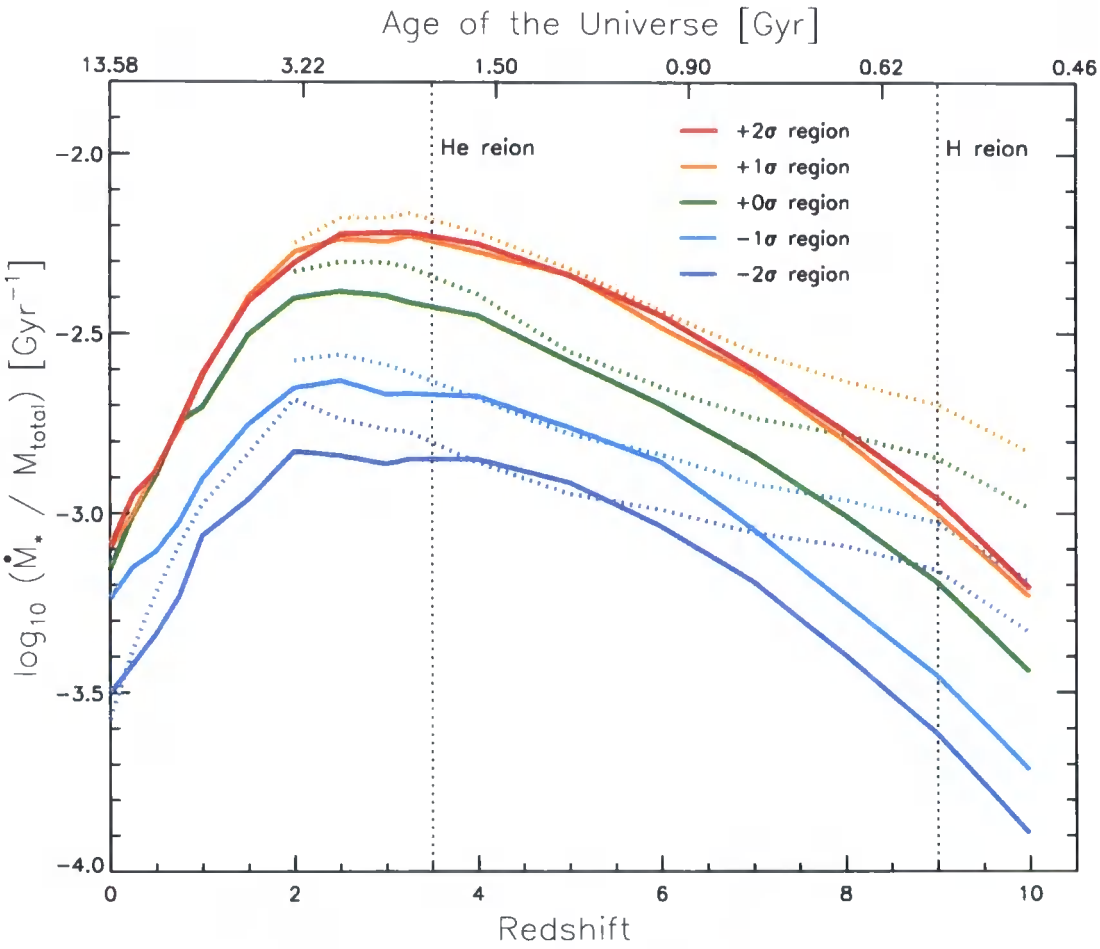

Figure 4.5: The evolution of the total star formation rate per unit mass, as a function of large-scale overdensity. As per Figure 4.4, the intermediate-resolution runs are shown wit solid lines, high-resolution runs with dotted lines. The residual offset between the regions demonstrates that the greater normalisation of $\dot{\rho}_\star(z)$ in overdense regions does not arise purely because they enclose a greater mass. The key difference is that a greater fraction of their enclosed mass is bound into more massive haloes that, in our model, exhibit higher star formation efficiencies.

- $\dot{\rho}_\star(z)$ rises more rapidly with decreasing z before reionisation (vertical dotted line at $z = 9$) than immediately after reionisation.

The SFR density (SFRD) rises monotonically from the -2σ to $+2\sigma$ regions at all z, but the difference between $+1\sigma$ and $+2\sigma$ regions is far smaller than, for example, between the -2σ and -1σ regions. The large differences in amplitude of $\dot{\rho}_\star$ between the different regions is not simply caused by the higher density regions having more mass: higher σ regions also have a higher *specific* star formation rate (sSFR, $\dot{M}_{\rm star}/M_{200}$; see Figure 4.5). The amplitude of the sSFR still varies by ~ 0.5 dex between the regions. This is one of the key results of this chapter.

The peak in star formation at $z \sim 2$ is significantly later than in the simulations of SH03b, which have comparable numerical resolution to ours. We think this is only partly due to our inclusion of metal line cooling affecting the SFR particularly at lower z, as discussed and illustrated in the analytical model of HS03. The largest volume simulations ($L = 32\ h^{-1}$ Mpc, thus yielding a similar volume to a single GIMIC sphere) of Oppenheimer and Davé (2006) have poorer resolution than our intermediate resolution simulations by a factor of ~ 3, and hence we expect their high-z results to suffer from lack of numerical convergence as well. The SFR in most of their models also peaks at higher z than ours. Both sets of simulations use the multi-phase model of SH03a for gas in galaxies, combined with an implementation of galactic winds. The details of the wind implementation are probably the main cause of the differences.

The SFR of a given simulation may depend on resolution because it fails to form haloes below the resolution limit, and/or because the star formation rate in haloes that do form depend on resolution. The particle mass of the high resolution simulation was chosen such that it can resolve the Jeans mass in the photo-ionised IGM, and hence that simulation should be able to follow the formation of all haloes in which the gas cools by atomic line cooling after reionisation. We show below that the star formation rate for resolved haloes is very similar for the two resolutions. We are therefore resonably confident that our estimate for $\dot{\rho}_\star(z)$ is close to numerically converged in our higher resolution simulation, but is not in the intermediate resolution one. Of course, the actual value of the star formation rate will still depend on our chosen sub-grid modelling, in particular on the implementation of galactic winds. Note that the lack of high-redshift convergence in the intermediate-resolution simulations has only a small effect on the distribution of

stellar ages at low-redshift, since the time-scale of this high-redshift period is small in comparison to the age of the Universe.

A striking feature of the SFR in the higher resolution simulations is the kink in $\dot{\rho}_\star$ at $z = 9$, which is when the IGM is ionised and heated following reionisation: the increase in $\dot{\rho}_\star$ with decreasing z slows considerably after this. The onset of reionisation has two key effects on gas evolution; the photo-heating boosts and maintains the temperature of the gas to a near-uniform level of $\sim 10^4$ K, whilst the photo-ionisation quenches HI line cooling (Efstathiou, 1992). Small haloes with too low a virial temperature cannot hold onto their photo-heated gas anymore, and star formation in them ceases. Okamoto et al. (2008a) present numerical simulations and a simple analytical model for how the characteristic mass $M_c(z)$, below which haloes lose most of their baryons, depends on the shape of the temperature-density relation for the IGM. The characteristic mass for the Haardt and Madau (2001) ionising background applied here, $M_c(z = 9) \simeq 10^7\ h^{-1}\ \mathrm{M}_\odot$, is not resolved in the intermediate resolution simulation, which explains the absence of the kink in that simulation.

4.4.2 Galaxy luminosity functions

The most fundamental description of simulations of galaxy formation comes from the galaxy luminosity function. Since we do not specifically discuss the properties of *galaxies* in this chapter, except in the context of the luminosity function, we defer a detailed description of our galaxy finding algorithm until Section 6.2. We simply note here that the algorithm is a modified version of SUBFIND (Springel et al., 2001a) that is described by Dolag et al. (2008). Our method for assigning broadband optical luminosities to simulated galaxies, based on stellar population synthesis modelling, is also described in detail later, in Section 6.4.

The galaxy luminosity functions of the GIMIC regions at $z = 0$, in the $K-$ and B-bands, are shown in Figure 4.6. In each plot, the corresponding observed luminosity function presented by Eke et al. (2005) is also plotted; note that we adopt the AB magnitude system (Oke, 1974) throughout. Clearly, the luminosity functions produced by the hydrodynamic simulations do not match the observed luminosity functions nearly so well as do most semi-analytic models (see, for example, Figure 3 of Bower et al., 2006). This partially reflects the fact that semi-analytic models typically use the $z = 0$ luminos-

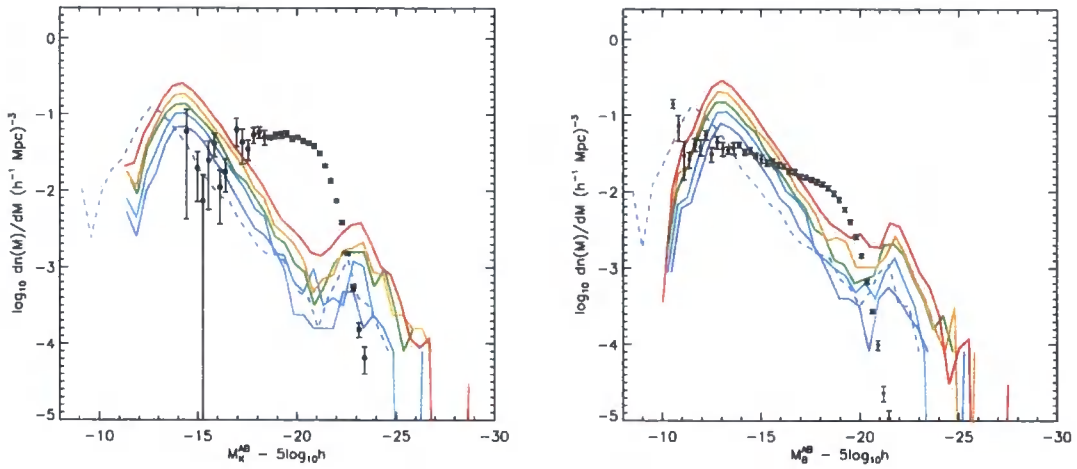

Figure 4.6: The galaxy luminosity functions of the GIMIC regions, at $z = 0$, in the K-band (*left panel*) and the B-band (*right panel*). All five regions are plotted at intermediate resolution (*solid lines*, colour scheme as per previous plots), and the -2σ region at high resolution is also shown (*dashed line*) to assess convergence. Overplotted data points are taken from Eke et al. (2005).

ity function as a primary constraint upon their parameter selection, but there are key differences between GIMIC and observations that are noteworthy.

Firstly, the extreme faint end of the simulated luminosity function features a strong decline (for $M_{\rm K} - 5\log_{10} h > -14$, $M_{\rm B} - 5\log_{10} h > -13$) that does not feature in the observed functions; this feature is almost certainly a resolution effect, since such faint systems are resolved with very few star particles in the simulations, and moreover the magnitude at which the downturn occurs shifts to fainter magnitudes (i.e. the same number of particles) in the high-resolution -2σ realisation. At the magnitude where the downturn occurs, the luminosity function peaks, and this peak is a factor of ~ 3 higher than the faint end of the Eke et al. (2005) K-band luminosity function, and a factor of ~ 10 higher than the observed B-band luminosity function. Our feedback schemes therefore do not sufficiently quench star formation in low-mass galaxies to fully reconcile the ΛCDM halo mass function with the paucity of faint galaxies observed locally.

At intermediate luminosities, the converse is true: our choice of star formation and feedback schemes leads to an under-production of galaxies at the magnitude where the luminosity function changes from a power-law to an exponential decay (the 'break scale'). This is particularly acute in the K-band, which is a more direct proxy for the

stellar mass function since, unlike the B-band, the emission here is not dominated by newly formed, highly luminous stars. The simulations are under-abundant in galaxies at the break scale, relative to the observations, by nearly two orders of magnitude. This is manifest as a dip in the luminosity function (at $M - 5\log_{10}h \sim -20$ in both bands), and this scale almost certainly follows from the scale imposed by our feedback scheme, parametrised by the wind velocity and mass loading.

The simulations also fail to reproduce the observed exponential decline of the most luminous galaxies. This, however, is unsurprising since the simulations do not include a prescription for feedback from AGN that, as argued in Chapter 3, is likely to be necessary as a means to quench cooling flows in massive haloes such as those that host galaxy groups and clusters. If the SFR of the galaxies that are fed, unabated in these simulations, by such cooling flows were suppressed by AGN, it follows that the simulated luminosity function would be boosted at fainter magnitudes; however, the number of systems affected by AGN would be relatively few, compared to the number of galaxies expected at the break scale, and so this effect would be small. Therefore, we can be confident that the under-abundance of galaxies at the break-scale follows directly from the impact of winds.

Whilst the simulations do not precisely reproduce the observed K- and B-band luminosity functions, it is argued here that this does not invalidate subsequent conclusions derived from these data. Firstly, the key aspect of these simulations is their ability to probe a wide range of environments; we shall argue later (Section 4.4.5) that environmental effects are driven by differences in the halo mass function of each region, rather than differences in the baryon physics, and so our conclusions are relatively robust to changes to the adopted star formation and feedback schemes. Secondly, it is argued that simulations of this sort are *necessary* as a means to understand the detailed effects of particular feedback implementations; indeed semi-analytic models have struggled for some time to reproduce key observations whilst simultaneously reproducing the $z = 0$ luminosity function.

4.4.3 The Millennium Simulation star formation rate density

The star formation rate of individual GIMIC regions can be combined[3] to estimate the net $\dot{\rho}_\star$ of the whole Millennium volume ($L = 500\ h^{-1}$ Mpc; Figure 4.7). The SFR increases with decreasing redshift to reach a plateau at $\approx 0.25\, h^{-1}\, M_\odot\, yr^{-1}\, Mpc^{-3}$ over the interval $1 \lesssim z \lesssim 3$, followed by a rapid decline by a factor of ~ 8 to $z = 0$, quantitatively similar to that of the mean density (0σ) region (compare Figures 4.4 & 4.7).

The coloured curves in Figure 4.4 decompose the SFR density into the contributions from haloes binned according to their mass at the epoch of observation; these bins are chosen to correspond approximately to the masses of haloes that at the present epoch host dwarf galaxies ('dwarf haloes'), regular late-type spirals ('galaxy haloes') and groups and clusters of galaxies ('group haloes'). As might be naïvely expected within the hierarchical assembly scenario, the peak of star formation within low mass haloes preceeds that of more massive galaxies in our simulations. For our particular classifications (delineated at the masses $(5 \times 10^{11}, 5 \times 10^{12})\ h^{-1}\ M_\odot$) these peaks are broad, occuring at $z \sim 4 - 5$ for dwarf haloes, $z \sim 2 - 3$ for galaxy haloes, and $z \sim 1 - 2$ for group haloes[4]. Since we make no attempt at this stage to separate the stellar mass within dark matter haloes into individual galaxies, we reserve judgement upon whether this finding is compatible with the 'downsizing' scenario that is frequently used to describe the observed evolution of galactic star formation rates.

The simulations store the *formation time* for each star particle, and this allows us to relate present day systems with the properties of the progenitors in which the stars formed. This 'archeological version'of the star formation history is computed by summing the birth mass of stellar particles within the spherical region at $z = 0$, binned by their formation redshift (Figure 4.8). The solid black curve, integrating over haloes of all masses, differs slightly from that of Figure 4.7 the left-hand plot at epochs other than $z = 0$, since the population of baryonic particles within the spherical region evolves subtly over time. This exercise shows that star formation is dominated at all redshifts by the progenitors of galaxies that today reside in the most massive haloes. This is a hierarchical build-up,

[3]We used the intermediate resolution simulation which underestimates the SFR above $z = 6$. For consistency with Figure 8 of Bower et al. (2006), we convert the observational data assuming the IMF of Kennicutt (1983), but we remind the reader that our simulations assume the IMF of Chabrier (2003). The difference in a stellar population's mass-to-light ratio varies by only ~ 10 per cent between these two IMFs.

[4]Note that the drop in SFRD above $z \sim 6$ is much reduced in the high-resolution simulations.

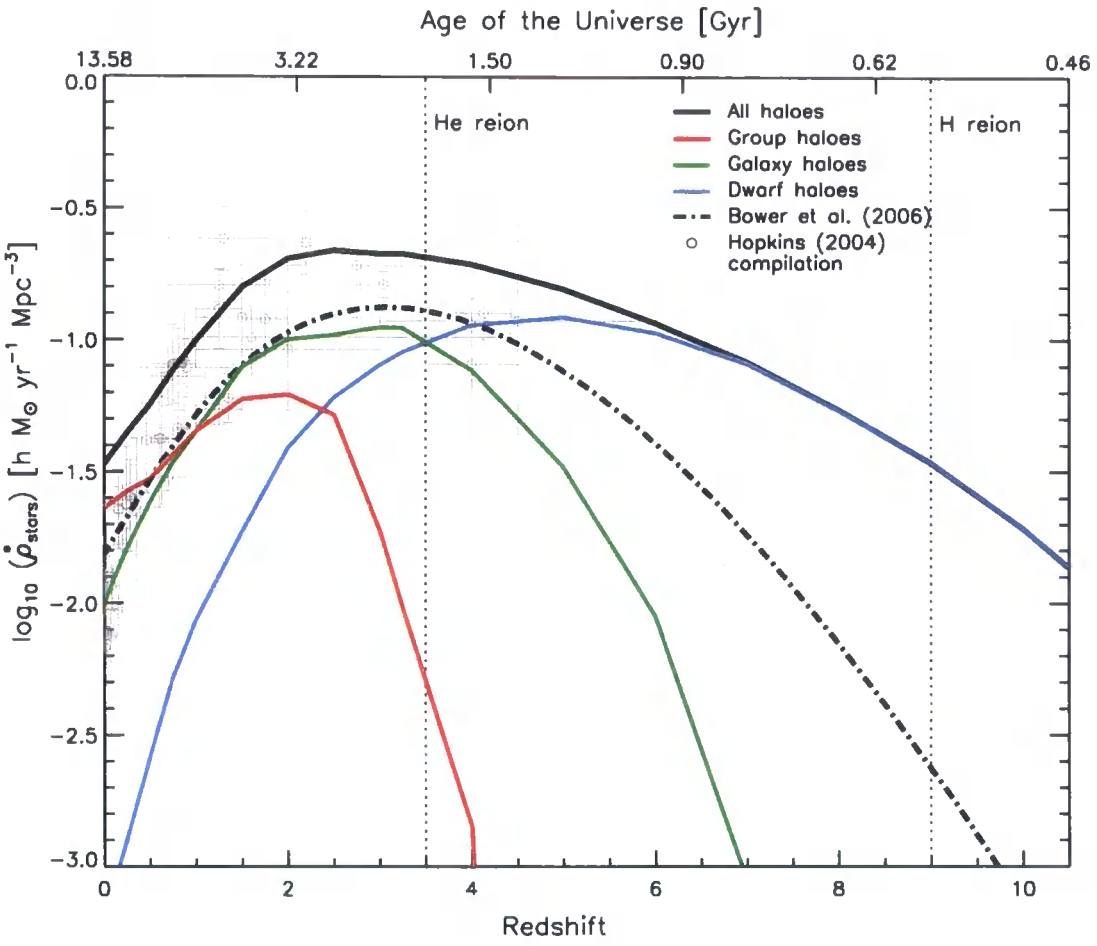

Figure 4.7: Star formation rate density, $\dot{\rho}_\star(z)$, of the entire $L = 500\ h^{-1}$ Mpc volume of the Millennium Simulation (black solid line), derived from a weighted average of the intermediate-resolution GIMIC simulations. The instantaneous contribution to the total from dwarf galaxy haloes, regular galaxy haloes and group/cluster haloes is shown as the blue, green and red solid lines respectively. The three categories of halo are delineated by the mass boundaries $(5 \times 10^{11}, 5 \times 10^{12})\ h^{-1}\ \mathrm{M}_\odot$. The total star formation rate density predicted by the semi-analytic calculation of Bower et al. (2006) is shown for comparison (black dot-dashed line). Symbols with error bars are observational estimates from the compilation of Hopkins (2004). The intermediate resolution simulation underestimates the SFR above $z = 6$, but below this the simulation is in good agreement with the data. The Bower et al. SFR is lower at all z, and in particular has far lower star formation above $z = 6$ due to its much lower resolution.

because the star formation in massive haloes became dominant only recently.

The simulated star formation history is generally in good agreement with the compilation of observational data by Hopkins (2004): a broad plateau with nearly constant star formation for $5 \gtrsim z \lesssim 1$, followed by a rapid drop to $z = 0$. The reduction in the SFRD towards the present day is smaller in the simulation than in the data, and is due to the high star formation rates of massive haloes, as can be seen in the left-hand panel. Recent semi-analytical models (e.g. Bower et al., 2006) include feedback from AGN to suppress the cooling of gas in such haloes and quench their star formation. Including such a recipe in our model will bring the simulated SFRD into better agreement with the data. This discrepancy occurs when the star formation rate is already rapidly declining, therefore has little effect on the global stellar mass density. The simulation predicts $\Omega_\star h$ at $z = 0$ of $\Omega_\star h = 2.3 \times 10^{-3}$, consistent with the observational estimate derived from the 2dFGRS survey ($\Omega_\star h = 1.1(\pm 0.05) \times 10^{-3}$ at $z = 0.1$, Eke et al. (2005)), given the typical systematic uncertainties in the observational estimate due to the choice of IMF of around a factor of two. The observational data at $z \gtrsim 6$ are uncertain and differ by a factor ~ 10 between authors (Bunker et al., 2006; Bouwens et al., 2008). The simulations favour a modest drop of $\sim 50\%$ in the SFRD from its peak at $z \sim 2$ to $z = 6$, with most stars forming in faint galaxies, which have star formation rates of $\lesssim 0.1\ \mathrm{M}_\odot\ \mathrm{yr}^{-1}$. Such star formation rates are typically an order of magnitude below the sensitivity limits of most surveys. In addition, the angular extent of each GIMIC region is $\sim 14' \times 14'$ on the sky at $z = 6$, which is large in comparison to these surveys: the simulation predicts that the SFRD varies by up to an order of magnitude, even on those large scales. The low SFR per halo compounded with the high degree of cosmic variance illustrates how demanding it will be to obtain accurate observational measurements of the SFRD at these early times. Interestingly the high-resolution simulation has a nearly constant SFRD from $z = 6$ to $z = 9$, and its star formation is dominated by small galaxies. If the escape fraction of ionising radiation from such small haloes is as high as predicted by the simulations of Wise and Cen (2008), ($\sim 25 - 80$ per cent when averaged over time), then these galaxies will be the dominant contributors to the ultraviolet-background at high z, and may have been the main sources of radiation that led to reionisation (Srbinovsky and Wyithe, 2008). The faintness of each individual source may then also reconcile the apparent dearth of sources of ultraviolet-photons with the inferred ionisation state of the intergalactic medium at $z \sim 6$

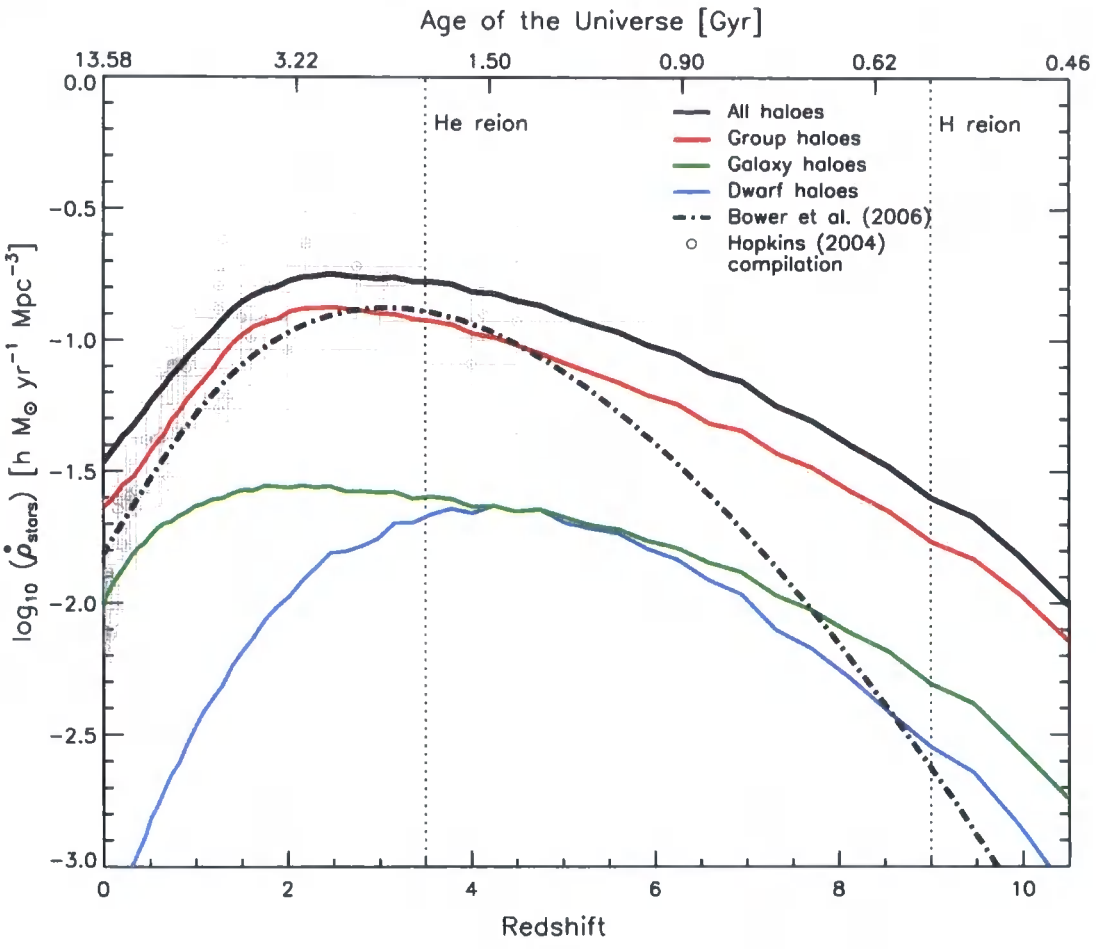

Figure 4.8: The 'archaelogical counterpart' to Figure 4.7; haloes are assigned to the same three bins based on their mass at $z = 0$, and the coloured curves show the star formation rate density of their progenitors. The coloured curves in this plot and Figure 4.7 therefore necessarily converge at $z = 0$. The star formation rate density of the Universe has always been dominated by the progenitors of galaxies that reside in the most massive haloes today (group/cluster haloes with $M \geq 5 \times 10^{12}\ h^{-1}\ \mathrm{M}_{\odot}$), yet these stars were predominantly formed either in dwarf haloes ($M \leq 5 \times 10^{11}\ \mathrm{M}_{\odot}$) before $z \sim 3.5$ or galaxy-sized haloes after that. Together these plots highlight the hierarchical nature of galaxy formation, in which massive galaxies form late yet their stars form early in much smaller progenitors. The star formation rate density of the most massive haloes becomes dominant at $z \simeq 0.5$, which may be an artefact of over cooling in massive haloes.

(Bolton and Haehnelt, 2007). The ratio $N_\gamma(z)/N_H$ between the number of ionising photons produced per unit volume by stars, N_γ, and the number of hydrogen atoms in that same volume, N_H, is plotted for the different GIMIC regions in Figure 4.9 as a function of redshift. We used the conversion factor $N_\gamma/M_\star = 3.2 \times 10^{60}/M_\odot$ that Benson et al. (2006) quote for their 'standard' initial mass function, but different assumptions about the IMF yield significantly different factors. Since the SFRD differs significantly between regions (Figure 4.4), so does $N_\gamma(z)/N_H$: the higher density regions produce significantly more ionising photons per baryon as also found by Ciardi et al. (2003). Reionisation requires $N_\gamma(z)/N_H \gtrsim r$, where r is greater than a few, with the exact value dependent on how many ionising photons are lost to recombinations. Because protoclusters (such as the $+2\sigma$ region) produce more ionising photons than protovoids (the -2σ region), gas at the same density in the proto-cluster region will be ionised earlier than gas in the protovoid (Trac et al., 2008). However, the recombination rate in protoclusters is also likely to be higher, and so reionisation may require a greater value of r. Assuming r does not vary with environment, the expected delay can be read from the inset panel of Figure 4.9: $\Delta z_{\rm reion} \sim 1.2$ between the $+1\sigma$ and -1σ regions, largely independent of z and the poorly known required value of r (since the offset in N_γ/N_H between regions is largely independent of z). Assuming the gas temperature drops adiabatically after reionisation implies that the gas temperature differs between the $+1$ and -2 regions by a factor $\sim (1+12)^2/(1+11)^2 \simeq 1.2$. This is probably too small to measure directly from the linewidths in the Lyman-α forest (Theuns et al., 2002), yet could be the origin of the inverted temperature-density relation in the intergalactic medium claimed by (Bolton et al., 2008), as discussed in Trac et al. (2008). The SFR density in the semi-analytical model of Bower et al. (2006) applied to the Millennium Simulation is shown as the dashed line in Figure 4.7. It falls below the simulated curves at all z, and in particular at high redshifts $z \geq 6$, and at $z \sim 0$. The semi-analytic calculation forms stars only within self-bound haloes and substructures of at least twenty particles identified within the collisionless Millennium Simulation, and hence has poorer numerical resolution than the intermediate resolution GIMIC simulations. Although this poorer resolution may go some way towards explaining the high-z difference, other factors such as the implementation of feedback also play a role. At low redshift, the offset between the two is very likely due to the efficient operation of the semi-analytic model's inclusion of AGN feedback to quench cooling of gas

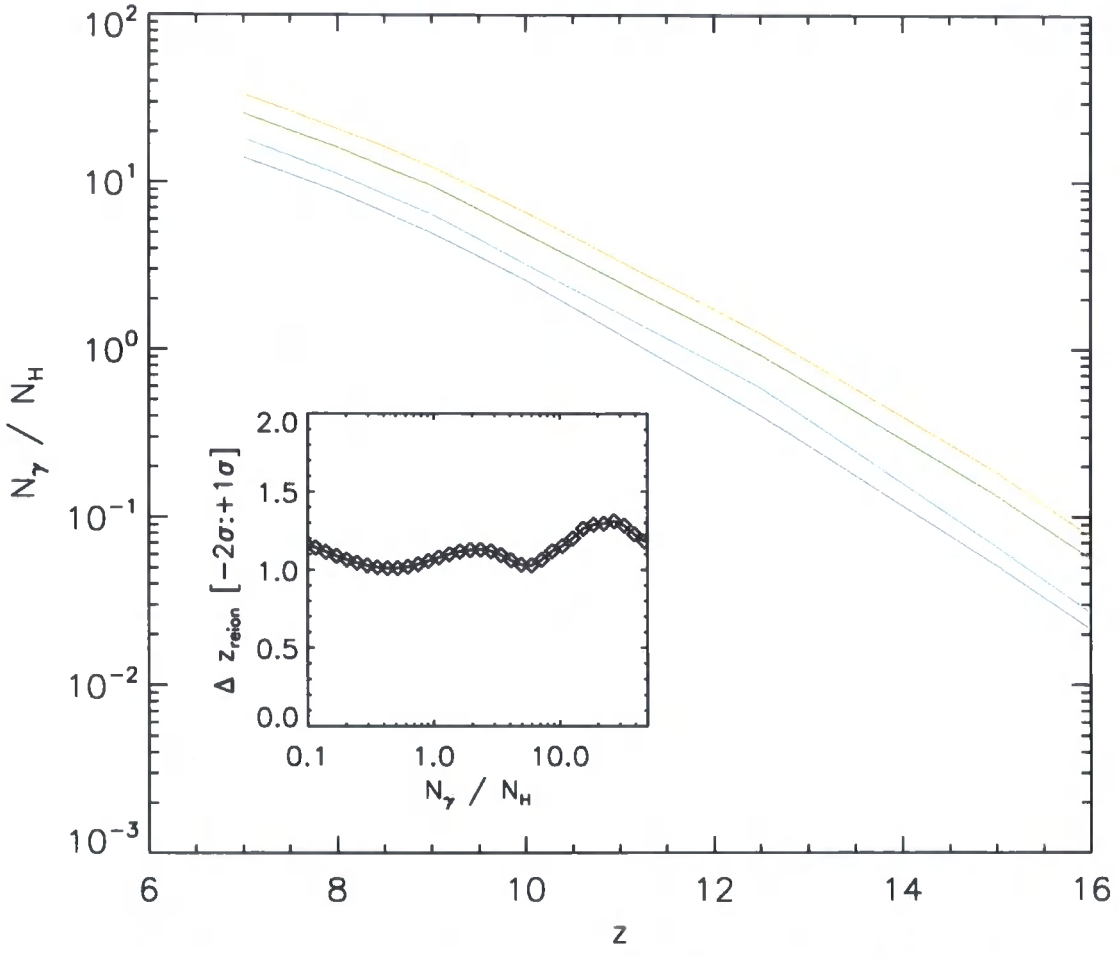

Figure 4.9: Ratio $r = N_\gamma/N_H$ of the number of ionising photons, N_γ, produced in each GIMIC region ($+1\sigma$ to -2σ from top to bottom) divided by the number of hydrogen atoms, N_H, in that region as a function of redshift, assuming $N_\gamma/M_\star = 3.2 \times 10^{60}\ M_\odot^{-1}$. It is thought that a region must produce $r \gtrsim 3$ ionising photons to fully reionise itself. Whereas the more vigorous star formation in the higher density regions results in larger values of r at given redshift, the recombination rate will be higher as well, so higher density regions may require higher values of r. For constant r, the delay in reionisation is almost independent of z, and is of order $\Delta z \sim 1$ between the -2 and $+1\sigma$ regions (inset).

in more massive haloes.

4.4.4 What shapes halo star formation rates?

The mean specific star formation rate (sSFR[5]) as a function of halo mass or circular velocity varies strongly with redshift, but is virtually identical for the five GIMIC regions (Figure 4.10). It shows a kink at a characteristic velocity of ~ 250 km s^{-1} due to the action of galactic winds, yet this occurs at significantly *lower* velocity than the speed with which galactic winds are actually launched ($v_w = 600$ km s^{-1}). The galactic wind feature grows more pronounced at later times. The sSFR of the higher resolution run is similar, but star formation is suppressed by a factor of a few when compared to the intermediate-resolution runs below the characteristic kink. The small box and whisker elements denote one and two standard errors on the mean sSFR, illustrating that this relation is very well defined, and is virtually independent of large-scale environment. The similarity of the sSFR between the GIMIC regions may be unexpected, given the large variation in the SFRD between them. We explain in the next section how to reconcile these results. Haloes of virial mass $M_{200} \sim 10^9 h^{-1}$ M$_\odot$ and circular velocity $v_c \sim 35$ km s^{-1} have low star formation rates of $\dot{M}_\star \lesssim 0.025$ M$_\odot$ yr^{-1} at redshifts $z \sim 6$. Such objects are ubiquitous at that time and they dominate the total star formation rate. The sSFR drops rapidly at lower masses as haloes lose their baryons due to a combination of stellar feedback and heating of their gas by the ultraviolet background. The GADGET2 simulations of Springel and Hernquist (2002a) yield quantitatively similar results, as do the AMR simulations of Wise and Cen (2008) of idealized dwarfs. In the latter simulations, blowout of baryons prevents star formation at masses below 10^8 M$_\odot$. In our simulations, the sSFR of these small haloes drops rapidly by more than two orders of magnitude toward $z = 0$. Above a circular velocity of ~ 250 km s^{-1}, where haloes are less susceptible to galactic winds in our model, the sSFR is almost constant at $\sim 10^{-1}$ Gyr^{-1} above $z \sim 3$. The level of this plateau drops by a factor ~ 5 to $z = 1$. The simulations of SH03b yield a sSFR for a $10^{12} h^{-1}$ M$_\odot$ halo of $10^{-1.7}$ Gyr^{-1} at $z = 3$, somewhat below our value of $10^{-1.2}$ Gyr^{-1}, with a drop to $z = 1.5$ of a factor of 5. Whereas the sSFR is nearly constant with mass for massive haloes in our simulations, the sSFR increases rapidly with halo mass in those of

[5]We define the sSFR as the ratio of the instantaneous star formation rate of a halo to its total SO mass, M_{200}, in all components (gas, stars & cold dark matter).

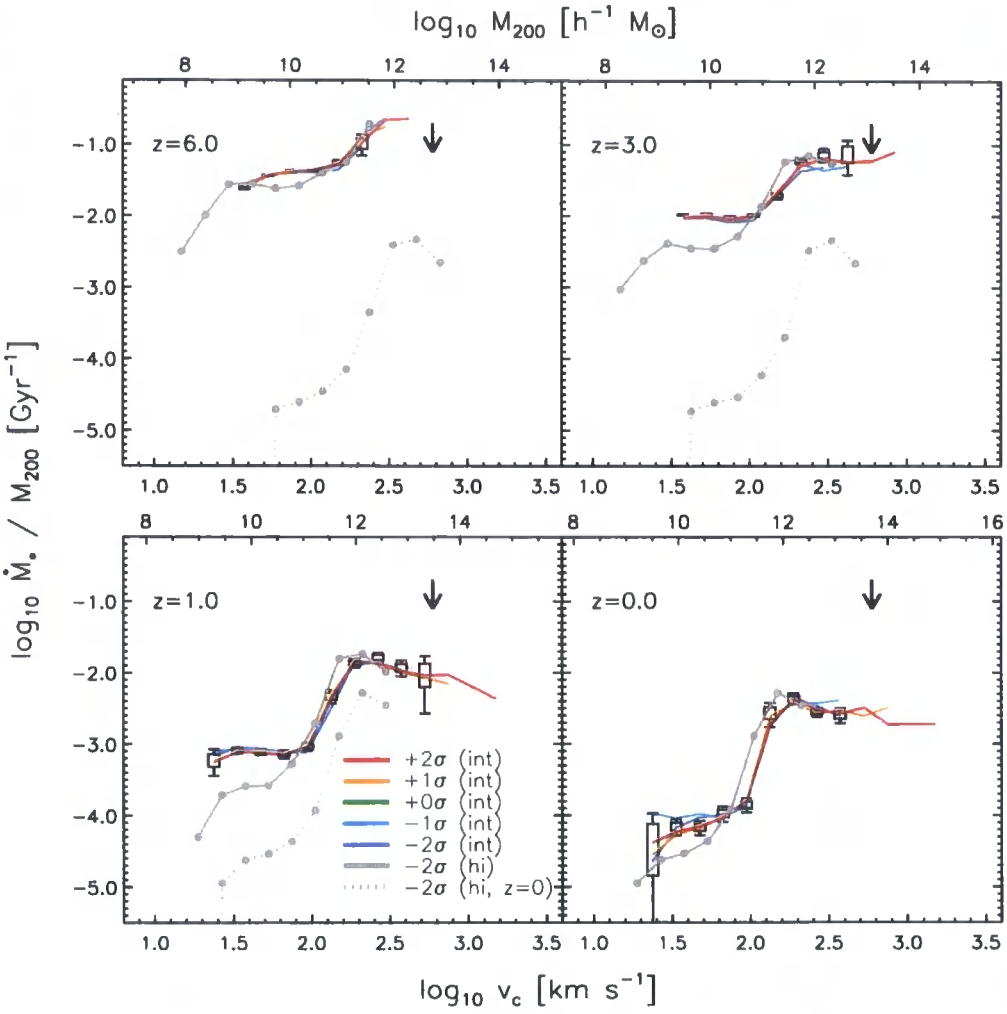

Figure 4.10: Specific star formation rates (sSFR) of haloes as a function of circular velocity (bottom axis) or halo mass (top axis) for the five different GIMIC regions (different colours) at intermediate resolution, and the -2σ region at high resolution, for different redshifts as indicated in the panels. Box and whisker elements (plotted for the 0σ region) indicate one and two standard errors on the mean: these are small, indicating that the sSFR is a well defined function of v_c. The $z = 0$ relation from the -2σ region at high resolution (solid grey line) is repeated in each panel for comparison (dotted grey line), demonstrating the strong redshift evolution of the sSFR. The vertical arrow points at the launch velocity of the winds.

SH03b. Observationally, the existing stellar mass provides a more convenient normalising factor for the SFR. The SFR/M_* inferred from the SDSS and DEEP2 redshift surveys by Chen et al. (2008) of galaxies of stellar mass $\sim 10^{10.5}$ $M_\odot$ are 8 $M_\odot$ yr^{-1} and ~ 2.5 $M_\odot$ yr^{-1} at redshift $z = 1$ and $z = 0$ respectively. As shown in Figure 4.11, this compares favourably with simulated galaxies of the same mass at $z = 1$: GIMIC yields an analogous value of 8.6 $M_\odot$ yr^{-1}. The drop-off towards $z = 0$ is not as steep as in the data, however, the simulations yielding a median of ~ 4.3 $M_\odot$ yr^{-1}. The strong redshift evolution of the sSFR is intriguing. Hernquist and Springel (2003, hereafter HS03) present an analytic model in which the sSFR of a halo of given circular velocity drops with redshift because star formation is limited by the cooling time, of its gas at intermediate z, and by the gas consumption time-scale at higher z where τ_c becomes small. The cooling time is defined as:

$$\tau_c(\rho) \equiv -\frac{u}{\dot{u}} = \frac{u}{\Lambda \rho}, \tag{4.1}$$

where u is the thermal energy per unit mass, and Λ the cooling rate, which depends on temperature, metallicity, and redshift (we shall discuss a more detailed description of Λ, including heating terms, in Chapter 5). At intermediate redshifts the cooling time, and hence the specific star formation rate, scales $\propto \Lambda^{-1}\rho^{-1}$. The analytic exploration of the evolving normalisation of the sSFR-v_c relation by HS03 starts from pseudo-isothermal initial gas profiles, and yields specific star formation rates for haloes of $T_{\rm vir} \simeq 10^7$ K that closely trace those in the simulations of SH03b at intermediate redshifts ($2 \lesssim z \lesssim 7$). We compare this analytic model with measurements of the sSFR of haloes from the GIMIC simulations in Figure 4.12, and use our own cooling function, $\Lambda(\rho, T, Z, z)$ - this introduces a redshift dependency, owing to the evolution of the ultraviolet background (as discussed in Section 2.4). We plot the analytic sSFR for group haloes ($v_c > 300$ km s^{-1}) only, since the sSFR of dwarfs is not regulated by the cooling time, and assume that halo gas resides at the mean virial temperature of simulated haloes that satisfy $v_c > 300$ km s^{-1}. Note therefore that this plot does not represent the *evolution* of the sSFR of a given halo, but rather the mean sSFR of haloes in a given circular velocity range at a given redshift. We adopt three different metallicities for the calculation: primordial composition, one-tenth of solar, and solar (the latter both assuming solar abundance ratios). The variation with metallicity is strong since, as shown in Figure 2.2, the contribution to cooling from heavy elements can dominate the primordial rate, particularly

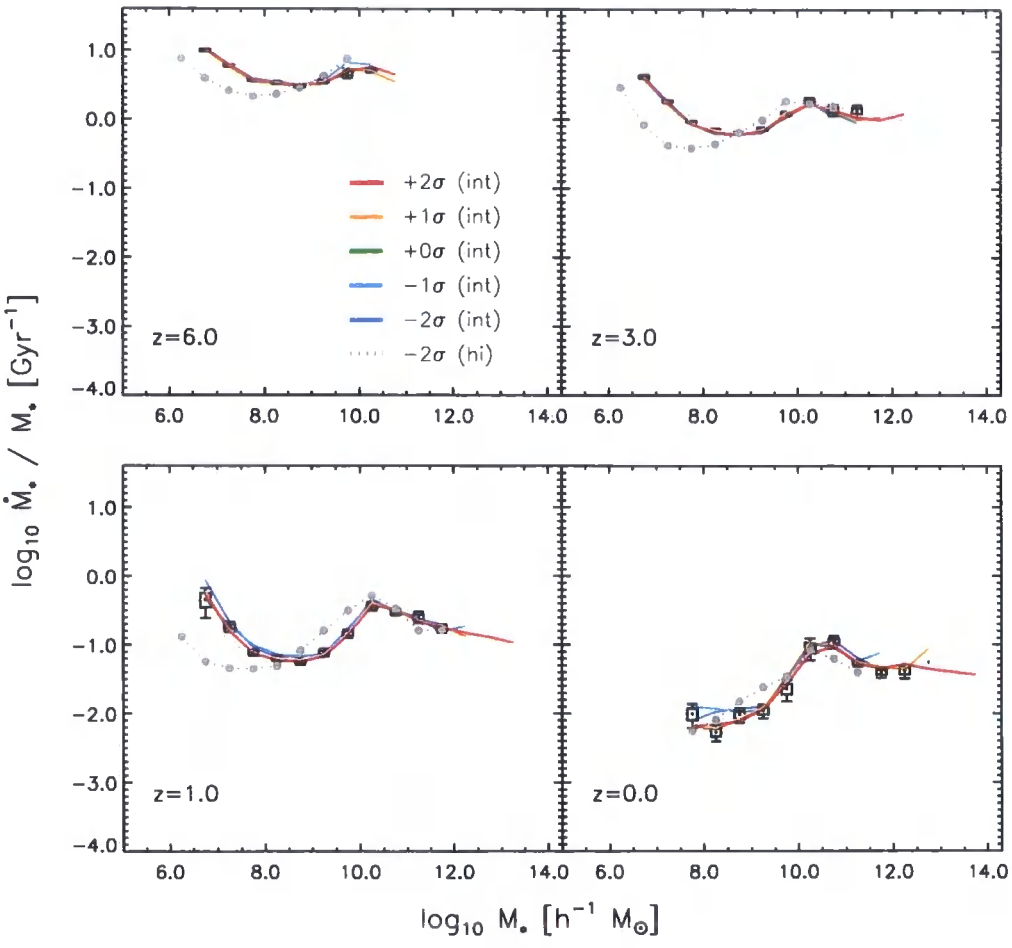

Figure 4.11: As per Figure 4.10, but here the SFR is normalised by, and plotted as a function of, stellar mass. As for Figure 4.10, no environmental signature is evident, but the normalised star formation rate is strongly sensitive to both stellar mass and redshift. The characteristic scale imposed by winds is now evident as a change in the gradient of the relation, indicating that the regulation of star formation becomes dominated by different mechanisms either side of this scale (i.e. feedback at lower masses, and the cooling time above it). Similarly to the sSFR-v_c relation, the difference between the intermediate- and high-resolution simulations is most evident for low mass objects that are not fully resolved in the intermediate-resolution simulations.

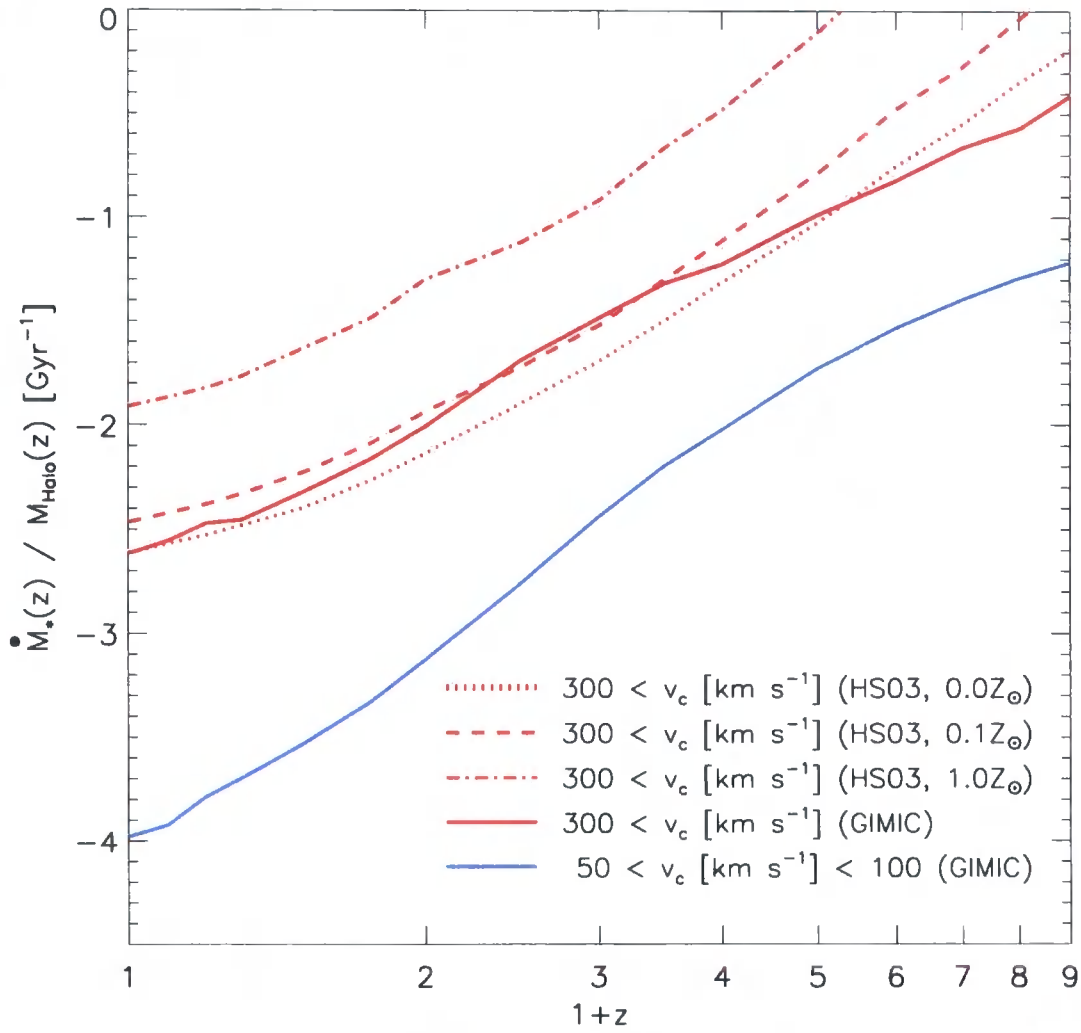

Figure 4.12: Specific star formation rate (sSFR; $\dot{M}_*/M_{200}$) as a function of redshift for massive haloes of circular velocity $v_c = 300$ km s^{-1} (*red*) and less massive haloes with $v_c = 50$ km s^{-1} (*blue*) for which galactic winds provide an effective feedback mechanism. The fall in sSFR for the more massive haloes follows the model of (Hernquist and Springel, 2003) (*dotted line*) in which star formation is limited by gas cooling: the lower density of haloes that form at lower z increases the cooling time and hence the star formation rate, but winds are never an effective feedback mechanism. In constrast, winds are very effective in the lower mass haloes and their sSFR drops considerably faster at late times.

for gas close to the virial temperature and mean density of galaxy/group haloes. The simple analytical prescription reproduces the sSFR of massive haloes very well, and is consistent with a weakly-evolving mean halo gas-phase metallicity of $0 < Z \lesssim 0.1\ Z_{\odot}$. We show in Chapter 5 that GIMIC predicts that hot-phase gas rapidly evolves to a mean enrichment of $Z \simeq 0.1\ Z_{\odot}$, and remains at this metallicity over the interval $9 \gtrsim z > 0$, just as required to explain the similarity of the analytic and simulated cooling times. The deviation at high-redshift reflects the very high cooling rate in dense haloes, such that it is the gas-consumption timescale (which follows from our star formation recipe, see Chapter 2 and Schaye and Dalla Vecchia (2008)) that regulates the star formation rate. Efficient feedback suppresses the normalisation of the sSFR for low-mass haloes far below the rate expected from cooling time arguments alone. The accelerated drop-off (relative to the trend for massive haloes) at $z \lesssim 3$ is due to feedback from galactic winds, which decrease the baryon fraction of small haloes very significantly.

The *shape* of the sSFR-v_c relation reflects the sensitivity of haloes of a given circular velocity or mass to the processes acting to regulate star formation. The imposed relation $P \propto \rho^{\gamma_{\rm EOS}}$ makes it unlikely that gas is compressed to very high densities where it would undergo vigorous star formation, whereas galactic winds quench star formation by removing gas from high-density regions. These winds also pollute the IGM with metals by powering a very dynamic cycling of baryons between galaxies and their surroundings, as we will discuss in more detail in the Chapter 5. The effect of winds is also reflected in the baryon fraction of haloes,

$$f_b \equiv \frac{M_{\rm b}/M_{200}}{\Omega_{\rm b}/\Omega_{\rm m}}, \tag{4.2}$$

which we plot in Figure 4.13. Massive haloes with circular velocity comparable to the launch speed of winds hold on to their baryons and have $f_b \sim 0.9$, as expected in the regime where non-gravitational processes are negligible (e.g. Eke et al., 1998a, Chapter 3). The baryon fraction drops to a minimum for haloes with $v_c \sim 100$ km s^{-1}, then rises again toward lower masses. Haloes with $v_c \sim 100$ km s^{-1} have virial temperature

$$T_{\rm vir} = \frac{1}{2}\frac{\mu m_{\rm p}}{k_{\rm B}} v_c^2 = 3.6 \times 10^5 \frac{\mu}{0.59} \left(\frac{v_c}{100 {\rm km\,s^{-1}}}\right)^2 {\rm K}, \tag{4.3}$$

for which cooling is very efficient (see Figure 5.1 in Chapter 5); the galactic winds that result from star formation are powerful enough to drive the gas out of the potential wells of these haloes, leaving them with low baryon fractions. The higher values of f_b,

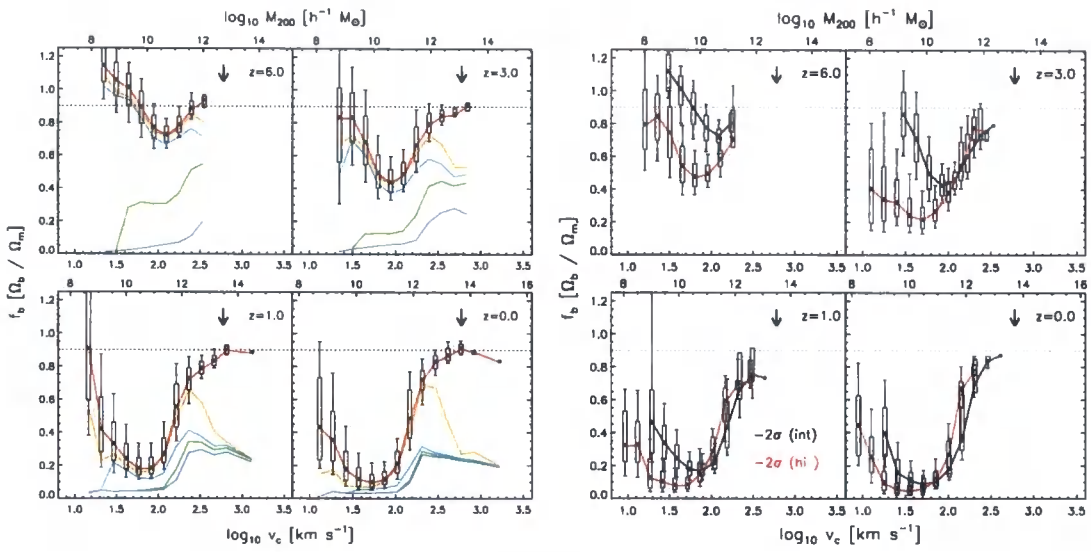

Figure 4.13: *Left*: the evolution of the baryon fraction of haloes drawn from all five GIMIC regions, normalised to the cosmic mean, as a function of circular velocity. At each redshift the equivalent halo mass, M_{200}, is shown on the upper axis. Box and whisker elements show the median and 10^{th},25^{th}, 75^{th} and 90^{th} percentiles of the total baryon fraction, and coloured curves decompose the total into the *cumulative* contribution of, in this order, stars (blue), equation of state gas (green), cold gas (cyan), warm gas (orange) and hot gas (red). Low-mass haloes exhibit a large scatter that is correlated with their stellar mass, since star formation induces winds that efficiently eject gas from their shallow potentials. In haloes with $v_{\rm c} \lesssim v_{\rm wind} = 600 {\rm km\,s^{-1}}$, winds steadily eject gas beyond the halo virial radius, with an efficiency that decreases with increasing $v_{\rm c}$. For $v_{\rm c} > v_{\rm wind}$, baryon fractions tend to ~ 90 per cent of the cosmic mean (horizontal dotted line), as expected in the regime where non-gravitational processes are negligible (e.g. Eke et al., 1998a, Chapter 3). Note that the break in the sSFR-$v_{\rm c}$ relation (Figure 4.10) approximately corresponds to the scale at which the fraction of halo baryons in the equation of state and cold phases peaks, $v_{\rm c} \simeq 250 {\rm km\,s^{-1}}$. *Right*: the total baryon fraction of haloes in the -2σ region at intermediate- (black) and high-resolution (red), thus showing the effect of resolution. Once again, the differences are largest in the systems that are poorly resolved in the intermediate-resolution simulation.

and the large scatter around the median, for the smallest resolved haloes is partly due to the less efficient cooling of their gas. The overall baryon fraction is decomposed into contributions from stars, gas upon which we impose a polytropic equation of state to mimic the ISM, cold gas, warm gas and hot gas. Cold and warm gas are delineated at $T = 10^5$ K, whilst warm and hot gas are delineated at $T = 10^{6.5}$ K. These temperatures, used extensively in Chapter 5 in reference to the IGM, are intended to illustrate the relative quantities of gas that may contribute to the WHIM, considered analogous to 'warm' phase gas in our model, and hot X-ray emitting gas, analogous to hot phase gas.

Whereas the total f_b is nearly independent of redshift for massive haloes, the fraction of that which is star forming gas drops dramatically from 40 per cent at $z = 6$ to an almost negligible fraction at $z = 0$, when ~ 75 per cent is in the form of hot gas. The very different cooling efficiency of this gas then goes a long way towards explaining the drop in star formation of such haloes over cosmic time, as discussed with reference to Figure 4.12 and the model of HS03. These massive haloes have high *stellar fractions* ($\sim$25 per cent), that are established as early as $z = 6$ and subsequently remain almost independent of redshift. AGN feedback, which might be necessary to quench star formation in those massive haloes at $z = 0$ might also reduce star formation at these much earlier times.

The overall baryon fraction of less massive haloes ($v_c \sim 100$ km s^{-1}) drops significantly with redshift by a factor ~ 2 between each of the shown redshifts $z = 6$, 3, 1 and 0. Their stellar fractions remain nearly constant with z at around 5 per cent, with the fraction of star forming gas decreasing very quickly even between $z = 6$ and $z = 3$. The lowest mass haloes initially have most of their baryons in the cold phase, which, as they lose typically more than half of their baryons, are either ejected or shocked into the warm or hot phases. These haloes are inefficient at forming stars, and the stellar fraction remains low at all times. Baryons are also subject to removal by other mechanisms such as the ram-pressure stripping of gas and the tidal stripping of stars.

How baryons are lost and cycled between phases is illustrated in more detail in Figure 4.14 for a low mass halo (left) and a massive halo (right). The cold phase is the major baryon reservoir in low mass haloes (left panel), and although most of that gas is lost from the galaxy due to winds, the fraction of gas in the cold phase remains similar at 50 per cent from $z = 6$ to $z = 0$. The stellar fraction is around 5 per cent of the cosmic mean baryon fraction at all z with no strong resolution dependence. Initially at $z \sim 6$

such haloes contain a considerable fraction of their gas in the star forming phase, but that fraction becomes nearly zero below $z = 2$. About 25 per cent of the baryons are in the warm phase at $z = 0$. The behaviour of the more massive halo (right panel) is quite different: equation of state gas dominates at high z, but is mostly converted into stars by $z = 2$, with the fractions of warm and hot gas combined reaching 60 per cent. The relative fractions are very similar for the two different resolutions. The net result is that $z \sim 0$ haloes in our model broadly fall into two categories: i) low-mass haloes with a very low baryon fraction dominated by stars and cold gas, and ii) more massive haloes that retain a significant fraction of their cosmic share of baryons, but are so massive that most of this is in the form of warm-hot phase gas that is not efficiently star-forming. The divide occurs for haloes with $v_c \sim 100$ km s^{-1}.

The stellar fractions of $f_\star \sim 25$ per cent for the most massive haloes ($\gtrsim 10^{12.5}\, h^{-1}\, \mathrm{M}_\odot$) in GIMIC are significantly higher than optical constraints at $z = 0$ (for a review see Balogh et al., 2001). Our wind model already uses approximately 80 per cent of the energy released by core-collapse supernovae within the Chabier IMF ($\epsilon_{\mathrm{SNII}} \simeq 1.8 \times 10^{49}$ erg $\mathrm{M}_\odot^{-1}$), and additional feedback energy is required to impose the equation of state of the star forming gas, $p \propto \rho_{\mathrm{EOS}}^{\gamma}$. An additional source of feedback, such as that derived from active galactic nuclei (AGN) may therefore be required. Benson et al. (2003) used semi-analytic models to estimate that at least 5×10^{49} erg $\mathrm{M}_\odot^{-1}$ is required to reconcile predictions of the bright end of the galaxy luminosity function with the data. AGN energy input is used in these models to suppress star formation in massive galaxies.

Whilst winds are less effective at arresting the star formation rate of massive haloes their effect remains significant. Our stellar fractions of $f_\star \sim 25$ per cent for massive haloes are significantly smaller than those obtained in the ART adaptive mesh refinement (AMR) simulations of Kravtsov et al. (2005), which did not include a treatment of kinetic feedback from winds. The SPH simulations of Ettori et al. (2006) yield a comparable if somewhat smaller value for $f_\star$, using the GADGET2 code of Springel and Hernquist (2003a) which includes a wind-based kinetic feedback treatment. Although their wind speed is lower ($v_{\mathrm{wind}} \simeq 340$ km s^{-1} as compared to our value of 600 km s^{-1}), they temporarily 'decouple' wind particles hydrodynamically making it easier for the gas to escape.

The loss of baryons in lower mass haloes causes their sSFR to drop much faster with

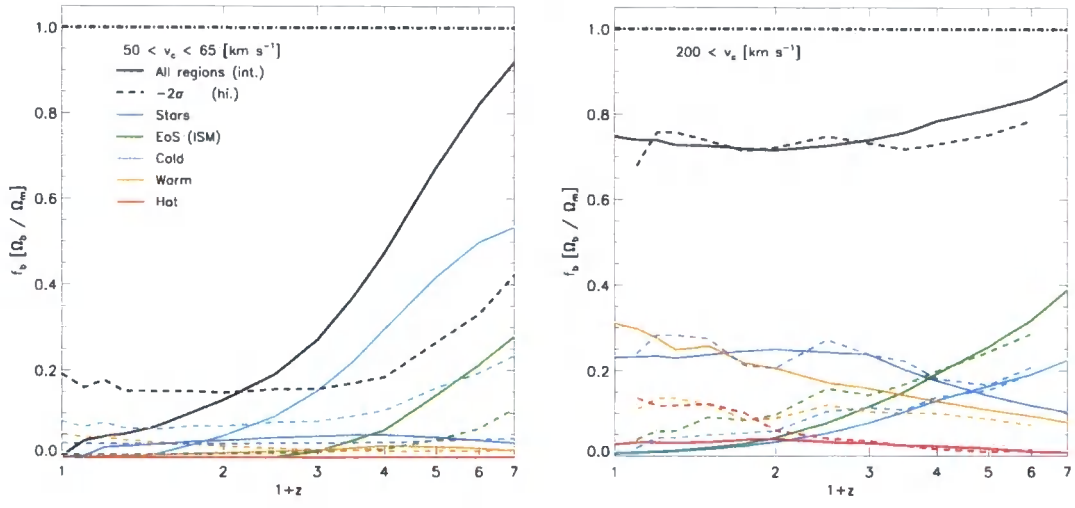

Figure 4.14: The time evolution of the total baryon fraction (black) and also the components of the baryon fraction, stars (blue), equation of state gas (green), cold gas (cyan), warm gas (orange) and hot gas (red). The fractions are normalised to the cosmic mean. The left-hand plot features 'small' haloes of $50 < v_c < 65$ km s^{-1}, the right-hand plot features larger haloes $v_c > 200$km s^1. Haloes are drawn from all regions at intermediate resolution (solid lines) and the -2σ region at high-resolution (dashed lines). The left-hand plot therefore highlights the evolution of haloes that are poorly resolved in the intermediate-resolution simulation, and so allows the origin of the differing baryon fractions to be elucidated. Significant differences are seen for low-mass haloes, with the baryon fraction of haloes in the intermediate-resolution simulations being higher at high-redshift, primarily due to a greater mass fraction of both equation of state gas and cold gas. These components rapidly deplete however, falling below the high-resolution simulation values by $z \sim 1 - 2$. The overall baryon fraction remains higher by $z = 0$ for the high-resolution haloes, as seen in Figure 4.13. The more massive haloes, in the right-hand plot, are well resolved by both the intermediate- and high-resolution runs, and exhibit remarkable similarity in their overall and individual component baryon fractions.

decreasing redshift than the sSFR of more massive haloes, in contrast to the simulations of SH03b. Massive haloes hold on to their baryons, and the sSFR of a halo with given v_c drops with redshift as the less dense gas cools less efficiently, as described in the model of HS03. Less massive haloes in contrast lose a significant fraction of their baryons due to winds, and their sSFR drops much faster. This explains the behaviour seen in Figure 4.12.

4.4.5 The multiplicity function of star formation

The notion of a 'distribution function of star formation' was introduced by HS03 and SH03b in order to describe to the cosmic star formation rate density of objects of a given mass as a function of redshift. Under the simplifying assumption that star formation occurs only in dark matter haloes, the star formation rate density may be expressed as

$$\dot{\rho}_\star(z) = \bar{\rho}_0 \int s(M,z) g(M,z)\, \mathrm{d}M, \tag{4.4}$$

where $\bar{\rho}_0 = 3\Omega_0 H_0^2/(8\pi G)$, $g(M,z)$ is the multiplicity function of dark matter haloes (as per Figure 4.3), and $s(M,z)$ is the specific star formation rate. SH03b and HS03 term the integrand,

$$S(M,z) = s(M,z) g(M,z) \tag{4.5}$$

the *multiplicity function of star formation*, a nomenclature we adopt here. A key motivation for the development of this factorisation was to facilitate a precise measurement of $s(M,z)$ from ensembles of gasdynamical simulations covering the relevant mass scales, which can be combined subsequently with analytic descriptions of the halo multiplicity function in order to reconstruct $\dot{\rho}_\star(z)$. In this fashion, the incomplete sampling of the high-mass end of the halo mass function by high-resolution periodic simulation volumes is circumvented. However, as discussed in our introduction, the unique initial conditions of the GIMIC simulations are specifically tailored to allow a wide range of environments to be simulated at high resolution and hence, as shown in Figure 4.3 and Figure 4.10 respectively, both $g(M,z)$ and $s(M,z)$ can be recovered with reasonable reliability.

Figure 4.15 shows the multiplicity of star formation, $S(M,z)$, from each intermediate-resolution GIMIC region as a shaded area. The star formation rate density of each region is hence proportional to the shaded area. The equivalent multiplicity function of FoF haloes, $g(M,z)$, is shown as a black histogram whose scale is shown on the right-hand

axis of each panel. As with Figure 4.3, the universal halo multiplicity function constructed by Reed et al. (2007) is also shown. As originally highlighted by SH03b, the history of $\dot{\rho}_\star(z)$ is shaped by the opposing action of the evolution of the functions $s(M,z)$ and $g(M,z)$. On one hand, advancing structure formation shifts an ever-increasing fraction of bound mass into more massive haloes, thereby pushing more and more gas above the efficiency thresholds imposed by our implementations of the photo-ionising background and feedback by galactic winds. Conversely, the amplitude of the sSFR-v_c is greatest at early times and drops steadily towards low-redshifts. The combination of these effects yields a broad plateau in $\dot{\rho}_\star$ at intermediate redshifts ($2 \lesssim z \lesssim 6$), from which it drops off towards lower and higher redshifts.

The multiplicity of star formation is also key to understanding the sensitivity of $\dot{\rho}_\star$ to large-scale environment. It is the differing forms of the halo multiplicity function, $g(M,z)$, that produce the large offset in the normalisation of the star formation rate between the GIMIC regions; Figure 4.15 clearly illustrates that a greater proportion of star formation occurs in more massive haloes within more overdense regions, and so it is the absence of massive, efficient star forming haloes from voids that so severely inhibits their overall star formation rate density.

4.4.6 Do haloes know about their local environment?

We have shown that the star formation rate-density in our simulations varies by an order of magnitude, across the extremes of the large-scale environments expected within the local Universe. We find that this is merely due to differences in the halo mass functions of these regions. As shown in Figure 4.10, any variation in the sSFR of haloes that is induced by large-scale environment - that is, on the scale of the GIMIC regions - is dwarfed by both the trend with halo mass, and the evolution of this trend with redshift.

It should be noted, however, that each GIMIC region hosts a wide range of smaller-scale overdensities that are roughly distributed as a Gaussian function; the probability density functions of overdensity for each region being slightly offset. It may be argued that the $18 - 25\ h^{-1}$ Mpc scale of the regions smoothes over potential effects that are induced by smaller-scale environmental extremes. To test this, we assign all dark matter haloes a 'small-scale' density, ρ_{ss}, by computing their local density with a top-hat smoothing filter of radius $1.25\ h^{-1}$ Mpc. The haloes from each region are then combined

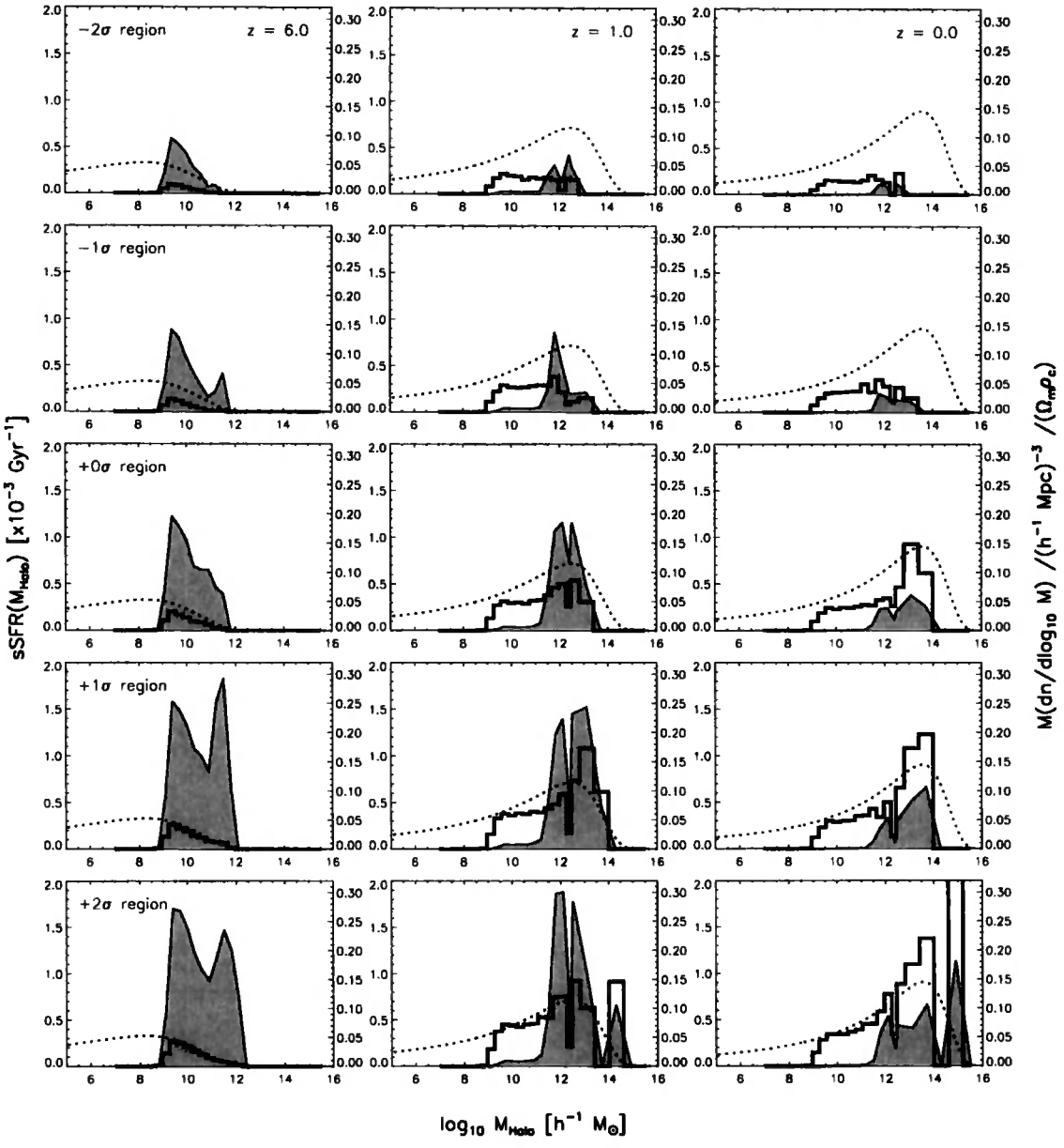

Figure 4.15: The multiplicity function of star formation (shaded) as a function of region (rows) and redshift (columns). We define this function as the product of the specific star formation rate of haloes and the fraction of bound mass in haloes, often referred to as the multiplicity function of haloes (see Figure 4.3), which is shown here as black histograms. Note that the vertical axis for these histograms is on the right-hand side of each plot. As per Figure 4.3, we overplot the Reed et al. (2007) multiplicity function for reference. The multiplicity of star formation succinctly explains the environmentally sensitive normalisation of $\dot{\rho}_\star$; lower-density environments not only feature fewer haloes, but they are particularly underabundant in massive haloes with high star formation efficiencies.

into a 'super-sample' and binned according to this new measure:

- Low density: $\rho_{ss} \leq \langle\rho\rangle$,
- Intermediate density: $\langle\rho\rangle < \rho_{ss} \leq 10\langle\rho\rangle$,
- High density: $\rho_{ss} > 10\langle\rho\rangle$.

The only significant correlation we find is a very small trend in halo baryon fractions, with haloes of any given mass less than $10^{12.5}\ h^{-1}\ M_\odot$ tending to retain a slightly greater baryon fraction if embedded in a higher density region. The scatter about the intermediate density trend at $z = 0$ is ~ 0.15 in units of the universal fraction, Ω_b/Ω_0. We find no such correlations for other baryonic properties of haloes, such as specific star formation rates and metallicities. We conclude, therefore, that even the local environment of a halo has little effect on its baryonic properties. However, this does not preclude the possibility of small-scale environment affecting the properties of galaxies; indeed, the structure of the halo itself is widely cited as the most likely source of localised environmental variation (e.g. Mo et al., 2004; Kauffmann et al., 2004; Blanton et al., 2006), and we intend to investigate effects on the galaxy population in a future study.

4.5 Summary

We have studied the role of cosmological environment upon the star formation rate density of the Universe using the *Galaxies-Intergalactic Medium Interaction Calculation*, a novel series of hydrodynamic simulations of the ΛCDM cosmogony. The unique nature of these initial conditions pushes the boundaries of present computational capability, allowing for the first time a large sample of galaxies to be numerically simulated at high-resolution, from the cosmological dark ages to the present epoch, within the range of cosmological environments expected to be present in the low-redshift Universe.

The main result of this chapter is the dependence of the star formation rate density, $\dot{\rho}_\star(z)$, on large-scale environment. The *shape* of this relation is largely independent of environment, and closely follows the form inferred from observations: a slow rise leading to a broad peak from $z = 4 - 1$, followed by a rapid drop to $z = 0$. The normalisation, however, varies by an order of magnitude between the most extreme environments, the -2σ and $+2\sigma$ regions. Since these environments correspond to the largest voids and

richest clusters that are expected within the local Universe, it follows that such variation in $\dot{\rho}_\star(z)$ should be considered as an additional systematic error in observational surveys that do not probe substantially greater volumes than probed in these simulations (see also Stringer et al., 2008). This result is likely to be robust to any reasonable changes in the implementation of physical processes within our model, since it is primarily driven by differences in the halo mass function of the regions. Void regions not only feature halo mass functions that are normalised lower than those of mean density regions, they are additionally underabundant in the more massive haloes whose specific star formation rates are more resilient to suppression by the feedback processes considered here.

Combining the five GIMIC regions, we construct an estimate of $\dot{\rho}_\star(z)$, effectively for the entire Millennium Simulation volume. This estimate yields a stellar mass density at $z = 0$ that concurs with observational estimates to within a factor of ~ 2. The excess star formation in our model, relative to the data, is a feature shared by other models of galaxy formation that do not include feedback from AGN. The estimated energy input from core collapse supernovae that Benson et al. (2003) estimate is required to reconcile the abundance of massive galaxies in simulations with the data is nearly a factor of three greater than that used in our model. Since we use ~ 80 per cent of the mechanical energy available from our choice of IMF, this energy input cannot be accomodated without recourse to other mechanisms. The relatively large stellar component of the baryon fraction of massive groups and clusters in these simulations, which violate optical constraints (e.g. Balogh et al., 2001), further hint at the requirement for additional energy input. Murray et al. (2005) propose that, in addition to the mechanical effect of SNe, winds can be driven by the radiation pressure generated by starbursts. The additional energy available in this form is potentially a factor of ~ 100 greater than the mechanical output of SNe, and has motivated galactic wind models that tap into this additional energy (e.g. Davé et al., 2006), but it remains unclear how this energy should be coupled to the gas. Clearly, detailed numerical studies of the role of radiative and AGN-driven feedback upon massive galaxies are a timely necessity.

Nonetheless, our feedback prescription yields a cosmic star formation history that concurs with the data at least as well as the popular semi-analytic model of Bower et al. (2006) which, incidentally, includes an implementation of AGN feedback. Before $z \sim 4$, star formation is dominated by low-mass haloes, with 'galaxy haloes' begin responsible

for the bulk of star formation below $z \sim 1.5$. Even though star formation builds-up in a hierarchical fashion, star formation is always dominated by small galaxies that have merged and reside within groups or clusters at the present epoch. Galactic winds are a crucial, and indeed effective, mechanism for quenching star formation to the observed levels in these smaller systems.

Since it is the halo mass function that largely drives the environmental sensitivity of $\dot{\rho}_\star(z)$, it follows that the specific star formation rate (sSFR) of haloes is *independent* of environment (Figure 4.10). However, we find that the sSFR is a strong function of both halo mass (or more directly, a proxy such the circular velocity or virial temperature) and redshift. This behaviour reflects the non-trivial interplay of the timescales for gas consumption and gas cooling, and of course feedback. For the most massive haloes, the simple analytic prescription for star formation regulation by gas cooling ($sSFR(z) \propto H^2(z)$) sketched by HS03 closely approximates the evolution seen in the simulations, but for low-mass haloes the efficiency of galactic winds as a means to offset cooling and eject bound gas renders simple cooling arguments invalid.

We have demonstrated that our numerical scheme achieves convergence for star formation rates for $z < 6$, but at earlier epochs the intermediate-resolution realisations fail to resolve most of the haloes that dominate star formation. In particular, reionisation of hydrogen globally suppresses star formation in the high-resolution realisations, but this feature is absent in their lower resolution counterparts, which do not form the low-mass haloes that lose their gas as the Universe is heated by the UV-background (Okamoto et al., 2008a). Since particle mass for the high-resolution realisations was chosen so that they would resolve all haloes that can cool due to atomic hydrogen cooling, it is unsurprising the realisations differ at early times. Note that our model does not follow Population III stars that form by H_2 cooling (e.g. Bromm and Larson, 2004). Having studied in detail the assembly of stellar mass in the GIMIC simulations, we now turn to the evolution of the IGM.

Chapter 5

The thermo- and chemodynamic evolution of cosmic baryons

5.1 Introduction

In Chapter 4 we demonstrated the striking impact of environment upon the star formation rate density. It is not unreasonable to presume that similar effects might be seen in the thermal and chemical properties of intergalactic gas, since heavy elements are synthesised in stars, and the feedback that accompanies stellar evolution (re)heats and redistributes cold gas and heavy elements from the ISM into the IGM. In this chapter we probe the evolution of the IGM in each of the GIMIC regions, tracking the mass of gas and heavy elements that evolves into particular thermal states. A key motivation for this study is a search for environmental variation in the mass and volume filling fraction of the WHIM; this phase is perhaps of the most pressing cosmological relevance since the *Cosmic Origins Spectrograph* is likely to start observing WHIM gas at low-redshift in the near future. We start this chapter with a review of the relevant physical processes that operate upon the IGM, and demonstrate the impact of these processes that follows from their implementation in GADGET3-BG.

5.2 Evolution of the gas

At the epoch of recombination, $z \sim 10^3$, the tight thermal coupling between photons and baryons ends. The gas temperature continues to track the photon temperature approximately, $T \approx T_{\rm CMB}$, due to the small remnant electron fraction left over after recombina-

tion until $z \sim 10^2$, but after this time it evolves adiabatically as $T \propto (1+z)^2$ (Giroux and Shapiro, 1996). Once structure formation commences, the stratification of the density field enhances adiabatic cooling at low densities whilst causing compressional heating at high densities. Sufficiently dense gas can cool radiatively, first[1] through H_2, and in more massive haloes through HI line cooling and thermal Bremsstrahlung (e.g. Black, 1981; Sutherland and Dopita, 1993; Katz et al., 1996). Efficient line-cooling in neutral hydrogen introduces a characteristic temperature plateau of $T \sim 10^4$ K at sufficiently high densities. The onset of reionisation reduces the HI cooling rate and changes the shape of this characteristic plateau; at low densities, photo-ionisation heating raises the minimum temperature to $\sim 10^4$ K, and the increased pressure evacuates gas from shallow dark matter potential wells (e.g. Doroshkevich et al., 1967; Couchman and Rees, 1986; Rees, 1986; Efstathiou, 1992; Thoul and Weinberg, 1996; Gnedin, 2000; Okamoto et al., 2008a, see also Figure 2.7). As structure formation proceeds, more gas cools inside dark matter potential wells, some being converted into stars or swallowed by black holes, whilst some gets shocked to such high temperatures that its cooling time becomes longer than the Hubble time. We shall discuss how these processes introduce characteristic regions in the temperature-density plane that depend on redshift, investigate the extent to which these are affected by feedback from galaxies, and determine how all this depends on the large-scale environment.

5.2.1 Thermal evolution

Gas at sufficiently low density and temperature (the 'diffuse intergalactic medium') is never strongly affected by radiative cooling. Therefore its thermal evolution is governed by adiabatic expansion cooling, reionisation, and photo-heating by the ultraviolet background. Before hydrogen reionises ($z_{\rm reion} = 9$ in the GIMIC simulations), the IGM cools adiabatically with the expansion of the Universe, except when shocked or compressed by other gas. This introduces a minimum temperature as a function of density, $T_{\rm min}(\rho) = T_0 (\rho/\langle\rho\rangle)^{\gamma-1}$ with $\gamma = 5/3$ and $T_0 \sim T_{\rm CMB}(z=100)[101/(1+z)]$.

During reionisation, neutral regions in the IGM are first overrun by an ionisation front, after which the now highly ionised gas continues to be photo-heated by the ambient ultraviolet background. We do not follow how radiation propagates from sources of

[1] We do not attempt to follow star formation through molecular hydrogen cooling in these simulations.

ultraviolet photons, but instead impose a redshift dependent but spatially uniform ultraviolet background with amplitude $J(\nu, z)$, as computed by Haardt and Madau (2001). This ultraviolet background is initially dominated by galaxies and later hardens as QSOs start to contribute. Once the IGM is highly ionised, each ionisation increases the thermal energy per ionised hydrogen atom by an amount that depends on the shape of the spectrum as

$$\epsilon = \int_{\nu_{\rm th}}^{\infty} \frac{J(\nu)}{h\nu} (h\nu - h\nu_{\rm th}) \sigma(\nu) d\nu \, / \int_{\nu_{\rm th}}^{\infty} \frac{J(\nu)}{h\nu} \sigma(\nu) d\nu. \quad (5.1)$$

Since the ionisation cross-section $\sigma(\nu)$ is sharply peaked around the threshold, $h\nu_{\rm th} = 13.6$ eV, this 'optically-thin' photo-heating is not very efficient, even when the ultraviolet background $J(\nu)$ is hard. In contrast during reionisation, *each* photon is able to ionise, hence the mean photo-ionisation energy ϵ is no longer weighted by the cross-section and is much higher,

$$\epsilon_{\rm reion} = \int_{\nu_{\rm th}}^{\infty} \frac{J(\nu)}{h\nu} (h\nu - h\nu_{\rm th}) d\nu \, / \int_{\nu_{\rm th}}^{\infty} \frac{J(\nu)}{h\nu} d\nu. \quad (5.2)$$

Radiative transfer effects will make the ionising spectrum seen by the average hydrogen atom harder than the source spectrum (Abel and Haehnelt, 1999). Modelling such hardening accurately, including the non-equilibrium effects during reionisation, requires detailed radiative transfer simulations. Here we approximate these by applying the optically thin photo-heating rate (Equation 5.1), but increasing the thermal energy per particle by a fixed amount $\epsilon_{\rm r} = 2$ eV/H $\sim 2.0 \times 10^{12}$ erg $\sim k_{\rm b} 10^4$ K during HI reionisation[2]. This value is much higher than $kT_{\rm min}$ before reionisation and therefore the IGM becomes nearly isothermal. After reionisation the temperature evolution is a balance between adiabatic expansion and photo-heating, which introduces a characteristic temperature-density relation $T(\rho, z) = T_0(z) (\rho/\langle\rho\rangle)^{(\gamma_{\rm IGM}-1)}$, where $\gamma_{\rm IGM} \sim 1$ close to reionisation, and $\gamma_{\rm IGM} \rightarrow 1.62$ asymptotically far from reionisation (Hui and Gnedin, 1997; Theuns et al., 1998). Gas below $T(\rho, z)$ gets heated quickly to $T(\rho, z)$ but shocked gas with $T > T(\rho, z)$ cools too slowly to rejoin the relation. This thermal evolution is illustrated in Figure 5.1.

The thermal evolution differs for gas at higher densities. Adiabatic compression and shocks heat dense gas as it accretes onto filaments and dark matter haloes, but efficient

[2]Harder source spectra imply higher $\epsilon_{\rm reion}$, but efficient inverse Compton cooling would bring the IGM temperature back to $\sim 10^4$ K. We introduce a similar increase in energy during HeII ionisation, in our simulations at $z = 3.5$.

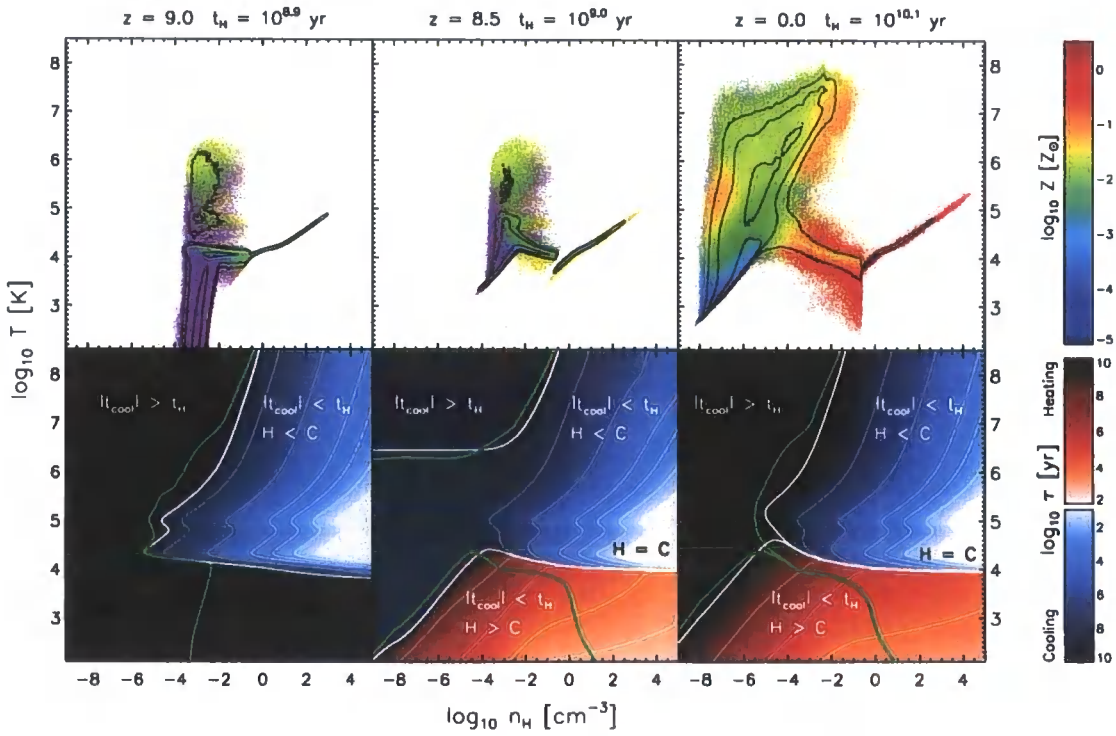

Figure 5.1: The temperature-density phase-space evolution of gas within the 0σ region, colour-coded by mass-weighted metallicity (*top row*), and the associated net radiative cooling time $t_{\rm cool} = u/\dot{u}$ (*bottom row*) at the epoch immediately preceeding hydrogen reionisation ($z = 9$), shortly after reionisation ($z = 8.5$) and the present epoch ($z = 0$). The mass distribution in the upper panels is shown as three contours enveloping the $10^{\rm th}$, $50^{\rm th}$ and $90^{\rm th}$ percentiles. In the lower panels, thin white contours and the colour scheme highlight the structure of the cooling time plane for gas of primordial composition. The thick white line delineates the plane into three regions, where i) cooling dominates ($\mathcal{C} > \mathcal{H}$), ii) heating dominates ($\mathcal{H} > \mathcal{C}$) and iii) where the timescales for both are longer than the Hubble time ($|t_{\rm cool}| > t_{\rm H}$). The thick green line is the equivalent for gas of solar composition. The occupancy of the $\rho - T$ plane by gas can be understood by considering the form the the radiative cooling time function and the mechanisms that induce shock-heating such as accretion and winds. A full explanation is provided in the text.

HI cooling before reionisation cools the gas to a plateau at $T \sim 10^4$ K. The suppression of cooling as hydrogen ionises (Efstathiou, 1992) changes the shape of this plateau, as does the enrichment of the gas as metals begin to contribute to cooling. The combination of these factors determines the shape of $T_{\rm min}(\rho)$ as a function of redshift at these higher densities. The effect of metals can be seen by the fact that higher metallicity gas has a lower $T(\rho, z)$ (Figure 5.1 , middle and right panels).

Radiative cooling and heating by the ultraviolet background change the thermal energy per unit mass, u, of gas at density ρ at a rate:

$$\rho \frac{du}{dt}|_{\rm rad} = (\mathcal{H} - C)\, n_{\rm H}^2\,, \tag{5.3}$$

where $n_{\rm H}$ denotes the number density of hydrogen. To recap the description of cooling given in Section 2.4.1, the normalized cooling rate C includes line-cooling from hydrogen, helium, and nine dominant species of 'metals' , in addition to Compton and thermal Bremsstrahlung, whereas the heating rate $\mathcal{H}$ is due to the imposed ultraviolet background as described by Haardt and Madau (2001). We define the net cooling time as

$$t_{\rm cool}(\rho, u) = -\frac{u}{\dot{u}} = \frac{3k_{\rm B}T}{2\mu} \frac{m_{\rm H}}{\rho(1-Y)^2(C-\mathcal{H})}, \tag{5.4}$$

where k_B is Boltzmann's constant, μ is the mean molecular weight, m_H is the proton mass and Y the fraction of helium by mass. Clearly, when $\mathcal{H} > C$ and $t_{\rm cool} < 0$ the gas heats rather than cools. Figure 5.1 (bottom panels) depicts the net cooling time as a function of redshift, with lines indicating where the net cooling time, $t_{\rm cool}(\rho, T)$, equals the Hubble time, $t_{\rm H}$ (white and green lines assume gas with primordial, and solar metallicity, respectively). Gas to the left of this line is essentially unaffected by heating or cooling. These lines divide the $\rho - T$ plane in two regions before reionisation; photo-heating after reionisation introduces a second line, where cooling balances heating, $C = \mathcal{H}$. The shape of these lines depends on redshift, as well as the metallicity of the gas.

The dependence of the cooling time on redshift, temperature and density is shown in Figure 5.1 (bottom panel), with blue and red shading when gas is cooling and heating on a timescale smaller than the Hubble time, respectively, and fading to black where $|t_{\rm cool}| > t_{\rm H}$. Before reionization (left panel), the thick white line where $t_{\rm cool} = t_{\rm H}$ has the shape of the cooling function $C(T)$ put on its side, with bumps due to line cooling by hydrogen and helium at $T \sim 10^4$ K and $T \sim 10^5$ K respectively, followed by the $T^{1/2}$

dependence of thermal Bremsstrahlung at higher T. The green curve representing solar metallicity gas has additional bumps due to a variety of elements at higher T as shown in detail by Wiersma et al. (2008), as well as metal cooling at $T < 10^4$ K. Thinner white lines highlight the contouring of the net cooling function in the $\rho - T$ plane; prior to the epoch of reionisation, their shapes do not vary with density. These curves appear very different after reionization (bottom-centre and bottom-right panels): cooling due to neutral hydrogen is strongly suppressed at low densities, $\rho \leq 10^{-2}$ cm^{-3}, and the region where gas does not cool breaks into two isolated islands due to efficient inverse Compton cooling in the now highly ionised gas. Low temperature ($T \lesssim 10^4$ K) gas is heated by the ultraviolet background, whereas for high temperature ($T \gtrsim 10^6$ K) and low density ($\rho \lesssim 10^{-2}$ cm^{-3}) gas the cooling time becomes longer than the Hubble time. The contouring of the net cooling time now markedly changes shape at high density, as the hydrogen becomes progressively more neutral and contributes to cooling. Heating introduces an extra line where cooling balances heating, $\mathcal{C} = \mathcal{H}$; at solar metallicity (green curve) increased metal cooling changes the shape of the equilibrium temperature significantly. Inverse Compton cooling becomes inefficient at low redshift, and the line where $t_{\rm cool} = t_{\rm H}$ runs diagonally over the $\rho - T$ plane. The presence of metals significantly decreases the equilibrium temperature where heating balances cooling.

The balance of heating and cooling as a function of temperature, density, metallicity and redshift, determine the distribution of gas in $\rho - T$ space, as plotted in the top panels of Figure 5.1. New to the current simulations is the very well defined $T(\rho)$ relation standing-out at high density, resulting from the imposed $P \propto \rho^{\gamma_{\rm EOS}}$ (with $\gamma_{\rm EOS} = 4/3$) pressure-density relation of star-forming gas in our 'quiescent stellar feedback' implementation (for more details see Chapter 2 and Schaye and Dalla Vecchia, 2008). The temperature associated with this gas has no direct physical significance since the relation represents the multi-phase interstellar medium. Some fraction of gas at these high-densities will be cold and molecular (the Giant Molecular Clouds that form stars), some warm and atomic (the gas in galactic disks), and finally some hot and ionised (gas heated by stellar feedback). The bend in $T(\rho)$ along the relation is due to the variation of the mean molecular weight, as the gas becomes neutral at higher ρ.

At z = 9 most gas falls into a pillar of shocked gas above the low CMB temperature, $T_{\rm CMB} \sim 27$ K. Efficient line cooling acts as a thermostat to restrict this gas to $T \sim 10^4$ K

in most haloes, yet there is some gas above this line, due to shocking in more massive haloes and also due to feedback from early star formation. Indeed, at higher densities stars form when gas moves onto the imposed equation of state track. A fraction of the gas in such star forming haloes is subjected to kinetic feedback, resulting in ejection from the protogalaxy and the formation of a population of hot enriched, low density gas. The colour coding according to metallicity shows that the hotter shocked gas arises predominantly through this feedback channel, having been cycled through a galaxy.

The middle panel at $z = 8.5$ looks very different from the pre-reionzation panel: photo-heating by the ultraviolet background has increased the temperature of all cold gas, imposing a relatively tight $T \propto \rho^{\gamma_{\rm IGM}-1}$ relation (Hui and Gnedin, 1997). As hydrogen is now mostly ionised, the thermostat at $T \sim 10^4$ K disappears and is replaced by the equilibrium $\mathcal{C} = \mathcal{H}$ track. Increased structure formation and feedback produces more shocked gas above this characteristic line. The panel at $z = 0$ has still more shocked gas, but the relatively tight $T \propto \rho^{\gamma_{\rm IGM}-1}$ relation of low-density IGM gas is still visible. Note also that the equilibrium track now extends to much higher density, and that metal rich gas lies at a lower temperature for given density along this track. Gas below this track gets efficiently photo-heated back onto the track. Above the track the cooling times are low, which explains the near absence of gas in between the cooling track and that of gas shocked to much higher temperature.

5.2.2 Characteristic regions in the temperature-density plane

It is instructive to split the temperature-density plane in different populations based on spatial location and/or temperature (Figure 5.2). In particular we distinguish gas inside FoF haloes - the 'halo medium' (HM) - from the remaining 'interhalo medium' (IHM). The FoF algorithm identifies gas above a density threshold of $\rho \approx 60\bar{\rho}$ (e.g. Lacey and Cole, 1994), therefore the HM/IHM populations are roughly segregated by a density cut. Structure formation increases the mass-fraction in the HM but its volume fraction is always small. A separate cut in temperature distinguishes cold (**C**, $T \leq 10^5$ K), warm (**W**, 10^5 K$< T \leq 10^{6.5}$ K) and hot gas (**H**, $T > 10^{6.5}$ K). Such cuts are commonly used in the literature (e.g. see also Cen and Ostriker, 1999c; Davé et al., 1999; Kay et al., 2000; Cen and Ostriker, 2006), and are useful since they roughly delineate:

1. atomic or molecular gas observed in absorption, the 21-cm hyperfine structure line,

or molecular lines (cold gas);

2. warm-hot gas that is difficult to detect in either absorption or emission owing to its relatively low density and high ionisation fraction;

3. the hot gas that may be detected due to its X-ray emission.

The presence of a significant mass of metals in the IHM especially in the warm and hot phases already demonstrates significant cycling of gas between HM and IHM due to stellar feedback between these different phases. In these simulations this is predominantly due to the action of galactic winds that drive plumes of enriched gas into the IHM surroundings, leaving low-density bubbles close to star forming halos. Since the winds preferentially penetrate lower density regions they tend to deposit metals in bubbles outside of the filaments that contain the haloes (Theuns et al., 2002). We discuss the enrichment of gas in further detail in Section 5.2.3, but note that the same enrichment of warm, diffuse IHM gas was produced in the mesh simulations of Cen and Ostriker (2006). The HM and IHM populations contain gas in all three thermal phases but with considerably different fractions of the gas in each. Both contain hot and warm-hot gas, with the HM typically at higher metallicity. However they differ significantly in the properties of their cold phase. The cold HM is mostly high metallicity gas either in thermal equilibrium, $\mathcal{H} = \mathcal{C}$, or star forming, $P \propto \rho^{\gamma_{\rm EOS}}$, and it closely traces star forming regions in the centres of dark matter haloes and substructures. As discussed earlier, the HM in this 'cold phase' mimicks the complex multi-phase structure of star forming gas, representing cold molecular, warm atomic, and hot ionised gas. The cold IHM is diffuse, with heating from the ultraviolet background balancing adiabatic cooling, $P \propto \rho^{\gamma_{\rm IGM}}$. The lowest-density cold IHM that follows the $P \propto \rho^{\gamma_{\rm IGM}}$ relation remains mostly pristine, and observationally forms the low-density tail of the Lyα forest.

The formation of these different phases is illustrated in Figure 5.3, which is made by weighting the individual GIMIC regions to obtain the evolution appropriate to the whole Millennium Simulation volume. Initially all gas starts in the form of cold, interhalo medium (C-IHM), and this remains the dominant baryon reservoir at all times. Structure formation, the ultraviolet background, cooling and stellar feedback lead to the appearance of the other phases and there is considerable cycling between them. The condensed phase of the C-HM in galaxies is the second most dominant baryon reservoir

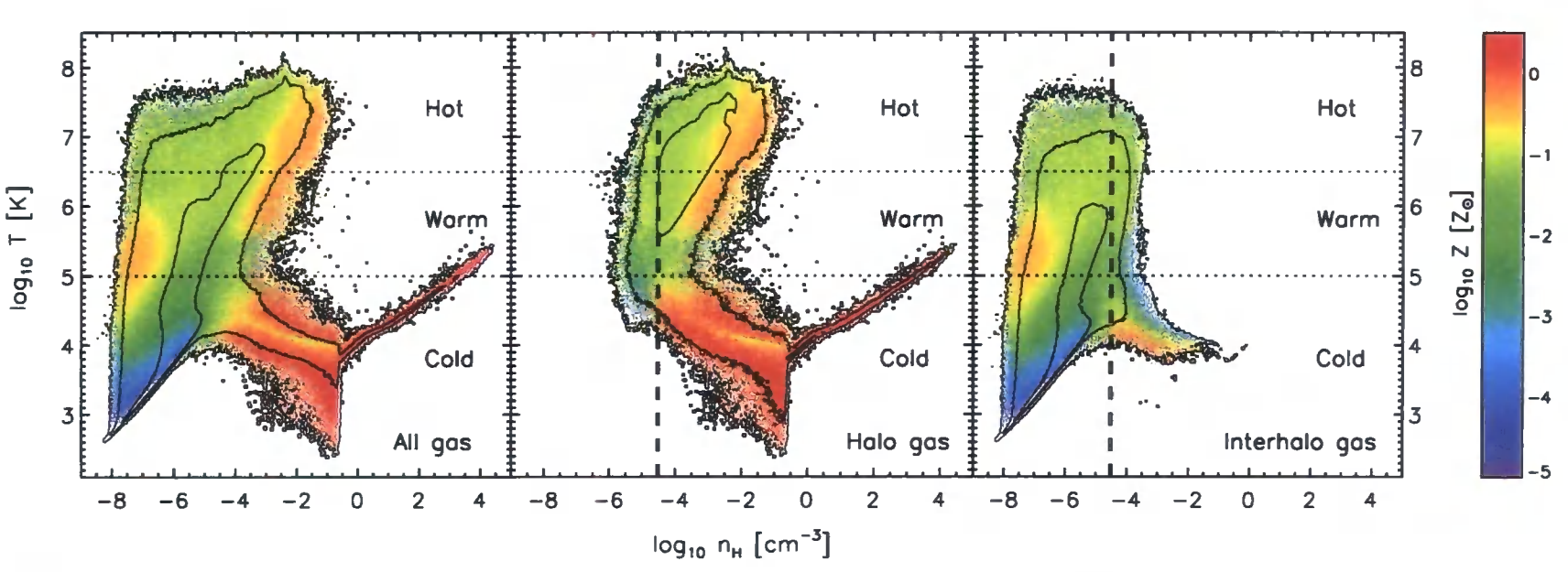

Figure 5.2: The $\rho - T$ diagram of gas drawn from the 0σ region at $z = 0$ (*left*), split into the halo medium (HM, *centre*) associated with FoF halos and interhalo medium (IHM; *right*) populations. Horizontal dotted lines delineate the thermal phases described in the text, whilst the vertical dashed lines in the central and right-hand panels show the approximate density threshold identified by our FoF algorithm. The diagrams are colour coded by mean mass-weighted metallicity, and the mass distribution is shown as three contours enveloping the 10^{th}, 50^{th} and 90^{th} percentiles. The HM gas is typically at higher metallicity, and follows a characteristic L-shape due to the short cooling time of gas at $\rho \sim 10^{-2}$ cm^{-3} and $T \sim 10^5$ K. The IHM consists of low-temperature nearly pristine gas, together with more enriched gas partly cycled through galaxies and expelled by winds. The IHM also contains some fraction of gas at surprisingly high densities: this gas is simply in the outskirts of 'resolved' haloes, or within groups of fewer than 20 particles.

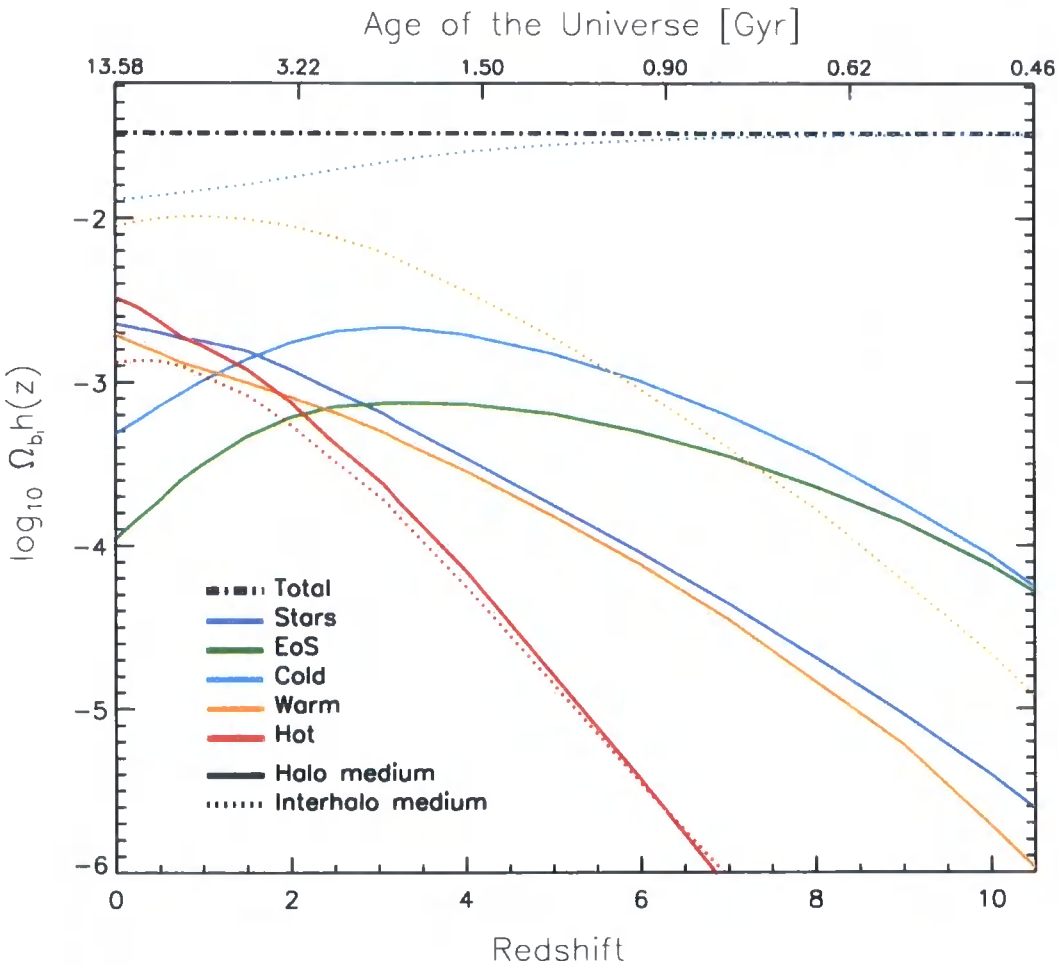

Figure 5.3: The mass fraction of baryons within the thermal phases of cosmic baryons, split into the contribution of the halo medium (HM; solid lines) or the interhalo medium (IHM; dotted lines). The curves represent a weighted average of the relative contributions to each phase from the five GIMIC regions. The phases sum to the cosmic baryon fraction, $\Omega_b/\Omega_0 = 0.045$, shown as a dot-dashed line.

up to $z \sim 4$, reaching a maximum mass-fraction of ≈ 10 per cent at $z \approx 4$, then declining to a few per cent at the present day. The build-up of the stars tracks that of the W-HM phase very closely, since warm gas is produced by thermodynamic shocks due to both (i) the accretion of gas onto haloes that, in the standard picture of galaxy formation, subsequently cools into star-forming gas (e.g Rees and Ostriker, 1977; White and Rees, 1978), and (ii) the impact upon the cold gas surrounding galaxies of material swept up by the galactic winds associated with bursts of star formation.

The fraction of hot HM rises much more rapidly, and at $z = 1$ halos contain almost equal amounts of baryons in stars, cold, warm-hot, and hot gas. A small fraction of stars is outside the virial radius of haloes due to tidal encounters. Most of the hot gas resides in large haloes as the intracluster medium, but since the distribution of gas in haloes is more extended than the underlying dark matter (e.g. Eke et al., 1998a, Chapter 3), a significant fraction of hot gas resides around the boundary of these haloes, as is clearly visible in the lower panel of the second column of Figure 5.4, which focusses on the thermal state of the cluster upon which the $+2\sigma$ region is centered. Therefore it is not surprising that the mass in this hot IHM tracks the hot HM closely. It is interesting to note that our mass fractions concur qualitatively with the low-resolution mesh simulations of Cen and Ostriker (2006), whose model for the thermal (and chemical) evolution of intergalactic gas predicts that warm-phase gas accounts for ~ 50 per cent by mass at $z = 0$, and hot gas accounts for ~ 10 per cent. Since their choice of the temperature delineating warm and hot gas is higher than ours ($T = 10^7$ K rather than $T = 10^{6.5}$ K), a consistent definition of the phases would bring the simulations into closer agreement. However, we reiterate the point we made in Section 1.3.2 that the spatial resolution of the Cen and Ostriker simulations is only $\sim 80\ h^{-1}$ kpc, a scale much larger than that of the galaxies; the treatment of both galactic winds, and also the transport of metals from galaxies into the IGM, is far from resolved and highly likely to be far from numerically converged in their models. This lack of resolution is a key motivation for the GIMIC simulations.

Interestingly, the evolution of the mass of the thermal fractions depends on the large-scale density and varies markedly between the different GIMIC regions, both for mass-weighted and volume weighted fractions. In particular, we highlight the strong environmental dependence of both fractions for the warm phase (i.e. W-HM and W-IHM)

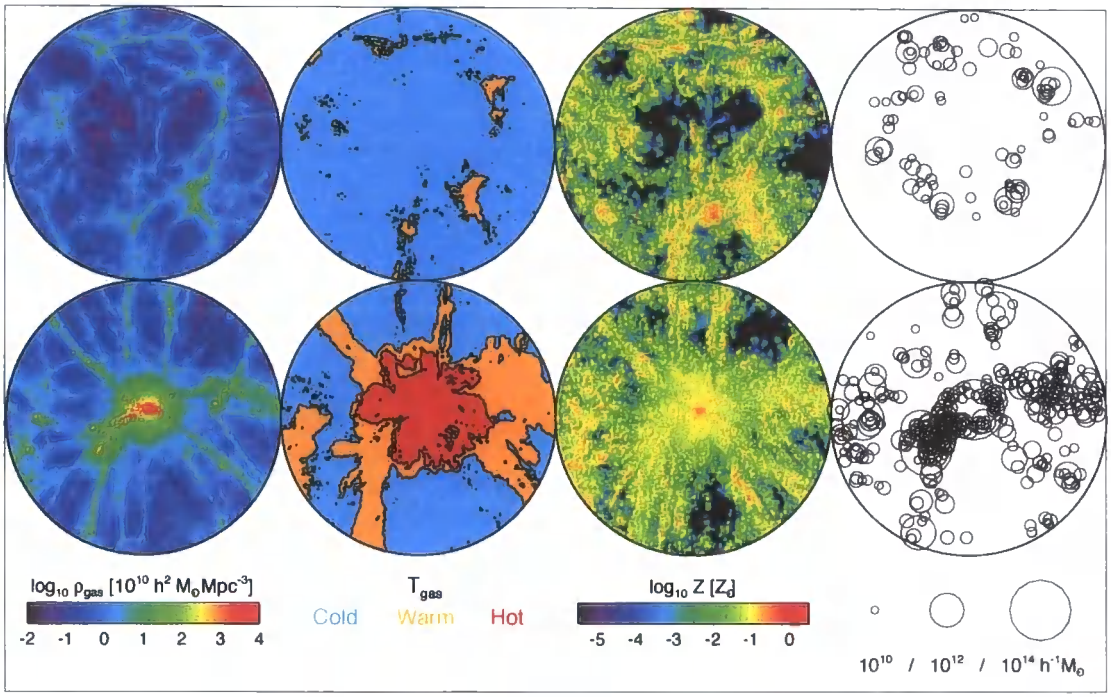

Figure 5.4: The association between the cosmic density (first column), temperature (second column) and metallicity fields (third column), and the distribution of self-bound dark matter haloes (fourth column). Each image is a projection over the central 1 h^{-1} Mpc of the region, and the SPH variables used to produce the first three columns are smoothed on a $\sim 70\ h^{-1}$ kpc scale. The most contrasting regions are shown, the -2σ (upper row) and $+2\sigma$ (lower row), to highlight the effect of environment on each quantity. The radii of the fields is 18 h^{-1} Mpc in all cases. The density and metallicity maps are shown scaled in log-space, whilst the temperature maps are binned according to the cold (cyan), warm (orange) and hot (red) phases defined in Section 5.2.2. The halo distribution shows all self-bound haloes of mass greater than $10^{10}\ h^{-1}\ M_{\odot}$, depicted by circles whose radii scale logarithmically with mass - note however that the symbols do not depict virial radii. The latter panels serve to highlight the strong differences in the halo mass functions (Figure 4.3) of these contrasting regions. The temperature distribution closely traces the large-scale structure, with hot gas confined to the largest haloes and the WHIM tracing filaments, with the intervening space suffused with cold, photo-ionised gas. Whilst the production of warm-hot gas is dominated by gravitational shocks in large-scale structures, metal synthesis is, by contrast, confined to galaxies. The distribution of metals is noisier than that of temperatures. This effect is also partly due to our chemodynamical treatment, since metals are carried by SPH particles and do not exhibit diffusion.

within each region, in Figure 5.5. We compute volume fractions by assigning mass-weighted temperatures of SPH gas particles to a 3-dimensional mesh of uniform resolution $\sim 70\ h^{-1}$ kpc using the SPH kernel and smoothing length. Cells are assigned to a given phase based on their mean temperatures. Whilst the volume occupied by gas associated with haloes is negligible when compared to the IHM, the mass of gas associated with haloes is of course significant. Therefore we split mass fraction of the WHIM into the separate halo (W-HM) and interhalo (W-IHM) contributions.

The W-IHM mass fraction in all regions rises slowly, peaks around $z = 1.5$, then declines gradually, and is a mostly monotonic function of large-scale overdensity. Its peak abundance is ≈ 35 per cent in all mean density and overdense GIMIC regions, significantly higher than the ≈ 28 and ≈ 22 per cent in -1σ and -2σ regions respectively. Interestingly, because of this skewing, the weighted-mean value of the W-IHM appropriate to the whole Millennium Simulation volume falls significantly below the mean density 0σ region. Mass-fractions in the $0\sigma, +1\sigma$ and $+2\sigma$ regions are very similar below $z \sim 1$, with a *smaller* value for the more overdense regions below $z = 1$. This is because, in the more overdense regions, a large fraction of gas gets shocked into the hot, X-ray emitting phase thus saturating the WHIM mass fraction. Whereas the mass fraction of W-IHM declines towards $z = 0$, the W-HM mass fraction increases steadily towards lower redshifts. Nevertheless, our model predicts that the mass of W-IHM is at least a factor of $\sim 2 - 3$ greater that of the W-HM at $z = 0$.

The comoving volume filling fraction occupied by warm gas (we consider W-HM and W-IHM as a single phase in this case) behaves in a simpler fashion, being a clearer monotonic function of large-scale overdensity, with the most contrasting regions offset by a factor of two and the average over the five regions closely tracing the 0σ trend. The filling fraction increases steadily over time, peaking at $z = 1.5 - 2$, at which time we estimate that, globally, the WHIM occupies ~ 22 per cent of the volume of the cosmos, before, in common with the WHIM mass fraction, decreasing towards the present day. The dependence of the various phases on environment is therefore quite striking, as illustrated in Figure 5.4, which contrasts the -2σ and $+2\sigma$ regions (the panels show the same volume for each). Both the haloes and the filaments in the denser $+2\sigma$ regions have significantly deeper potential wells than those in the -2σ region, which explains why there is so much more hot and warm-hot gas in the denser regions, as compared to

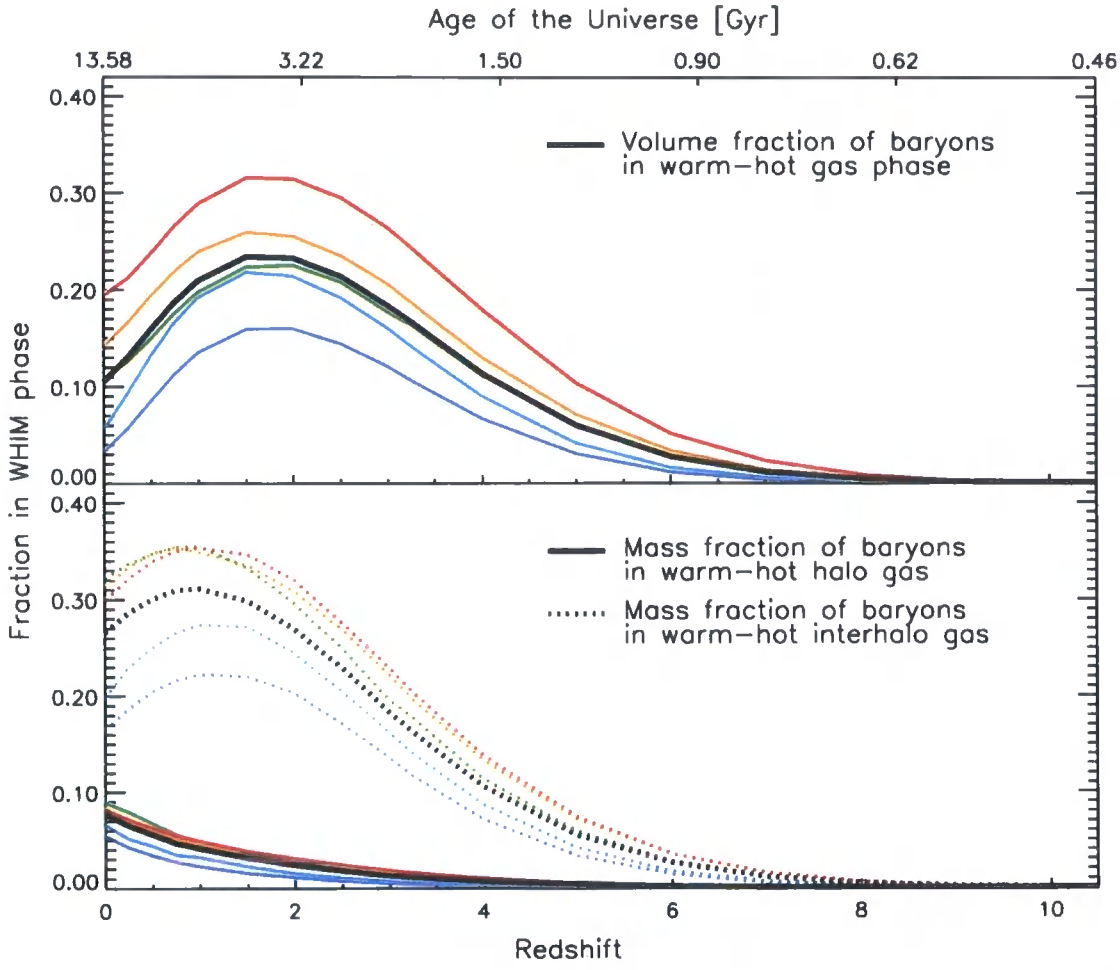

Figure 5.5: The evolution of the volume filling fraction (*top*) and baryon mass fraction (*bottom*) of the WHIM. In the latter case, the contribution from the interhalo medium (W-IHM; *dotted lines*) and haloes (W-HM; *solid lines*) are considered. The black lines in each case show the Millennium Simulation volume estimate derived from a weighted average of the GIMIC regions, whilst the coloured lines correspond to the different regions: -2σ (blue), -1σ (cyan), 0σ (green), $+1\sigma$ (orange), $+2\sigma$ (red).

in voids. A comparison of the temperature fields of the two regions illustrates a striking environmental variation in the volume filling factor of the WHIM; since the filaments surrounding massive haloes are more massive and extended than those surrounding low mass haloes, the mass and volume of gas in the WHIM is commensurately greater. In addition, as shown by Figure 4.3, the normalisation of the halo mass function is higher in overdense regions, and hence these regions host a greater number density of haloes with warm coronae. Similarly, the volume filling fraction of enriched gas is clearly greater in the $+2\sigma$ region, since it hosts many more efficiently star-forming, and therefore metal synthesising, dark matter haloes.

The decline in both the mass fraction and comoving filling fraction of the WHIM over the redshift interval $0 < z \lesssim 1$ warrants further inspection, and motivates the question *where does the WHIM come from, and where does it go?* Since both quantities peak at $z \sim 1.5$ we identify all WHIM particles within the 0σ region at this epoch, and trace their spatial, thermo- and chemodynamical properties both backwards and forwards in time, to $z = 4$ and $z = 0$. In Figure 5.6 we plot a projection of the spatial coordinates of these particles at each epoch, colour coded by their temperature phase at that time: cold (cyan), warm (orange), hot (red), within an 18 h^{-1} Mpc aperture. Beneath each spatial plot we show the temperature-density diagram for these particles, with colour coding illustrating the metallicity of the particles and contours showing their mass distribution. By definition, all particles at $z = 1.5$ are coloured orange in the spatial plot, and occupy only the temperature range $10^5 < T[\mathrm{K}] \leq 10^{6.5}$. The spatial plots highlight the nature of the sources and sinks of the WHIM; at high redshift the selected gas traces a similar comoving volume, but much of it (~ 74 per cent) is too cold to contribute to the WHIM. A small fraction (< 1 per cent) has been shock heated into the hot phase and will cool by $z = 1.5$. The upper right panel, showing the spatial distribution of the selected gas at $z = 0$, clearly shows a decrease in the comoving volume occupied by the WHIM, relative to $z = 1.5$. A significant fraction has accreted onto collapsed haloes, leading to either strong shock heating into the hot phase or rapid radiative cooling into star forming gas. Both populations are clearly visible in the right-hand temperature-density diagram. The filling fraction of the gas remaining in the warm phase also decreases because the filamentary structures with which the gas is associated also collapse under their self-gravity. Finally, as the $z = 0$ spatial plot shows, some warm gas becomes diffuse and cools into

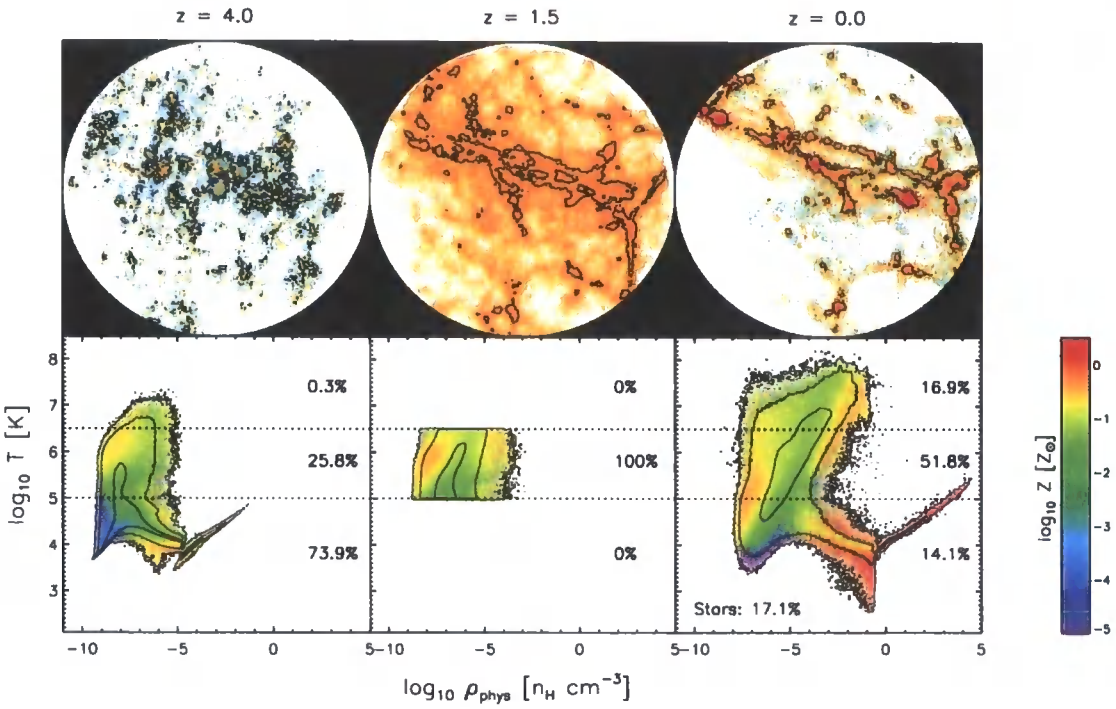

Figure 5.6: The distribution and thermodynamic state, at $z = (4, 1.5, 0)$, of the gas comprising the WHIM at its peak volume filling redshift of $z = 1.5$. The top row shows the spatial distribution of this gas projected over the entire 18 h^{-1} Mpc sphere (see Section 4.2.2), colour-coded by temperature binned into cold (*cyan*), warm (*orange*) and hot (*red*). Overplotted contours show particularly concentrated regions, corresponding to the upper 10 per cent of the mass-per-pixel distribution. The bottom row shows the distribution in temperature-density phase-space, colour-coded by mass-weighted metallicity with contours illustrating the mass distribution. The mass fraction of gas in each thermodynamic phase is also shown. The gas comprising the WHIM at $z = 1.5$ had a diverse past, with ~ 74 per cent sourced from colder gas, either due to accretion from the low-density IGM, or the ejection of galactic gas by winds. With approximately half of the mass of the WHIM baryons at $z = 1.5$ not residing in the WHIM at $z = 0$, the thermodynamic future of the $z = 1.5$ WHIM is similarly diverse: ~ 17 per cent is shocked to very high temperatures, and ~ 14 per cent cooling either into galaxies or back into the diffuse IGM. A greater mass fraction, ~ 17 per cent, of the $z = 1.5$ WHIM becomes locked up in stars by $z = 0$.

the cold IHM. This cooling occurs due to both radiative cooling - much of the gas is significantly enriched - and adiabatic cooling due to the Hubble expansion.

The diverse phase-space history of the gas particles comprising the WHIM at $z = 1.5$ suggests that the WHIM is far from being a thermodynamically static baryon reservoir, but rather is subject to continuous depletion and replenishment. Figure 5.7 demonstrates that this is indeed the case. In this plot we select all warm phase particles at each of the redshifts $z = [9, 6, 3, 1.5, 0]$, as shown along the diagonal marked with red boxes, and for each sample show their distribution in the temperature-density plane at the same redshifts. In each panel we display two percentages: the upper value shows the fraction of the sample, by mass, that is currently in the warm phase; by definition this is 100 per cent along the diagonal marked by red boxes. The lower value shows the mass fraction that has been converted into stars; by definition this cannot be non-zero for the selection epoch, denoted by the red box, or earlier times. We find that the thermodynamic history of warm gas selected at any epoch is qualitatively similar: the WHIM is sourced from both hot gas that has radiatively cooled and cold gas that has shock heated via accretion or kinetic feedback, and is depleted by shock heating into the hot phase, and/or radiatively cooling into the cold phase. The WHIM is clearly then a dynamic baryon reservoir that is continually processed. By tracking the maximum temperature that particles attain during the simulation, we find that by $z = 0$ the globally averaged fraction of baryons that have been processed through the WHIM is $\sim 0.6\Omega_b$, and varies from $0.4\Omega_b$ in the -2σ region to $0.75\Omega_b$ in the $+2\sigma$ region. Our average value is similar to the value of $0.5\Omega_b$ reported by Oppenheimer and Davé (2007).

5.2.3 Chemical enrichment

The abundance and distribution of metals is a fossil record of the cosmic history of star formation and feedback, since the heavy elements are synthesised in stars and are distributed by winds from stars and supernovae. However, the evolution of metal abundances remains poorly understood. Contrary to naïve expectation, the high redshift ($z \gtrsim 6$) IGM already exhibits significant enrichment (e.g. Barth et al., 2003; Becker et al., 2006; Ryan-Weber et al., 2006; Simcoe, 2006), whilst at intermediate redshifts ($z \sim 2 - 3$) significant enrichment variations exist, with damped Lyα absorbers (DLAs) exhibiting metal fractions between 0.01 and 0.5 times the solar metal fraction (Prochaska and Wolfe,

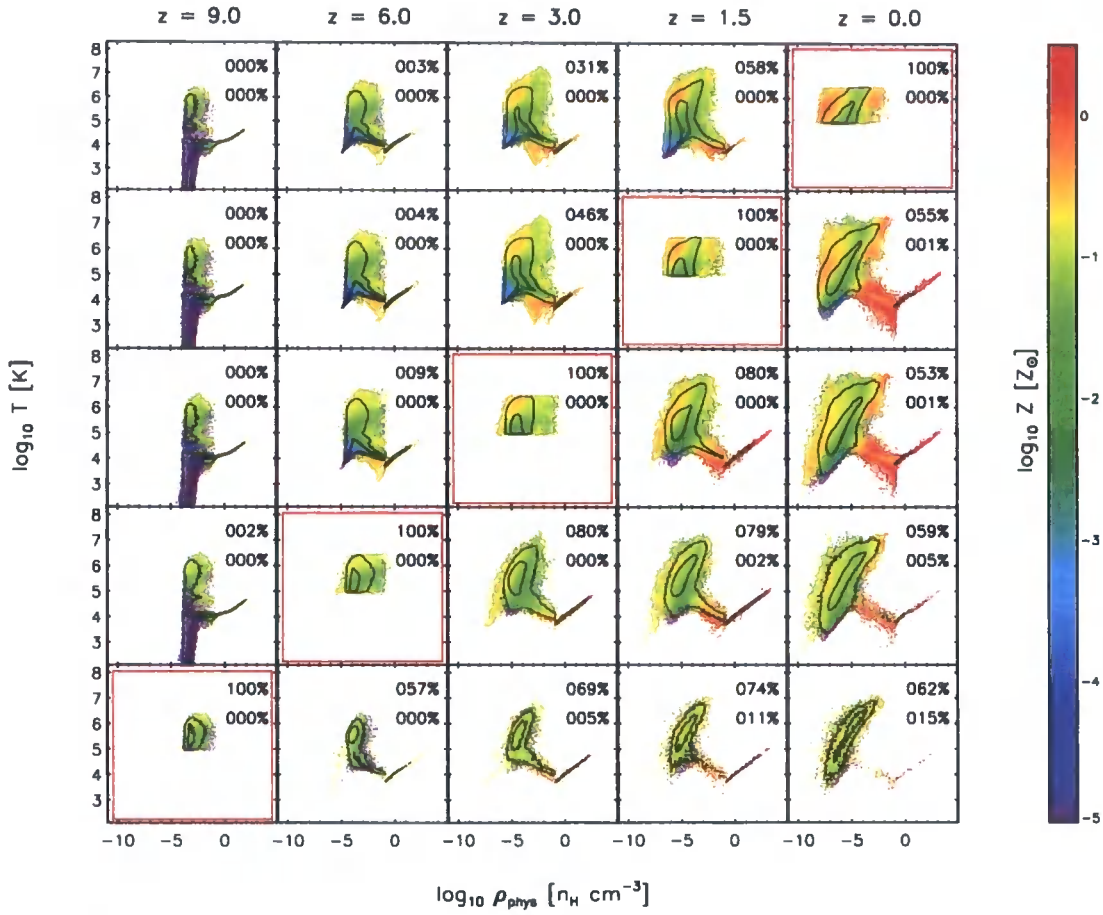

Figure 5.7: The 'life story' of WHIM gas, over the last thirteen gigayears. We adopt the simple definition that any SPH particle with $10^5 < T < 10^{6.5}$ K is considered to be WHIM, and in each row chart the thermodynamic and enrichment history of the gas comprising the WHIM at the epoch denoted by a red square. Panels are colour-coded by the mass-weighted gas metallicity, and the mass distribution is shown with contours. Each panel features two values; the upper is the mass fraction of the selected gas that resides in the WHIM at the given corresponding epoch, and so by definition must be 100 per cent along the diagonal marked by red boxes. The lower value shows the mass fraction that has converted into stars, and can only be non-zero to the right of the diagonal. The plot demonstrates that the WHIM is far from being a static baryon reservoir, but is in fact highly dynamic and subject to continuous depletion and replenishment. The life story of WHIM identified at any given epoch is remarkably similar.

1997). At these intermediate redshifts, the total observed metal mass within Lyman-break galaxies also falls far short of that extrapolated from the combination of observations of the star formation history of the Universe with expected metal yields (e.g. Pettini, 1999; Pagel, 2002). Barring a considerable error in our understanding of heavy element synthesis in stars, or the nature of the IMF at early times, this discrepancy hints that the metals are either hidden in an unobservable form, or reside outside of galaxies, a possibility that has attracted considerable theoretical interest (e.g. Cen and Ostriker, 1999a; Theuns et al., 2002; Ferrara et al., 2005; Oppenheimer and Davé, 2006; Davé and Oppenheimer, 2007; Sommer-Larsen and Fynbo, 2008).

Where are the metals?

In analogous fashion to the evolutionary baryon census presented in Section 5.2.2, in Figure 5.8 we trace the distribution of metal mass density amongst baryon phases, for a weighted average of the five GIMIC regions. We find that the equation of state gas in haloes - a population designed to mimic the interstellar medium - is the primary metal repository until $z = 2.5$, at which point stars become dominant, and by $z = 0$ we find that ~ 75 per cent of heavy elements are locked up in stars, producing a stellar metal mass density of $\Omega_{Z,\star}h \simeq 1.6 \times 10^{-4}$. As stellar evolution modelling remains relatively ill constrained, this value is consistent with observations of the present day stellar metal mass density, which yield $\Omega_{Z,\star}h \simeq 7 \times 10^{-5}$ (Edmunds and Phillipps, 1997; Pagel, 2002).

Much as the fraction of baryons residing in the warm phase peaks at $z \sim 1$, (Figure 5.3), the simulation shows that the fraction of metals associated with the WHIM rises to a peak, at $z \sim 4 - 5$, before declining to ~ 10 per cent by the present day (Figure 5.8). An offset between the redshifts at which the WHIM baryon and metal fractions peak occurs because the decline in the latter does not arise solely due to the former: at low redshift dark matter haloes become increasingly efficient at retaining enriched stellar ejecta, due to their growing potentials and the decrease in gas cooling timescales induced by heavy element enrichment. This increase catalyses the rapid shift in the metal distribution to stars at $z \lesssim 2$. Nonetheless, the simulations show that warm gas is an important metal repository at all observable epochs, containing $\simeq 30$ per cent of metals at $z = 4$ and declining steadily to $\simeq 10$ per cent at low redshift.

We note that our metal distribution differs slightly from that found by Davé and

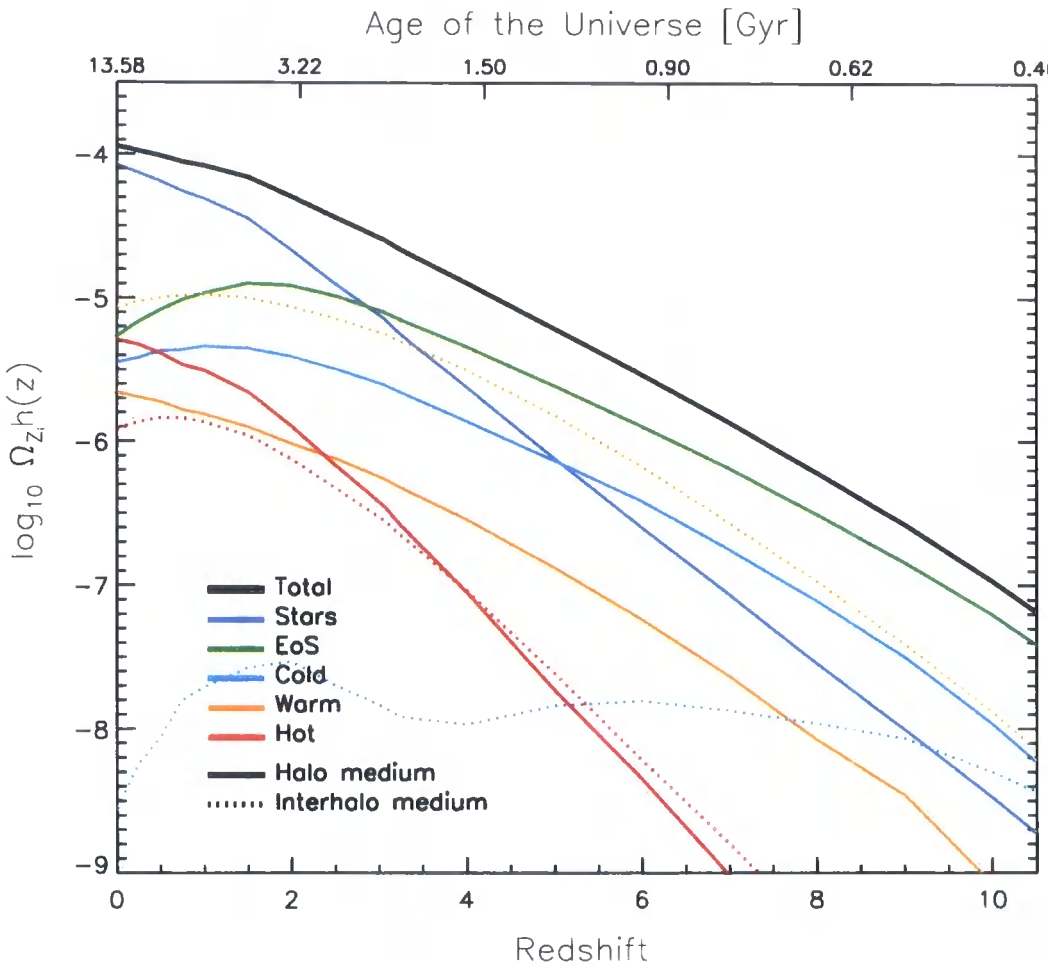

Figure 5.8: The density parameter of metals within each thermal phase, split by whether they are associated with halo gas (*solid lines*) or the interhalo medium (*dotted lines*), as a function of redshift. The solid black line denotes the evolving total metal mass density. At $z = 0$ the simulations produce a total metal mass density of $\Omega_Z h = 1.1 \times 10^{-4}$ and therefore we estimate a mean mass-weighted metallicity of the Millennium Simulation volume of 0.27 $Z_\odot$. At high redshift the metals are found preferentially in the cold, virialised gas that fuels galaxy formation and is likely to be observable via damped Lyα absorption. For $z \lesssim 3$, stars are the dominant metal repository, and by $z = 0$ they host 75 per cent by mass of the heavy elements, with 3 per cent residing in cold virialised gas. By the present epoch, the ejection of enriched gas via galactic winds deposits the remaining metals into the WHIM and the ICM.

Oppenheimer (2007), who found that metals resided preferentially in the diffuse IGM at early times, and that the stellar metal fraction at low-redshift was significantly lower than here, at ~ 43 per cent. These differences are likely to be a reflection of a key difference in the implementation of kinetic feedback between the simulations: whilst wind particles in our code are treated as regular SPH particles with an additional velocity kick, Davé and Oppenheimer (2007) temporarily decouple wind particles from hydrodynamic forces in order to assist the transport of enriched gas from the dense environments of galaxies into their surroundings. Dalla Vecchia and Schaye (2008) have demonstrated within idealised simulations the strong influence of ram pressure effects induced by this coupling on the structure and morphology of galactic discs and outflows, and so differences in enrichment patterns are to be expected.

Figure 5.9 shows the globally averaged metallicity of each baryon phase. The mean mass-weighted metallicity of the cosmos evolves steadily with redshift; at the redshifts important for the missing metals problem, the mean value increases from ~5 to 10 per cent of solar from $z = 3$ to $z = 2$, reaching $\sim 0.3 Z_\odot$ at $z = 0$. We find that winds enrich both warm-hot and hot gas at very early times ($z \sim 10$) to $Z \sim 0.1\ Z_\odot$, and then maintain these phases at this level of enrichment for all future epochs. This suggests that the synthesis of metals and the production of heated gas are tightly coupled processes. The enrichment level of $0.1\ Z_\odot$ in the warm gas tallies with the observations of Danforth et al. (2006) who find similar values in the WHIM. Having simulated several massive groups and a very massive cluster amongst the GIMIC regions we are able to address the question raised by Renzini (1998) of how closely the metallicity of galaxy clusters traces the global mean metallicity of the Universe. As shown by Figure 5.9, our simulations yield significantly differing enrichment histories for the hot halo gas that we associate with the ICM, and the Universe as a whole. The best tracer of the global mean metallicity, at $z \lesssim 3$ at least, is in fact the cold gas within haloes, which closely follows the Universal trend except at ~ 0.5 dex greater enrichment.

Environmental diversity in the metals?

Since heavy element abundances reflect the star formation history of the cosmos, it is clear from the star formation rate densities of the regions (Figure 4.4) that their overall metal mass and enrichment must differ. We find that by $z = 0$ the overall metal mass

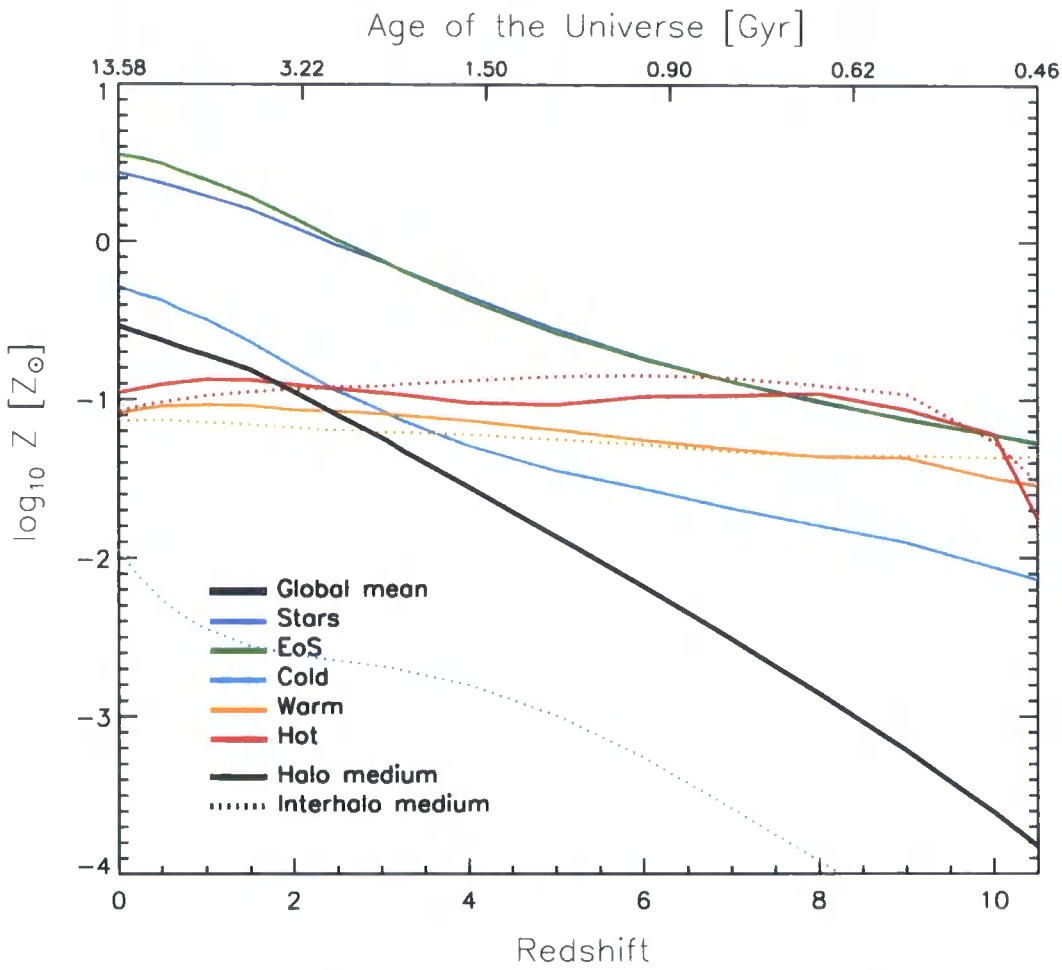

Figure 5.9: The mean mass-weighted metallicity of each phase, in this case the solid black line denotes the global mean. The evolution of the mean metallicity of a given thermodynamic phase is driven not only by the mass of metals deposited into it but also the evolving mass fraction of baryons that are within it. Since the mass of metals deposited into hot halo gas grows in proportion to the mass of baryons in that phase, its mean metallicity remains roughly constant at 0.1 $Z_\odot$ at all epochs. The ICM is thus a poor tracer of the mean metallicity of the Universe, which rises steadily at all times, reaching $\sim 0.1\ Z_\odot$ by $z = 0$.

density, in direct analogy to the star formation rate density, differs by an order of magnitude from the -2σ to $+2\sigma$ region whilst the difference in the mean mass-weighted enrichment varies by ~ 0.5 dex. The contrasting metal distributions are evident in Figure 5.4. Whilst the distribution is noisier than the temperature map, a consistent picture of the metal distribution is apparent, in which the gas associated with massive haloes is strongly enriched, whilst the metals ejected from haloes by winds enriches the filaments to intermediate and high overdensities.

Cen and Ostriker (1999a) first noted the strong relationship between metallicity and overdensity that arises due to the relative overabundance of stars in the highest density regions. The difference between the GIMIC environments is primarily a difference in the distribution of overdensities, and so the metallicity-density relation factors out effects due to the additional mass or greater halo abundance in the overdense regions. We therefore construct this relation in the same fashion as Figure 5.4, assigning the metallicity and density of SPH particles to a 3D mesh of uniform resolution $\sim 70\,h^{-1}$ kpc. We can therefore use this plot, Figure 5.10, to test whether the environmental dependence in the mass density and distribution of metals is an intrinsic effect, or once more a reflection of the different level of structure formation in each region.

We show the relationship at $z = 0$ (solid lines), $z = 3$ (dotted lines), and $z = 6$ (dashed lines) for each region. Whilst some environmental variation is discernable, which presumably arises from the greater overall star formation efficiency of the overdense regions in our model (see Section 4.4.5), it is clearly much weaker than the strong redshift evolution. At $z = 6$, the metallicity drops off rapidly for gas at overdensities less than $\sim 10^3$. Over the interval $z = 6$ to $z = 0$ the metallicity of the most overdense gas increases by approximately an order of magnitude (note that the scale of our mesh smoothes over the dense gas surrounding galaxies, and so overdensities of $\sim 10^5$ are the greatest that we resolve here). However, it is at the lower densities corresponding to filaments and voids that the greatest evolution is seen, as winds (and thermal expansion of gas resulting from wind-induced shocks) transport metals from galaxies into the IGM. For overdensities greater than ~ 10, our model reproduces the trend fitted by Schaye et al. (2003) to their observations at $z = 3$, however this trend exhibits a much more subtle drop in enrichment towards lower densities than is seen in our simulations.

To explore this further we have checked the numerical limitation of our chemo-

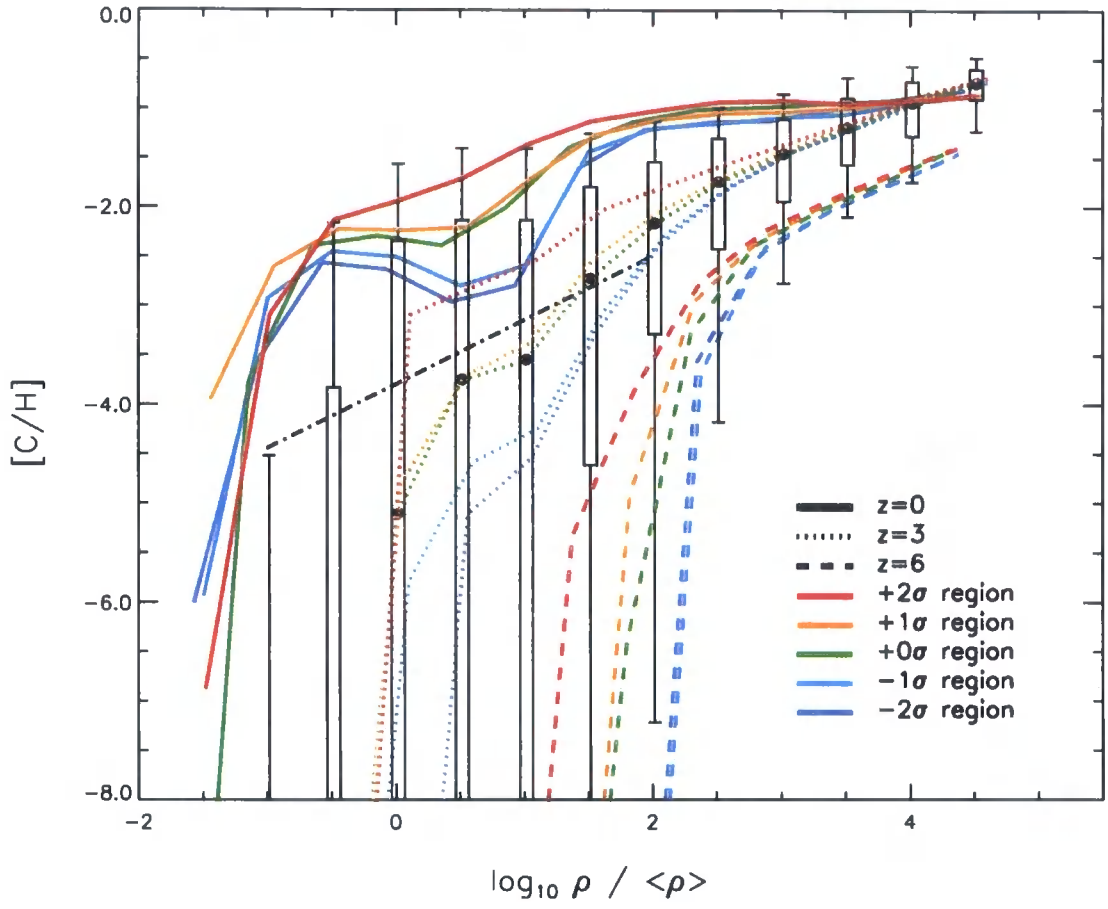

Figure 5.10: The carbon fraction, [C/H], as a function of overdensity, for each GIMIC region at $z = 0$ (*solid lines*), $z = 3$ (*dotted lines*) and $z = 6$ (*dashed lines*). The overplotted trend (*black dot-dashed line*) is the best fit to proposed by Schaye et al. (2003) to observations at $z = 3$. Box and whisker elements are plotted for the 0σ region at each redshift, showing the 10^{th}, 25^{th}, 50^{th}, 75^{th} and 90^{th} percentiles of the distribution. The scatter in the relationship is large, but the regions form a well-defined metallicity-density trend, whose evolution with redshift is evidently stronger than the environmental difference on these scales. Comparison with the data suggests that the model underpredicts the enrichment of the lowest-density regions at $z = 3$.

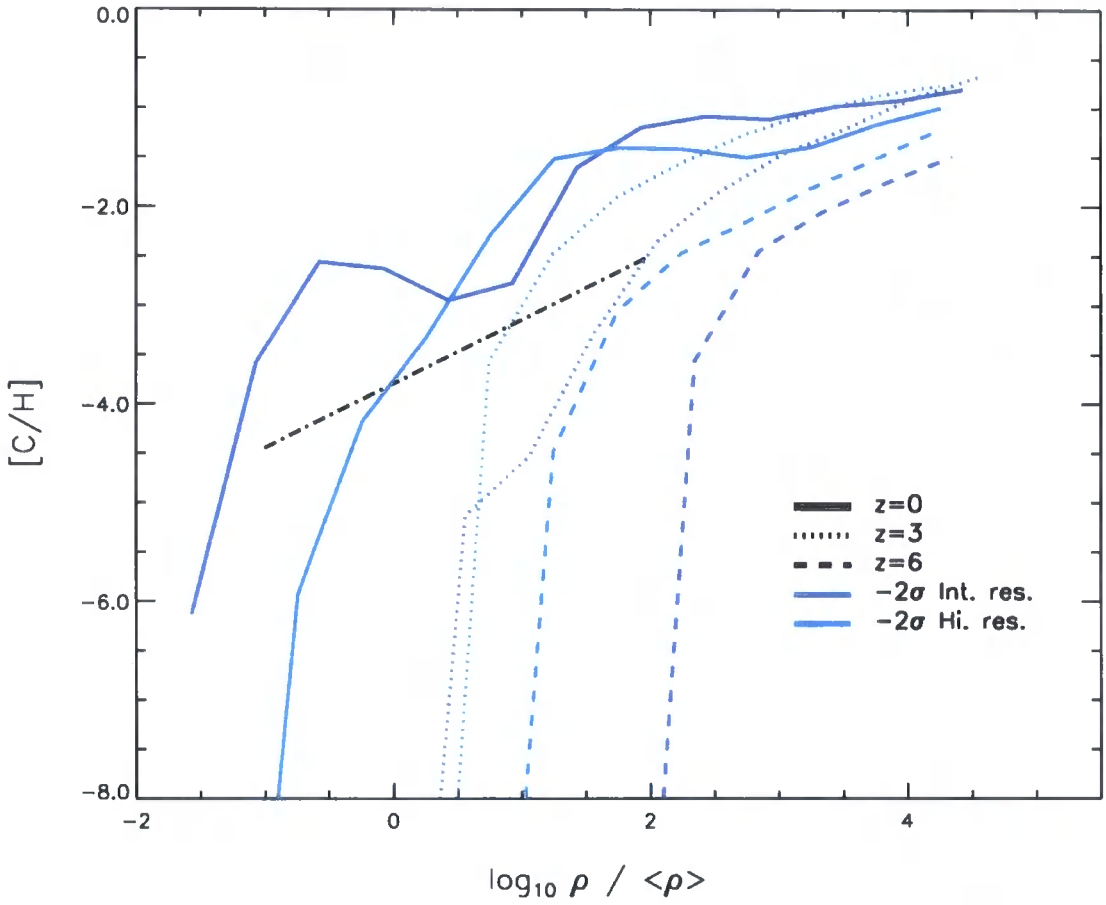

Figure 5.11: A comparison of the metallicity-density relation for the -2σ region at both intermediate- and high-resolution, in order to ascertain the numerical limitation of our code in terms of the metal distribution. At high densities (i.e. within haloes and galaxies) the relation is similar for both simulations (for $z \leq 6$), but in the lower densities of the IGM the agreement is relatively poor, highlighting a lack of convergence. We attribute this to our SPH-based metal transport scheme, which does not efficiently diffuse and mix metals.

dynamical scheme by comparing the metallicity-density relation of the -2σ region at both intermediate- and high-resolution (Figure 5.11). Although the relation is similar for $\rho/\bar{\rho} \gtrsim 10^2$, which is close to the approximate boundary separating haloes from the IHM, at lower densities the agreement is poor. At high-redshift ($z = 6$), the metallicity is seen to drop off very rapidly as one progresses to lower densities, however the density where this drop occurs is approximately an order of magnitude higher in the intermediate resolution simulation. At lower redshift, the relations are closer but the differences do not vary in a simple, monotonic fashion. We therefore conclude that the distribution of metals in low-density regions is an aspect of these simulations that is susceptible to numerical resolution, and the consequences of this are difficult to predict. This is perhaps not a particularly surprising finding, since our chemodynamical implementation requires that metals are carried by SPH particles. In low density regions, where the number density of SPH particles is low, the metal distribution is therefore noisy. This is compounded by the lack of a diffusion mechanism in our code; the expected 'thinning' of an expanding shell of metals via a simple r^{-2} dilution therefore does not occur. The low-level of mixing that occurs in SPH (due to its suppression of fluid instabilities) also serves to inhibit the smooth distribution of metals into the IGM.

Table 5.1: A comparison of the predictions yielded by the GIMIC simulations at $z = 0$ for the fraction of baryons in particular phases, with the latest observational measurements. Note that the GIMIC fractions do not sum to 100 per cent, since not all phases are used in this comparison. Observed fractions do not sum to 100 per cent either, for similar reasons, and also because of observational uncertainties. We show both the predictions derived from the individual regions in order to show the environmental scatter, and also the weighted average for the entire Millennium Simulation volume. The particular phases used in the simulation to derive the predictions for each component are given in the second column, with the abbreviations 'HM' and 'IHM' referring to the halo medium and interhalo medium respectively, as defined in Section 5.2.2.

Component	Selected Phases	GIMIC $\Omega_b, 10^{-3}$	Millennium estimate $\Omega_b, 10^{-3}$	Observational estimate $\Omega_b, 10^{-3}$	Source
Stars	Stars (HM + IHM)	-2σ: $0.42\,h^{-1}$ -1σ: $0.99\,h^{-1}$ 0σ: $2.27\,h^{-1}$ $+1\sigma$: $3.31\,h^{-1}$ $+2\sigma$: $5.51\,h^{-1}$	$2.3h^{-1}$ (7 per cent)	$1.1 - 2.3\,h^{-1}$	Eke et al. (2005)
HI	Gas on equation of state (HM + IHM)	-2σ: $0.03\,h^{-1}$ -1σ: $0.06\,h^{-1}$ 0σ: $0.11\,h^{-1}$ $+1\sigma$: $0.16\,h^{-1}$ $+2\sigma$: $0.21\,h^{-1}$	$0.11h^{-1}$ (< 1 per cent)	$0.35(\pm0.04)\,h^{-1}$	Zwaan et al. (2005)
Diffuse IGM	Cold (IHM)	-2σ: 13.06 -1σ: 16.78 0σ: 15.14 $+1\sigma$: 17.27 $+2\sigma$: 14.47	18.0 (40 per cent)	10.1(±2.0)	Lehner et al. (2007)
WHIM	Warm (HM + IHM)	-2σ: 3.89 -1σ: 6.76 0σ: 14.72 $+1\sigma$: 18.59	15.1 (34 per cent)	$\gtrsim 9.0$	Lehner et al. (2007)

Continued on Next Page...

		$+2\sigma$: 22.96			
ICM	Hot (HM)	-2σ: 0.13 $h^{-3/2}$ -1σ: 0.67 $h^{-3/2}$ 0σ: 2.47 $h^{-3/2}$ $+1\sigma$: 4.55 $h^{-3/2}$ $+2\sigma$: 8.94 $h^{-3/2}$	2.85 $h^{-3/2}$ (5 per cent)	1.8($\pm$0.7) $h^{-3/2}$	Fukugita and Peebles (2004)

Table 5.3: As per Table 5.2, but this time comparing the metal mass fraction in each phase.

Component	Selected Phases	GIMIC $\Omega_Z, 10^{-5}$	Millennium estimate $\Omega_Z, 10^{-5}$	Observational estimate $\Omega_Z, 10^{-5}$	Source
$z = 0.0$					
Total	All (HM + IHM)	-2σ: 2.12 h^{-1} -1σ: 4.94 h^{-1} 0σ: 11.26 h^{-1} $+1\sigma$: 16.40 h^{-1} $+2\sigma$: 27.35 h^{-1}	11.44 h^{-1}		
Stars	Stars (HM + IHM)	-2σ: 1.31 h^{-1} -1σ: 3.45 h^{-1} 0σ: 8.39 h^{-1} $+1\sigma$: 12.67 h^{-1} $+2\sigma$: 21.03 h^{-1}	8.60 h^{-1} (75 per cent)	7 h^{-1}	Pagel (2002)
$z = 2.5$					
Total	All (HM + IHM)	-2σ: 0.94 h^{-1} -1σ: 1.68 h^{-1} 0σ: 3.43 h^{-1} $+1\sigma$: 5.81 h^{-1} $+2\sigma$: 6.67 h^{-1}	3.63 h^{-1}	Poorly constrained	N/A
Galaxies (Stars & ISM)	Stars & gas on EoS (HM)	-2σ: 0.34 h^{-1} -1σ: 0.88 h^{-1} 0σ: 2.09 h^{-1} $+1\sigma$: 4.01 h^{-1} $+2\sigma$: 4.59 h^{-1}	2.31 h^{-1} (64 per cent)	1.35 h^{-1}	Bouché et al. (2006)
WHIM	Warm (IHM)	-2σ: 0.51 -1σ: 0.71 0σ: 1.02	1.00	> 5.2	Finoguenov et al. (2003)

Continued on Next Page...

		$+1\sigma$: 1.26	(20 per cent)		
		$+2\sigma$: 1.41			
		-2σ: 0.04			
Shocked	Warm & Hot	-1σ: 0.07			
galactic halo	(HM)	0σ: 0.17	0.20	$0.8-1.7$	Finoguenov et al. (2003)
gas		$+1\sigma$: 0.35	(4 per cent)		
		$+2\sigma$: 0.45			

Baryon census: results and observational comparisons

We now present a overview of the apportioning of baryons into various phases, by way of comparing the model with current observations and generating predictions for future programmes. In Table 5.2, we state which baryons in our simulations that we use for each observational comparison, and present the baryon fraction in that phase, for both the weighted average (our Millennium Simulation prediction), and the value within each GIMIC region individually in order to show the scatter.

As discussed in Section 4.4.3 our model predicts a global stellar mass density of $\Omega_\star h = 2.3 \times 10^{-3}$, in excellent agreement with observational estimate of Eke et al. (2005), $\Omega_\star h = 1.1(\pm 0.05) \times 10^{-3}$, assuming the Kennicutt (1983) IMF. The quoted uncertainty on the observation is the random error, the choice of IMF is in fact the greatest systematic uncertainty. Applying the Salpeter (1955) IMF revises the estimate to $\Omega_\star h \simeq 2.3(\pm 0.05) \times 10^{-3}$; however, we reiterate that our choice of kinetic feedback parameters were guided by the desire to match the global star formation rate density, and so this excellent agreement is not wholly unexpected.

In simple terms, star formation is fuelled by the cold gas of the interstellar medium (ISM). Whilst the ISM is a complex, multiphase gas comprising molecular clouds and ionised material within planetary nebulae and supernovae, the mass of its atomic hydrogen content is readily probed via the 21cm hyperfine transition. Zwaan et al. (2005) exploited the excellent sky coverage of the HI Parkes All Sky Survey (HIPASS) to derive a HI mass density of $\Omega_{\rm HI} h = 3.5(\pm 0.4) \times 10^{-4}$. Since our model explicitly considers the ISM as a single-phase medium, we make the simplifying assumption that all the mass of HI is well approximated by the mass of gas upon which we impose a polytropic equation of state. This simple assumption produces a good fit to observations, in particular those at intermediate redshifts (e.g. Péroux et al., 2003; Prochaska et al., 2005; Rao et al., 2006) based upon measurements of damped Lyα absorption. At the present epoch, our best estimate of $\Omega_{\rm HI}(z = 0) = 1.1 \times 10^{-4}$ compares favourably with observations based upon emission.

The baryon fractions of massive galaxy clusters are well established from X-ray observations of their thermal bremsstrahlung emission. Fukugita and Peebles (2004) used the survey of Reiprich and Böhringer (2002) to estimate the contribution of the intracluster medium to the overall baryon budget, finding $\Omega_{\rm ICM} h^{3/2} = 1.8(\pm 0.7) \times 10^{-3}$. We

estimate the matter density in the hot ICM from the mass of hot gas in haloes; the global average at $z = 0$ is $\Omega_{\rm ICM} h^{3/2} = 2.9 \times 10^{-3}$, and so once more the simulated fraction is close to the observational estimate.

Our model mimics the present day matter density of baryons in phases for which well constrained observations exist. We are therefore well placed to comment upon the contribution to the budget of the baryons that are difficult to account for observationally, those in the intergalactic medium and, in particular, the diffuse but highly ionised warm-hot intergalactic medium. Hydrodynamic simulations are universal in their prediction that the majority of baryons remain in a diffuse, low density state at all epochs (e.g. Cen and Ostriker, 1999c; Davé et al., 1999, 2001; Cen and Ostriker, 2006), and our model concurs with this prediction. These baryons are observed as the Lyα forest, and consequently were not detected at low-redshift ($z \lesssim 1.5$), for which the absorption occurs in the ultraviolet, until the relatively recent advent of space-based spectroscopy (e.g. Morris et al., 1991). Space observatories such as the *Far Ultraviolet Spectroscopic Explorer* (*FUSE*) and *HST* equipped with the Space Telescope Imaging Spectrograph (STIS) have fostered a rapid development of our understanding of the contribution of diffuse baryons to the overall budget, not least since they confirmed the existence of the WHIM via searches for collisionally ionised metals such as OVI and NeVIII (e.g. Tripp et al., 2000; Danforth and Shull, 2005; Savage et al., 2005). These searches yielded estimates of mass density of the WHIM of $\gtrsim 5$ per cent (e.g. Sembach et al., 2004; Tripp et al., 2006). Recently Lehner et al. (2007) analysed HI absorption systems in seven QSO sightlines and concluded that diffuse baryons account for at least 30 per cent of the baryons, and could possibly comprise more than 50 per cent. Using the broadening of the Lyα absorption line to segregate the HI systems into two populations: narrow Lyα absorbers (NLAs), associated with cold ($T < 10^5$ K) gas and broad Lyα absorbers (BLAs) that in the absence of significant non-thermal broadening can be associated with the WHIM, they estimated that the cold photo-ionised phase contains 20-30 per cent of the baryons, and at least 20 per cent is in the WHIM. Note that the relatively poor constraints on the baryon budget of the IGM follows from several significant systematic uncertainties in the analysis, such as the level of non-thermal broadening, the gas temperature and the nature of weakly absorbing systems. Estimates using metal line absorption are also susceptible to systematics arising from the necessary assumption of the level of enrichment. Our model suggests that state

of the art observational censuses still miss a significant fraction of the diffuse baryons; our best estimate for mass fraction of baryons in the the cold, diffuse IGM is 40 per cent, with the WHIM contributing nearly as much mass, at 34 per cent. Recall from Figure 5.6, and Table 5.2, however, that the WHIM fraction is subject to strong environmental fluctuations.

We now turn to the distribution of metals amongst the various baryon phases. We saw in Figure 5.8 that stars dominate the metal budget in these simulations at low-redshift, a result in common with the simulations of Davé and Oppenheimer (2007), however we note that the dominance of stars as a metal repository in our model (75 per cent by mass) is significantly greater than in their case (43 per cent). It is highly likely that this discrepancy arises because of the key difference in the implementation of galactic winds between their model and that adopted for GIMIC, as discussed in Section 5.2.3. We are encouraged, however, by the similarity of our metal density with the observational measurement of Pagel (2002), the two agreeing to within 20 per cent.

In GIMIC, at $z = 2.5$ both stars and the dense, star-forming gas of the ISM already contain ~ 30 per cent of $\Omega_Z(z = 0)$. This is the key epoch for the missing metals problem, and so we review here the compatibility of our results at this epoch with current observations. Accounting for potential incompleteness in the sample of Bouché et al. (2006), our total metal mass in galaxies (stars and star-forming gas) is consistent with observations, as is the metal mass in warm interhalo gas, when compared with OVI measurements of Finoguenov et al. (2003). We find that the warm-hot gas bound to dark matter haloes at $z = 2.5$ accounts for a very small fraction of metals ($\simeq 4$ per cent), in stark contrast to the prediction of Ferrara et al. (2005) that up to 90 per cent of the cosmic metal inventory could be accomodated in this phase.

In conclusion, results derived from the GIMIC simulations join the growing body of evidence, from both simulations and observations, in support of the view that cosmic baryons and heavy elements are distributed across a wide range of phases in temperature-density space, and should not be expected to reside wholly within galaxies.

5.3 Summary

In contrast to semi-analytic modelling, hydrodynamical simulations facilitate a study of the evolution of the intergalactic medium and its interaction with galaxies, their parent haloes and their outflows. The novel initial conditions developed for GIMIC allow the environmental aspects of this relationship to be probed in a large-scale cosmological context, whilst allowing the gas to be reliably separated into the halo and interhalo media and, in our high-resolution realisations, resolving the Jeans scale in the IGM.

GIMIC demonstrates the strong dependence of the baryonic density, temperature and metallicity fields upon large-scale cosmological environment. This leads to the key result that both the mass and volume-filling fraction of the observationally elusive warm-hot phase of the IGM are sensitive to their surroundings; in voids, the WHIM might account for less than 20 per cent of the baryon mass, and occupy less than 5 per cent of the volume. By constrast, the overdense surroundings of clusters and massive filaments are rich in this shocked, enriched gas. As is the case with measurements of the star formation rate density (see discussion in Section 4.5), this environmental variation should therefore be considered as an additional systematic uncertainty within surveys.

Perhaps the key result of this chapter is our finding that the WHIM is not a static reservoir of gas that remains *in-situ* once formed. The short cooling time of warm-phase gas, decreased still further by peaks in the cooling function from coolants such as oxygen, renders a parcel of WHIM gas unlikely to remain in this phase for a significant fraction of the Hubble time. The low-redshift plateau in $\Omega_{\rm WHIM}(z)$ once it has peaked at $z \sim 2$ (Figures 5.3 and 5.5) indicates that cooling losses are offset by the creation of 'fresh WHIM' from both cold, diffuse gas that shocks when accreted onto haloes, and cold dense gas within halo centres that is shocked by violent interaction with galactic winds. We predict that this cycling is so rapid that by $z = 0$ roughly 60 per cent of all baryonic mass has, at some stage in cosmic history, comprised part of the WHIM.

The apportioning of baryons between the cold and warm phases of the IGM in our calculation tallies well with rapidly tightening observational constraints, as traced by the narrow and broad lines of the Lyα forest (e.g Penton et al., 2004; Sembach et al., 2004; Lehner et al., 2007), and metal-line absorbers (e.g. Tripp et al., 2000; Danforth and Shull, 2005). Confidence in our predictions for the poorly constrained mass density of

the WHIM is bolstered by the accurate reproduction of the relatively well-constrained global mass density of baryons in stars, atomic hydrogen and intracluster plasma.

Finally, we have studied the enrichment of cosmic baryons by the heavy elements synthesised in stars. We find that star forming gas is the dominant metal repository in our simulations until $z \simeq 3$, at which point stars become dominant. We find a greater metal mass, and greater metal mass fraction, in stars than reported by Davé and Oppenheimer (2007), which we believe is due to differences in the implementation of galactic winds. Our overall stellar metal mass prediction tallies well with observations.

The simulations exhibit a remarkable lack of evolution in the metallicity of warm and hot gas, both of which remain constant at $Z \sim 0.1\ Z_{\odot}$ over the redshift interval $9 \gtrsim z > 0$. This appears to result from a tight coupling between the creation of warm and hot phase gas (say from both gravitational and feedback shock-heating), and the injection of metals into this gas by the star formation that i) follows the gravitational shocking of gas accreting onto haloes and ii) shortly precedes the generation of galactic winds. Consequently, we find that the metallicity of hot cluster gas does not follow that of the Universe as a whole, which grows steadily with redshift. This casts doubt upon suggestions that clusters are an accurate probe of the global metallicity (e.g. Renzini, 1998).

We find only a small 'intrinsic' environmental trend in the production of metals, as traced by the metallicity-density relation. As with the star formation rate density discussed in Chapter 4, the differing metal mass seen in each GIMIC region is due to the relative under- and over-abundance of massive haloes in differing regions, relative to the cosmic mean. In our model, it is these haloes that are the most efficient producers of metals. As with the sSFR-v_c relation (Figure 4.10), the environmental variation of the metallicity-density is dwarfed by the redshift evolution. We find good agreement at $z = 3$ with the observations of Schaye et al. (2003), but note that the metallicity of low-density gas is an area within these simulations that appears to be most susceptible to numerical limitations, which we attribute to the details of our metal transport scheme.

Chapter 6

The X-ray haloes of galaxies

6.1 Introduction

A universal idea in analytic and semi-analytic schemes is that spiral galaxies, which are the most abundant galaxies in the low-redshift Universe (e.g. Fukugita et al., 2007), form via the accretion of gas at relatively late epochs. This temporal constraint upon disc formation is believed to be necessary because discs are generally considered to be fragile to both merger events (e.g. Walker et al., 1996) and instabilities triggered by their own self-gravity (Efstathiou et al., 1982; Mao et al., 1998; Mo et al., 1998; Syer et al., 1999). Consequently, discs are expected to be still in the process of formation at the present epoch, thus requiring that the cooling of hot gas from the dark matter halo onto galactic discs be ubiquitous in the low-redshift Universe. This process is typically assumed to be represented by a spherically symmetric, single phase cooling flow, similar to those seen in some galaxy clusters. Similarity solutions for such a model were presented by Bertschinger (1989).

Since hot halo gas is never far from hydrostatic equilibrium, its temperature must be close to the virial temperature of the halo (Equation 4.3). For the haloes that are expected to host the archetypal late-type galaxy at the present epoch, $M_{200} \sim 10^{12}$ $M_{\odot}$, or $v_c \sim 200$ km s^{-1}, this equates to $T_{vir} \sim 10^6$ K. At such high temperatures, thermal Bremsstrahlung (see Figure 2.2) contributes significantly to the cooling rate. A sufficiently high cooling rate, therefore, will produce a signature X-ray flux. Following the cooling flow models of Thomas et al. (1986), White and Frenk (1991, hereafter WF91) posit that the X-ray flux varies as

$$L_X \sim \frac{5}{2}\dot{M}_{cool}v_c^2, \tag{6.1}$$

where the coefficient is sensitive to the structure of the halo potential and the cooling flow, and v_c is the circular velocity. Note that v_c is used here as a proxy for halo mass; in WF91 the assumption of isothermal density profiles removes any radial variation in v_c. Since the profiles of the simulated haloes need not be isothermal, we adopt the convention that $v_c = v_c(r_{200}) \equiv v_{200}$. The rate at which cold gas is accreted, $\dot{M}_{\rm cool}$ is given by:

$$\dot{M}_{\rm cool} = 4\pi\rho_{\rm g}(r_{\rm cool})r_{\rm cool}^2\frac{{\rm d}r_{\rm cool}}{{\rm d}t}, \tag{6.2}$$

where $r_{\rm cool}$ is the radius at which the cooling time is equal to the age of the Universe (WF91).

Owing to the strong dependence upon circular velocity, a disc hosted by a massive halo ($v_c \simeq 250$ km s^{-1}) should produce a substantial X-ray flux, leading WF91 to predict that the flux from such haloes would be detectable with the *ROSAT* satellite. Whilst extended emission is routinely detected in the hot gas associated with galaxy groups and clusters (as discussed in Section 1.2.2), this does not constrain hierarchical galaxy formation theory (such as that laid out by WF91), since it is not this gas that is believed to feed disc formation. Extended emission is also commonly detected around massive elliptical galaxies (e.g. Forman et al., 1985; Kim et al., 1992; Sun et al., 2007; Jeltema et al., 2008), but similarly, this does not constitute a clean test of the theory since the source of the hot gas is unclear; alternative interpretations include shock heating following merger-induced gas ejection (Mathews and Brighenti, 1998; Read and Ponman, 1998) or radiation from a collapsed galaxy group (Ponman et al., 1994). In addition, since most ellipticals are not believed to be actively star forming, the presence (or absence) of diffuse X-ray emission does not constrain the WF91 scenario.

The systems for which detection of extended emission would lead to the optimal constraints are therefore massive, isolated, quiescently star-forming disc galaxies. Benson et al. (2000, hereafter B00) targeted three such galaxies (NGC 2841, 4594 & 5529) with *ROSAT*, and inferred upper limits on the X-ray flux of their haloes that were roughly an order of magnitude below the WF91 prediction, thus highlighting a key challenge for galaxy formation theories. In the same study, B00 cite a number of potential means by which the theory and observations might be reconciled, such as the effect of feedback, changes to the cosmological parameters[1], the effect of a multiphase gas halo and cooling

[1]This point is particularly relevant, as they assumed $\Omega_{\rm m} = 1$, $\Omega_{\rm b} = 0.06$, and $h = 0.5$

flow, changes to the halo profile, and the effect of metals.

Surprisingly few theoretical attempts have been made to follow-up this study in greater detail. Most notably, Toft et al. (2002) used the TREESPH code (Hernquist and Katz, 1989) to simulate the formation of isolated discs in haloes of circular velocity $130 < v_c < 325$ km s^{-1}, in both ΛCDM and warm dark matter (WDM) cosmogonies. Considering SPH particles as packets of optically thin thermal plasma, they computed X-ray luminosities in the 0.012-12.4 keV band using the MEKA plasma emissivity code (Mewe et al., 1986). Whilst their galaxies exhibited a well defined $L_X - v_c$ relation of the same slope predicted by single phase cooling models, $L_X \propto v_c^5$, its normalisation was typically one or two orders of magnitude below the WF91 prediction, with large scatter. Toft et al. cited the complex and dynamic structure of cooling flows in their simulations as the source of the discrepancy with analytic models, and used them to estimate a modest exposure time of $\sim 10^3$ s for a 5σ detection of extended emission around massive, nearby spirals with the *XMM-Newton* and *Chandra* X-ray satellites[2].

Alternative scenarios have been proposed to explain the absence of extended emission, most notably the notion that the generation of virial accretion shocks, which are assumed to be ubiquitous in analytic models such as WF91, do not in fact develop in low-mass haloes ($M_{200} \lesssim 10^{11}$ M$_\odot$), nor haloes of any mass that assemble at high redshift, $z \gtrsim 2$ (Birnboim and Dekel, 2003). Simply via energy conservation arguments, it follows that infalling gas must convert its potential energy and therefore a shock must still occur, but in this regime it is delayed until the gas arrives at the disc. Therefore a quasi-hydrostatic halo is not created, but rather a highly-ionised region close the disc that is more likely to be visible via Lyα emission resulting from recombinations. However, this model is not of direct relevance to this particular test, since the optimal systems to observe are more massive than 10^{11} M$_\odot$, and still actively star-forming at late times.

The commissioning of *XMM-Newton* and *Chandra* has yielded detections of X-rays from the haloes of spiral galaxies, but these are commonly very close to the disc (within several kiloparsecs), and are most likely the signature of on-going stellar feedback (e.g. Tüllmann et al., 2006; Li et al., 2006). However, extended emission around NGC 5746, an SBb galaxy at a distance of $\simeq 30$ Mpc with circular velocity $v_c \simeq 300$ km s^{-1}, was recently

[2]*Chandra* is the preferred satellite for these observations, since its better angular resolution facilitates better point-source removal.

reported by Pedersen et al. (2006, hereafter P02) following a 37-kilosecond exposure with *Chandra*. Since its infrared luminosity indicates that it is quiescently star-forming (SFR of 1.2 $M_\odot$ yr^{-1}, Moshir et al., 1990), this appeared to represent an ideal test case, but doubt has since been cast over this detection (Wang, 2007) due to technical issues pertaining to the ACIS-I detector on *Chandra*, and a possible inadequate removal of point-sources. Warwick et al. (2007) have also recently reported a putative detection of extended emission from the *face-on* late-type galaxy M101 (NGC 5457) with *XMM-Newton*, although the reported luminosity is relatively low, $L_X \simeq 2 \times 10^{39}$erg s^{-1}.

The continued absence of definitive observations of cooling flows in isolated low-redshift disc galaxies remains a concern for galaxy formation theory, and warrants further, detailed, investigation. GIMIC is an ideal resource with which to probe the X-ray emissivity of disc galaxies, since it features a large number of haloes at $z = 0$ with circular velocities in the desired range, across a wide-range of environments and simulated with great enough particle number (at intermediate-resolution) to resolve the structure of discs and cooling flows. Having simulated the -2σ region to $z = 0$ at high-resolution, we are also able to ascertain the degree of numerical limitation in our findings. The detailed metal and redshift dependent cooling tables developed for GADGET3-BG are also a key advantage, since the increase in cooling rate caused by enrichment must necessarily alter the mass deposition rate (e.g. WF91), and potentially introduce scatter into the $L_X - v_c$ relation (Toft et al., 2002). In this chapter, we therefore describe the initial stages of a study that uses GIMIC to investigate the co-evolution of galaxies and their hot gas haloes.

6.2 Tracing the evolution of galaxies

Key to this study is the ability to trace the co-evolving properties of dark matter haloes, and their associated baryons that form the associated galaxies and hot gas halo. We achieve this via a series of steps that lead to the construction of a *merger tree*, as shown schematically in Figure 6.1:

- *Identify substructures*: the identification of virialised objects is simple, but identifying the substructures that may survive for a long time inside them is more challenging. Most authors define substructures as locally overdense and self-bound

objects; their identification hence requires an *unbinding* procedure. For this, we adopt the SUBFIND algorithm (Springel et al., 2001a) that identifies background haloes with FoF, and then finds substructures using a topological criterion that requires them to be bounded by an isodensity contour traversing a saddle point in density space. All unbound particles (i.e. total energy is positive) are excluded from the substructure.

Since we aim to identify *galaxies* we in fact adopt the version of SUBFIND described by Dolag et al. (2008), which is modified to account for baryons (i.e. gas and star particles) in addition to CDM. To this end, the algorithm includes the baryonic contribution to the density field. To avoid systematic biases in the density estimate (performed using SPH interpolation), the contributions are computed for each species (i.e. gas, stars, CDM) individually, since in general the distribution of each component is quite different. Stars trace the most concentrated features in the density field, and their inclusion adds noise to the density field, so this particular version of SUBFIND smoothes over three (rather than the default two) particles when detecting saddle points.

We therefore consider a 'galaxy' to be the stellar component of a self-bound substructure; the gas bound to the substructure therefore forms the ISM and hot halo of the galaxy. This is an attractive scheme because it makes the assignment of particles to particular galaxies unambiguous, and closely mirrors the procedure adopted for semi-analytic models that adopt merger trees from N-body simulations, for which galaxies are assumed to form within substructures (e.g. Bower et al., 2006; Croton et al., 2006; De Lucia et al., 2006; Font et al., 2008). Note that the SUBFIND algorithm commonly results in the existence of a dominant subhalo that comprises the majority of the mass of the FoF halo.

- *Construct merger trees*: a merger tree connects together the progenitors of a given structure that are identified at each snapshot of a simulation. This is achieved by searching through all snapshots for descendants of the objects identified at each epoch. A descendant is found by following the most bound 10 per cent (or 10 most bound particles, if this constitutes a greater mass); the descendant is the subhalo at the subsequent output time that contains the greatest number of these particles.

We construct merger trees for each *subhalo* (rather than FoF haloes) identified at $z = 0$, and include information relating to all of their progenitor subhaloes. The nomenclature of a 'subhalo' may therefore appear confusing, since in the merger tree structure the largest structure is always a 'subhalo'; this is because all subhaloes are substructures of a FoF halo, and the identification of the latter is the initial stage of the SUBFIND algorithm. However, our merger trees are constructed only from the self-bound subhaloes.

A schematic of the final four output times of an example merger tree is shown in Figure 6.1; as the simulation progresses, hierarchical assembly results in subhaloes merging, such that smaller subhaloes either become substructure of a larger one, or cease to be recognisable as separate substructures, and are subsumed into the larger object.

6.2.1 Traced properties

Gas properties

As shown in Chapter 5, halo gas has a complex multiphase structure. We wish to follow this in detail in order to elucidate the multiphase nature of galactic cooling flows, and so retain the thermal classification for gas that we defined in that chapter, namely i) EoS gas, ii) cold gas ($T \leq 10^5$ K), iii) warm gas ($10^5 < T \leq 10^{6.5}$ K) and iv) hot gas ($T > 10^{6.5}$ K). For each subhalo, and for each thermal phase, we output the mass and star formation rate, and compute the mean (particle mass weighted) metallicity.

Stellar properties

We have argued that the $L_X - v_c$ relation of quiescent disc galaxies represents the cleanest test of hierarchical galaxy formation models. Thus it is critical to have an algorithm that classifies simulated galaxies according to morphology. We achieve this by considering the stellar dynamics, using a simplified version of the dynamical decomposition algorithm (e.g. Abadi et al., 2003b; Okamoto et al., 2005), whereby the galaxy is considered as a superposition of a rotationally-supported disc and a dispersion-supported spheroid. Under the assumption that the spheroid is non-rotating (i.e. has zero total angular momentum), the spheroid mass may be estimated as twice the summed mass of all

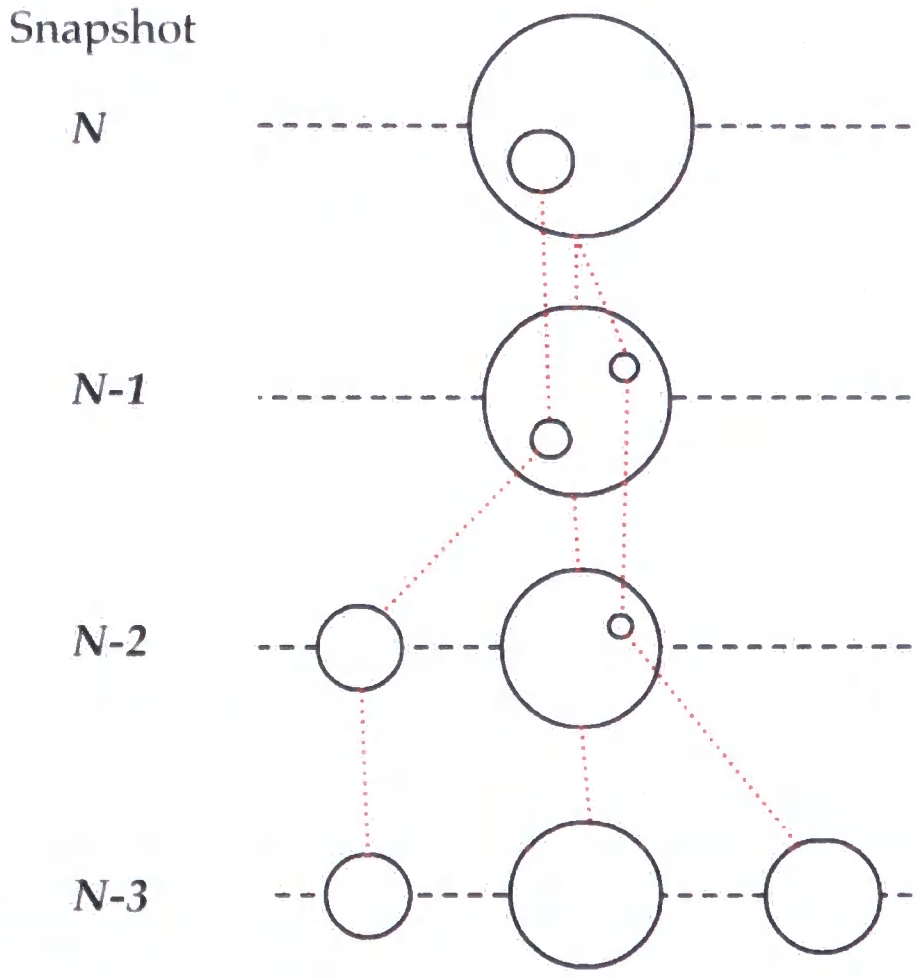

Figure 6.1: Schematic showing the final four output times of an example subhalo merger tree. Each circle represents a separate subhalo, which may or may not be a substructure of a larger subhalo (the potentially confusing 'sub'-halo nomenclature is retained because all subhaloes are substructures of FoF haloes). Dotted red lines connect subhaloes to their descendants at subsequent outputs.

star particles that counter-rotate with respect to the overall angular momentum vector, $\mathbf{L} = \mathbf{r} \times \mathbf{p}$, of the galaxy. The remaining mass is then the disc mass.

Galaxy sampling

The unique initial conditions developed for GIMIC facilitate an exploration of the effects of both cosmological environment and numerical resolution. We therefore construct trees for all five GIMIC regions, [-2, -1, 0, +1, +2]σ at intermediate-resolution, and also the -2σ region at high-resolution. Since we wish to analyse only well-resolved, isolated systems, in all subsequent analyses we consider only those galaxies i) with $M_\star \geq 10^{10}\, h^{-1}\, \mathrm{M}_\odot$ and ii) with $M_{\rm sub} \geq 0.9 M_{\rm FoF}$. The first criterion ensures that we only consider systems with at least $\sim$ [1250, 10000] star particles at [intermediate/high] resolution, whilst the second ensures that we only consider isolated, central galaxies.

6.3 Galactic morphology

A disc-dominated galaxy (D/T = 0.83) identified with this procedure is shown in Figure 6.2. The left-hand column shows the gas properties (i.e. ρ, T, Z) for an infinitesimal slice through the halo centre, whilst the right-hand column shows the disc in three orthogonal projections. A highly anisotropic distribution of gas is evident; as the density field is far from isotropic, and higher density regions are associated with cooler gas. Throughout the halo (the virial radius, $r_{200} = 131.5\, h^{-1}$ kpc is marked by a white circle) those regions between the inflowing streams are filled by the hot gas ($T \sim 10^6$ K), as posited by WF91. Much of the gas in the halo is enriched, thus reducing the cooling time, whilst the absence of considerable quantities of enriched gas beyond the virial radius hints that little gas has recently been ejected by winds from this particular galaxy. The disc-dominated galaxy is contrasted with a bulge dominated galaxy of similar stellar mass and halo mass, in Figure 6.3. In this case, the halo is completely filled with gas close to $T_{\rm vir}$, except at the very centre close to the galaxy.

Figure 6.4 shows the distribution of the ratio of stellar disc mass to stellar total mass (D/T) for each GIMIC simulation at both $z = 1$ and $z = 0$. The number of galaxies satisfying the selection criteria is also given; across all intermediate resolution simulations we find a total of 884 galaxies at $z = 1$, declining to 752 galaxies at $z = 0$ because many

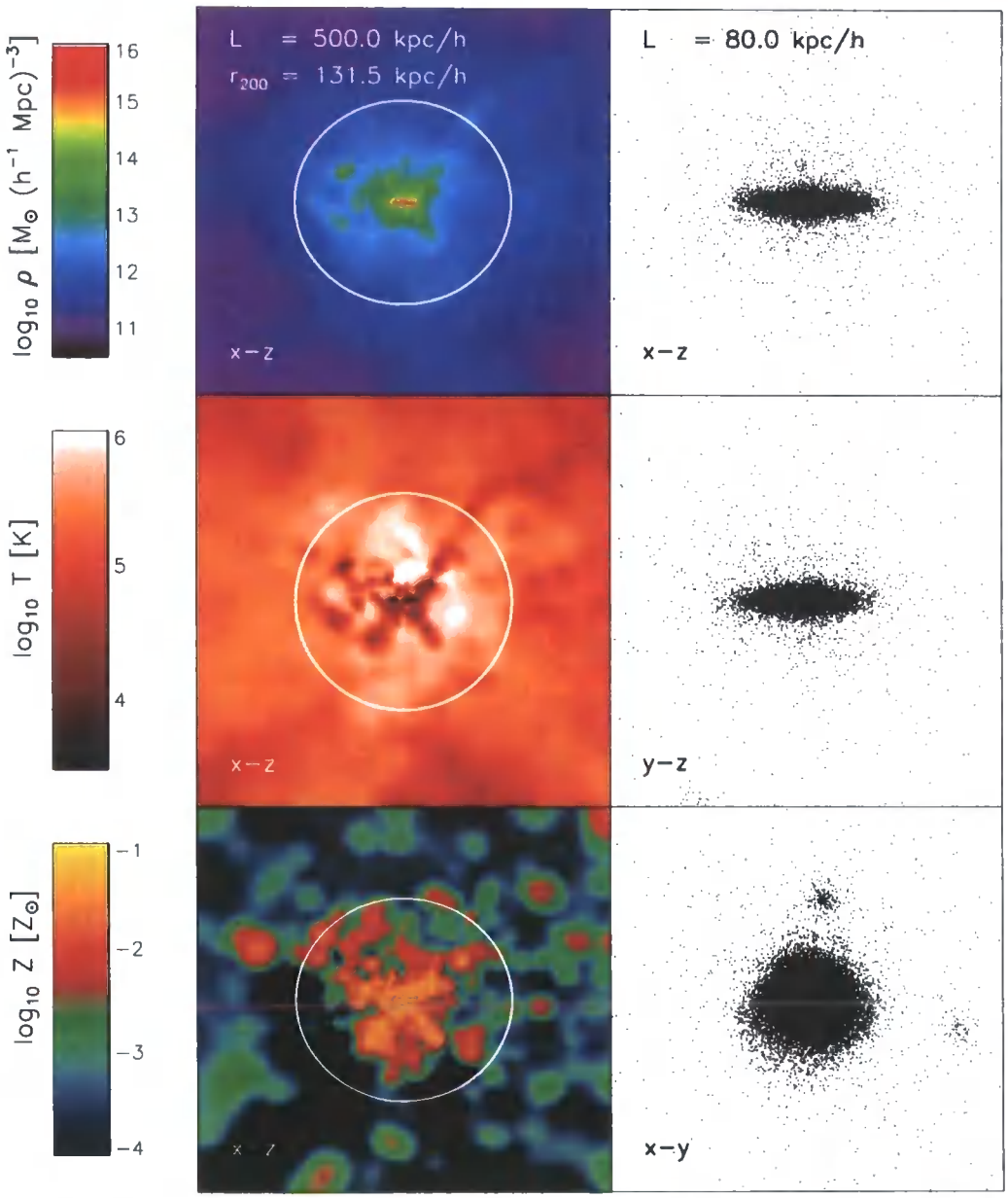

Figure 6.2: A disc-dominated galaxy (D/T = 0.83) of halo mass $M_{200} = 5 \times 10^{11}\ h^{-1}\ \mathrm{M}_{\odot}$ and disc mass $M_{\star} = 2.8 \times 10^{10}\ h^{-1}\ \mathrm{M}_{\odot}$, from the high-resolution -2σ region at $z = 0$. The left-hand column shows the gas properties smoothed onto an infinitesimally thin mesh of 512^2 cells and scale $L = 500\ h^{-1}$ kpc, through the centre of the halo; the z-axis corresponds to the angular momentum vector of the stars. The right-hand panel shows the star particles in the disc from three orthogonal projections, again the z-axis corresponds to the angular momentum axis of the stars.

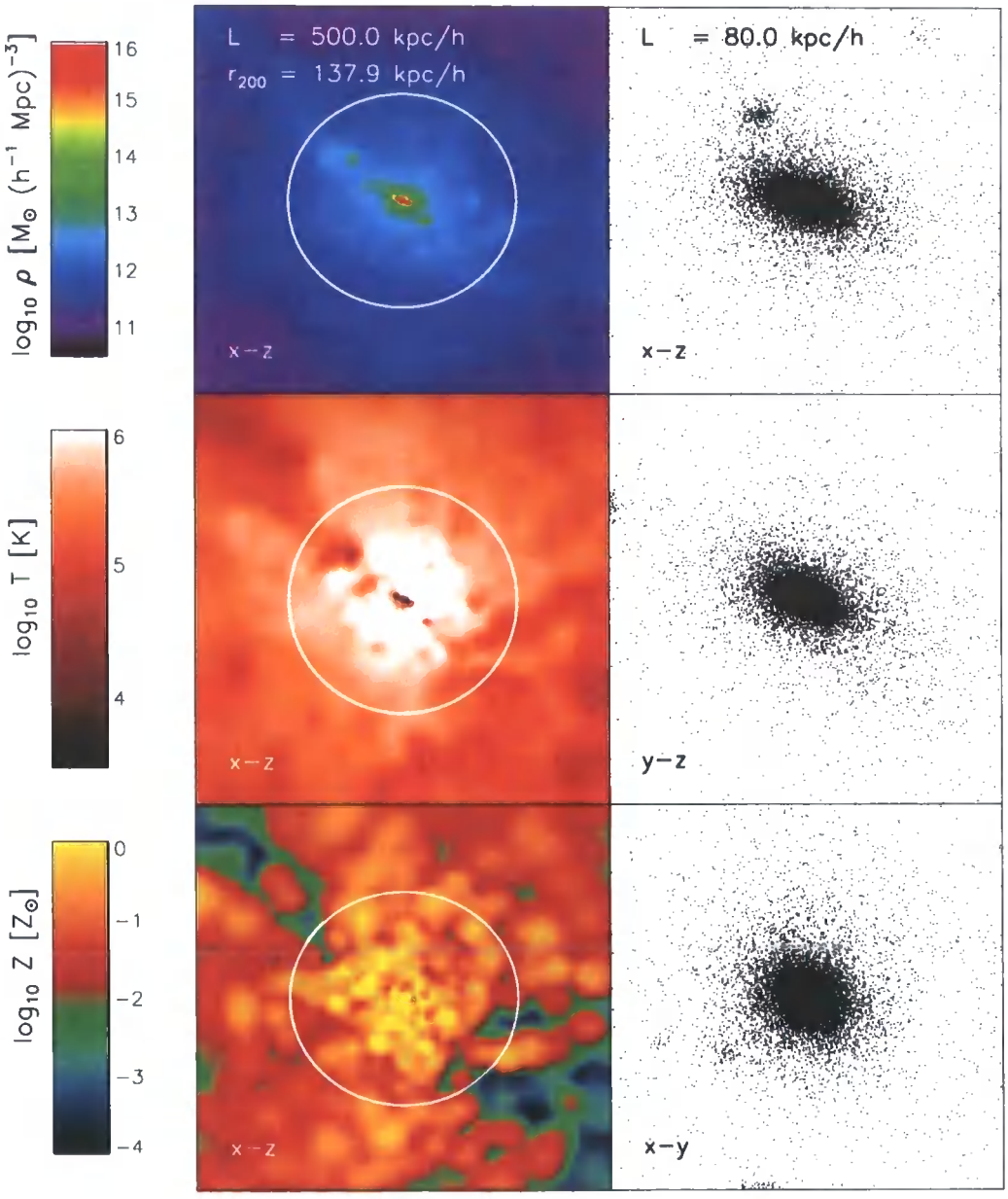

Figure 6.3: A spheroid-dominated galaxy (D/T = 0) of halo mass $M_{200} = 6 \times 10^{11}\ h^{-1}\ \mathrm{M}_{\odot}$ (similar therefore to the halo in Figure 6.2) and stellar mass $M_{\star} = 6.2 \times 10^{10}\ h^{-1}\ \mathrm{M}_{\odot}$, from the high-resolution -2σ region at $z = 0$. Since the angular momentum vector does not pick out a well-defined 'disc axis', we leave the particles in the simulation coordinate frame here.

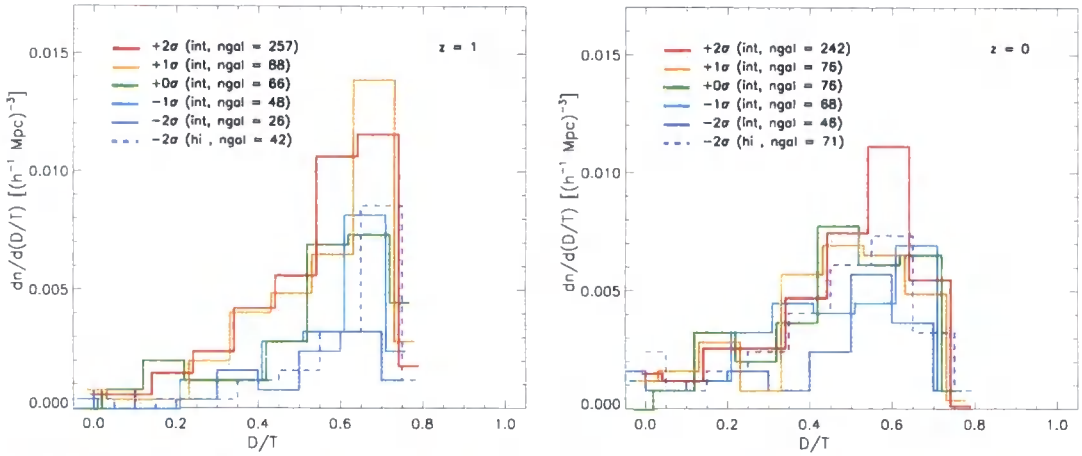

Region	-2σ (hi.)	-2σ (int.)	-1σ (int.)	0σ (int.)	$+1\sigma$ (int.)	$+2\sigma$ (int.)
Med(D/T), $z = 0$	0.54	0.58	0.52	0.55	0.54	0.58
Med(D/T), $z = 1$	0.72	0.62	0.68	0.65	0.67	0.65

Figure 6.4: *Top:* The distribution of D/T ratios for galaxies within the five intermediate resolution GIMIC regions (solid histograms) and the high-resolution -2σ region (dashed histogram), at $z = 1$ (left) and $z = 0$ (right). High D/T values are preferred at $z = 1$, but evolution towards the present day shifts galaxies to lower values as mergers disrupt discs. No large-scale environmental trend is evident, but the effect of resolution is marked, with the high-resolution -2σ region featuring a greater fraction of disc galaxies, particularly at $z = 1$. *Bottom*: the median D/T of the sample drawn from each region at $z = 1$ and $z = 0$. Each region is similar at both epochs, the shift over this period being ~ -0.1 for the intermediate resolution runs.

isolated haloes at $z = 1$ merge into groups and clusters by the present epoch. In all regions (including the -2σ region at high-resolution), the median D/T declines from $z = 1$ to $z = 0$, primarily due to mergers converting discs into spheroids. In all regions the median D/T at $z = 0$ is a little greater than 0.5, indicating an approximate equipartition between disc- and spheroid-dominated galaxies. In all regions at both epochs the maximum D/T is approximately 0.8.

This distribution of D/T ratios is encouraging, since the formation of disc galaxies in simulations is a central astrophysical problem, and it has proven challenging to create disc-dominated galaxies in simulations: for example Abadi et al. (2003b) created a disc with D/T of 0.45, and Okamoto et al. (2005) ran a set of initial conditions with three

differing schemes for coupling feedback energy to gas and found that the resulting D/T ratio was very sensitive to feedback, varying from 0.21 to 0.48 for their models. More recent models have proven more successful: Governato et al. (2007) produced a disc with a D/T of 0.74, and in a separate study, Okamoto et al. (2008b) reused the initial conditions from Okamoto et al. (2005) to implement a model incorporating kinetic feedback from winds, and this time found D/T in the range 0.67-0.76. Whilst the Governato et al. (2007) model did not include a kinetic feedback scheme, it should be noted that their cooling tables were based on primordial rates, thus lengthening the cooling time and rendering their thermal feedback more efficient.

The periodic volume simulations of Croft et al. (2008) found, at $z = 1$, very few disc-dominated galaxies. Using the same dynamical decomposition scheme as used here, their sample yielded only 3.5 per cent of galaxies with D/T > 0.5, and so their split between 'early-' and 'late'-type galaxies was made at the rather low D/T value of 0.2. This contrasts strongly with our findings, since the median D/T in the intermediate-resolution GIMIC runs lies in the range 0.62-0.68 at $z = 1$. We note that resolution appears to play a role, since the median D/T ratio of the -2σ region at this epoch rises from 0.62 at intermediate-resolution to 0.72 at high-resolution. However, the particle mass of the Croft et al. (2008) simulation is bracketed by those of the intermediate- and high-resolution GIMIC runs, and thus it is likely that the difference in galactic morphology is due to the sensitivity of disc formation to the implementation of the baryon physics, as argued by Okamoto et al. (2005).

In the local Universe, observations suggest that the range of D/T values spans a similar range to that found in our simulations. Graham (2001) observed 86 spiral galaxies, finding a median D/T of 0.75. However, one might imagine that this value is biased slightly high, since the sample omits spheroidal / elliptical galaxies that necessarily have low D/T values. Decompositions of observed galaxies are also based on photometry, and might also favour higher D/T values due to the lower mass-to-light ratio of discs. Therefore, the similarity of the GIMIC morphologies with the data, and its contrast with older, less successful simulations, is encouraging.

A clear trend in D/T as a function of stellar mass is evident in the left-hand panel of Figure 6.5. For the intermediate-resolution simulations, D/T peaks at a stellar mass of $\sim 10^{10.7}\,h^{-1}\,\mathrm{M}_{\odot}$, declining at lower and higher masses. The origin of the decline to lower

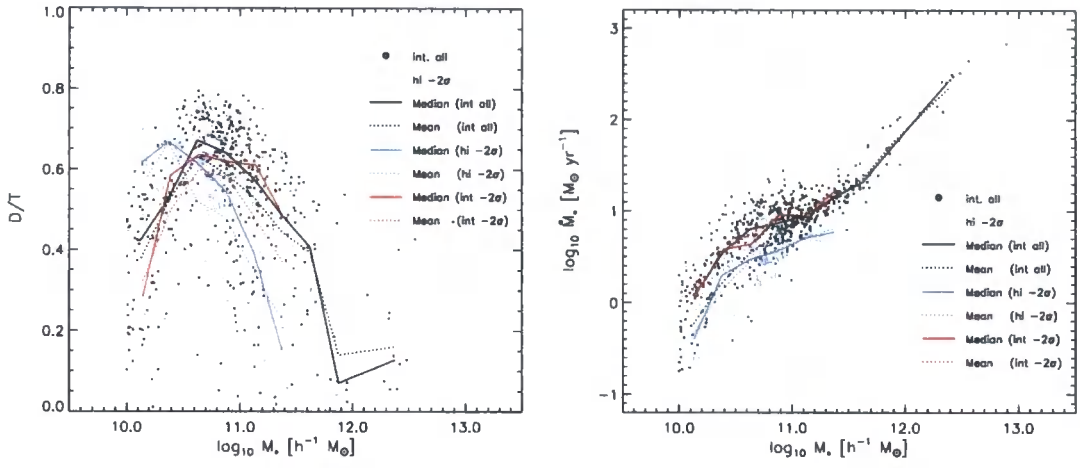

Figure 6.5: *Left:* the disc-to-total stellar mass ratio (D/T) as a function of stellar mass, at $z = 0$, for galaxies satisfying our selection criteria (see text). Galaxies from all five intermediate-resolution simulations (filled black circles) and the high-resolution -2σ region are shown. Solid and dotted lines show the median and mean respectively, of the distributions. Also shown are the median and mean of the -2σ galaxies at intermediate resolution for a direct resolution comparison. The relation is sensitive to resolution, the peak in D/T shifting to lower masses at higher resolution. *Right:* the SFR of the same sample of galaxies.

masses is not clear; most likely a combination of resolution and physical effects such as an increased merger rate for small objects. The decline at higher masses is expected, since massive galaxies i) are more susceptible to instabilities (e.g. Efstathiou et al., 1982) and ii) are commonly experience major mergers (e.g. Guo and White, 2008). In the right-hand panel of the same figure, the SFR of the same galaxy sample is shown, also as a function of stellar mass and at $z = 0$. This plot highlights the scatter in star formation properties of the galaxies we have selected for investigating X-ray emissivity; at a stellar mass comparable to that of the Milky Way, the scatter is approximately one decade, ranging from a few, to a few tens, of solar masses per year. One might therefore expect a scatter in the X-ray properties. It is also worth reiterating (i.e. see Chapter 4) that the SFR of the most massive galaxies is higher than observed, and so the simulations feature a population of massive blue elliptical galaxies that are unlikely to be realistic.

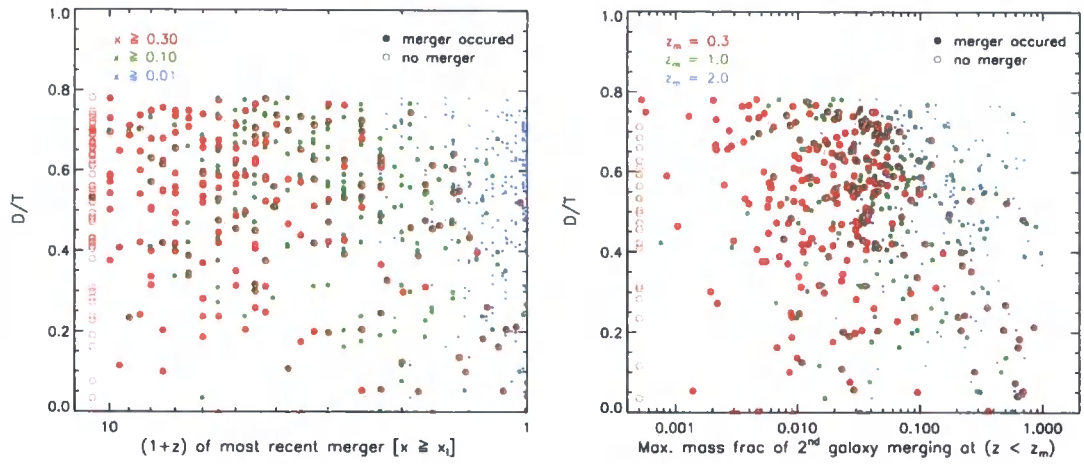

Figure 6.6: The relationship between galactic morphology (quantified by D/T ratio) and the merger history of the parent subhalo. *Left:* the redshift of the most recent major merger, for three values of the mass ratio defining a 'major' merger. *Right:* the maximum mass ratio for mergers occurring after three given redshift limits.

6.3.1 Correlation with merger history

The fragility of discs to merger events frequently guides the selection of the haloes that are used for disc formation studies with zoomed ICs. The halo resimulated by Okamoto et al. (2005) and Okamoto et al. (2008b) was chosen because its last major merger occurred at $z > 1$, whilst the halos adopted by Governato et al. (2007) all had their last major merger at $z \geq 2.3$. Merger trees enable an examination of the relationship between the redshift of the last 'major merger' (and the mass ratio adopted to define a major merger) and the resulting D/T at $z = 0$. The left-hand panel of Figure 6.6 shows the D/T ratio as a function of the redshift of the last major merger of a galaxy's parent subhalo. The mass ratio of the merger,

$$x = \frac{M_{secondary}}{M_{primary}}, \tag{6.3}$$

between the parent (primary) subhalo and the merging (secondary) subhalo, that is used to define a major merger, was varied, $x \geq [0.01, 0.1, 0.3]$, so that each galaxy contributes three points to the plot. The naïve expectation that high D/T ratios are achieved when the most recent major merger occurred at high redshift, is found to be a good approximation, as illustrated by the dearth of red points (i.e. high mass ratio mergers) at low redshift and high D/T. Moreover, we see that a weak trend is present such that, in gen-

eral, higher merger ratios are restricted to higher redshifts in order to yield a given D/T, as illustrated by the dearth of red points (i.e. high mass ratio mergers) at low redshift and high D/T. The right-hand panel shows the 'orthogonal' projection of the problem, showing the maximum merger ratio, x, of a galaxy's subhalo when the final major merger occurs at a redshift below a given value. The naïve expectation in this case is that a higher redshift limit will enable a galaxy to retain a high D/T for higher values of x. This is also found to be reasonable, as no red points (recent mergers) are found at high D/T and high mass ratio.

It is not advocated here that a precise prediction of a galaxy's morphology can be ascertained from knowledge of the merger history of its parent subhalo, but nonetheless a fair rule of thumb follows from these plots: in general, D/T > 0.5 requires the final merger of $x \sim 0.1$ to have taken place at $z > 0.3$, for mergers of $x \sim 0.3$ the restriction is $z \sim 1$, whilst mergers occurring at $z > 2$ have little effect upon the morphology of a galaxy at $z = 0$.

6.4 Emission properties

To allow a simple comparison of the properties of galaxies and their associated gas, it is desirable to compute, in post-processing, the optical luminosity (e.g. in the K-band) of galaxies, and the X-ray luminosity (e.g. in the *ROSAT* 0.5-2.0 keV band, which is commonly also cited for *Chandra* luminosities) of the hot gas surrounding the galaxies.

6.4.1 Optical luminosity

Optical properties are computed by considering each star particle as a simple stellar population (SSP), a reasonable assumption since the masses of star particles are comparable to the masses of star clusters. The population synthesis software of Bruzual and Charlot (2003, hereafter BC03) returns, for a given age, metallicity and IMF, a normalised (to 1 $M_\odot$) spectral energy distribution (SED) for an SSP, in the range 91 Å to 160 μm. The spectrum is multiplied by the transmission function of a given filter and integrated over wavelength to yield a filter-specific luminosity for each particle. The galactic luminosity is simply the sum of its constituent particle luminosities; it is reasonable to neglect dust in this case since K-band corrections for extinction are small.

6.4.2 X-ray luminosity

The X-ray luminosity, L_X, at a frequency, ν, of a parcel of gas is given by:

$$L_X(\nu) = \int n_e n_H \Lambda(T, Z_i, \nu) dV, \tag{6.4}$$

where n_e and n_H are the electron and proton number densities of the gas, dV is the volume, and $\Lambda(T, Z_i, \nu)$ is the spectral cooling function[3], which depends on the temperature T and the abundance of elements, Z_i. In the regime where Bremsstrahlung emission dominates the cooling function, the most important contributors are iron and oxygen.

We compute X-ray luminosities by assigning particle densities, temperatures, and element abundances to a uniform 3D mesh using the SPH smoothing kernel. We excise the contribution of dense equation of state particles and cold particles ($T < 10^5$ K) by setting their SPH kernel weight to zero when interpolating to the mesh. The cold particles will not affect the X-ray emission anyway, but the dense equation of state particles can unduly affect the emission properties of neighbouring hot, low density gas particles (e.g. Ritchie and Thomas, 2001; Toft et al., 2002).

For each grid cell we also compute the value of the cooling function by interpolating within a pre-computed table cooling function table that we generate using the Astrophysical Plasma Emission Code[4] (APEC). For a given temperature and set of abundances, APEC calculates an ensemble of X-ray spectra (one for each elemental species) over the range 0.02-50 keV. The spectra that APEC produces assume the solar abundance ratios of Anders and Grevesse (1989), however it is straightforward to modify the spectra for arbitrary abundances. In particular, the normalisation of each spectrum is adjusted to account for the abundances computed self-consistently in the GIMIC simulations. The individual spectra are then summed to yield a composite X-ray spectrum, which is then integrated over the soft X-ray band of 0.5-2.0 keV. This summation is therefore the numerical solution of Equation 6.4.

The total X-ray luminosity of a system is the summation of all individual cell luminosities for cells whose geometric centres lie within the virial radius of the system. We have verified the accuracy of our results by comparing the luminosities computed using the grid method described above versus a method which computes the luminosities of

[3]Heating is negligible in this regime.

[4]see http://cxc.harvard.edu/atomdb/sources_apec.html

individual SPH particles (e.g. as per Roncarelli et al., 2006). The results are typically within a few percent of each other for the two methods. We prefer the grid method, as it allows us to produce X-ray maps; maps corresponding to the galaxies shown in Figures 6.2 & 6.3 are shown in Figure 6.7.

6.5 Results

A stringent test of the simulations, and our post-processing techniques, is provided by the $L_X - L_K$ relation, since it is well constrained observationally and compares a gas property with a stellar property. This relation is shown in Figure 6.8, and compared with the observed scaling relations for early-type galaxies, given by Jeltema et al. (2008, hereafter JBM08), which are separated into field, group and cluster samples. By construction, the sample of simulated galaxies features only relatively isolated galaxies, that are best considered as field galaxies at low-masses, or the brightest galaxy within a group or cluster at higher masses. To elucidate any trends with the morphological type of the galaxy, we plot late-types (D/T > 0.5) with blue triangles and early-types (D/T < 0.5) with red squares. Whilst the scatter in the relation is rather large, both morphological types appear to adhere to the same approximate scaling relation, which is roughly fit by the JBM08 relations over two orders of magnitude in *K*-band luminosity, and five orders of magnitude in soft X-ray luminosity. The simulations therefore appear to produce a realistic halo luminosity for a given stellar mass (for which *K*-band luminosity is an excellent observational proxy). The correspondence between the simulated and observed $L_X - L_K$ relations indicates that GIMIC realistically reproduces the emission properties of galaxies and their haloes. The assumption that the simulated $L_X - v_c$ also bears a close resemblance to the actual relation therefore seems reasonable. We show the simulated relation in Figure 6.9, and compare with both the simple analytic prediction of WF91, and the upper limits inferred from the observations of B00. We also include modifications to the WF91 model; as described by B00, assuming the hot gas has an isothermal density profile ($\rho(r) \propto r^{-2}$). In this case the cooling time is given by

$$t_{\rm cool}(r) = \frac{192\pi\Omega_{\rm m} G m_{\rm H}^2 r^2}{49 f_{\rm g}\Omega_{\rm b}\Lambda}, \tag{6.5}$$

where $f_{\rm g}$ is the fraction of the universal baryon density, in the halo, remaining in gaseous form: this is commonly assumed to be unity. It follows that cold gas flows into the

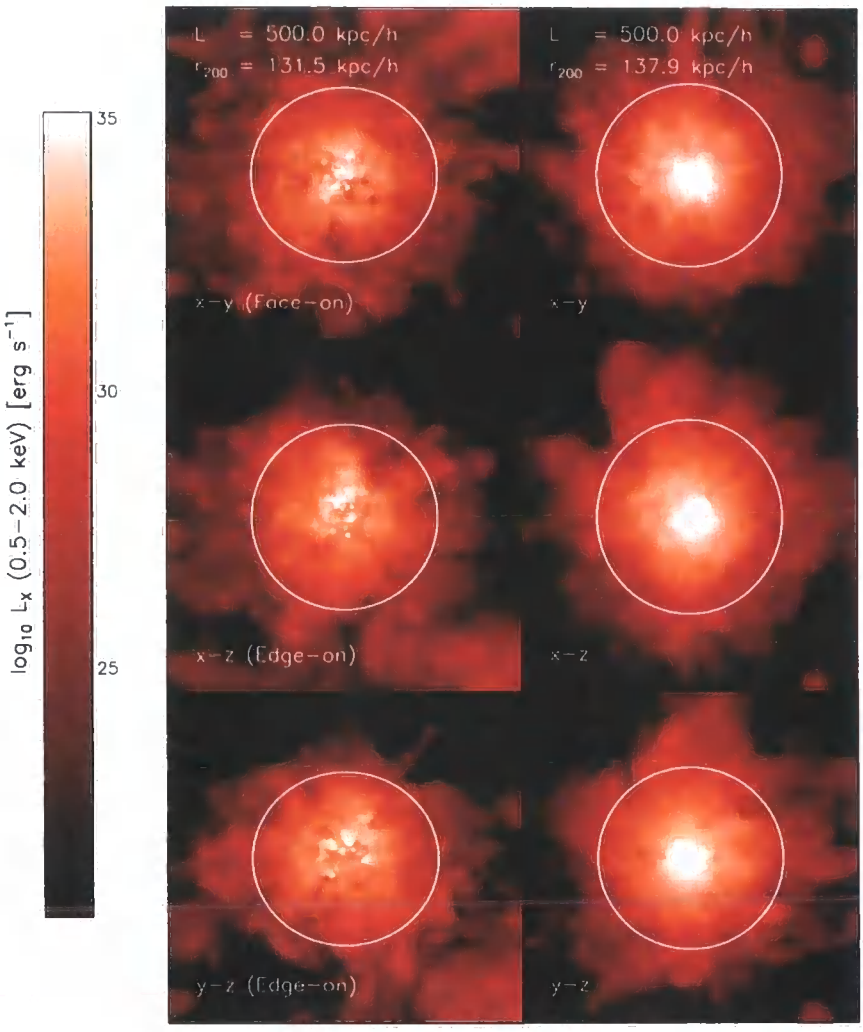

Figure 6.7: Projected X-ray emission, summed along each of the three principal axes, from the haloes of the galaxies shown in Figures 6.2 and 6.3. The late-type galaxy is shown in the left-hand column, the early-type in the right-hand column. The centre panel (x-z) is the corresponding projection to those in Figures 6.2 & 6.3 . The strong dependence of emissivity on density ($L_X \propto \rho^2$) is evident, as emission peaks sharply towards the halo centre.

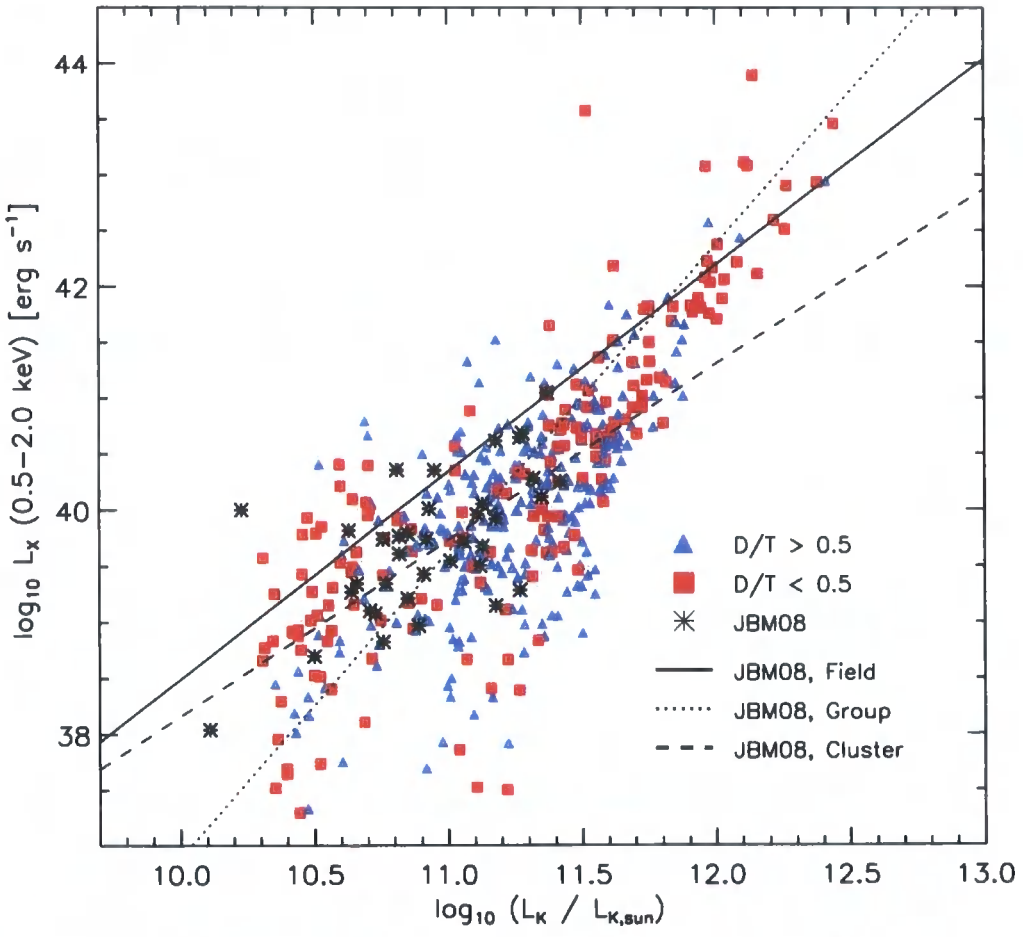

Figure 6.8: The soft X-ray (0.5-2.0 keV) luminosity of the sampled gas haloes as a function of the *K*-band luminosity of their galaxies. Galaxies are split into late- (blue triangles) and early-types (red squares). Data points are from Jeltema et al. (2008) (black asterisks), as are the overplotted fits to their sample, split by the environment of the galaxy.

cooling radius at a rate

$$\dot{M}_{\rm cool}(r_{\rm cool}) = \frac{1}{2}\frac{f_{\rm g}\Omega_{\rm b}}{\Omega_{\rm m}}\frac{v_{\rm c}^2(r_{\rm cool})r_{\rm cool}(v_{\rm c},z)}{Gt_0}, \tag{6.6}$$

where t_0 is the characteristic cooling time of the system. Following WF91, we assume this is the Hubble time at $z = 0$. We construct the analytic relationship using the GIMIC cooling rate, $\Lambda(\rho, T, Z, z)$ assuming $\rho = 200 f_{\rm g}\Omega_{\rm b}\rho_{\rm c}(z)$, $f_g = 1$, $T = T_{200}$ and primordial abundance. This model is labelled '(WF91)' on Figure 6.9. Since winds have a marked effect on the fraction of halo mass in the gaseous form (e.g. Section 4.4.4), we also construct an $L_{\rm X} - v_{\rm c}$ relation for which we replace $f_{\rm g} = 1$ in Equations 6.5 & 6.6 with the median fraction of baryons in the gas phase with $T > 10^5$ K, within bins of $v_{\rm c}$. This model is labelled '(WF91, fb)'. Similarly, we create a model featuring this modification, for which we also modify the cooling rate to account for the median metallicity of this gas; this model is labelled '(WF91, fb, Z)'. The emissivity of the simulated haloes follows a well-defined trend whose scatter at $v_{\rm c} \sim 200$ km s^{-1} (similar to that of the Milky Way's halo, Binney and Tremaine, 1987) is approximately an order of magnitude, similar to the scatter in the star formation rate of galaxies hosted by similar haloes (Figure 6.5). Galaxies exhibiting very high emissivity at high circular velocity correspond to the anomalous class of massive blue ellipticals with very high star formation rates.

The simplest cooling flow model is a poor approximation to the simulated X-ray emissivity, particularly for low-mass haloes: at $v_{\rm c} = 100$ km s^{-1} the simulated emissivity is roughly 2-3 orders of magnitude below the WF91 prediction. Incorporating the measured gas fraction from the simulated haloes markedly improves the agreement between the analytic and simulated values, indicating that $f_{\rm g} = 1$ is a poor approximation, albeit one that is trivially remedied by calibration from numerical simulations. The (WF91, fb) predicted emissivity remains greater than the simulated values, however, and the inclusion of the mean halo gas metallicity from the simulations drives the analytic prediction higher still, since efficient metal cooling reduces $t_{\rm cool}$ and so increases $\dot{M}_{\rm cool}$.

A significant discrepancy between the analytic model and the simulated haloes remains, and is indicative of inaccurate assumptions in the cooling flow model. The fundamental basis of the model is the gas profile, assumed here to be isothermal, $\rho(r) \propto r^{-2}$, however it is not unreasonable to suspect that the profiles of simulated haloes differ strongly from isothermal, perhaps because of winds. Spherically averaged radial density profiles, measured from the simulations for haloes binned by mass, are shown in Figure

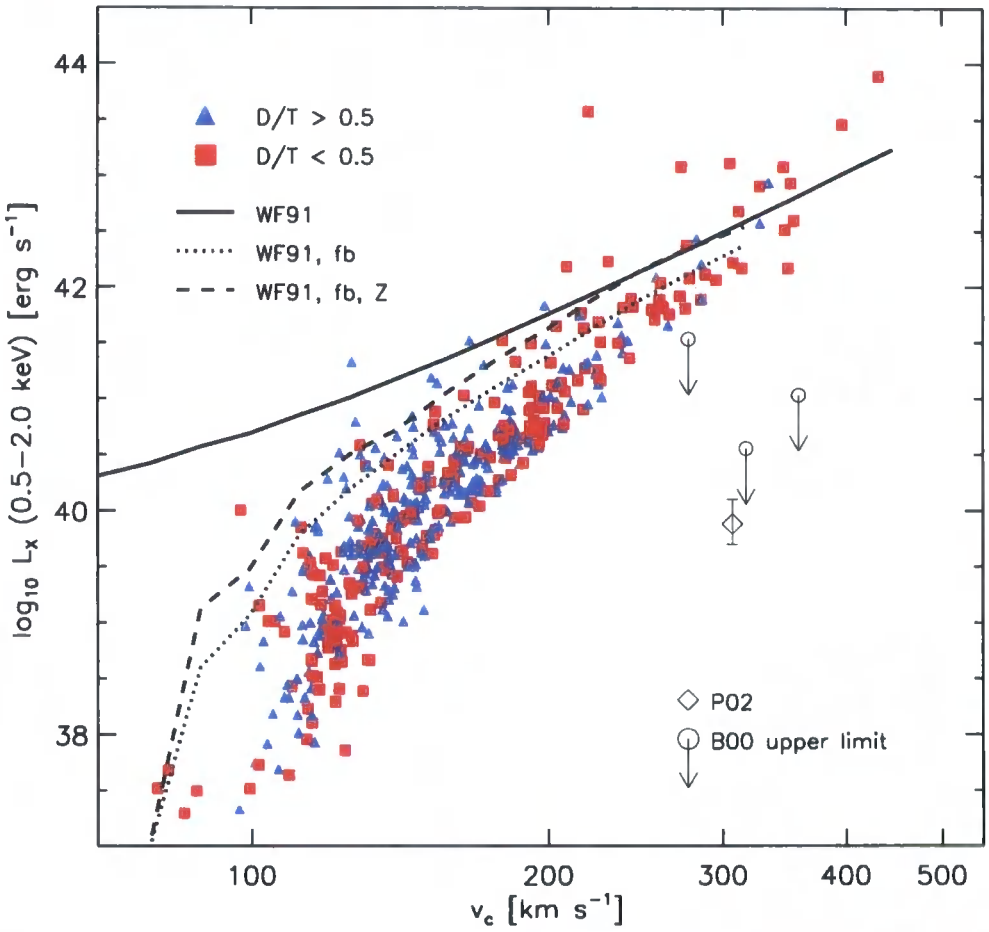

Figure 6.9: The $L_X - v_c(r_{200})$ relation constructed from the halo sample, and compared with the analytic prediction of WF91 (solid line). Also shown are modified analytic relations, based on WF91, that use the simulated haloes to calibrate the variation of the gas fraction with mass in one case (dotted line), and both the gas fraction and the gas metallicity with mass in another (dashed line). The upper limits from the B00 study are shown (circles with arrows), as is the detection reported by P02 (diamond).

6.10 and compared with an isothermal profile that is normalised to have mean enclosed density of $200(\Omega_b/\Omega_m)\rho_c$. The profiles are not self-similar, the lowest mass haloes deviating strongly from isothermal and exhibiting a constant density core within the inner ~ 20 per cent of r_{200}. More massive haloes do not exhibit cores but are nonetheless underdense relative to the isothermal profile. This is unsurprising, since it was shown in Chapter 4 (Figures 4.13 & 4.14) that winds eject baryons efficiently from low mass haloes, and redistribute and reheat gas in more massive haloes.

Variation in the gas profiles leads to differences in the cooling time profiles, $t_{cool}(r) = u(r)/\dot{u}(r)$. Cooling profiles measured from the simulated haloes (in the same mass bins as Figure 6.10) are shown in Figure 6.11. We compute t_{cool} using the same grid from which we produce the X-ray maps: cells are binned (using their geometric centre) into spherical annuli, and the cooling time:

$$t_{cool}(\rho, u) = -\frac{u}{\dot{u}} = \frac{3k_B T}{2\mu} \frac{m_H}{\rho(1-Y)^2(\mathcal{C}-\mathcal{H})}, \tag{6.7}$$

is computed, using SPH-interpolated quantities. The measured profiles are compared with the WF91 profiles (Equation 6.5), shown with dotted lines. As noted by WF91, $t_{cool} \propto f_{gas}^{-1}$, so the cooling time profile resembles an inversion of the gas density profile. Moreover, the normalisation of $t_{cool}(r)$ as a function of mass, is inverted relative to the analytic trends. The analytic prescription posits that low mass haloes are the most rapidly cooling, since their virial temperatures are the lowest, but the simulations indicate that the most massive haloes have the shortest cooling times since they retain the greatest gas fraction.

Single phase cooling flow models (Thomas et al., 1986; Bertschinger, 1989, WF91) posit that the X-ray emissivity varies linearly with the deposition rate of cold gas, $\dot{M}_{cold}$, which itself is inversely proportional to the characteristic cooling time of a halo, t_0. The significant differences between the analytic cooling time profiles and those measured from the simulated haloes, are the reason for the difference between the WF91 $L_X - v_c$ relation and that measured from the simulations. Whilst some fraction of the gas in haloes is lost to star formation, this is dwarfed by the very efficient gas ejection that results from the implementation of galactic wind feedback in the GIMIC simulations: this is therefore the chief omission from the WF91 model that results in its over-prediction of the soft X-ray emissivity of galactic haloes.

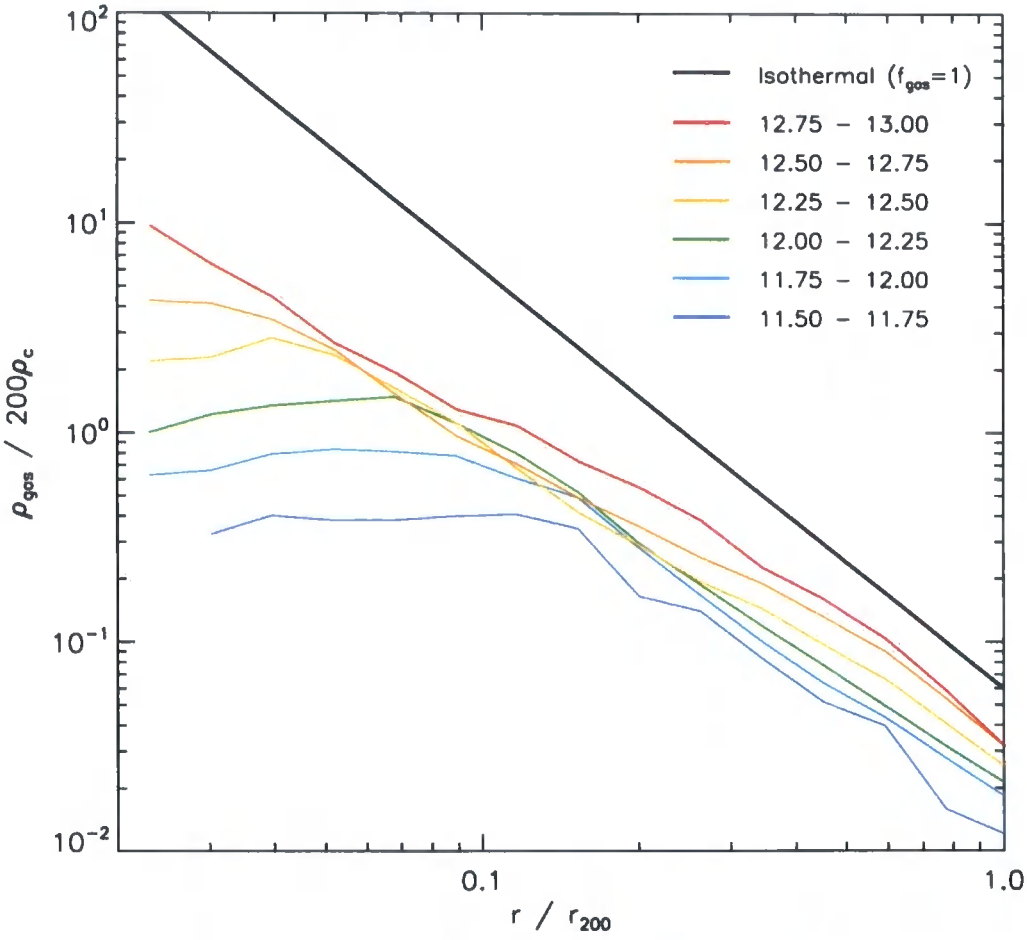

Figure 6.10: Spherically averaged radial gas density profiles, for the halo sample binned by total halo mass. Colours correspond to mass bins as shown in the legend: quoted limits are $\log_{10} M_{200}$ [$M_\odot$]. For comparison, the isothermal profile of a halo retaining its cosmic baryon share is also shown. Low-mass haloes in particular exhibit a strong deviation, featuring a constant density core, whilst more massive haloes exhibit a more subtle change in slope towards the centre.

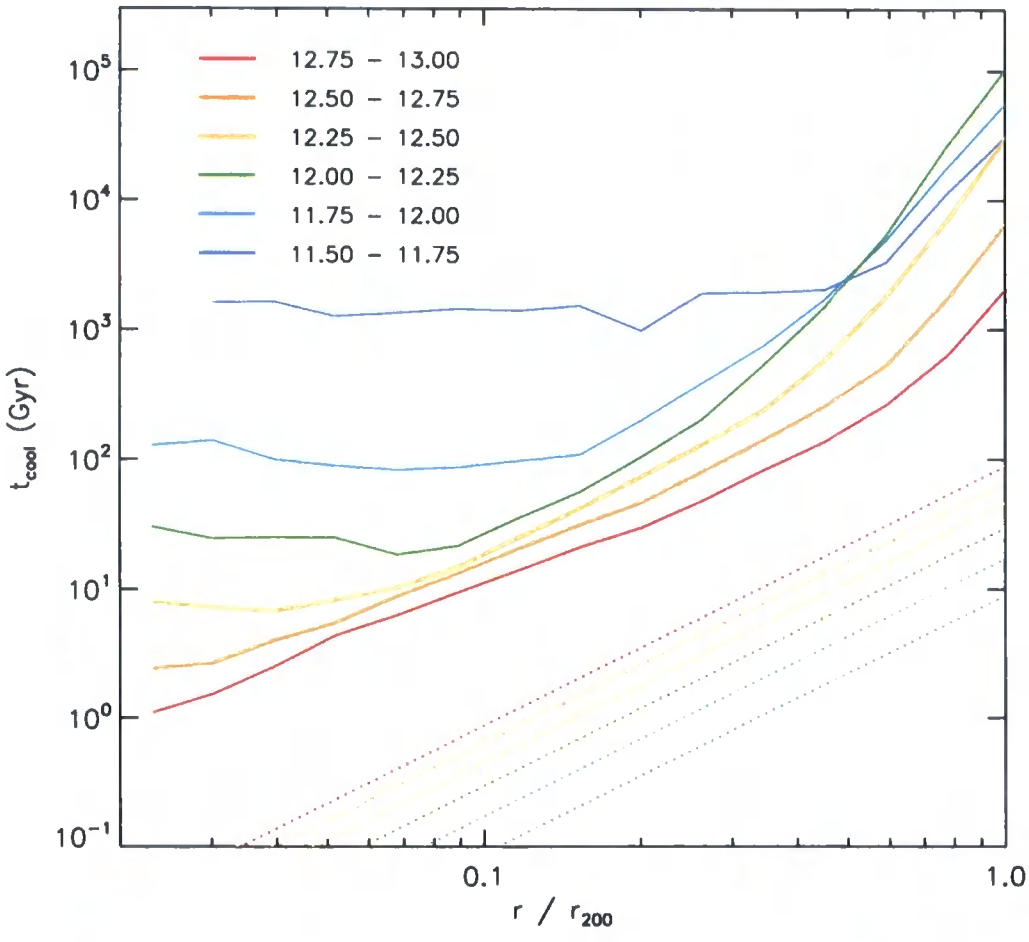

Figure 6.11: Spherically averaged radial gas cooling time profiles, for the halo sample binned by halo mass (solid lines). For comparison, the corresponding WF91 cooling time for haloes with the central mass (in log space) of each bin is shown with a dotted line. See text for further details.

In spite of the correspondence between the $L_X - L_K$ relation in the simulations and the data of JBM08, it remains unclear whether the X-ray emissivity of the simulated haloes, as a function of circular velocity, is a close approximation to reality, since few observational constraints exist. The lower X-ray emissivity measured in GIMIC, relative to WF91, remains far in excess of the upper limits derived by B00 from *ROSAT* data. We note that a reduction in the estimated circular velocities of their host haloes would ease some tension: this seems reasonable, because the v_c in this case was estimated from the maximum rotation velocity of the optical disc, assuming an isothermal halo (i.e. v_c independent of r). Haloes in N-body (i.e. collisionless) simulations are more accurately fitted by the NFW profile, for which $v_c(r_{200})$ is lower than the maximum rotation velocity. An NFW starts as $\rho(r) \propto r^{-1}$ at the centre, becomes isothermal, $\rho(r) \propto r^{-2}$, at the scale radius, and decays as $\rho(r) \propto r^{-3}$. The circular velocity curve is therefore $v_c(r) \propto r^{1/2}$ at the centre, $v_c(r) \propto r^0$ at the scale radius, and $v_c(r) \propto \ln(r/2)$ at towards the virial radius, such that it rises from the centre to a broad peak before dropping. Adiabatic contraction of haloes induced by the accumulation of baryons at their centre (e.g. Eggen et al., 1962; Barnes and White, 1984; Gnedin et al., 2004) is likely to exacerbate the difference between the simulated curves and an isothermal profile. We show the peak of the circular velocity curve, as a function of the value at the virial radius, in Figure 6.12. The peak is typically a factor of two higher than the virial value for all haloes; the difference is exacerbated at higher resolution. Lowering the estimated circular velocity of the B00 and P02 values by this factor would bring the data and the simulations into close agreement.

6.6 Discussion

Analytic models of galaxy formation posit that late-type galaxies remain in the act of formation at the present epoch. Consequently, it is expected that the accretion of gas onto the disc from the outer halo exhibits a strong cooling signature that should be readily visible with modern X-ray observatories as extended diffuse emission around the galaxy and inner halo. The dearth of observations of such cooling flows presents a challenge for galaxy formation models; hydrodynamic simulations represent an excellent tool for testing such models, since they eschew several key approximations inherent to the analytic prescriptions.

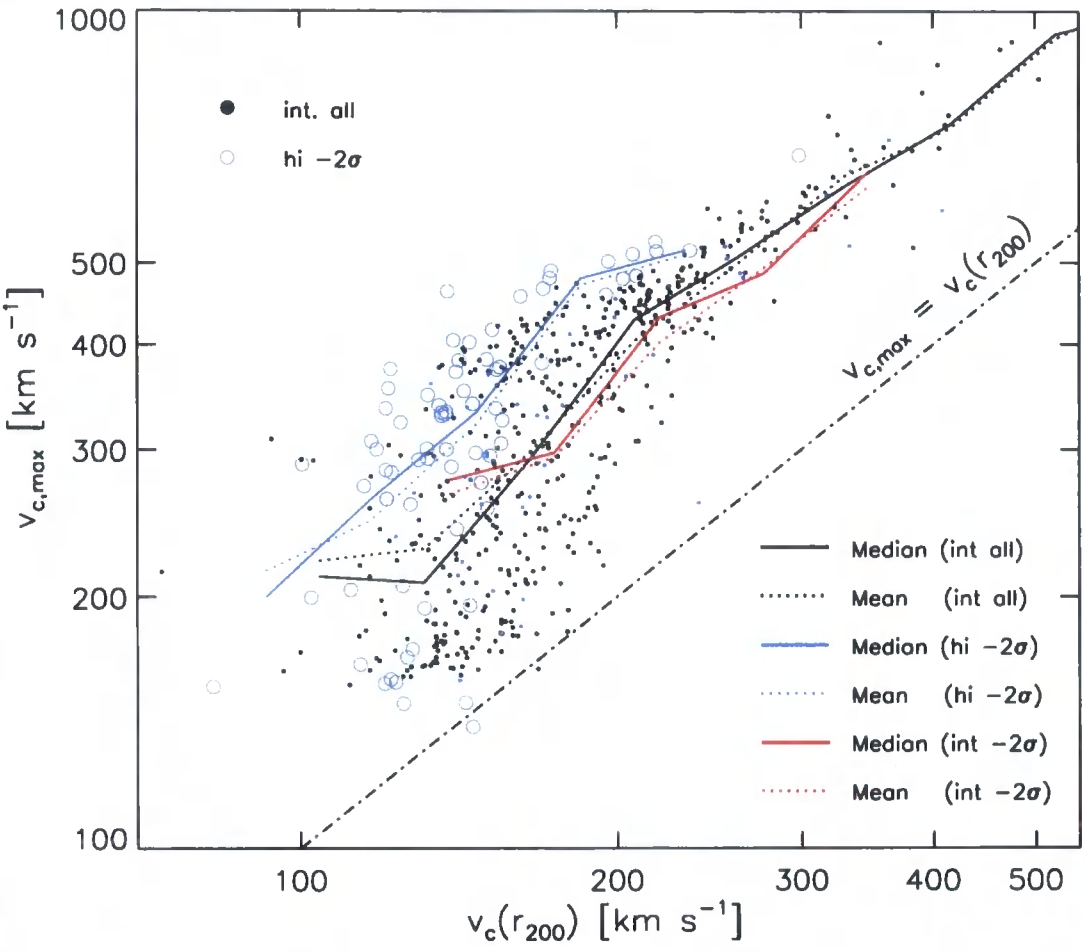

Figure 6.12: The maximum value of the circular velocity profile, $v_c(r)$ as a function of the circular velocity at the virial radius, $v_c(r_{200})$. Since the circular velocity curve is flat only for an isothermal profile, the non-isothermal profiles of the simulated haloes do not follow the 1:1 relationship (dot-dashed line), but rather their peak is significantly greater than the value at the virial radius.

We have described methods to classify simulated galaxies according to morphology, and to compute both their optical and X-ray emissivities. The GIMIC simulations appear to produce higher, more realistic fractions of late-type galaxies than comparable simulations. From a basic comparison with high-resolution simulations of individual discs featuring different feedback prescriptions, it is tentatively suggested that the inclusion of the kinetic feedback scheme is largely responsible for this. The relatively high-resolution of the latest generation of simulations may also assist the production of galaxies with higher disc-to-total (D/T) ratios, since we find that resolution has a significant effect upon the morphology of galaxies in these simulations. In agreement with naïve expectation, morphology is also found to correlate with merger history, such that high D/T ratios require, in general, that any high mass ratio mergers take place at high redshift, and similarly, that any low-redshift mergers are of a low mass ratio. At $z = 0$, high D/T ratio galaxies are found preferentially at $M_\star \sim 10^{10.5} - 10^{11}\ h^{-1}\ \mathrm{M}_\odot$.

However, we find that the morphology of simulated galaxies has no clear effect upon the X-ray properties of their host halo: splitting galaxies into early- (D/T < 0.5) and late-types (D/T > 0.5), we find similar $L_X - L_K$ and $L_X - v_c$ relations. The $L_X - L_K$ relation of the simulated haloes corresponds closely to that observed by JBM08 for a sample of early-type galaxies. Comparison of the $L_X - v_c$ relation for the simulated haloes with the prediction of the WF91 analytic model indicates that a simple modification of the assumed gas fraction (as a function of halo mass, $f_{\mathrm{gas}}(M_{200})$) significantly improves the correspondence between the model and the simulations, and highlights the importance of numerical simulations as a means to calibrate analytic (and semi-analytic) models.

However, modification of the gas fraction does not fully resolve the difference in $L_X(v_c)$; we show that this is due to the assumption of isothermal gas density profiles. Significant changes to f_{gas} result in gas profiles that deviate from isothermal, such that low mass haloes (for which f_{gas} is most strongly reduced by kinetic feedback) have gas density profiles exhibiting constant density cores. The change in density profile directly affects the cooling time profile, because $t_{\mathrm{cool}}(r) \propto f_{\mathrm{gas}}(r)^{-1}$. More significantly, the efficient ejection of gas from low-mass haloes by kinetic feedback means that massive haloes have the shortest cooling times in the simulations. This is the contrary to the prediction of WF91 that low-mass haloes are the most rapidly cooling. For this reason, the X-ray emissivity of simulated haloes drops off very rapidly towards low circular velocity, rela-

tive to the WF91 model.

It remains difficult to connect this area of galaxy theory with the real Universe, owing to the dearth of confirmed detections of, and upper limits for, extended galactic X-ray emission. Whilst the correspondence of the GIMIC $L_X - L_K$ relation with the data is indicative that the X-ray properties of the simulated haloes are reasonable, direct comparisons with the data of B00 and P02 indicate the even the lower luminosities measured from the simulations remain far in excess of the data: the P02 detection of NGC 5746 is two orders of magnitude less luminous than comparable galaxies in GIMIC, and has even been questioned by Wang (2007).

However, we argue that the simplification of associating the maximum observed disc rotation speed with the circular velocity of the host dark matter halo at the virial radius, v_c, is a poor approximation. Theoretically, this is formally accurate for a density profile (of both baryons and dark matter) that is isothermal, and unaffected by the evolution of baryonic mass within the halo. Dark matter-only simulations indicate that the NFW profile is a more accurate fit to halo profiles; the peak in the circular velocity profile is greater than the value at r_{200} for this functional form. Contraction of the halo due to the formation of the central galaxy exacerbates this difference, and so it seems reasonable to suppose that the circular velocities of the B00 and P02 *may* have been overestimated. In this case, the tension between the observations and theory is eased.

Minor modifications to simplified analytic theories of galaxy formation yield a close agreement between their predicted X-ray luminosities and those measured from detailed numerical simulations - simulations that successfully reproduce many other observed properties of galaxies and their gas haloes. It is reasonable to argue that the primary driver for further advances in this field will therefore be improved observational constraints on the X-ray emissivity of gas haloes. Such constraints are a timely necessity, since they may being into sharper focus the root cause of this serious discrepancy between theory and observation, and may provide further insight into the nature of feedback from galaxies. We have shown here that feedback significantly affects the expected X-ray emissivity of gas haloes and, as argued throughout this thesis, is responsible for shaping many key observable properties of galaxies.

Chapter 7 | *Conclusions*

7.1 Discussion

Galaxy formation has become a more precise science in recent times, owing to a number of synergistic observational and theoretical developments. Firstly, ambitious surveys of both the cosmic microwave background radiation and the local galaxy distribution have ushered in the era of precision cosmology. Analyses of these data have firmly established the Λ cold dark matter paradigm as a widely accepted theory of structure formation, that serves as a basis for the construction of galaxy formation models. Secondly, huge strides have been made in observing both galaxies and the IGM at high-redshift, thus allowing evolutionary trends to be inferred. Finally, the field has been driven rapidly by consistent developments of algorithms and computing hardware that enable ever more detailed and ambitious models to be tested numerically.

This thesis has focussed on the evolution of cosmic baryons within the ΛCDM cosmogony using numerical hydrodynamical simulations. Using an ensemble of non-radiative simulations run with the GADGET2 TreePM-SPH code, we showed in Chapter 3 with unprecedented statistical power that virialised dark matter haloes of any mass - from the haloes that are expected to host dwarf galaxies, to those hosting rich clusters of galaxies - accrete gas in a self-similar fashion, leading to a universal baryon fraction of ~ 90 per cent. This result is at odds with the 'pre-virialisation' gravitational heating scenario (Mo et al., 2005), that predicts a suppression of accretion onto low-mass haloes caused by heating from the partial collapse of large-scale structures. In Chapter 3 we also developed a toy model to test the effect of photo-heating on the accretion of gas by low-mass haloes. Our findings suggest that photo-ionisation heating weakly affects accretion, perhaps suppressing star formation in only the smallest dwarf spheroidal galaxies, and that its efficacy may be overestimated in semi-analytic models. This latter prediction has recently been supported by the analysis of more detailed simulations by Okamoto et al.

(2008a).

In Chapter 4 we introduced the *Galaxies-Intergalactic Medium Interaction Calculation* (GIMIC), a new suite of simulations featuring a wide range of physical mechanisms relevant to galaxy formation, such as radiative cooling and heating, star formation, chemodynamical evolution, and both thermal and kinetic feedback from supernovae. The key result of Chapter 4 is the dependence of the star formation rate density, $\dot{\rho}_\star(z)$, on large-scale environment. Whilst the shape of this quantity is independent of environment, and broadly follows the form inferred observationally, its normalisation varies by a factor of ~ 10 from the deepest voids to the richest clusters. We argue that this result is largely independent of our model implementation, following primarily from the differing shapes of the mass function in different environments. This finding should be considered as an additional systematic uncertainty for observational surveys.

The combination of $\dot{\rho}_\star(z)$ from each GIMIC simulation, into an overall estimate for the entire Millennium Simulation volume, concurs well with observational estimates. However, we find that the star formation rate at low-redshift in our simulations is greater than observed, and so we infer that an additional source of feedback, such as the energy output of AGN, might be required to reconcile our model with the data. This conclusion is similarly inferred from the finding that the stellar fraction of groups and clusters in GIMIC exceeds observational constraints, and so it appears that the star formation rate of massive galaxies is not suppressed sufficiently by our feedback scheme. Nonetheless, we find that galactic winds prove to be a crucial mechanism for regulating star formation, since the massive galaxies for which AGN might additionally be required, are assembled from smaller systems that form at high redshift, and without winds these progenitors galaxies would grow far too massive.

In Chapter 5 we explored the evolution of the cosmic baryons, again focussing upon the role of large-scale environment. The key result from this chapter is the sensitivity of the mass fraction, and volume-filling fraction, of the warm-hot intergalactic medium (WHIM). The overall mass density of baryons in the Universe is predicted by nucleosynthesis arguments, and observations of the cosmic microwave background radiation, to be significantly greater than the mass currently accounted for observationally. It is widely believed that the 'missing mass' resides in the WHIM, which is difficult to detect observationally owing to its low density and high ionisation state; the prediction in Chapter

5 that its distribution is very sensitive to environment is therefore timely, since efforts to detect the WHIM shall be stepped up with the forthcoming installation of the *Cosmic Origins Spectrograph* aboard *HST*. It is interesting to note that the 'life-story' of the gas comprising the WHIM is remarkably independent of the redshift at which the WHIM is selected: i.e. the sources and sinks of the gas comprising the WHIM at $z = 4$ are similar to those of the gas comprising the WHIM at low redshift. This hints at a rapid cycling of gas through the galactic and WHIM phases, and we find that this is indeed the case: by $z = 0$, we estimate that 60 per cent of all baryonic mass has been in the WHIM phase.

We also showed in Chapter 5 the evolution of the metal mass-density, and the metallicity, of gas as a function of temperature, and whether it resides in dark matter haloes, or the interhalo medium. Our modelling indicates that for $z \lesssim 3$, stars are the dominant metal repository, and that galactic gas and warm, interhalo gas (the dominant component of the WHIM) host a roughly equal mass of heavy elements. However, the vastly different *overall* mass in these phases is very different, and so the metallicity of galactic gas is a factor of ~ 30 greater than that of warm, interhalo gas. Our modelling leads to a mean stellar metallicity at $z = 0$ that is supersolar, at $\sim 3\ Z_{\odot}$. The mean metallicity of the Universe reaches $\sim 0.1\ Z_{\odot}$ following a steady rise from the earliest epoch of the simulation, but in contrast the metallicity of shocked gas (warm and hot gas, both within and external to haloes) remains remarkably constant in metallicity ($Z \sim 0.1\ Z_{\odot}$) over the period $9 \gtrsim z > 0$.

Finally, in Chapter 6 we exploited the very detailed treatments of baryon physics in GIMIC to compare the cooling rate and X-ray emissivity of haloes with the predictions of the analytic model of White and Frenk (1991). In this chapter, we presented post-processing techniques to classify simulated galaxies according to morphology, to trace the properties of galaxies and their haloes throughout simulations using merger trees, and to compute the optical luminosity of galaxies and the associated soft X-ray luminosity of their gas haloes. The galaxies identified in the GIMIC simulations exhibit greater disc-to-total (D/T) stellar mass ratios than generally reported in the literature; we believe this is due to our adoption of a kinetic feedback scheme to regulate star formation. Our dynamical decomposition scheme demonstrates that morphology correlates with stellar mass, with the fraction of galaxies of a high D/T value peaking at $M_{\star} \sim 10^{10.5} - 10^{11}\ h^{-1}\ M_{\odot}$. This mass is slightly lower in the -2σ region at high resolu-

tion, and so we infer that morphology is also weakly sensitive to resolution; however, the implementation of the baryon physics is of greater significance. The D/T ratios found by Croft et al. (2008) from GADGET2 simulations, of resolution bracketed by that of the intermediate- and high-resolution GIMIC simulations, were much lower than reported here. Finally, we show that the D/T ratio of a galaxy is significantly affected by the merger history of its parent (sub)halo, since high D/T ratios are not found for galaxies that have experienced recent major mergers.

Contrary to naïve expection, morphology does not affect the scaling relations of halo X-ray luminosity with either the *K*-band luminosity of the hosted galaxy, nor the halo circular velocity. Early- and late-type galaxies from the simulations closely follow the observed $L_X - L_K$ trend for early-type galaxies derived by Jeltema et al. (2008). We infer that, since this observed trend is accurately reproduced by the simulations, the $L_X - v_c$ relation yielded by the simulations also accurately reflects the true relation, for which observations are sparse; unlike the $L_X - L_K$ relation, an observed trend for early-types cannot be constructed since $v_c(r_{200})$ is inferred from the rotation speed of galaxy discs.

X-ray luminosities from the simulations are, in general, lower than predicted by WF91, particularly for low-mass haloes. We have demonstrated that this is primarily due to the ejection of gas from haloes, which is not accounted for by the analytic theory; by calibrating $f_g(M_{200})$ with the simulated haloes, the analytic model and the simulations are brought into much closer agreement. The remaining difference can be traced to the assumption of isothermal gas density profiles by the analytic theory, which is only a reasonable approximation for the massive haloes that are resilient to gas ejection from winds. In low mass haloes, we find that constant density cores are established, producing a knock-on effect in the cooling time profile of halo gas. A key difference is then that low-mass haloes have the *longest* cooling times in the simulations, in contrast to the analytic model for which they have the shortest cooling times.

It is argued here that greater observational constraints are a timely necessity for further constraining this area of galaxy formation theory, since very little data exists for the $L_X - v_c$ relation, and that that does is either an upper limit (B00) or has been questioned (P02). We also highlight the potential for misinterpretation of the disc rotation speed as a proxy for the halo mass, via the assumptions i) that the circular velocity profile of the halo is flat, and ii) that the disc rotation speed traces the circular velocity. We have

demonstrated that the maximum of the circular velocity profile is typically a factor of two higher than the value at r_{200}, owing to deviation from an isothermal density profile, hinting that v_c may have been significantly overestimated in the samples of B00 and P02. Further analysis of the GIMIC simulations would indicate whether the second assumption is accurate.

7.2 Future directions

There are two key aspects to the extension of the work detailed in this thesis: i) improvements to the model adopted for GIMIC, to make our conclusions more robust, and ii) astrophysical applications that can be exploited by this work.

7.2.1 Modelling improvements

The discrepancy between the simulated and observed luminosity functions (Figure 4.6), is a key area for improvement; reconciling the ΛCDM halo mass function with the observed luminosity function is a central question in galaxy formation theory. It is well known that feedback is a critical element of the galaxy formation process, and whilst the adopted scheme within our simulations successfully reproduces the star formation rate density of the Universe, the apportioning of star formation amongst galaxies (or haloes) of differing masses does not precisely concur with observations.

Since the discrepancies are most severe at intermediate and high luminosity, the focus of future improvements should clearly be kinetic feedback (i.e. wind) schemes, and also whether feedback from AGN is necessary. We have shown here that fixed velocity winds imprint an unrealistic feature into the luminosity function at a fixed magnitude (or stellar mass) scale, and so variable velocity winds, such as those advocated by Oppenheimer and Davé (2008a), represent a natural area for exploration. However, winds much faster than the $v_w = 600$ km s^{-1} adopted have not been observed and, moreover, our adopted scheme already invests ~ 80 per cent of the mechanical energy available from the Chabrier IMF, it seems unlikely that such a scheme can, on its own, reproduce the observed $z = 0$ luminosity function.

Investing additional energy into feedback highlights three key options: i) appealing to the radiative energy released by core-collapse SNe, ii) using a top-heavy IMF in

regimes where not ruled out by observations, and iii) coupling feedback from AGN to the cooling gas. Murray et al. (2005) argue that the radiative output of SNe can dominate their mechanical energy by a factor of ~ 100, and so if this energy can be coupled to cooling gas, it would provide an easy solution to the feedback problem, however the degree to which this energy does couple remains highly uncertain. Baugh et al. (2005) appealed to a top heavy IMF during starbursts as a means to reproduce the observed abundance of submillimetre galaxies; in this case, strong winds were sufficient to produce a reasonable fit to the local luminosity function, but this model assumed that baryons could be re-accreted after ejection, and also required an unrealistically high energy budget. Feedback from AGN is perhaps, therefore, the most appealing mechanism with which to augment winds.

Since calculations of the scale of GIMIC are very computationally expensive, smaller simulations would provide a useful test bed for new implementations of feedback mechanisms; either cosmological simulations of smaller volumes, or idealised simulations of isolated haloes, as used by the 'test studies' for the GIMIC and OWLS projects that were presented by Schaye and Dalla Vecchia (2008) and Dalla Vecchia and Schaye (2008). A central question to ask of such tests would be whether new schemes allow a greater abundance of galaxies of luminosity $M_K^{AB} - 5\log_{10} h \sim -20$ to form by $z = 0$, whilst also suppressing the growth of the more luminous galaxies that form in groups and clusters.

7.2.2 Exploiting the simulations

The simulations presented here, in spite of their inability to reproduce precisely the local luminosity function, still represent the forefront of hydrodynamical simulations of galaxy formation. Therefore, a wide range of astrophysical questions may be probed in detail with these resources. In particular, the key advantages of GIMIC should be exploited, namely searches for environmental effects, and the interaction of galaxies and the IGM.

The Lyman-α forest in each region is likely to exhibit strong signatures of environmental variation. This is being pursued in a forthcoming paper (Theuns et al., *in preparation*), whilst the environmental variation of the WHIM, as first highlighted in Chapter 5 (Figure 5.5), is also being followed up in greater detail - with an emphasis on the observable signatures of this effect - in a separate paper (Crain et al., *in preparation*). One key

effect where environment and galaxy-IGM interaction are intimately linked is the ram pressure stripping of gas from satellite galaxies in groups and clusters; a paper exploring this effect is planned (McCarthy et al, *in preparation*), and shall focus on the correspondence between the effect seen in cosmological simulations (i.e. GIMIC), with the analytic model presented by McCarthy et al. (2008), which was derived from idealised simulations of merging haloes.

We also intend to explore the $+2\sigma$ simulation in greater detail, since few clusters have been simulated at such high resolution with a detailed radiative hydrodynamic treatment. We intend to investigate its Sunyaev-Zel'dovich effect signature, with an emphasis on whether the *Planck* satellite might be able to directly image the filaments surrounding massive local clusters such as Coma (McCarthy, Crain & Frenk, *in preparation*). One might also consider studying this system at high redshift, in order to compare its properties with Lyα observations of protoclusters (e.g. Steidel et al., 2000; Matsuda et al., 2004; Ouchi et al., 2008).

In conclusion, we have demonstrated a wide range of applications of cosmological hydrodynamic simulations as tools for generating detailed predictions and for interpreting observations. In particular, the latest generation of calculations such as GIMIC not only accurately reproduce a number of key cosmological measurements, thus strengthening key areas of galaxy formation theory, but also indicate the areas upon which theorists and observers alike might gain the greatest benefit from focussing their efforts, such as the modelling of AGN feedback, directing searches for the WHIM in high-density regions, or acquiring better observational constraints of the X-ray luminosity of gas haloes. Clearly, numerical simulations have an important role to play in the future of this field.

Bibliography

Abadi, M. G., Navarro, J. F., Steinmetz, M., and Eke, V. R.: 2003a, ApJ **591**, 499

Abadi, M. G., Navarro, J. F., Steinmetz, M., and Eke, V. R.: 2003b, ApJ **597**, 21

Abel, T., Bryan, G. L., and Norman, M. L.: 2002, *Science* **295**, 93

Abel, T. and Haehnelt, M. G.: 1999, ApJ **520**, L13

Abel, T., Wise, J. H., and Bryan, G. L.: 2007, ApJ **659**, L87

Adelberger, K. L., Steidel, C. C., Shapley, A. E., and Pettini, M.: 2003, ApJ **584**, 45

Agertz, O., Moore, B., Stadel, J., Potter, D., Miniati, F., Read, J., Mayer, L., Gawryszczak, A., Kravtsov, A., Nordlund, Å., Pearce, F., Quilis, V., Rudd, D., Springel, V., Stone, J., Tasker, E., Teyssier, R., Wadsley, J., and Walder, R.: 2007, MNRAS **380**, 963

Aguirre, A., Hernquist, L., Katz, N., Gardner, J., and Weinberg, D.: 2001a, ApJ **556**, L11

Aguirre, A., Hernquist, L., Schaye, J., Katz, N., Weinberg, D. H., and Gardner, J.: 2001b, ApJ **561**, 521

Aguirre, A., Hernquist, L., Schaye, J., Weinberg, D. H., Katz, N., and Gardner, J.: 2001c, ApJ **560**, 599

Aguirre, A., Schaye, J., Hernquist, L., Kay, S., Springel, V., and Theuns, T.: 2005, ApJ **620**, L13

Allen, S. W., Schmidt, R. W., Ebeling, H., Fabian, A. C., and van Speybroeck, L.: 2004, MNRAS **353**, 457

Anders, E. and Grevesse, N.: 1989, Geochim. Cosmochim. Acta **53**, 197

Ascasibar, Y., Sevilla, R., Yepes, G., Müller, V., and Gottlöber, S.: 2006, MNRAS **371**, 193

Babcock, H. W.: 1939, *Lick Observatory Bulletin* **19**, 41

Bagla, J. S. and Ray, S.: 2005, MNRAS **358**, 1076

Baldry, I. K., Balogh, M. L., Bower, R. G., Glazebrook, K., Nichol, R. C., Bamford, S. P., and Budavari, T.: 2006, MNRAS **373**, 469

Balogh, M. L., Babul, A., and Patton, D. R.: 1999, MNRAS **307**, 463

Balogh, M. L., Navarro, J. F., and Morris, S. L.: 2000, ApJ **540**, 113

Balogh, M. L., Pearce, F. R., Bower, R. G., and Kay, S. T.: 2001, MNRAS **326**, 1228

Balsara, D. S.: 1995, *Journal of Computational Physics* **121**, 357

Bardeen, J. M., Bond, J. R., Kaiser, N., and Szalay, A. S.: 1986, ApJ **304**, 15

Barker, S., de Grijs, R., and Cerviño, M.: 2008, A&A **484**, 711

Barnes, J. and Hut, P.: 1986, Nature **324**, 446

Barnes, J. and White, S. D. M.: 1984, MNRAS **211**, 753

Barnes, J. E. and Hernquist, L. E.: 1991, ApJ **370**, L65

Barth, A. J., Martini, P., Nelson, C. H., and Ho, L. C.: 2003, ApJ **594**, L95

Baugh, C. M.: 2006, *Reports of Progress in Physics* **69**, 3101

Baugh, C. M., Lacey, C. G., Frenk, C. S., Granato, G. L., Silva, L., Bressan, A., Benson, A. J., and Cole, S.: 2005, MNRAS **356**, 1191

Becker, G. D., Sargent, W. L. W., Rauch, M., and Simcoe, R. A.: 2006, ApJ **640**, 69

Beckwith, S. V. W., Stiavelli, M., Koekemoer, A. M., Caldwell, J. A. R., Ferguson, H. C., Hook, R., Lucas, R. A., Bergeron, L. E., Corbin, M., Jogee, S., Panagia, N., Robberto, M., Royle, P., Somerville, R. S., and Sosey, M.: 2006, AJ **132**, 1729

Bell, E. F., McIntosh, D. H., Katz, N., and Weinberg, M. D.: 2003, ApJS **149**, 289

Belokurov, V., Evans, N. W., Irwin, M. J., Lynden-Bell, D., Yanny, B., Vidrih, S., Gilmore, G., Seabroke, G., Zucker, D. B., Wilkinson, M. I., Hewett, P. C., Bramich, D. M., Fellhauer, M., Newberg, H. J., Wyse, R. F. G., Beers, T. C., Bell, E. F., Barentine, J. C., Brinkmann, J., Cole, N., Pan, K., and York, D. G.: 2007a, ApJ **658**, 337

Belokurov, V., Walker, M. G., Evans, N. W., Faria, D. C., Gilmore, G., Irwin, M. J., Koposov, S., Mateo, M., Olszewski, E., and Zucker, D.: 2008, *ArXiv e-prints* 807

Belokurov, V., Zucker, D. B., Evans, N. W., Kleyna, J. T., Koposov, S., Hodgkin, S. T., Irwin, M. J., Gilmore, G., Wilkinson, M. I., Fellhauer, M., Bramich, D. M., Hewett, P. C., Vidrih, S., De Jong, J. T. A., Smith, J. A., Rix, H.-W., Bell, E. F., Wyse, R. F. G., Newberg, H. J., Mayeur, P. A., Yanny, B., Rockosi, C. M., Gnedin, O. Y., Schneider, D. P., Beers, T. C., Barentine, J. C., Brewington, H., Brinkmann, J., Harvanek, M., Kleinman, S. J., Krzesinski, J., Long, D., Nitta, A., and Snedden, S. A.: 2007b, ApJ **654**, 897

Belokurov, V., Zucker, D. B., Evans, N. W., Wilkinson, M. I., Irwin, M. J., Hodgkin, S., Bramich, D. M., Irwin, J. M., Gilmore, G., Willman, B., Vidrih, S., Newberg, H. J., Wyse, R. F. G., Fellhauer, M., Hewett, P. C., Cole, N., Bell, E. F., Beers, T. C., Rockosi, C. M., Yanny, B., Grebel, E. K., Schneider, D. P., Lupton, R., Barentine, J. C., Brewington, H., Brinkmann, J., Harvanek, M., Kleinman, S. J., Krzesinski, J., Long, D., Nitta, A., Smith, J. A., and Snedden, S. A.: 2006, ApJ **647**, L111

Bennett, C. L., Halpern, M., Hinshaw, G., Jarosik, N., Kogut, A., Limon, M., Meyer, S. S., Page, L., Spergel, D. N., Tucker, G. S., Wollack, E., Wright, E. L., Barnes, C., Greason, M. R., Hill, R. S., Komatsu, E., Nolta, M. R., Odegard, N., Peiris, H. V., Verde, L., and Weiland, J. L.: 2003, ApJS **148**, 1

Benson, A. J., Bower, R. G., Frenk, C. S., Lacey, C. G., Baugh, C. M., and Cole, S.: 2003, ApJ **599**, 38

Benson, A. J., Bower, R. G., Frenk, C. S., and White, S. D. M.: 2000, MNRAS **314**, 557

Benson, A. J., Lacey, C. G., Baugh, C. M., Cole, S., and Frenk, C. S.: 2002, MNRAS **333**, 156

Benson, A. J., Sugiyama, N., Nusser, A., and Lacey, C. G.: 2006, MNRAS **369**, 1055

Bertschinger, E.: 1989, ApJ **340**, 666

Binney, J.: 1977, ApJ **215**, 483

Binney, J. and Tremaine, S.: 1987, *Galactic dynamics*, Princeton, NJ, Princeton University Press, 1987, 747 p.

Birnboim, Y. and Dekel, A.: 2003, MNRAS **345**, 349

Black, J. H.: 1981, MNRAS **197**, 553

Blais-Ouellette, S., Carignan, C., Amram, P., and Côté, S.: 1999, AJ **118**, 2123

Blanton, M. R., Eisenstein, D., Hogg, D. W., and Zehavi, I.: 2006, ApJ **645**, 977

Blumenthal, G. R., Faber, S. M., Primack, J. R., and Rees, M. J.: 1984, Nature **311**, 517

Bolton, J. S. and Haehnelt, M. G.: 2007, MNRAS **382**, 325

Bolton, J. S., Viel, M., Kim, T.-S., Haehnelt, M. G., and Carswell, R. F.: 2008, MNRAS **386**, 1131

Booth, C. M., Theuns, T., and Okamoto, T.: 2007, MNRAS **376**, 1588

Bouché, N., Lehnert, M. D., and Péroux, C.: 2006, MNRAS **367**, L16

Bouwens, R. J., Illingworth, G. D., Franx, M., and Ford, H.: 2008, *ArXiv e-prints* 803

Bower, R. G., Benson, A. J., Malbon, R., Helly, J. C., Frenk, C. S., Baugh, C. M., Cole, S., and Lacey, C. G.: 2006, MNRAS **370**, 645

Bromm, V., Coppi, P. S., and Larson, R. B.: 2002, ApJ **564**, 23

Bromm, V. and Larson, R. B.: 2004, ARA&A **42**, 79

Bruzual, G. and Charlot, S.: 2003, MNRAS **344**, 1000

Bryan, G. L. and Norman, M. L.: 1997, in D. A. Clarke and M. J. West (eds.), *Computational Astrophysics; 12th Kingston Meeting on Theoretical Astrophysics*, Vol. 123 of *Astronomical Society of the Pacific Conference Series*, pp 363–+

Bryan, G. L. and Norman, M. L.: 1998, ApJ **495**, 80

Bullock, J. S., Kravtsov, A. V., and Weinberg, D. H.: 2000, ApJ **539**, 517

Bundy, K., Ellis, R. S., and Conselice, C. J.: 2005, ApJ **625**, 621

Bunker, A., Stanway, E., Ellis, R., McMahon, R., Eyles, L., and Lacy, M.: 2006, *New Astronomy Review* **50**, 94

Buote, D. A.: 2000, MNRAS **311**, 176

Carignan, C. and Freeman, K. C.: 1988, ApJ **332**, L33

Caucci, S., Colombi, S., Pichon, C., Rollinde, E., Petitjean, P., and Sousbie, T.: 2008, *ArXiv e-prints* 801

Cen, R., Miralda-Escudé, J., Ostriker, J. P., and Rauch, M.: 1994, ApJ **437**, L9

Cen, R. and Ostriker, J.: 1992, ApJ **393**, 22

Cen, R. and Ostriker, J. P.: 1993, ApJ **417**, 415

Cen, R. and Ostriker, J. P.: 1999a, ApJ **519**, L109

Cen, R. and Ostriker, J. P.: 1999b, ApJ **514**, 1

Cen, R. and Ostriker, J. P.: 1999c, ApJ **514**, 1

Cen, R. and Ostriker, J. P.: 2006, ApJ **650**, 560

Chabrier, G.: 2003, PASP **115**, 763

Chen, Y.-M., Wild, V., Kauffmann, G., Blaizot, J., Davis, M., Noeske, K., Wang, J.-M., and Willmer, C.: 2008, *ArXiv e-prints* 808

Ciardi, B., Stoehr, F., and White, S. D. M.: 2003, MNRAS **343**, 1101

Clowe, D., Bradač, M., Gonzalez, A. H., Markevitch, M., Randall, S. W., Jones, C., and Zaritsky, D.: 2006, ApJ **648**, L109

Coil, A. L., Newman, J. A., Croton, D., Cooper, M. C., Davis, M., Faber, S. M., Gerke, B. F., Koo, D. C., Padmanabhan, N., Wechsler, R. H., and Weiner, B. J.: 2008, ApJ **672**, 153

Cole, S.: 1991, ApJ **367**, 45

Cole, S., Aragon-Salamanca, A., Frenk, C. S., Navarro, J. F., and Zepf, S. E.: 1994, MNRAS **271**, 781

Cole, S., Lacey, C. G., Baugh, C. M., and Frenk, C. S.: 2000, MNRAS **319**, 168

Cole, S., Norberg, P., Baugh, C. M., Frenk, C. S., Bland-Hawthorn, J., Bridges, T., Cannon, R., Colless, M., Collins, C., Couch, W., Cross, N., Dalton, G., De Propris, R., Driver, S. P., Efstathiou, G., Ellis, R. S., Glazebrook, K., Jackson, C., Lahav, O., Lewis, I., Lumsden, S., Maddox, S., Madgwick, D., Peacock, J. A., Peterson, B. A., Sutherland, W., and Taylor, K.: 2001, MNRAS **326**, 255

Coles, P. and Lucchin, F.: 2002, *Cosmology: The Origin and Evolution of Cosmic Structure, Second Edition*, Cosmology: The Origin and Evolution of Cosmic Structure, Second Edition, by Peter Coles, Francesco Lucchin, pp. 512. ISBN 0-471-48909-3. Wiley-VCH , July 2002.

Colless, M., Dalton, G., Maddox, S., Sutherland, W., Norberg, P., Cole, S., Bland-Hawthorn, J., Bridges, T., Cannon, R., Collins, C., Couch, W., Cross, N., Deeley, K., De Propris, R., Driver, S. P., Efstathiou, G., Ellis, R. S., Frenk, C. S., Glazebrook, K., Jackson, C., Lahav, O., Lewis, I., Lumsden, S., Madgwick, D., Peacock, J. A., Peterson, B. A., Price, I., Seaborne, M., and Taylor, K.: 2001, MNRAS **328**, 1039

Cooley, J. W. and Tukey, J. W.: 1965, *Mathematics of Computation* **19**, 297

Couchman, H. M. P.: 1991, ApJ **368**, L23

Couchman, H. M. P. and Rees, M. J.: 1986, MNRAS **221**, 53

Cowie, L. L. and Songaila, A.: 1998, Nature **394**, 44

Cowie, L. L., Songaila, A., Hu, E. M., and Cohen, J. G.: 1996, AJ **112**, 839

Croft, R. A. C., Di Matteo, T., Springel, V., and Hernquist, L.: 2008, *ArXiv e-prints* 803

Croston, J. H., Pratt, G. W., Böhringer, H., Arnaud, M., Pointecouteau, E., Ponman, T. J., Sanderson, A. J. R., Temple, R. F., Bower, R. G., and Donahue, M.: 2008, A&A **487**, 431

Croton, D. J., Springel, V., White, S. D. M., De Lucia, G., Frenk, C. S., Gao, L., Jenkins, A., Kauffmann, G., Navarro, J. F., and Yoshida, N.: 2006, MNRAS **365**, 11

Crowl, H. H., Kenney, J. D. P., van Gorkom, J. H., and Vollmer, B.: 2005, AJ **130**, 65

Dalla Vecchia, C. and Schaye, J.: 2008, *ArXiv e-prints* 801

Danforth, C. W. and Shull, J. M.: 2005, ApJ **624**, 555

Danforth, C. W., Shull, J. M., Rosenberg, J. L., and Stocke, J. T.: 2006, ApJ **640**, 716

Davé, R., Cen, R., Ostriker, J. P., Bryan, G. L., Hernquist, L., Katz, N., Weinberg, D. H., Norman, M. L., and O'Shea, B.: 2001, ApJ **552**, 473

Davé, R., Finlator, K., and Oppenheimer, B. D.: 2006, MNRAS **370**, 273

Davé, R., Hernquist, L., Katz, N., and Weinberg, D. H.: 1999, ApJ **511**, 521

Davé, R. and Oppenheimer, B. D.: 2007, MNRAS **374**, 427

Davis, D. S., Mulchaey, J. S., and Mushotzky, R. F.: 1999, ApJ **511**, 34

Davis, M., Efstathiou, G., Frenk, C. S., and White, S. D. M.: 1985, ApJ **292**, 371

de Blok, W. J. G. and McGaugh, S. S.: 1997, MNRAS **290**, 533

De Lucia, G., Springel, V., White, S. D. M., Croton, D., and Kauffmann, G.: 2006, MNRAS **366**, 499

Dehnen, W.: 2000, ApJ **536**, L39

Dekel, A. and Silk, J.: 1986, ApJ **303**, 39

Di Matteo, T., Croft, R. A. C., Springel, V., and Hernquist, L.: 2004, ApJ **610**, 80

Di Matteo, T., Springel, V., and Hernquist, L.: 2005, Nature **433**, 604

Diemand, J., Kuhlen, M., Madau, P., Zemp, M., Moore, B., Potter, D., and Stadel, J.: 2008, Nature **454**, 735

Dolag, K., Borgani, S., Murante, G., and Springel, V.: 2008, *ArXiv e-prints* 808

Doroshkevich, A. G., Zel'dovich, Y. B., and Novikov, I. D.: 1967, *Soviet Astronomy* **11**, 233

Dressler, A.: 1980, ApJ **236**, 351

Drory, N., Bender, R., Feulner, G., Hopp, U., Maraston, C., Snigula, J., and Hill, G. J.: 2003, ApJ **595**, 698

Drory, N., Salvato, M., Gabasch, A., Bender, R., Hopp, U., Feulner, G., and Pannella, M.: 2005, ApJ **619**, L131

Dubinski, J. and Carlberg, R. G.: 1991, ApJ **378**, 496

Edmunds, M. G. and Phillipps, S.: 1997, MNRAS **292**, 733

Efstathiou, G.: 1992, MNRAS **256**, 43P

Efstathiou, G., Davis, M., White, S. D. M., and Frenk, C. S.: 1985, ApJS **57**, 241

Efstathiou, G., Lake, G., and Negroponte, J.: 1982, MNRAS **199**, 1069

Eggen, O. J., Lynden-Bell, D., and Sandage, A. R.: 1962, ApJ **136**, 748

Einstein, A.: 1915, *Sitzungsberichte der Königlich Preußischen Akademie der Wissenschaften (Berlin), Seite 844-847.* pp 844–847

Einstein, A.: 1916, *Annalen der Physik* **354**, 769

Eke, V. R., Baugh, C. M., Cole, S., Frenk, C. S., King, H. M., and Peacock, J. A.: 2005, MNRAS **362**, 1233

Eke, V. R., Navarro, J. F., and Frenk, C. S.: 1998a, ApJ **503**, 569

Eke, V. R., Navarro, J. F., and Frenk, C. S.: 1998b, ApJ **503**, 569

Ellison, S. L., Songaila, A., Schaye, J., and Pettini, M.: 2000, AJ **120**, 1175

Ettori, S., Dolag, K., Borgani, S., and Murante, G.: 2006, MNRAS **365**, 1021

Evrard, A. E.: 1988, MNRAS **235**, 911

Evrard, A. E.: 1990, ApJ **363**, 349

Evrard, A. E. and Henry, J. P.: 1991, ApJ **383**, 95

Evrard, A. E., Summers, F. J., and Davis, M.: 1994, ApJ **422**, 11

Ferland, G. J., Korista, K. T., Verner, D. A., Ferguson, J. W., Kingdon, J. B., and Verner, E. M.: 1998, PASP **110**, 761

Ferrara, A., Scannapieco, E., and Bergeron, J.: 2005, ApJ **634**, L37

Field, G. B.: 1972, ARA&A **10**, 227

Finoguenov, A., Burkert, A., and Böhringer, H.: 2003, ApJ **594**, 136

Flores, R., Primack, J. R., Blumenthal, G. R., and Faber, S. M.: 1993, ApJ **412**, 443

Font, A. S., Bower, R. G., McCarthy, I. G., Benson, A. J., Frenk, C. S., Helly, J. C., Lacey, C. G., Baugh, C. M., and Cole, S.: 2008, MNRAS pp 1000–+

Fontana, A., Pozzetti, L., Donnarumma, I., Renzini, A., Cimatti, A., Zamorani, G., Menci, N., Daddi, E., Giallongo, E., Mignoli, M., Perna, C., Salimbeni, S., Saracco, P., Broadhurst, T., Cristiani, S., D'Odorico, S., and Gilmozzi, R.: 2004, A&A **424**, 23

Forman, W., Jones, C., and Tucker, W.: 1985, ApJ **293**, 102

Freedman, W. L., Madore, B. F., Gibson, B. K., Ferrarese, L., Kelson, D. D., Sakai, S., Mould, J. R., Kennicutt, Jr., R. C., Ford, H. C., Graham, J. A., Huchra, J. P., Hughes, S. M. G., Illingworth, G. D., Macri, L. M., and Stetson, P. B.: 2001, ApJ **553**, 47

Frenk, C. S., Evrard, A. E., White, S. D. M., and Summers, F. J.: 1996, ApJ **472**, 460

Frenk, C. S., White, S. D. M., Bode, P., Bond, J. R., Bryan, G. L., Cen, R., Couchman, H. M. P., Evrard, A. E., Gnedin, N., Jenkins, A., Khokhlov, A. M., Klypin, A., Navarro, J. F., Norman, M. L., Ostriker, J. P., Owen, J. M., Pearce, F. R., Pen, U.-L., Steinmetz, M., Thomas, P. A., Villumsen, J. V., Wadsley, J. W., Warren, M. S., Xu, G., and Yepes, G.: 1999, ApJ **525**, 554

Friedman, A.: 1922, *Zeitschrift für Physik A Hadrons and Nuclei* **10**, 377

Fryxell, B., Olson, K., Ricker, P., Timmes, F. X., Zingale, M., Lamb, D. Q., MacNeice, P., Rosner, R., Truran, J. W., and Tufo, H.: 2000, ApJS **131**, 273

Fukugita, M., Nakamura, O., Okamura, S., Yasuda, N., Barentine, J. C., Brinkmann, J., Gunn, J. E., Harvanek, M., Ichikawa, T., Lupton, R. H., Schneider, D. P., Strauss, M. A., and York, D. G.: 2007, AJ **134**, 579

Fukugita, M. and Peebles, P. J. E.: 2004, ApJ **616**, 643

Fukushige, T. and Makino, J.: 1997, ApJ **477**, L9+

Gerritsen, J. P. E. and Icke, V.: 1997, A&A **325**, 972

Ghigna, S., Moore, B., Governato, F., Lake, G., Quinn, T., and Stadel, J.: 1998, MNRAS **300**, 146

Gingold, R. A. and Monaghan, J. J.: 1977, MNRAS **181**, 375

Giroux, M. L. and Shapiro, P. R.: 1996, ApJS **102**, 191

Gnedin, N. Y.: 2000, ApJ **542**, 535

Gnedin, O. Y., Kravtsov, A. V., Klypin, A. A., and Nagai, D.: 2004, ApJ **616**, 16

Goobar, A., Hannestad, S., Mörtsell, E., and Tu, H.: 2006, *Journal of Cosmology and Astro-Particle Physics* **6**, 19

Governato, F., Mayer, L., Wadsley, J., Gardner, J. P., Willman, B., Hayashi, E., Quinn, T., Stadel, J., and Lake, G.: 2004, ApJ **607**, 688

Governato, F., Willman, B., Mayer, L., Brooks, A., Stinson, G., Valenzuela, O., Wadsley, J., and Quinn, T.: 2007, MNRAS **374**, 1479

Graham, A. W.: 2001, AJ **121**, 820

Green, J. C., Wilkinson, E., and Morse, J. A.: 2003, in J. C. Blades and O. H. W. Siegmund (eds.), *Future EUV/UV and Visible Space Astrophysics Missions and Instrumentation. Edited by J. Chris Blades, Oswald H. W. Siegmund. Proceedings of the SPIE, Volume 4854, pp. 72-80 (2003).*, Vol. 4854 of *Presented at the Society of Photo-Optical Instrumentation Engineers (SPIE) Conference*, pp 72–80

Gunn, J. E. and Gott, J. R. I.: 1972, ApJ **176**, 1

Gunn, J. E. and Peterson, B. A.: 1965, ApJ **142**, 1633

Guo, Q. and White, S. D. M.: 2008, MNRAS **384**, 2

Guth, A. H.: 1981, Phys. Rev. D **23**, 347

Haardt, F. and Madau, P.: 2001, in D. M. Neumann and J. T. V. Tran (eds.), *Clusters of Galaxies and the High Redshift Universe Observed in X-rays*

Harfst, S., Theis, C., and Hensler, G.: 2006, A&A **449**, 509

Heckman, T. M., Armus, L., and Miley, G. K.: 1990, ApJS **74**, 833

Heckman, T. M., Lehnert, M. D., Strickland, D. K., and Armus, L.: 2000, ApJS **129**, 493

Hernquist, L. and Katz, N.: 1989, ApJS **70**, 419

Hernquist, L., Katz, N., Weinberg, D. H., and Miralda-Escudé, J.: 1996, ApJ **457**, L51+

Hernquist, L. and Springel, V.: 2003, MNRAS **341**, 1253

Hockney, R. W. and Eastwood, J. W.: 1981, *Computer Simulation Using Particles*, Computer Simulation Using Particles, New York: McGraw-Hill, 1981

Hoeft, M., Yepes, G., Gottlöber, S., and Springel, V.: 2006, MNRAS **371**, 401

Hopkins, A. M.: 2004, ApJ **615**, 209

Hoyle, F.: 1948, MNRAS **108**, 372

Hoyle, F. and Narlikar, J. V.: 1964, *Royal Society of London Proceedings Series A* **278**, 465

Hubble, E. and Humason, M. L.: 1931, ApJ **74**, 43

Huchra, J., Davis, M., Latham, D., and Tonry, J.: 1983, ApJS **52**, 89

Hughes, J. P.: 1989, ApJ **337**, 21

Hui, L. and Gnedin, N. Y.: 1997, MNRAS **292**, 27

Hultman, J. and Pharasyn, A.: 1999, A&A **347**, 769

Jeltema, T. E., Binder, B., and Mulchaey, J. S.: 2008, ApJ **679**, 1162

Jenkins, A., Frenk, C. S., Pearce, F. R., Thomas, P. A., Colberg, J. M., White, S. D. M., Couchman, H. M. P., Peacock, J. A., Efstathiou, G., and Nelson, A. H.: 1998, ApJ **499**, 20

Jenkins, A., Frenk, C. S., White, S. D. M., Colberg, J. M., Cole, S., Evrard, A. E., Couchman, H. M. P., and Yoshida, N.: 2001, MNRAS **321**, 372

Juneau, S., Glazebrook, K., Crampton, D., McCarthy, P. J., Savaglio, S., Abraham, R., Carlberg, R. G., Chen, H.-W., Le Borgne, D., Marzke, R. O., Roth, K., Jørgensen, I., Hook, I., and Murowinski, R.: 2005, ApJ **619**, L135

Kaiser, N.: 1991, ApJ **383**, 104

Kang, X., Jing, Y. P., Mo, H. J., and Börner, G.: 2005, ApJ **631**, 21

Katz, N.: 1992, ApJ **391**, 502

Katz, N. and Gunn, J. E.: 1991, ApJ **377**, 365

Katz, N., Hernquist, L., and Weinberg, D. H.: 1992, ApJ **399**, L109

Katz, N., Weinberg, D. H., and Hernquist, L.: 1996, ApJS **105**, 19

Kauffmann, G., Colberg, J. M., Diaferio, A., and White, S. D. M.: 1999, MNRAS **303**, 188

Kauffmann, G., White, S. D. M., and Guiderdoni, B.: 1993, MNRAS **264**, 201

Kauffmann, G., White, S. D. M., Heckman, T. M., Ménard, B., Brinchmann, J., Charlot, S., Tremonti, C., and Brinkmann, J.: 2004, MNRAS **353**, 713

Kay, S. T., Pearce, F. R., Jenkins, A., Frenk, C. S., White, S. D. M., Thomas, P. A., and Couchman, H. M. P.: 2000, MNRAS **316**, 374

Kay, S. T., Thomas, P. A., Jenkins, A., and Pearce, F. R.: 2004, MNRAS **355**, 1091

Kennicutt, Jr., R. C.: 1983, ApJ **272**, 54

Kennicutt, Jr., R. C.: 1998, ARA&A **36**, 189

Kim, D.-W., Fabbiano, G., and Trinchieri, G.: 1992, ApJ **393**, 134

Klypin, A., Kravtsov, A. V., Bullock, J. S., and Primack, J. R.: 2001, ApJ **554**, 903

Klypin, A. A. and Shandarin, S. F.: 1983, MNRAS **204**, 891

Kochanek, C. S., Pahre, M. A., Falco, E. E., Huchra, J. P., Mader, J., Jarrett, T. H., Chester, T., Cutri, R., and Schneider, S. E.: 2001, ApJ **560**, 566

Kodama, T., Balogh, M. L., Smail, I., Bower, R. G., and Nakata, F.: 2004, MNRAS **354**, 1103

Kravtsov, A. V.: 1999, *Ph.D. thesis*, AA(NEW MEXICO STATE UNIVERSITY)

Kravtsov, A. V., Klypin, A., and Hoffman, Y.: 2002, ApJ **571**, 563

Kravtsov, A. V., Klypin, A. A., Bullock, J. S., and Primack, J. R.: 1998, ApJ **502**, 48

Kravtsov, A. V., Nagai, D., and Vikhlinin, A. A.: 2005, ApJ **625**, 588

Lacey, C. and Cole, S.: 1993, MNRAS **262**, 627

Lacey, C. and Cole, S.: 1994, MNRAS **271**, 676

Lacey, C. and Silk, J.: 1991, ApJ **381**, 14

Larson, R. B., Tinsley, B. M., and Caldwell, C. N.: 1980, ApJ **237**, 692

Lehner, N., Savage, B. D., Richter, P., Sembach, K. R., Tripp, T. M., and Wakker, B. P.: 2007, ApJ **658**, 680

Li, Z., Wang, Q. D., Irwin, J. A., and Chaves, T.: 2006, MNRAS **371**, 147

Lilly, S. J., Le Fevre, O., Hammer, F., and Crampton, D.: 1996, ApJ **460**, L1+

Loken, C., Norman, M. L., Nelson, E., Burns, J., Bryan, G. L., and Motl, P.: 2002, ApJ **579**, 571

Lucy, L. B.: 1977, AJ **82**, 1013

Mac Low, M.-M. and Ferrara, A.: 1999, ApJ **513**, 142

Madau, P., Ferguson, H. C., Dickinson, M. E., Giavalisco, M., Steidel, C. C., and Fruchter, A.: 1996, MNRAS **283**, 1388

Mao, S., Mo, H. J., and White, S. D. M.: 1998, MNRAS **297**, L71

Marigo, P.: 2001, A&A **370**, 194

Martin, C. L.: 1999, ApJ **513**, 156

Martin, C. L.: 2005, ApJ **621**, 227

Mathews, W. G. and Brighenti, F.: 1998, ApJ **503**, L15+

Matsuda, Y. et al.: 2004, AJ **128**, 569

McCarthy, I. G., Babul, A., and Balogh, M. L.: 2002, ApJ **573**, 515

McCarthy, I. G., Balogh, M. L., Babul, A., Poole, G. B., and Horner, D. J.: 2004, ApJ **613**, 811

McCarthy, I. G., Frenk, C. S., Font, A. S., Lacey, C. G., Bower, R. G., Mitchell, N. L., Balogh, M. L., and Theuns, T.: 2008, MNRAS **383**, 593

McGaugh, S. S. and de Blok, W. J. G.: 1998, ApJ **499**, 41

McKee, C. F. and Ostriker, J. P.: 1977, ApJ **218**, 148

Mewe, R., Lemen, J. R., and van den Oord, G. H. J.: 1986, A&AS **65**, 511

Mihos, J. C. and Hernquist, L.: 1994, ApJ **437**, 611

Miralda-Escude, J. and Babul, A.: 1995, ApJ **449**, 18

Miralda-Escudé, J., Cen, R., Ostriker, J. P., and Rauch, M.: 1996, ApJ **471**, 582

Mo, H. J., Mao, S., and White, S. D. M.: 1998, MNRAS **295**, 319

Mo, H. J., Yang, X., van den Bosch, F. C., and Jing, Y. P.: 2004, MNRAS **349**, 205

Mo, H. J., Yang, X., van den Bosch, F. C., and Katz, N.: 2005, MNRAS **363**, 1155

Mohapatra, R. N., Antusch, S., Babu, K. S., Barenboim, G., Chen, M.-C., de Gouvêa, A., de Holanda, P., Dutta, B., Grossman, Y., Joshipura, A., Kayser, B., Kersten, J., Keum, Y. Y., King, S. F., Langacker, P., Lindner, M., Loinaz, W., Masina, I., Mocioiu, I., Mohanty, S., Murayama, H., Pascoli, S., Petcov, S. T., Pilaftsis, A., Ramond, P., Ratz, M., Rodejohann, W., Shrock, R., Takeuchi, T., Underwood, T., and Wolfenstein, L.: 2007, *Reports of Progress in Physics* **70**, 1757

Monaghan, J. J. and Gingold, R. A.: 1984, *Journal of Computational Physics* **52**, 374

Monaghan, J. J. and Lattanzio, J. C.: 1985, A&A **149**, 135

Moore, B., Governato, F., Quinn, T., Stadel, J., and Lake, G.: 1998, ApJ **499**, L5+

Moore, B., Quinn, T., Governato, F., Stadel, J., and Lake, G.: 1999, MNRAS **310**, 1147

Morris, S. L., Weymann, R. J., Savage, B. D., and Gilliland, R. L.: 1991, ApJ **377**, L21

Moshir, M., Kopan, G., Conrow, T., McCallon, H., Hacking, P., Gregorich, D., Rohrbach, G., Melnyk, M., Rice, W., Fullmer, L., White, J., and Chester, T.: 1990, in *Bulletin of the American Astronomical Society*, Vol. 22 of *Bulletin of the American Astronomical Society*, pp 1325–+

Motl, P. M., Burns, J. O., Loken, C., Norman, M. L., and Bryan, G.: 2004, ApJ **606**, 635

Murray, N., Quataert, E., and Thompson, T. A.: 2005, ApJ **618**, 569

Mushotzky, R., Loewenstein, M., Arnaud, K. A., Tamura, T., Fukazawa, Y., Matsushita, K., Kikuchi, K., and Hatsukade, I.: 1996, ApJ **466**, 686

Navarro, J. F. and Benz, W.: 1991, ApJ **380**, 320

Navarro, J. F., Frenk, C. S., and White, S. D. M.: 1995, MNRAS **275**, 720

Navarro, J. F., Frenk, C. S., and White, S. D. M.: 1996, ApJ **462**, 563

Navarro, J. F., Frenk, C. S., and White, S. D. M.: 1997, ApJ **490**, 493

Navarro, J. F., Hayashi, E., Power, C., Jenkins, A. R., Frenk, C. S., White, S. D. M., Springel, V., Stadel, J., and Quinn, T. R.: 2004, MNRAS **349**, 1039

Navarro, J. F. and White, S. D. M.: 1993, MNRAS **265**, 271

Navarro, J. F. and White, S. D. M.: 1994, MNRAS **267**, 401

Nicastro, F., Mathur, S., Elvis, M., Drake, J., Fang, T., Fruscione, A., Krongold, Y., Marshall, H., Williams, R., and Zezas, A.: 2005, Nature **433**, 495

Norman, M. L. and Bryan, G. L.: 1999, in S. M. Miyama, K. Tomisaka, and T. Hanawa (eds.), *Numerical Astrophysics*, Vol. 240 of *Astrophysics and Space Science Library*, pp 19–+

Okamoto, T., Eke, V. R., Frenk, C. S., and Jenkins, A.: 2005, MNRAS **363**, 1299

Okamoto, T., Gao, L., and Theuns, T.: 2008a, *ArXiv e-prints* 806

Okamoto, T., Nemmen, R. S., and Bower, R. G.: 2008b, MNRAS **385**, 161

Oke, J. B.: 1974, ApJS **27**, 21

Oppenheimer, B. D. and Davé, R.: 2006, MNRAS **373**, 1265

Oppenheimer, B. D. and Davé, R.: 2007, *ArXiv e-prints* 712

Oppenheimer, B. D. and Davé, R.: 2008a, MNRAS **387**, 577

Oppenheimer, B. D. and Davé, R. A.: 2008b, *ArXiv e-prints* 806

O'Shea, B. W., Nagamine, K., Springel, V., Hernquist, L., and Norman, M. L.: 2005, ApJS **160**, 1

Ouchi, M., Ono, Y., Egami, E., Saito, T., Oguri, M., McCarthy, P. J., Farrah, D., Kashikawa, N., Momcheva, I., Shimasaku, K., Nakanishi, K., Furusawa, H., Akiyama, M., Dunlop, J. S., Mortier, A. M. J., Okamura, S., Hayashi, M., Cirasuolo, M., Dressler, A., Iye, M., Jarvis, M. J., Kodama, T., Martin, C. L., McLure, R. J., Ohta, K., Yamada, T., and Yoshida, M.: 2008, *ArXiv e-prints*

Pagel, B. E. J.: 2002, in R. Fusco-Femiano and F. Matteucci (eds.), *Chemical Enrichment of Intracluster and Intergalactic Medium*, Vol. 253 of *Astronomical Society of the Pacific Conference Series*, pp 489–+

Peacock, J. A.: 1999, *Cosmological Physics*, Cosmological Physics, by John A. Peacock, pp. 704. ISBN 052141072X. Cambridge, UK: Cambridge University Press, January 1999.

Pedersen, K., Rasmussen, J., Sommer-Larsen, J., Toft, S., Benson, A. J., and Bower, R. G.: 2006, *New Astronomy* **11**, 465

Peebles, P. J. E.: 1970, AJ **75**, 13

Peebles, P. J. E.: 1971, Ap&SS **10**, 280

Peebles, P. J. E.: 1973, PASJ **25**, 291

Peebles, P. J. E.: 1974, ApJ **189**, L51+

Peebles, P. J. E.: 1980, *The large-scale structure of the universe*, Research supported by the National Science Foundation. Princeton, N.J., Princeton University Press, 1980. 435 p.

Peebles, P. J. E. and Dicke, R. H.: 1968, ApJ **154**, 891

Pen, U.-L.: 1997, *New Astronomy* **2**, 309

Pen, U.-L.: 1998, ApJS **115**, 19

Penton, S. V., Stocke, J. T., and Shull, J. M.: 2004, ApJS **152**, 29

Perlmutter, S., Aldering, G., Goldhaber, G., Knop, R. A., Nugent, P., Castro, P. G., Deustua, S., Fabbro, S., Goobar, A., Groom, D. E., Hook, I. M., Kim, A. G., Kim, M. Y., Lee, J. C., Nunes, N. J., Pain, R., Pennypacker, C. R., Quimby, R., Lidman, C., Ellis, R. S., Irwin, M., McMahon, R. G., Ruiz-Lapuente, P., Walton, N., Schaefer, B., Boyle, B. J., Filippenko, A. V., Matheson, T., Fruchter, A. S., Panagia, N., Newberg, H. J. M., Couch, W. J., and The Supernova Cosmology Project: 1999, ApJ **517**, 565

Péroux, C., McMahon, R. G., Storrie-Lombardi, L. J., and Irwin, M. J.: 2003, MNRAS **346**, 1103

Pettini, M.: 1999, in J. R. Walsh and M. R. Rosa (eds.), *Chemical Evolution from Zero to High Redshift*, pp 233–+

Pettini, M., Rix, S. A., Steidel, C. C., Adelberger, K. L., Hunt, M. P., and Shapley, A. E.: 2002a, ApJ **569**, 742

Pettini, M., Rix, S. A., Steidel, C. C., Hunt, M. P., Shapley, A. E., and Adelberger, K. L.: 2002b, Ap&SS **281**, 461

Pettini, M., Shapley, A. E., Steidel, C. C., Cuby, J.-G., Dickinson, M., Moorwood, A. F. M., Adelberger, K. L., and Giavalisco, M.: 2001, ApJ **554**, 981

Pfrommer, C., Enßlin, T. A., Springel, V., Jubelgas, M., and Dolag, K.: 2007, MNRAS **378**, 385

Pichon, C., Vergely, J. L., Rollinde, E., Colombi, S., and Petitjean, P.: 2001, MNRAS **326**, 597

Ponman, T. J., Allan, D. J., Jones, L. R., Merrifield, M., McHardy, I. M., Lehto, H. J., and Luppino, G. A.: 1994, Nature **369**, 462

Portinari, L., Chiosi, C., and Bressan, A.: 1998, A&A **334**, 505

Power, C.: 2003, *Ph.D. thesis*, THE UNIVERSITY OF DURHAM

Power, C., Navarro, J. F., Jenkins, A., Frenk, C. S., White, S. D. M., Springel, V., Stadel, J., and Quinn, T.: 2003, MNRAS **338**, 14

Pozzetti, L., Cimatti, A., Zamorani, G., Daddi, E., Menci, N., Fontana, A., Renzini, A., Mignoli, M., Poli, F., Saracco, P., Broadhurst, T., Cristiani, S., D'Odorico, S., Giallongo, E., and Gilmozzi, R.: 2003, A&A **402**, 837

Press, W. H. and Schechter, P.: 1974, ApJ **187**, 425

Prochaska, J. X., Herbert-Fort, S., and Wolfe, A. M.: 2005, ApJ **635**, 123

Prochaska, J. X. and Wolfe, A. M.: 1997, ApJ **474**, 140

Quilis, V.: 2004, MNRAS **352**, 1426

Quilis, V., Moore, B., and Bower, R.: 2000, *Science* **288**, 1617

Quinn, T., Katz, N., and Efstathiou, G.: 1996, MNRAS **278**, L49

Rao, S. M., Turnshek, D. A., and Nestor, D. B.: 2006, ApJ **636**, 610

Read, A. M. and Ponman, T. J.: 1998, MNRAS **297**, 143

Reed, D. S., Bower, R., Frenk, C. S., Jenkins, A., and Theuns, T.: 2007, MNRAS **374**, 2

Rees, M. J.: 1986, MNRAS **218**, 25P

Rees, M. J. and Ostriker, J. P.: 1977, MNRAS **179**, 541

Reiprich, T. H. and Böhringer, H.: 2002, ApJ **567**, 716

Renzini, A.: 1997, ApJ **488**, 35

Renzini, A.: 1998, *ArXiv Astrophysics e-prints*

Richstone, D., Ajhar, E. A., Bender, R., Bower, G., Dressler, A., Faber, S. M., Filippenko, A. V., Gebhardt, K., Green, R., Ho, L. C., Kormendy, J., Lauer, T. R., Magorrian, J., and Tremaine, S.: 1998, Nature **395**, A14+

Riess, A. G., Filippenko, A. V., Challis, P., Clocchiatti, A., Diercks, A., Garnavich, P. M., Gilliland, R. L., Hogan, C. J., Jha, S., Kirshner, R. P., Leibundgut, B., Phillips, M. M., Reiss, D., Schmidt, B. P., Schommer, R. A., Smith, R. C., Spyromilio, J., Stubbs, C., Suntzeff, N. B., and Tonry, J.: 1998, AJ **116**, 1009

Ritchie, B. W. and Thomas, P. A.: 2001, MNRAS **323**, 743

Robertson, B., Yoshida, N., Springel, V., and Hernquist, L.: 2004, ApJ **606**, 32

Roncarelli, M., Ettori, S., Dolag, K., Moscardini, L., Borgani, S., and Murante, G.: 2006, MNRAS **373**, 1339

Rupke, D. S., Veilleux, S., and Sanders, D. B.: 2005, ApJS **160**, 115

Ryan-Weber, E. V., Pettini, M., and Madau, P.: 2006, MNRAS **371**, L78

Salpeter, E. E.: 1955, ApJ **121**, 161

Sandvik, H. B., Möller, O., Lee, J., and White, S. D. M.: 2007, MNRAS **377**, 234

Sasaki, S.: 1996, PASJ **48**, L119

Savage, B. D., Lehner, N., Wakker, B. P., Sembach, K. R., and Tripp, T. M.: 2005, ApJ **626**, 776

Scannapieco, C., Tissera, P. B., White, S. D. M., and Springel, V.: 2005, MNRAS **364**, 552

Scannapieco, E. and Oh, S. P.: 2004, ApJ **608**, 62

Schaye, J.: 2004, ApJ **609**, 667

Schaye, J., Aguirre, A., Kim, T.-S., Theuns, T., Rauch, M., and Sargent, W. L. W.: 2003, ApJ **596**, 768

Schaye, J. and Dalla Vecchia, C.: 2008, MNRAS **383**, 1210

Schaye, J., Theuns, T., Rauch, M., Efstathiou, G., and Sargent, W. L. W.: 2000, MNRAS **318**, 817

Schmidt, M.: 1959, ApJ **129**, 243

Seljak, U. and Zaldarriaga, M.: 1996, ApJ **469**, 437

Sembach, K. R., Tripp, T. M., Savage, B. D., and Richter, P.: 2004, ApJS **155**, 351

Shapley, A. E., Steidel, C. C., Pettini, M., and Adelberger, K. L.: 2003, ApJ **588**, 65

Sheth, R. K. and Tormen, G.: 2002, MNRAS **329**, 61

Sijacki, D., Springel, V., di Matteo, T., and Hernquist, L.: 2007, MNRAS **380**, 877

Silk, J.: 1977, ApJ **211**, 638

Simcoe, R. A.: 2006, ApJ **653**, 977

Sirko, E.: 2005, ApJ **634**, 728

Sofue, Y. and Rubin, V.: 2001, ARA&A **39**, 137

Somerville, R. S.: 2002, ApJ **572**, L23

Somerville, R. S. and Primack, J. R.: 1999, MNRAS **310**, 1087

Sommer-Larsen, J. and Fynbo, J. P. U.: 2008, MNRAS pp 211–+

Sommer-Larsen, J., Gelato, S., and Vedel, H.: 1999, ApJ **519**, 501

Sommer-Larsen, J., Götz, M., and Portinari, L.: 2003, ApJ **596**, 47

Songaila, A. and Cowie, L. L.: 1996, AJ **112**, 335

Spergel, D. N., Bean, R., Doré, O., Nolta, M. R., Bennett, C. L., Dunkley, J., Hinshaw, G., Jarosik, N., Komatsu, E., Page, L., Peiris, H. V., Verde, L., Halpern, M., Hill, R. S., Kogut, A., Limon, M., Meyer, S. S., Odegard, N., Tucker, G. S., Weiland, J. L., Wollack, E., and Wright, E. L.: 2007, ApJS **170**, 377

Spergel, D. N., Verde, L., Peiris, H. V., Komatsu, E., Nolta, M. R., Bennett, C. L., Halpern, M., Hinshaw, G., Jarosik, N., Kogut, A., Limon, M., Meyer, S. S., Page, L., Tucker, G. S., Weiland, J. L., Wollack, E., and Wright, E. L.: 2003, ApJS **148**, 175

Springel, V.: 2005, MNRAS **364**, 1105

Springel, V. and Farrar, G. R.: 2007, MNRAS **380**, 911

Springel, V. and Hernquist, L.: 2002a, MNRAS **333**, 649

Springel, V. and Hernquist, L.: 2002b, MNRAS **333**, 649

Springel, V. and Hernquist, L.: 2003a, MNRAS **339**, 289

Springel, V. and Hernquist, L.: 2003b, MNRAS **339**, 312

Springel, V., White, S. D. M., Jenkins, A., Frenk, C. S., Yoshida, N., Gao, L., Navarro, J., Thacker, R., Croton, D., Helly, J., Peacock, J. A., Cole, S., Thomas, P., Couchman, H., Evrard, A., Colberg, J., and Pearce, F.: 2005, Nature **435**, 629

Springel, V., White, S. D. M., Tormen, G., and Kauffmann, G.: 2001a, MNRAS **328**, 726

Springel, V., Yoshida, N., and White, S. D. M.: 2001b, *New Astronomy* **6**, 79

Srbinovsky, J. and Wyithe, S.: 2008, *ArXiv e-prints* 807

Steidel, C. C., Adelberger, K. L., Shapley, A. E., Pettini, M., Dickinson, M., and Giavalisco, M.: 2000, ApJ **532**, 170

Steidel, C. C., Kollmeier, J. A., Shapley, A. E., Churchill, C. W., Dickinson, M., and Pettini, M.: 2002, ApJ **570**, 526

Strickland, D. K. and Stevens, I. R.: 2000, MNRAS **314**, 511

Stringer, M. J., Benson, A. J., Bundy, K., Ellis, R. S., and Quetin, E. L.: 2008, *ArXiv e-prints* 806

Sun, M., Jones, C., Forman, W., Vikhlinin, A., Donahue, M., and Voit, M.: 2007, ApJ **657**, 197

Sunyaev, R. A. and Zel'dovich, I. B.: 1980, ARA&A **18**, 537

Sutherland, R. S. and Dopita, M. A.: 1993, ApJS **88**, 253

Swaters, R. A., Madore, B. F., and Trewhella, M.: 2000, ApJ **531**, L107

Syer, D., Mao, S., and Mo, H. J.: 1999, MNRAS **305**, 357

Tasker, E. J., Brunino, R., Mitchell, N. L., Michielsen, D., Hopton, S., Pearce, F. R., Bryan, G. L., and Theuns, T.: 2008, *ArXiv e-prints* 808

Tassis, K., Abel, T., Bryan, G. L., and Norman, M. L.: 2003, ApJ **587**, 13

Thacker, R. J. and Couchman, H. M. P.: 2000, ApJ **545**, 728

Thacker, R. J. and Couchman, H. M. P.: 2001, ApJ **555**, L17

Thacker, R. J., Scannapieco, E., and Davis, M.: 2002, ApJ **581**, 836

Theuns, T., Leonard, A., Efstathiou, G., Pearce, F. R., and Thomas, P. A.: 1998, MNRAS **301**, 478

Theuns, T., Viel, M., Kay, S., Schaye, J., Carswell, R. F., and Tzanavaris, P.: 2002, ApJ **578**, L5

Thielemann, F.-K., Argast, D., Brachwitz, F., Hix, W. R., Höflich, P., Liebendörfer, M., Martinez-Pinedo, G., Mezzacappa, A., Panov, I., and Rauscher, T.: 2003, *Nuclear Physics A* **718**, 139

Thomas, P. A. and Couchman, H. M. P.: 1992, MNRAS **257**, 11

Thomas, P. A., Fabian, A. C., Arnaud, K. A., Forman, W., and Jones, C.: 1986, MNRAS **222**, 655

Thoul, A. A. and Weinberg, D. H.: 1996, ApJ **465**, 608

Toft, S., Rasmussen, J., Sommer-Larsen, J., and Pedersen, K.: 2002, MNRAS **335**, 799

Tormen, G.: 1997, MNRAS **290**, 411

Trac, H., Cen, R., and Loeb, A.: 2008, *ArXiv e-prints* 807

Tripp, T. M., Bowen, D. V., Sembach, K. R., Jenkins, E. B., Savage, B. D., and Richter, P.: 2006, in G. Sonneborn, H. W. Moos, and B.-G. Andersson (eds.), *Astrophysics in the Far Ultraviolet: Five Years of Discovery with FUSE*, Vol. 348 of *Astronomical Society of the Pacific Conference Series*, pp 341–+

Tripp, T. M., Savage, B. D., and Jenkins, E. B.: 2000, ApJ **534**, L1

Tüllmann, R., Pietsch, W., Rossa, J., Breitschwerdt, D., and Dettmar, R.-J.: 2006, A&A **448**, 43

van den Bosch, F. C. and Swaters, R. A.: 2001, MNRAS **325**, 1017

Veilleux, S., Cecil, G., and Bland-Hawthorn, J.: 2005, ARA&A **43**, 769

Vikhlinin, A., Kravtsov, A., Forman, W., Jones, C., Markevitch, M., Murray, S. S., and Van Speybroeck, L.: 2006, ApJ **640**, 691

Voit, G. M., Balogh, M. L., Bower, R. G., Lacey, C. G., and Bryan, G. L.: 2003, ApJ **593**, 272

Voit, G. M., Bryan, G. L., Balogh, M. L., and Bower, R. G.: 2002, ApJ **576**, 601

Wadsley, J. W., Stadel, J., and Quinn, T.: 2004, *New Astronomy* **9**, 137

Walker, I. R., Mihos, J. C., and Hernquist, L.: 1996, ApJ **460**, 121

Wang, Q. D.: 2007, in *EAS Publications Series*, Vol. 24 of *EAS Publications Series*, pp 59–72

Warwick, R. S., Jenkins, L. P., Read, A. M., Roberts, T. P., and Owen, R. A.: 2007, MNRAS **376**, 1611

Weil, M. L., Eke, V. R., and Efstathiou, G.: 1998, MNRAS **300**, 773

Weinmann, S. M., van den Bosch, F. C., Yang, X., Mo, H. J., Croton, D. J., and Moore, B.: 2006, MNRAS **372**, 1161

White, S. D. M.: 1994, *ArXiv Astrophysics e-prints*

White, S. D. M. and Frenk, C. S.: 1991, ApJ **379**, 52

White, S. D. M., Frenk, C. S., and Davis, M.: 1983, ApJ **274**, L1

White, S. D. M., Navarro, J. F., Evrard, A. E., and Frenk, C. S.: 1993, Nature **366**, 429

White, S. D. M. and Rees, M. J.: 1978, MNRAS **183**, 341

Wiersma, R. P. C., Schaye, J., and Smith, B. D.: 2008, *ArXiv e-prints* 807

Wilman, R. J., Gerssen, J., Bower, R. G., Morris, S. L., Bacon, R., de Zeeuw, P. T., and Davies, R. L.: 2005, Nature **436**, 227

Wise, J. H. and Abel, T.: 2007, ApJ **665**, 899

Wise, J. H. and Cen, R.: 2008, *ArXiv e-prints* 808

Xu, G.: 1995, ApJS **98**, 355

Yepes, G., Kates, R., Khokhlov, A., and Klypin, A.: 1995, in S. Maurogordato, C. Balkowski, C. Tao, and J. Tran Thanh van (eds.), *Clustering in the Universe*, pp 209–
+

Yepes, G., Kates, R., Khokhlov, A., and Klypin, A.: 1997, MNRAS **284**, 235

York, D. G., Adelman, J., Anderson, Jr., J. E., Anderson, S. F., Annis, J., Bahcall, N. A., Bakken, J. A., Barkhouser, R., Bastian, S., Berman, E., Boroski, W. N., Bracker, S., Briegel, C., Briggs, J. W., Brinkmann, J., Brunner, R., Burles, S., Carey, L., Carr, M. A., Castander, F. J., Chen, B., Colestock, P. L., Connolly, A. J., Crocker, J. H., Csabai, I., Czarapata, P. C., Davis, J. E., Doi, M., Dombeck, T., Eisenstein, D., Ellman, N., Elms, B. R., Evans, M. L., Fan, X., Federwitz, G. R., Fiscelli, L., Friedman, S., Frieman, J. A., Fukugita, M., Gillespie, B., Gunn, J. E., Gurbani, V. K., de Haas, E., Haldeman, M., Harris, F. H., Hayes, J., Heckman, T. M., Hennessy, G. S., Hindsley, R. B., Holm, S., Holmgren, D. J., Huang, C.-h., Hull, C., Husby, D., Ichikawa, S.-I., Ichikawa, T., Ivezić, Ž., Kent, S., Kim, R. S. J., Kinney, E., Klaene, M., Kleinman, A. N., Kleinman, S., Knapp, G. R., Korienek, J., Kron, R. G., Kunszt, P. Z., Lamb, D. Q., Lee, B., Leger, R. F., Limmongkol, S., Lindenmeyer, C., Long, D. C., Loomis, C., Loveday, J., Lucinio, R., Lupton, R. H., MacKinnon, B., Mannery, E. J., Mantsch, P. M., Margon, B., McGehee, P., McKay, T. A., Meiksin, A., Merelli, A., Monet, D. G., Munn, J. A., Narayanan, V. K., Nash, T., Neilsen, E., Neswold, R., Newberg, H. J., Nichol, R. C., Nicinski, T., Nonino, M., Okada, N., Okamura, S., Ostriker, J. P., Owen, R., Pauls, A. G., Peoples, J., Peterson, R. L., Petravick, D., Pier, J. R., Pope, A., Pordes, R., Prosapio, A., Rechenmacher, R., Quinn, T. R., Richards, G. T., Richmond, M. W., Rivetta, C. H., Rockosi, C. M., Ruthmansdorfer, K., Sandford, D., Schlegel, D. J., Schneider, D. P., Sekiguchi, M., Sergey, G., Shimasaku, K., Siegmund, W. A., Smee, S., Smith, J. A., Snedden, S., Stone, R., Stoughton, C., Strauss, M. A., Stubbs, C., SubbaRao, M., Szalay, A. S., Szapudi, I., Szokoly, G. P., Thakar, A. R., Tremonti, C., Tucker, D. L., Uomoto, A., Vanden Berk, D., Vogeley, M. S., Waddell, P., Wang, S.-i., Watanabe, M., Weinberg, D. H., Yanny, B., and Yasuda, N.: 2000, AJ **120**, 1579

Zel'dovich, Y. B.: 1970, A&A **5**, 84

Zhang, Y., Anninos, P., and Norman, M. L.: 1995, ApJ **453**, L57+

Zhang, Y., Anninos, P., Norman, M. L., and Meiksin, A.: 1997, ApJ **485**, 496

Zucker, D. B., Belokurov, V., Evans, N. W., Kleyna, J. T., Irwin, M. J., Wilkinson, M. I., Fellhauer, M., Bramich, D. M., Gilmore, G., Newberg, H. J., Yanny, B., Smith, J. A.,

Hewett, P. C., Bell, E. F., Rix, H.-W., Gnedin, O. Y., Vidrih, S., Wyse, R. F. G., Willman, B., Grebel, E. K., Schneider, D. P., Beers, T. C., Kniazev, A. Y., Barentine, J. C., Brewington, H., Brinkmann, J., Harvanek, M., Kleinman, S. J., Krzesinski, J., Long, D., Nitta, A., and Snedden, S. A.: 2006a, ApJ **650**, L41

Zucker, D. B., Belokurov, V., Evans, N. W., Wilkinson, M. I., Irwin, M. J., Sivarani, T., Hodgkin, S., Bramich, D. M., Irwin, J. M., Gilmore, G., Willman, B., Vidrih, S., Fellhauer, M., Hewett, P. C., Beers, T. C., Bell, E. F., Grebel, E. K., Schneider, D. P., Newberg, H. J., Wyse, R. F. G., Rockosi, C. M., Yanny, B., Lupton, R., Smith, J. A., Barentine, J. C., Brewington, H., Brinkmann, J., Harvanek, M., Kleinman, S. J., Krzesinski, J., Long, D., Nitta, A., and Snedden, S. A.: 2006b, ApJ **643**, L103

Zwaan, M. A., Meyer, M. J., Staveley-Smith, L., and Webster, R. L.: 2005, MNRAS **359**, L30

Zwicky, F.: 1933, *Helvetica Physica Acta* **6**, 110